Applying Satellite Geomagnetism to Probe Ocean Flow

Thesis submitted in accordance with the requirements of
the University of Liverpool for the degree of Doctor in Philosophy

by

James Brian Hawe

March 2009

Abstract

In this thesis, magnetic fields generated as a result of motional induction in the global oceans are investigated. Observations, from both ground and satellite based data sources, are used in conjunction with numerous analytical and statistical techniques to comprehensively study these fields on both global and local scales and in periodic and non-periodic regimes.

Research focuses on the magnetic signatures of three key flows; localised periodic circulation in the Argentine basin, global tides and large scale non-periodic wave motions in the form of oceanic Rossby waves. By studying these cornerstone flow types, it is hoped that the understanding of these magnetic fields and the limitations and possibilities of their future study can be greatly improved.

Analysis of the Argentine basin reveals several signs of magnetic field behaviour (in both satellite and observatory data) that correspond well with target circulation characteristics identified using oceanographic techniques. However, results are compromised by low magnetic field magnitudes and the possible presence of a global scale overprinting field with an origin that is possibly external to the Earth.

Study of tidally generated magnetic fields has two phases. The first presents a successful confirmation of previous work to isolate filtered tidal estimates, while the second phase advances this preliminary study to produce a multi-constituent tidal magnetic field model that provides unfiltered tidal field estimates for the first time (when working with magnetic observations). While this model correlates well with filtered tidal estimates, confirming the method's robustness, comparisons with numerical estimates of full tidal fields are less successful, particularly at ground level, suggesting the need for additional data processing and the inclusion of low altitude data in future models.

However, the study of Rossby waves is less successful. Despite the use of several image processing techniques (Radon and 2D Fourier transforms), few signs of Rossby wave activity are found in magnetic data, with minor peaks in plots of Radon transform variance (not in all cases) being the only results that correspond to theoretical estimates.

This work is concluded with a proposed plan of optimised future study, where investigation takes a top-down, global to local scale approach, favouring periodic flow over its non-periodic counterpart. In this way, it may be possible to both improve the study of each individual flow, whilst providing a larger number of future study targets.

Contents

List of Figures

List of Tables

Variable Notations, Mathematical Constants & Abbreviations

Variable Notations

β	Meridional gradient of coriolis parameter f (Planetary vorticity)
γ	Generalised least squares inversion data vector
Δf	2D-FT frequency axis pixel resolution
Δk	2D-FT wavenumber axis pixel resolution
Δt	LT plot time axis pixel resolution
Δx	LT plot longitude axis pixel resolution
ζ	Relative vorticity
θ	1. Co-latitude 2. Latitude (when considering the coriolis parameter f) 3. Rossby wave Radon transform angle
θ_0	Initial unperturbed fluid latitude (Rossby waves)
θ_1	1. Perturbed fluid latitude (Rossby waves) 2. Lower theoretical Rossby wave Radon transform target angle
θ_2	Upper theoretical Rossby wave Radon transform target angle
λ	Wavelength of a Rossby wave
σ	1. Model misfit standard deviation when conducting iterative tidal field modelling 2. Ocean conductivity (motional induction equations)
σ^2	3 component vector of isotropic tidal field modelling errors
σ_x^2	X component of isotropic data error vector σ^2
σ_y^2	Y component of isotropic data error vector σ^2
σ_z^2	Z component of isotropic data error vector σ^2
ϕ	Longitude
ϕ_1	Lower theoretical Rossby wave target angle in LT plots
ϕ_2	Upper theoretical Rossby wave target angle in LT plots
χ	Rotational uncertainty of a satellite star camera about its bore-sight
ψ	Angular uncertainty in the direction of a satellite star camera bore-sight

ω	Harmonic modelling signal frequency
∇	Gradient vector operator
∇_H	Horizontal component of the gradient vector operator
∂_t	Partial differential operator with respect to time
$\mathbf{A}$	Generalised least squares inversion operations matrix
$\mathbf{A^T}$	Transpose of operations matrix $\mathbf{A}$
$\mathbf{B}$	A 3 component main field model prediction (from CHAOS), used during multi-constituent tidal field modelling
B_ϕ	Geomagnetic field magnitude in eastward direction
B_θ	Geomagnetic field magnitude in southward direction
$\mathbf{B_e}$	A 3 component vector of along track filter values, used during multi-constituent tidal field modelling
B_{ex}	X component of along track filter vector $\mathbf{B_e}$
B_{ey}	Y component of along track filter vector $\mathbf{B_e}$
B_{ez}	Z component of along track filter vector $\mathbf{B_e}$
$\mathbf{B_{main}}$	Ambient geomagnetic field (motional induction equations)
$\mathbf{B_{ocean}}$	Secondary ocean generated magnetic field (motional induction equations)
B_r	Geomagnetic field magnitude in outward radial direction
$\mathbf{B_{rmain}}$	Ambient radial (predominantly dipolar) geomagnetic field, used during geostrophic/ageostrophic flow arguments (chapter 3)
B_x	X component of CHAOS predicted field vector $\mathbf{B}$
B_y	Y component of CHAOS predicted field vector $\mathbf{B}$
B_z	Z component of CHAOS predicted field vector $\mathbf{B}$
c	1. Tidal wave speed 2. Rossby wave phase speed
$\mathbf{C_e^{-1}}$	3×3 block diagonal error covariance matrix (used during multi-constituent tidal field modelling)
D	Magnetic field declination
$\mathbf{E}$	Local induced electric field (motional induction equations)
F	Magnetic field intensity
f	1. Coriolis parameter/planetary vorticity 2. Frequency (2D-FTs)
$+f$	Maximum coriolis parameter within a system (North pole on Earth)
$-f$	Minimum coriolis parameter within a system (South pole on Earth)
f_0	Coriolis Parameter at reference latitude θ_0
$\mathbf{F_c}$	Coriolis force
g_n^m	Cosine Gauss co-efficient for a harmonic degree n and order m
H	1. Radon transform of an image h 2. 2D-FT of an image h

	3. Geomagnetic field direction projected onto the horizontal plane
h	1. A time dependent image of a scalar field
	2. Water column depth
h_n^m	Sine Gauss co-efficient for a harmonic degree n and order m
$\mathbf{I}$	3×3 identity matrix
I	Magnetic field inclination
$\mathbf{J}$	Local electric current density (motional induction equations)
k	Wavenumber
k_n^m	Cosine Gauss co-efficient for a harmonic degree n and order m
l_n^m	Sine Gauss co-efficient for a harmonic degree n and order m
M	1. Unknown harmonic magnitude to be found using harmonic modelling
	2. Number of pixels along the longitude axis of an image when conducting 2D-FTs
$\mathbf{m}$	A vector of model parameters derived during generalised least squares inversion
m	1. Spherical harmonic order
	2. Longitude axis pixel index of an image when conducting 2D-FTs
$M(t_i)$	Observed magnetic field at time t
M_i	Sine harmonic modelling parameter
M_o	Unmodulated, static harmonic modelling parameter
M_r	Cosine harmonic modelling parameter
$M_x(t_i)$	X component of multi-constituent tidal field modelling data vector γ
$M_y(t_i)$	Y component of multi-constituent tidal field modelling data vector γ
$M_z(t_i)$	Z component of multi-constituent tidal field modelling data vector γ
N	1. Truncation degree of a spherical harmonic expansion
	2. Number of pixels along the time axis of an image when conducting 2D-FTs
$\hat{\mathbf{n}}$	A unit vector describing satellite attitude (for use in multi-constituent tidal field modelling)
n	Degrees of freedom available when determining statistical significances of correlations and coherences
n	1. Spherical harmonic degree
	2. Number of input series in an EOF or CEOF analysis
	3. Rossby wave mode number
	4. Time axis pixel index of an image when conducting 2D-FTs
$\mathbf{P_n^m}$	Legendre function at harmonic degree n and order m
p	1. Length of data vector γ
	2. Wavenumber axis pixel index of a 2D-FT
q	1. Length of model parameter vector $\mathbf{m}$
	2. Frequency axis pixel index of a 2D-FT
q_n^m	Sine Gauss co-efficient for a harmonic degree n and order m

r	Altitude of an observation when modelling using spherical harmonic expansions
s_n^m	Cosine Gauss co-efficient for a harmonic degree n and order m
t	1. Time 2. Y-axis of an image when applied to Radon transforms and 2D-FTs
t'	Y-axis of an LT plot, rotated by angle θ when applying to the Radon transform
t_i	Time of observation for a data point during multi-constituent tidal field modelling
$\mathbf{u}$	1. Flow velocity 2. Geostrophic flow velocity
u	Mean East-West background flow speed (when calculating Rossby wave phase speeds)
$\mathbf{V}$	Scalar potential field
X	Geomagnetic field magnitude in northward direction
x	X-axis of an image when applied to Radon transforms and 2D-FTs
$\hat{x}$	X component of satellite attitude unit vector $\hat{\mathbf{n}}$
x'	X-axis of LT plots, rotated by angle θ when applying to the Radon transform
Y	Geomagnetic field magnitude in eastward direction
y	Meridional displacement from a reference latitude θ_0 (Rossby waves)
$\hat{y}$	Y component of satellite attitude unit vector $\hat{\mathbf{n}}$
Z	Geomagnetic field magnitude in an inward radial direction
$\hat{z}$	Z component of satellite attitude unit vector $\hat{\mathbf{n}}$

Mathematical Constants

μ_0	$4\pi \times 10^{-7}$ Hm^{-1} (Magnetic permeability)
Ω	7.29×10^{-5} $\mathrm{rad.s}^{-1}$ (Earth's rotation rate)
a	6371.2 km (Earth's radius)
g	9.81 $\mathrm{m.s}^{-2}$ (Gravitational acceleration)

Abbreviations/Acronyms

2D-FT	2 Dimensional Fourier Transform
Ørsted	A Danish maintained geomagnetic field observation satellite, named

	after Hans Christian Ørsted (1777-1851 A.D.)
ACC	Antarctic Circumpolar Current
AIA	Vernadsky magnetic observatory (Faraday/Argentine Islands)
BGS	British Geological Survey
CEOF	Complex Empirical Orthogonal Function
CHAMP	CHAllenging Minisatellite Payload (German Earth observation satellite)
CHAOS	CHAmp, Ørsted & Sac-c derived geomagnetic field model
CM4	Comprehensive Model 4 (geomagnetic field model)
CO2003	A geomagnetic field model derived using CHAMP, Ørsted & SAC-C data (Holme et al. [2003])
CONAE	Argentine commission on space activities (a collaborator of the SAC-C satellite mission)
cpd	Cycles Per Day (used as a unit of frequency during Argentine basin signal analysis)
DLR	The German space agency
DMI	Danish Meteorological Institute (responsible for Ørsted data distribution and satellite maintainence)
Dst	Disturbance storm time magnetic index
Dst/dt	Time derivative of the Dst index
EOF	Empirical Orthogonal Function
ETOP02v2	2 minute resolution, global relief model (satellite derived surface topography and ocean bathymetry)
FACs	Field Aligned Currents (external magnetic field phenomena)
GEOSPACE	Geomagnetic Earth Observation from SPACE (scientific consortium)
GFZ	The German research centre for geoscientists (located in Potsdam, Germany)
gufm1	Historical geomagnetic field model by Jackson et al. [2000] (1590-1990 A.D.)
ICOM	Imperial College Ocean Model
IGRF	International Geomagnetic Reference Field (model)
IMF	Interplanetary Magnetic Field (used in external magnetic field studies and geomagnetic field model parameterisation)
Kp	A planetary index of K-indices, a measure of geomagnetic external field activity
LT	Longitude/Time (plot)
MAGSAT	MAGnetic field SATellite (the first dedicated geomagnetic field observing satellite)
MF4	Magnetic Field model 4 (lithospheric)
MJD	Modified Julian Days (time reference, post year 2000.0)
NASA	National Aeronautics and Space Administration (US space Agency)
NEC	North, East, Centre (co-ordinate system)

NGDC	National Geophysical Data Centre
NGK	Neimgk magnetic observatory (Germany)
OCCAM	the Ocean Circulation and Climate Advanced Modelling project (ocean circulation model)
OGCM	Ocean General Circulation Model
PCn	Polar Cap magnetic index (North pole)
POGO	Polar Orbiting Geophysical Observatory (a source of early satellite geomagnetic field observations)
POLCOMS	the Proudman Oceanographic Laboratory Coastal Ocean Modelling System
PST	Port Stanley magnetic observatory (Falkland Islands)
PV	Potential Vorticity (a fluid dynamical quantity associated with fluid rotation)
SAC-C	Scientific Applications Satellite -C (Argentine Earth observation satellite)
SHA	Spherical Harmonic Analysis
Sq	the Solar Quiet external field current system
SSH	Sea Surface Height
SST	Sea Surface Temperature
SWARM	The Earth's magnetic field and environment explorers (3 satellite constellation)
TOPEX/ POSEIDON	the ocean TOPography EXperiment/named after the Greek god of the ocean, Poseidon (ocean observation satellite)
WDMAM	World Digital Magnetic Anomaly Map (lithospheric field)

Acknowledgements

I would like to take this opportunity to thank the numerous people that have advised and supported me during my 4 years of postgraduate research.

Firstly I would like to thank Richard Holme for his persistent support, were it not for his tireless patience I doubt this project would have ever reached completion. I would also like to thank him for his invaluable input on numerous technical matters, his knowledge of geomagnetism and field modelling in particular have provided much food for thought.

I would also like to thank Chris Hughes for being a continued source of information and guidance on all oceanographic issues.

Rob Tyler also deserves my deepest thanks for his support during my 3 month stay in Seattle, along with the invaluable insights into electromagnetic induction he provided during our many discussions. I would also like to thank Nel and Keith, for their warmth and hospitality during my stay.

The GEOSPACE consortium and its members also deserve a great deal of thanks, for the initiation of this project and also their continued scientific support and suggestions.

I would also like to thank all my colleagues in the Earth and Ocean Sciences department who have made the last four years so enjoyable. In particular I would like to thank Ed Horncastle, Ben Edwards, Vijay Tymms, Neil Hurst, John Watson, Chris Cooper and Alex Lodge, all of whom helped me retain a little sanity, particularly during the last 12 months.

NERC must also receive thanks for providing the studentship that has helped support me financially throughout the project.

Finally, special thanks must go to my family for their never ending support and understanding, without them this thesis would never have been written.

Chapter 1

Introduction

1.1 Overview

Since circa 1600 A.D. the geomagnetic field has been recognised as an integral component of the complex Earth system. While many aspects of the geomagnetic field have been extensively investigated in recent years, attention tends to focus on the large contributions made from the core, lithosphere and external sources. One source to receive little attention is the ocean. Although it may seem unlikely that the global oceans can contribute to the geomagnetic field, simple physical mechanisms allow the flowing oceans to generate their own magnetic signature, courtesy of the magnetic field produced in the core. In recent years ($\sim$15 years), interest in this topic has steadily grown, giving rise to several research projects such as this one, which all hope to explore the role ocean flow has within the already complex geomagnetic system.

In this chapter, background information relevant to this work will be discussed. Initially describing the geomagnetic field and how we observe and learn from it, this introduction will then outline the various large scale sources of Earth's magnetic field and their characteristics. Following this description will be a discussion of the mechanism that generates ocean magnetic signals and the characteristics different modes of ocean flow transmit into their magnetic counterparts. The chapter will conclude by outlining the aims and structure of the research contained within this thesis.

1.2 Earth's Magnetic Field

1.2.1 Geomagnetic Field Observations: Past & Present

Observation of Earth's magnetic field is not something new. For around a thousand years man has been taking direct measurements of the geomagnetic field. However, until the 16th century these tended to be isolated occurances. Only with the advent of maritime voyages and the increased use of the compass, did measurement of Earth's magnetic field become

a widespread activity. Although relatively sparse, this information is invaluable to field modellers, as when it is combined with newer, high precision satellite and observatory data, models which replicate Earth's magnetic field to extremely high accuracy can be derived [Jackson et al., 2000].

Continual monitoring of the geomagnetic field is not a simple task, although with current technology it is possible to measure its strength and direction using high precision scalar and vector magnetometers. In fact, due to the work of Carl-Fredrich Gauss [1777 A.D - 1855 A.D.] (who in addition to other revolutionary ideas, developed the first widely used technique of magnetic intensity measurement), magnetic observatories currently measure the geomagnetic field at the Earth's surface with great accuracy. However, it was the introduction of geomagnetic field observation satellites that would change the face of geomagnetism forever. With this advancement, researchers were able to study the geomagnetic field with near global data coverage and, coupled with the high temporal resolution of observatory data, new models describing the evolution of the geomagnetic field were derived (see Bloxham and Jackson [1992]). Since then, newer, more accurate satellite missions have been launched (e.g. CHAMP, Ørsted and SAC-C), once again providing high quality, global data with even greater accuracy than achieved previously.

In recent times, interest in the geomagnetic field of the past has grown substantially. By sampling magnetised rock, both in the form of igneous outcrops and sediments, along with some archaeological artifacts (typically ceramics and pottery), it is possible to remotely measure the intensity, and occasionally direction of Earth's magnetic field from the time of emplacement. However, due to geological constraints (i.e magmatic and archaeological locations), coupled with the large uncertainties in field measurements and age dating of samples, reliable samples are sparse. Recently this has changed with the introduction of microwave based field sampling. Rather than heat the sample to retrieve a field measurement, risking thermal alteration and contamination of the sample, it is bombarded with microwaves, allowing paleomagnetists to resolve magnetic field components within the sample without direct heating. This greatly reduces alteration, increasing the number of reliable samples available for use in paleomagnetic studies. Using these paleomagnetic samples it has been shown that a magnetic field has persisted on Earth for at least the last 3.5 billion years (see figure 1.1). This figure may be larger, although the chances of verifying this are low due to the constant reworking of surface material back into the Earth's interior. In either case, the data we have is enough to study the large scale behaviour of the geomagnetic field on times scales of thousands to millions of years. By studying such processes from the past, scientists hope to predict when such events may occur in the future, an example being a field reversal, another of which according to predictions, is overdue. Modellers are also able to use such data to construct field models that can replicate in detail, Earth's magnetic field spanning several millenia (see Korte et al. [2005] & Korte and Constable [2005]).

Earth's magnetic field can be thought of as a vector potential field, represented by 7 distinct

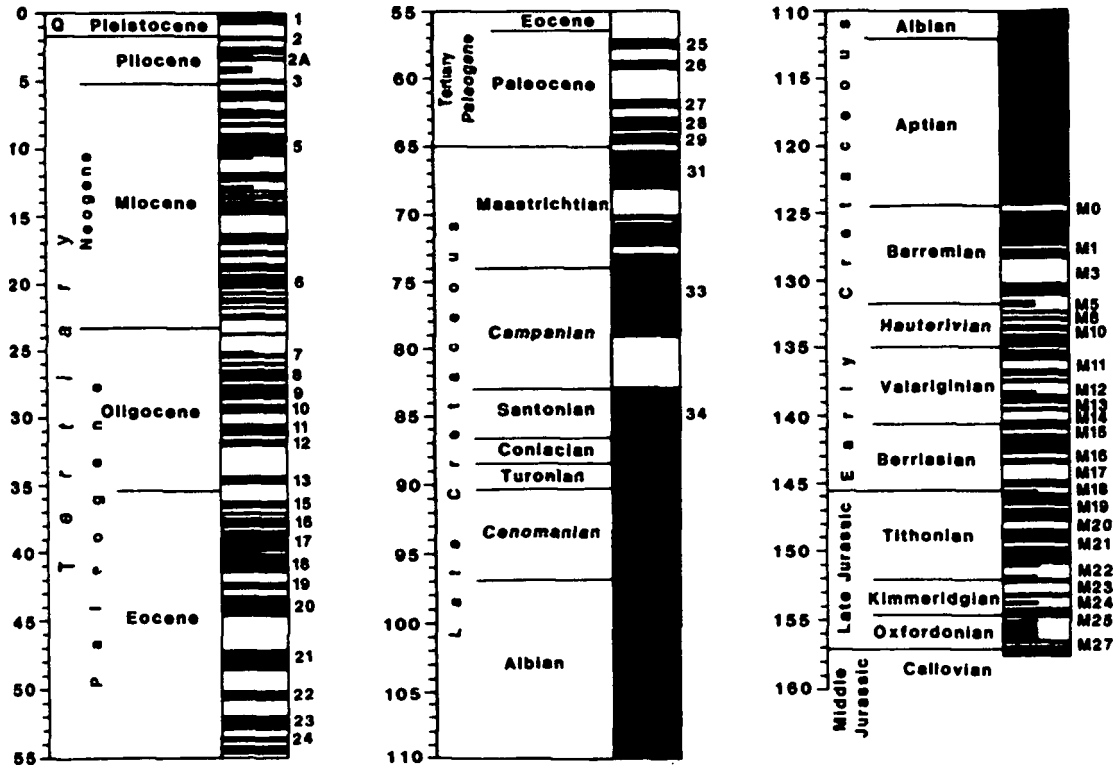

Figure 1.1: An illustration of Earth's magnetic field polarity history for the last 160 million years. Black sections denote periods of normal polarity and white sections reversed polarity. Note that the extremely long period of normal polarity in the Cretaceous is considerably longer than anything before or since. *From Fowler [1990]*

parameters (although only a few are needed to reconstruct the field). Figure 1.2 shows these parameters in their realistic configuration.

Of the 5 directional field parameters, only 2 are scalar values ($F = \left(\sqrt{X^2 + Y^2 + Z^2}\right)$ is the full scalar intensity and $H = \left(\sqrt{X^2 + Y^2}\right)$ is the horizontal component of F). Note that if only these parameters are available, the vector characteristics of the geomagnetic field cannot be understood. The remaining three parameters are (along with F) the primary field values used in this research, and are able to determine any of the other 4 field values. If the geomagnetic field is considered in NEC co-ordinates, the three elements represent X(North), Y(East) and Z(centre), but are also often represented in spherical co-ordinates, transforming each component so that $B_\theta = -X$, $B_\phi = Y$ and $B_r = -Z$.

1.2.2 Large Scale Field Sources

Compared to the large magnitude field from the core, ocean generated fields have a very small amplitude. Therefore to study these fields in detail it is important to understand the other major field sources within the geomagnetic system. This section will address each of the 3 major field sources (moving radially outwards) in turn, discussing its origins and

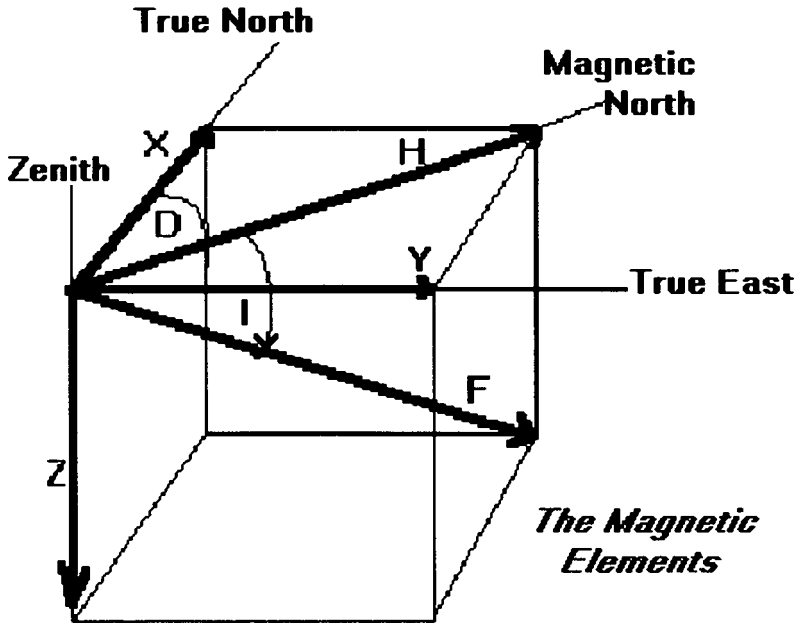

Figure 1.2: A graphical representation of geomagnetic field components and their directional relationships. Note that only two of the 7 field elements are non-directional, with declination (D) being the angular separation of North and the horizontal field direction and inclination (I) being the angle between the full field direction and its horizontal expression. *Taken from ngdc.noaa.gov*

operational mechanisms.

Main Core Field: The magnetic field emanating from the Earth's core is thought to constitute over 97% of the total geomagnetic field, generated by the flowing outer core that surrounds Earth's central inner core. However, many mysteries still remain about this field source and its underlying mechanisms, making it one of the more vigorously studied geomagnetic field sources.

At Earth's centre lies a metallic core, consisting of a predominantly solid iron inner core, surrounded by a slightly less dense convecting outer core, thought to consist of iron and a small percentage of other 'light' elements (although which ones remains a contentious issue). Seismic evidence currently places the radius of the inner core at $\sim$ 1000km [Stevenson, 1981], although this number continues to grow due the solidification of outer core material into the inner core as the Earth cools (see Buffet et al. [1992]). It is this solidification, coupled with the buoyant movement of lighter elements through the outer core and radioactive heating that causes the outer core to convect. How though, does this convection generate the magnetic field we observe? The answer lies in a mechanism known as the geodynamo (see Buffet [2000] among others), a process capable of sustaining the geomagnetic field over a prolonged period of time. The theory of geodynamo action is one which conveniently links an initial magnetic field (one candidate being the interplanetary magnetic field) and fluid motions in the outer

core. Due to the predominantly metallic nature of the outer core, it behaves as a flowing conductor. Therefore, given an initial magnetic field, as the outer core flows through it electric currents are induced within the fluid, which subsequently generate secondary magnetic fields due to basic laws of electromagnetism. In the case of a rotating body (such as the Earth), coriolis forces arising from Earth's rotation tend to organise these electric currents into rolls aligned to the rotational axis generating the coriolis force. At this point two distinctly different scenarios can occur. The first is that the secondary field counteracts the initial magnetic field and they cancel, eventually leaving the body with no magnetic field. The second (as is the case on Earth) is that the configuration of the secondary field enhances the initial field, facilitating its continuous replenishment as it decays, allowing the magnetic field of the body to remain while outer core convection persists. However, processes that occur in the core are extremely complex and so it is only in recent years that advances in technology have provided the computing power required to model the dynamics of the geodynamo numerically (see Roberts and Glatzmaier [2000]) in a manner realistic enough to complement experimental results (Berhanu et al. [2007], Gillet et al. [2007]).

As the core magnetic field of Earth is driven by fluid motion, it varies on a range of time-scales. As previously discussed, full polarity reversals of the core field are the longest period processes currently known to exist, but at shorter periods a host of other processes occur. Chief amongst these are geomagnetic jerks and the most well known feature of the core field, westward drift. Geomagnetic jerks occupy the high frequency end of core field processes currently observed, along with more general secular variation, with time scales in the order of years. However, other wave processes internal to the Earth's core (e.g. gravity waves) are thought to operate on shorter time-scales, although such processes are difficult to observe with current technology. Jerks, easily identified as abrupt changes of gradient in plots of ground observatory secular variation [Mandea and Mouël, 2000], have also been recently linked with changes in the length of day [Holme and de Viron, 2005], hinting at an internal source for this process. While jerks represent some of the most rapidly varying core features and field reversals some of the slowest, westward drift lies somewhere in between the two with a time scale of centuries to millenia. Westward drift (Bullard et al. [1950], Mouël et al. [1981], Bloxham and Gubbins [1985], Bloxham et al. [1989]), first observed by Halley in the 17th century, is well known as the process by which high magnitude magnetic flux patches drift westward over time and is also noticeable when studying the temporal evolution of other magnetic elements using field models such as *gufm1* [Jackson et al., 2000] (although the drift velocity is not uniform globally). In an effort to solve this issue and many others, much effort has been made to determine the physical mechanism responsible for the presence of westward drift in the magnetic record.

Lithospheric Field: While other major magnetic field sources show temporal variation, the lithospheric field is to a large extent static through time (at least on observable

time scales). The magnetic field due to magnetisation of the crust and lithosphere of Earth has two parts. The first can be attributed to induction in the lithosphere due to the core field and varies both temporally and spatially. The second is static with time and represents the remnant magnetisation captured in the lithosphere and crust as it formed, achieved during cooling after emplacement. The magnetic minerals within the rock align to match the direction of the ambient magnetic field and as the sample cools below the Curie temperature for each mineral, the orientation of the field is frozen into that mineral. Magnetisation can also occur during or shortly after sediment deposition, or chemically as minerals (such as magnetite) form. As such, it is possible to trace the history of the magnetic field in many geological settings (Purucker and Dyment [2000], Hemant and Maus [2005] & Maus et al. [2006]), although striping in ocean basins where a spreading ridge is active (e.g. in the Atlantic) is one of the clearest examples.

Although the lithospheric field has a much lower magnitude than that of the core, it can still tell us a great deal about the small scale structure of the crust. At larger length scales, the lithospheric field tends to be swamped by contributions from the core, but due to attenuation of the small scale core field, it is possible to infer geological features of the lithosphere and crust from the smaller magnetic length scales we are able to observe. For many years, exploration geophysicists have conducted aeromagnetic surveys as a means of gaining a regional understanding of lithospheric fields on very small length scales. Unfortunately, levelling problems between surveys, combined with the time and resource consuming method of surveying, mean that global coverage using such an approach is difficult to achieve, although with the advent of high precision satellites such as CHAMP, it is now possible to derive models of the lithospheric field with unprecedented resolution and accuracy. The most popular lithospheric field model currently in circulation is the MF series, now in its fifth generation [Maus et al., 2007a]. With this current generation of satellite derived lithospheric field models it is possible to identify widely recognisable geological features, as illustrated in figure 1.3.

However, by implementing more sophisticated analysis techniques, the gap in spatial resolution between satellite derived field models and aeromagnetic surveys is gradually closing. The ultimate goal is to combine the two approaches, producing a product which covers a whole spectrum of length scales, ranging from the 1000km scale achieved by satellites to the 10km resolution achieved by aeromagnetic surveys. The first completed product from this effort has been the World Digital Magnetic Anomaly Map (WDMAM), released in 2007 (see Maus et al. [2007b]). This map successfully meshes the latest satellite derived models with large volumes of re-leveled aeromagnetic survey data, achieving near global coverage of the Earth's lithospheric field on very small length scales. Figure 1.4 illustrates the level of detail this approach can achieve.

External Field: Earth's external magnetic field is an extremely complex system, with many inter-linking components and is too complicated to cover in great detail here. Unlike other geomagnetic field sources, external fields are heavily influenced by factors outside

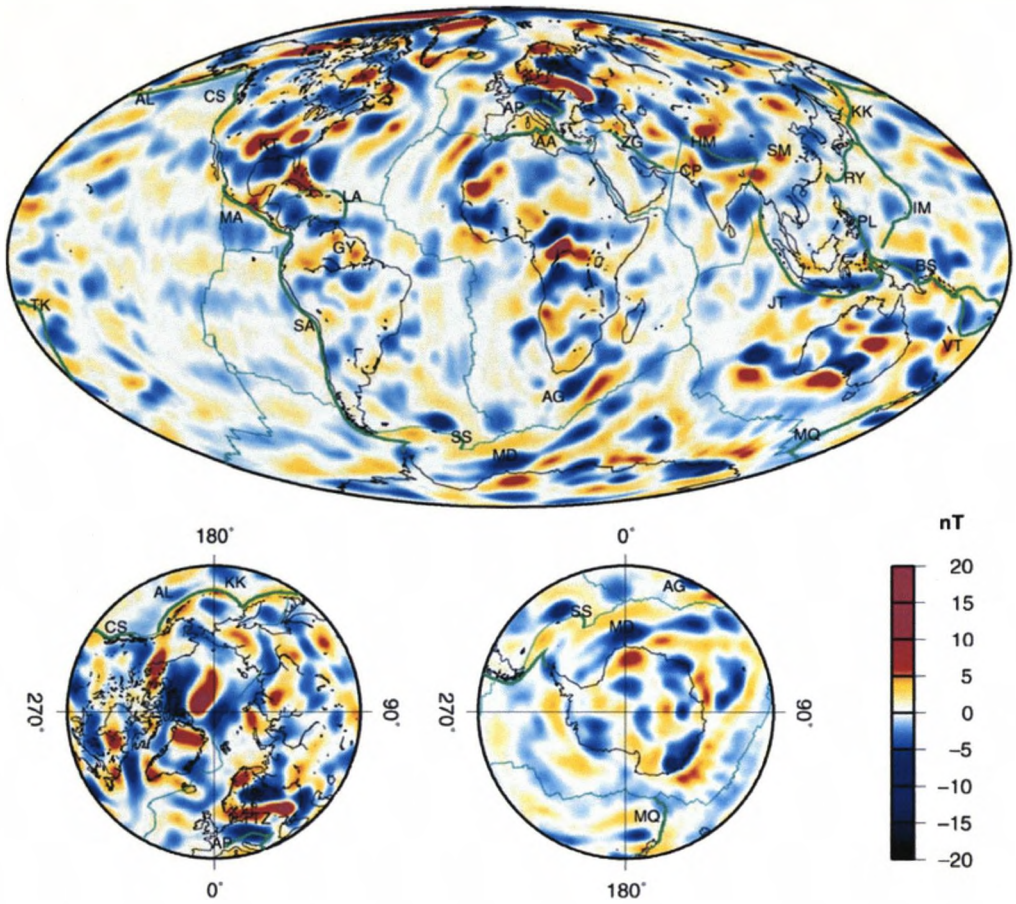

Figure 1.3: Plots of the lithospheric field (vertical component) at an altitude of 400km (from MF4). Subduction zones are highlighted by thick green lines and plate boundaries with thin green lines. It is possible to identify features such as the Bangui and Kursk anomalies, as well the magnetic striping associated with the mid Atlantic ridge system. *Taken from Maus et al. [2006].* The upper plot displays a global map of the lithospheric field, while the lower 2 plots show North (left) and South (right) polar field projections.

the Earth system. Figure 1.5 illustrates the various sources of the Earth's external field schematically.

Unlike other field sources whose generation regions are restricted to the solid earth, current systems responsible for external field generation occupy a much larger volume, with the resulting fields often extending between 10 and 40+ earth radii into space, depending on how you are oriented [Kivelson and Russell, 1995] (fields facing the Sun are compressed by the solar wind). Note that while affecting external field morphology, the interplanetary magnetic field and solar wind also directly influence the electric currents responsible for external field generation, meaning that records of solar wind and interplanetary magnetic field correlate strongly with external magnetic field strength.

Fortunately, this complex system can be broken into key current systems, each operating in a different region of space. Ionospheric fields comprise the equatorial and auroal electrojets, along with the magnetic field associated with the Sq current system.

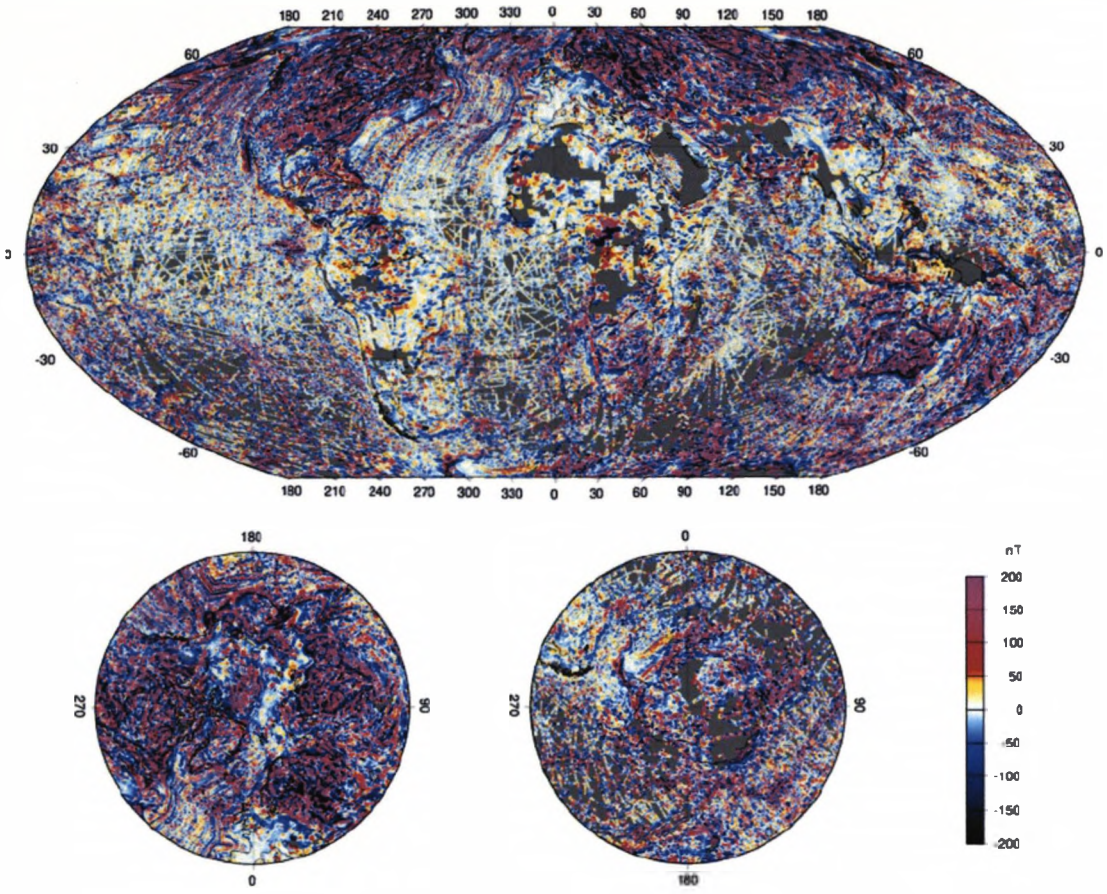

Figure 1.4: Maps of the NGDC WDMAM candidate. The upper panel shows a global map projection with a cutoff of $\pm 70^{o}$ latitude, while the lower half features 2 polar projections extending to $\pm 40^{o}$ latitude, with the left hand map showing the North pole and the right hand map displaying the South pole. *Taken from Maus et al. [2007b]*

Driven by day-side heating of the Earth, these fields are usually located on the day-side and are largely sun-line locked. Cumulatively they can reach magnitudes of several thousand nT, although magnitudes of several hundred nT are more common during quiet periods. Magnetospheric fields, driven by the ring current and currents generated due to Earth's interaction with the solar wind, are located within the magnetopause and magnetotail and are often closed via field aligned currents (FACs). Magnitudes typically reach several tens of nT, but may increase during disturbed periods, tending to show dipolar configurations that vary in strength with time of day.

It is also possible to link these sources (as in the case of FACs), in which case we have a much more complicated system to parameterise. Fortunately, recent field models (Sabaka et al. [2002] & Sabaka et al. [2004]) have focused much attention on attempting to parameterise these signals in a comprehensive framework. This effort has two benefits. Firstly, purely as a scientific exercise, it is helpful to understand the dynamics of the external magnetic field in detail and secondly, given that external current systems tend to extend to only a few tens of kilometres from the Earth surface and

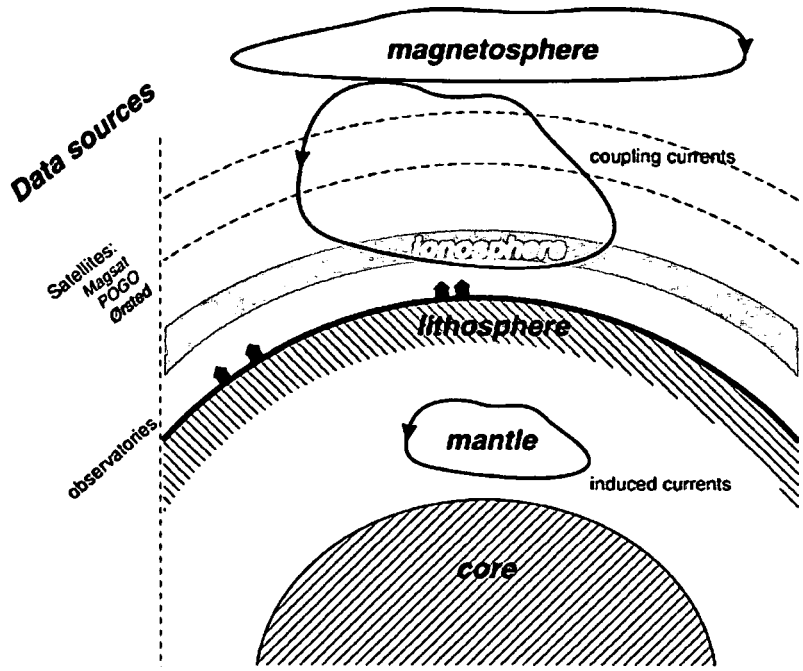

Figure 1.5: A schematic illustration of external magnetic field sources (in terms of the major electric currents generated). *Taken from Sabaka et al. [2002]*

can reach many hundreds of kilometres in height, much of the data used in the study of the geomagnetic field tends to be heavily contaminated by external signals and so a detailed approximation of these fields is desirable (for the purposes of conducting additional data processing prior to further analysis).

1.3 Ocean Induced Magnetic Fields

1.3.1 Oceanographic Context

Over two thirds of Earth is covered by water and unlike the continents, only a tiny percentage of that area is well understood. For many years the study of the global ocean and its hidden treasures has fascinated scientists, not only in terms of the ocean itself, but also the biology it contains and its effect on global climate when coupled with the atmosphere. It is for this reason that the global oceans have been heavily researched in recent decades.

In the past, the greatest challenge facing oceanographers was how to observe the deep ocean. While it may have been possible to use human observations at the surface, at depth the collection of large volumes of data over a prolonged period was an impossibility. Therefore, for a considerable period of time after the first ocean observations were made in the late 18th and 19th centuries, observations were largely limited to the surface. However, things changed in the late 19th century with the announcement of the Challenger expedition (*www.challenger-society.org.uk*). Over the course of 4 years, numerous deep sea observations were made,

greatly improving our understanding of the deep ocean and as a result many nations across the globe initiated their own oceanographic programs. Today, due to political impetus, dedicated scientific cruises are undertaken to research the ocean. While intensive measurements of the ocean surface are still taken, given the improvement in technology since those early voyages, deep ocean observations are far more common place than in the past. The arrival of robotic floats and gliders, capable of observing the whole water column continuously over a prolonged period, now enables scientists to directly observe the behaviour of the deep ocean interior. However, technological improvements have not been limited to deep ocean observation. In a similar manner to that of other remote sensing projects, satellites such as TOPEX/POSIEDON are currently able to continuously monitor the ocean at high altitude with near global coverage, measuring a whole host of oceanic variables such as surface elevation and temperature. When combined with surface observations from dedicated research cruises and automated deep sea measurements, present day oceanographers have a vast amount of data at their disposal, and so the oceans have never been better understood.

However, many oceanographic processes exist where the chances of observing them directly are remote. To address this, numerical modelling has become widespread in recent years. Since the introduction of oceanography as a major research area, extensive work has been conducted by theoreticians to explain the complex behaviour of the global oceans using mathematical theorems, usually based heavily on the Navier-Stokes equations of fluid motion. Using this approach it is possible to calculate numerous oceanographic variables (e.g. flow velocity), allowing the study of many oceanic processes. Figure 1.6 shows results from a typical model (in this case OCCAM [Saunders et al., 1999]).

Circulation models do, however, have limitations. Due to computational constraints at the time of OGCM (Ocean General Circulation Model) introduction, early models were traditionally integrated onto rigid rectangular grids, resulting in several technical issues. The first lies in the inability of a rectangular grid to mimic the coastlines and bottom topography of the highly variable ocean. This problem has been reduced somewhat with the arrival of higher resolution models, but the problem essentially remains. Given the number of processes that interact with the coastline and bottom topography and the role they play in whole ocean circulation, this is a region which should be modelled as accurately as possible, while a lack of grid resolution can also impact circulation in the ocean interior. Due to the range of scales the ocean operates on, some small scale features such as eddies, will not be resolvable by models. As these small scale processes feedback into large scale circulation and vice versa, an inability to parameterise small features may introduce errors into predictions of general circulation. One way in which modellers have attempted to address this issue (to some extent) is to produce OGCMs with variable resolution. This is achieved by producing an initial model grid of coarse resolution which is then nested with higher resolution grids in areas where small scale variability is expected (e.g the Gulf stream), with the regional grid providing the boundary conditions for the localised mesh (see figure 1.7).

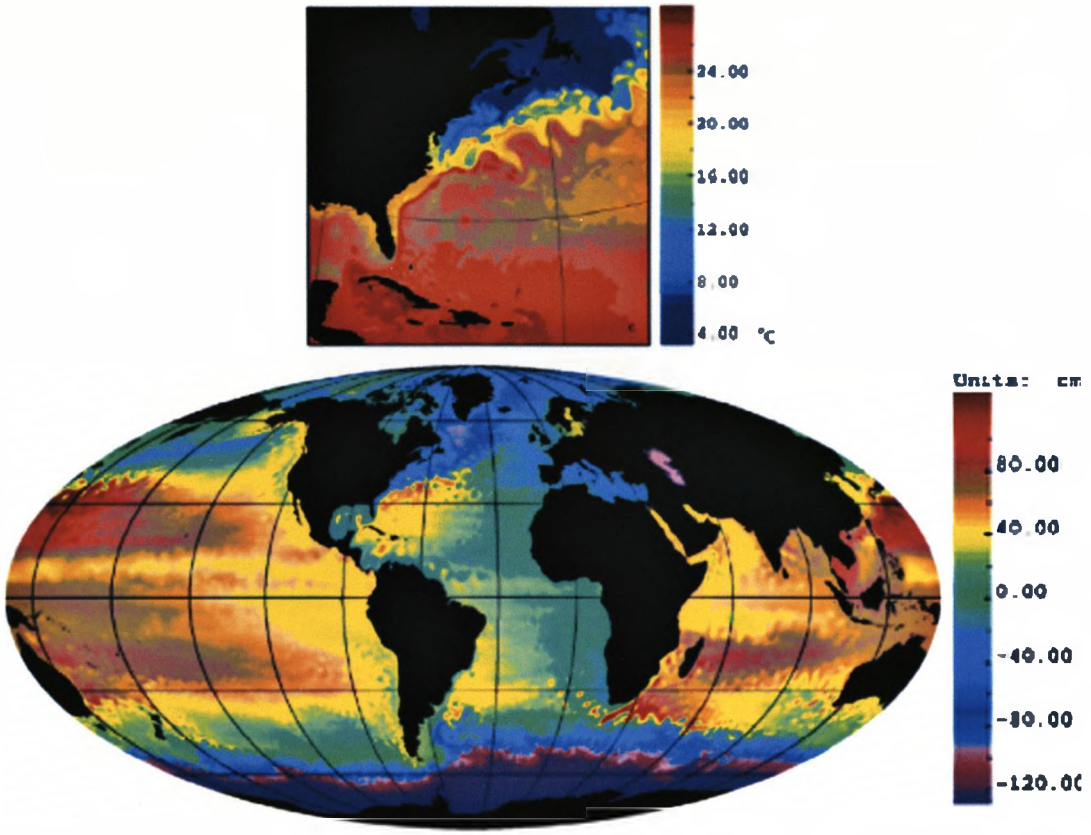

Figure 1.6: An example of results from finite difference based OGCM, OCCAM. The top panel shows surface temperature (SST) and illustrates the ability to model small scale structure while also modelling large scale variability, as shown in the lower panel of surface elevation (SSH). *From Coward et al. [2002]*

While these early OGCMs were based on rigid grids with grid-nesting being the only means of achieving higher resolution, recent increases in computing power have enabled the introduction of more complex, adaptive unstructured meshes (Pain et al. [2005] gives a detailed discussion of the advantages of such an approach over other meshing methods.). In addition, many models now use this increased computer power to use finite element methods in their model integration (rather than finite difference), although this step is not a necessity. Figures 1.8 and 1.9 illustrate the power of unstructured and adaptive meshing when applied to two different scenarios. When studying static systems, rigid, variable resolution grids are often used (figure 1.8). However, when investigating highly dynamic systems such as the ocean, it is important that an initial model grid adapts to allow maximum resolution of the solution, a process regularly achieved by embedding adaptive meshing algorithms into model solvers [Behrens et al., 2005]. Before initiating the algorithm a starting mesh must be defined and the model integrated through a time step; at this point the adaptive algorithm takes effect. Between each subsequent time step integration of the model equations the adaptive algorithm determines which regions of the model mesh are experiencing the greatest variability and adds grid nodes to compensate, locally increasing the resolution of the model. Importantly,

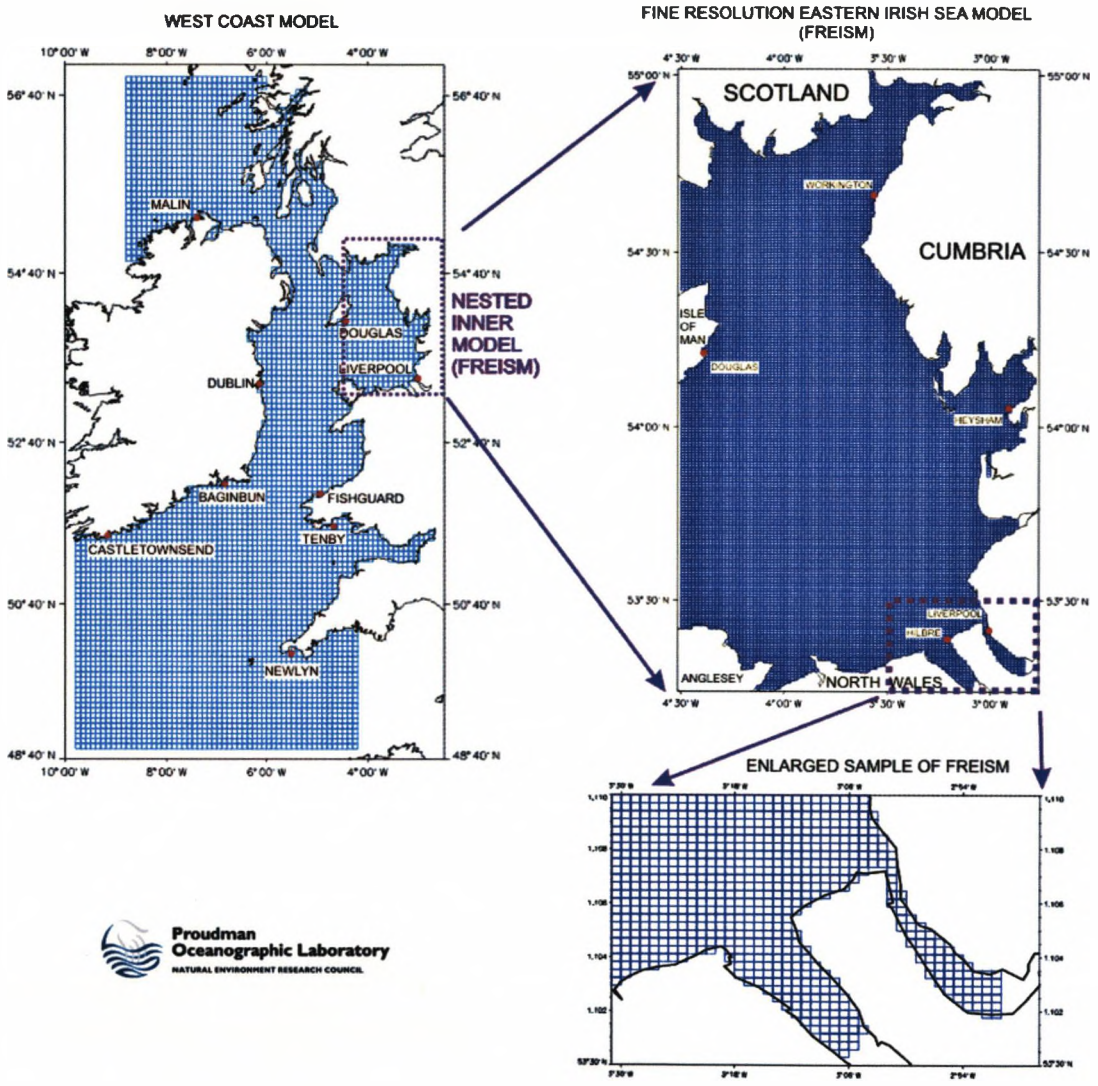

Figure 1.7: An example of nested grids in a finite difference model. Here the model parameterises flow on the western coast of the UK and Irish Sea. Note that while the model grid is rigid, in areas of high variability and small scale flow (eastern Irish Sea), the model grid has been nested with a higher resolution mesh producing a model that can predict important small scale flow. *This image has been reproduced with the permission of the Proudman Oceanographic Laboratory. From www.pol.ac.uk*

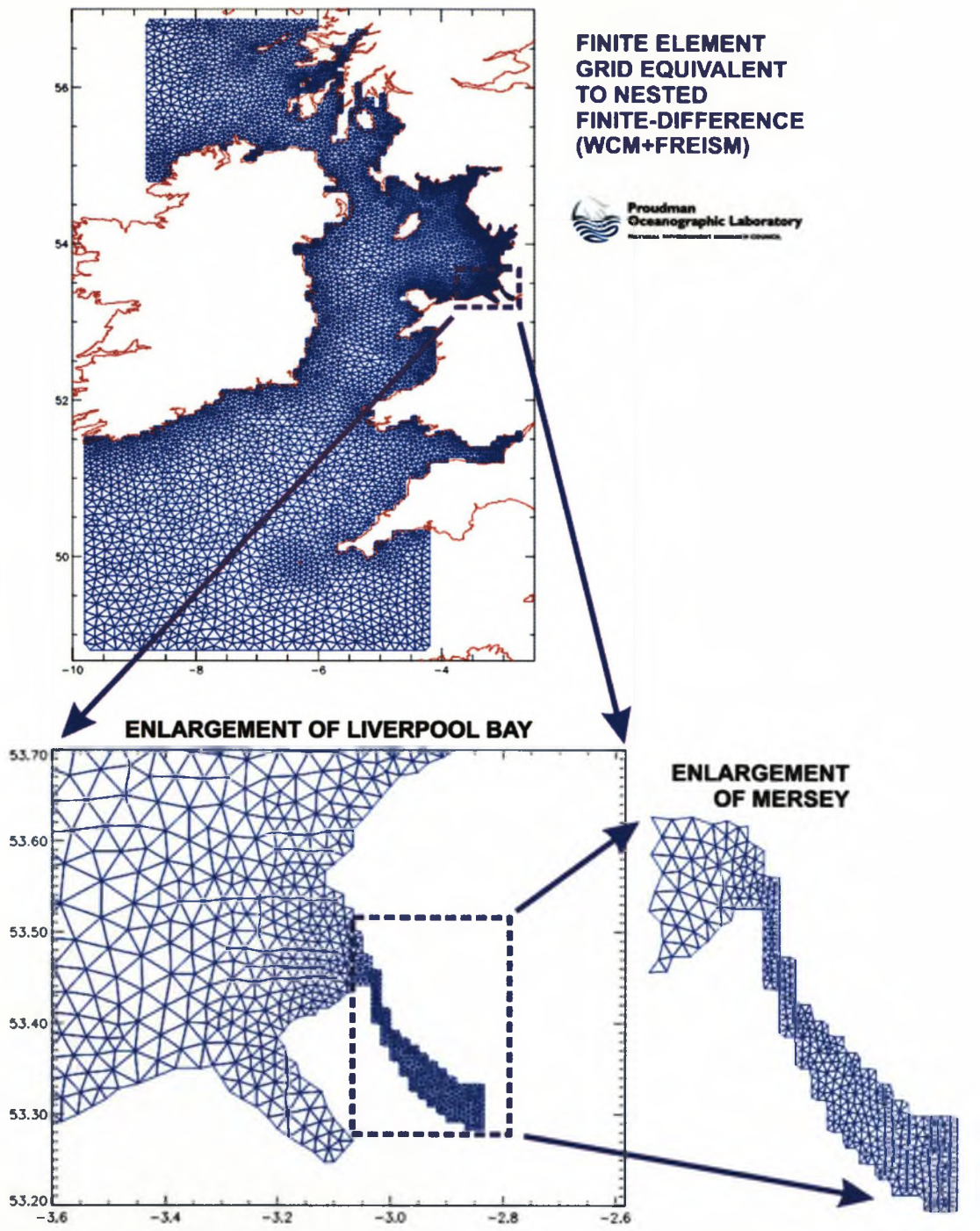

Figure 1.8: An unstructured mesh used in a finite element model of the west coast UK and Irish Sea (POLCOMS). Note that higher resolutions along coastlines and in particular Liverpool Bay and the Mersey are achieved by reducing node spacings. *This image has been reproduced with the permission of the Proudman Oceanographic Laboratory. From www.pol.ac.uk*

the additional nodes are relocated from areas of lower variability, achieving a higher local resolution while still retaining acceptable model run times. However, the most important aspect of adaptive algorithms is that the adjusted model grid can be altered with each time step, retaining optimal grid configuration throughout the entire model run and allowing the tracking of small scale flow processes whilst also parameterising large scale circulation. A particularly good example of this modelling approach is ICOM (Ford et al. [2004a] & Ford et al. [2004b]), developed as a collaboration between Imperial College London, Oxford University and the National Oceanography Centre in Southampton, with figure 1.9 illustrating the use of ICOM to model the M2 tide.

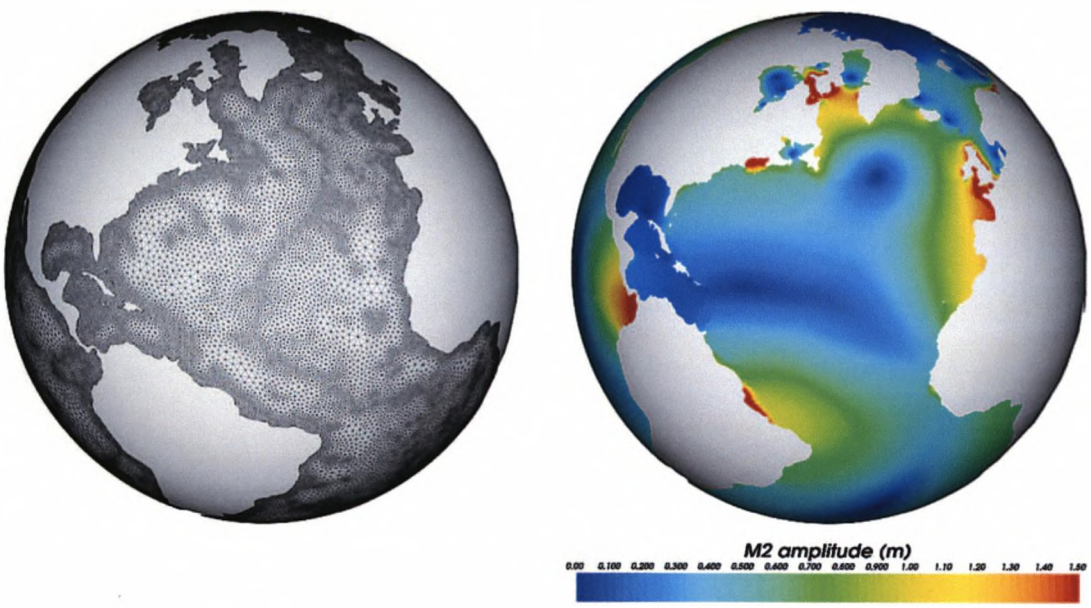

Figure 1.9: An example of adaptive mesh ocean modelling on a global scale (ICOM). In this case, the left hand panel shows the model mesh used to simulate the M2 tide in the right hand panel. *From amcg.ese.ic.ac.uk*

However, many numerical simulations are underpinned by potentially problematic assumptions made about the dynamics of the system. Therefore, to refine and verify these approximations, many numerical frameworks assimilate both in-situ and remote observations into models to both provide initial driving parameters and act as a benchmarking dataset to test model output. As such, it is imperative that observations used in data assimilation are of the highest quality. As previously discussed, the distribution and quality of both in-situ and remote observations made using conventional oceanographic methods have improved in recent years, although one data source still widely unused are the magnetic fields generated by ocean flow. While these data are undoubtedly of great use globally, some regions are in a greater need of this under used data source than others. Due to the presence of sea ice in polar regions, both in-situ and remote observations of the ocean using standard oceanographic methods have always been difficult to make, meaning that polar oceanic regions are greatly

under sampled. However, observations of magnetic fields generated by ocean flow under sea ice suffer from no such effects. While direct surface observations are still difficult to make due to the physical presence of sea ice, geomagnetic field observation satellites suffer from none of the screening effects oceanographic spacecraft have to endure. Therefore, if a clear link between the magnetic fields measured by satellites and the flows they originate from can be made, then it may be possible to greatly increase data volumes available to oceanographic modellers, particularly towards the poles. How, though, is it possible to produce a magnetic field from the flowing ocean? The answer to that question and its oceanographic implications are discussed in the following section.

1.3.2 Motional Induction

While magnetic fields generated due to ocean induction may be a useful tool for monitoring oceanic circulation and the associated chemical, biological and heat transports (particularly in the polar regions), these fields are also a vital tool in geomagnetism. Given the cumulative magnitude of the core, lithospheric and external fields, it is no surprise that a lot of effort is made in geomagnetic research to understand the three major sources in greater detail. However, magnetic fields generated via motional induction, although small in magnitude, are still important when attempting to improve models of small scale fields, from the lithosphere for example [Maus et al., 2006] and several groups have invested a great deal of time in the study of these fields and their oceanographic implications (Sanford [1971], Kuvshinov and Olsen [2005], Tyler [2005] & Manoj et al. [2006]). It is also important to understand these fields so they can be integrated into existing field models, allowing the continued study of field sources with magnitudes lower than those from oceanic sources.

While it may be useful to study these fields, it is important to understand the physical mechanism that causes their generation, along with the governing equations of the system. The mechanism in question is a rather specific form of magnetohydrodynamic coupling. In a fully coupled case, not only would ocean flow influence the magnetic field that is generated, but the magnetic field would feedback to influence ocean flow. However, at the present time no evidence exists to suggest this fully coupled case is in action in the ocean. This simplified version of magnetohydrodynamic coupling is known as motional induction and is facilitated by the salinity of the ocean. Given the high concentration of salt in the oceans, they can be considered as an ionised fluid and as the oceans flow around the globe they carry the ions with them. The other requirement of motional induction is the presence of an ambient magnetic field. In the case of Earth, we satisfy this criteria easily given the presence of the core field. The combination of moving ions (in this case the flowing ocean) through an ambient background field forces the ions in the fluid to be deflected due to the Lorentz force. Over time and given steady background circulation, these charged ions will tend to form patches of charge, initiating two processes. The first is that as charge accumulates, electric fields are induced to prevent further charge migration, while the second involves the

shorting of charge patches through the water column and surrounding conductive sediments, inducing electric currents which generate secondary magnetic fields due to basic laws of electromagnetism. It is the magnetic fields generated in this second case that are the focus of this thesis. However, the process is not so simple. We can split ocean induced magnetic fields into two categories. The first, known as toroidal, includes all electric currents that close in the vertical plane, generating magnetic fields with magnitudes in the range of 100nT. The specific details of these fields cannot, however, be verified using satellite or ground based observations, as the fields produced are trapped within the ocean and surrounding sediments. The second category, known as poloidal, generates the fields we detect in the observatory and satellite record. The currents generating these fields close in the horizontal plane and typically generate magnetic fields with magnitudes in the 1-10nT range. However, in reality most flows will be a combination of these two geometrical configurations and so by studying flows which are thought to produce predominantly poloidal fields, the chances of a positive outcome can be maximised.

However, not all ocean flows produce detectable magnetic fields. In some cases, a lack of mass transport can cause a problem, with the lack of fluid volume and more importantly ion volume, leading to reduced electric current and secondary magnetic field amplitudes. For others, flow geometries are simply unfavourable for magnetic field generation.

In order to gain an idea of suitable targets, basic flow behaviours and their implications regarding magnetic field generation must be known. In the past, much attention was paid to phase locked, periodic ocean processes, typically tides (Tyler et al. [2003], Maus and Kuvshinov [2004]). Not only are the tides one of the largest ocean signals detected in ground observatory and satellite magnetic observations, but they are also one of, if not the easiest, signals to isolate due to their periodic nature. In many ocean magnetic studies one of the major hurdles faced is noise. Oceanic signals are typically rather small in terms of amplitude and so unless treated carefully they can easily be swamped by background noise. By stacking data and knowing a precise operational frequency it becomes far easier to isolate periodic signals compared to their non periodic counterparts above background noise. However, not all ocean flows are periodic and phase locked. In that case, before beginning analysis, an approximate flow geometry must be known, otherwise attempting to differentiate one flow from another can be extremely difficult and potentially erroneous. Whilst the majority of this work is based on flows which exhibit periodic tendencies, some is based on non periodic signals, where attempts are made to address the issue of noise by ensuring flow geometries and anticipated magnetic signals are understood before analysis begins. When combined with methodology designed specifically for each analysis, I believe this approach maximises the chances of success.

While it is vital to understand the physical mechanisms behind motional induction, it is also important to know the governing equations of the system. These equations are vitally important for the numerical simulation of ocean induced magnetic fields, that commonly

form the backbone of many studies of this type (e.g Maus and Kuvshinov [2004]). The suite of equations that govern this particular process and link flow velocities, induced electric currents and secondary magnetic fields are as follows:

$$\textbf{Ohm's law: } \mathbf{J} = \sigma\left(\mathbf{E} + \mathbf{u} \times \mathbf{B}_{\mathbf{main}}\right) \tag{1.1}$$

where the local current density $\mathbf{J}$ can be calculated using the local conductivity σ, the local flow velocity $\mathbf{u}$ and local ambient magnetic field $\mathbf{B}_{\mathbf{main}}$. In this equation, $\mathbf{E}$ represents the local electric field that opposes the induced electric current.

$$\textbf{Ampere's law: } \nabla \times \mathbf{B}_{\mathbf{ocean}} = \mu_0 \mathbf{J} \tag{1.2}$$

where $\mathbf{B}_{\mathbf{ocean}}$ represents the ocean induced magnetic field, μ_0 is magnetic permeability and $\mathbf{J}$ is as in equation 1.1. Combining equations 1.1 and 1.2, an equation for electric field induction can be formed;

$$\mathbf{E} = \frac{1}{\mu_0 \sigma} \nabla \times \mathbf{B}_{\mathbf{ocean}} - \mathbf{u} \times \mathbf{B}_{\mathbf{main}} \tag{1.3}$$

where $\mathbf{E}$, μ_0, σ, $\mathbf{B}_{\mathbf{ocean}}$, $\mathbf{u}$ and $\mathbf{B}_{\mathbf{main}}$ are as in equations 1.1 and 1.2, while the rotational part of this equation obeys Faraday's law of electromagnetic induction;

$$\textbf{Faraday's law of EM induction: } \partial_t \mathbf{B}_{\mathbf{ocean}} = -\nabla \times \mathbf{E} \tag{1.4}$$

where the partial derivative of the ocean generated magnetic field $\mathbf{B}_{\mathbf{ocean}}$ (with respect to time t) is calculated as a function of the induced electric field $\mathbf{E}$. Combining the curl of equation 1.3 with equation 1.4, a general motional induction equation that can derive the ocean generated magnetic field associated with a given flow velocity, conductivity distribution and background magnetic field is formed;

$$\partial_t \mathbf{B}_{\mathbf{ocean}} = \nabla \times \left(\mathbf{u} \times \mathbf{B}_{\mathbf{main}} - \frac{1}{\mu_0 \sigma} \nabla \times \mathbf{B}_{\mathbf{ocean}}\right) \tag{1.5}$$

where $\mathbf{B}_{\mathbf{ocean}}$, $\mathbf{B}_{\mathbf{main}}$, $\mathbf{u}$, μ_0 and σ are all as previously. The fields calculated using these equations also obey Laplace's equation ($\nabla^2 \mathbf{V} = 0$), assuming that $\mathbf{B}_{\mathbf{ocean}}$ can be represented as a scalar potential $\mathbf{V}$ that satisfies ($\mathbf{B}_{\mathbf{ocean}} = -\nabla \mathbf{V}$) outside of the current filled source region.

However, keeping equation 1.5 in its general form can often make visualisation and implementation of the induction equation difficult when forward modelling for expected secondary magnetic signatures. Therefore, in recent years several groups (Tyler and Mysak [1997], Vivier et al. [2004], Maus and Kuvshinov [2004], Kuvshinov and Olsen [2005], Manoj et al. [2006]) have developed schemes whereby equation 1.5 is rewritten in a more physically relevant framework. Two such schemes are widely used at the present time. The first is known as the volume integral approach and is adopted in many recent studies (e.g. Maus and Kuvshinov [2004], Kuvshinov and Olsen [2005], Manoj et al. [2006]). The method involves the simulation of electromagnetic fields excited by given sources within a spherical 3D electrical conductivity model, including estimates of conductivity for the ocean, sediments, crust and mantle (although in some instances the mantle is assumed to be insulating). As in any forward modelling scheme, estimates of ocean flow velocity and ambient magnetic field are required, with estimates being taken from the relevant ocean circulation and geomagnetic main field models. Due to the complex mathematical nature of this method, attention on this occasion is merely drawn to the relevant scientific studies (Kuvshinov and Olsen [2005], Manoj et al. [2006]) for a full and detailed mathematical proof of the approach.

The second approach used when forward modelling oceanically generated magnetic fields is the thin shell approximation, also widely used within the electromagnetic modelling community. The concept behind this approach is one which relies upon the assumption that the ocean (and conductive sediments around and beneath it) can be considered as a thin conductive shell sitting on an insulating sphere (representing the lithosphere and mantle), with an electrically insulating region radially outward from the thin shell (representing the atmosphere, a more robust assumption than that of an insulating mantle, as the lower atmosphere typically has a conductivity of $\sim 10^{-14}$ Sm^{-1}). As in the volume integral approach, sediment conductivities, ocean transports and ambient geomagnetic fields are approximated across the thin shell using estimates from relevant models (the exact suite of models used varies from study to study). Detailed reasoning for the assumptions involved in this approach, along with full mathematical proofs of the methodology and governing equations (beginning with the integration of equation 1.5 across the thin shell) can be found in several papers, notably Tyler and Mysak [1997] & Vivier et al. [2004].

1.4 Research Aims

Due to the emerging nature of this research, there are many avenues to explore. However, in an attempt to be thorough whilst also making the most of the time available, I have chosen to follow a series of initial project aims as closely as possible.

- Given the complex nature of the geomagnetic system, before any isolation of oceanic signals can begin, all significant contributions from other sources must be removed. Signals from the core, lithosphere and external regions all have the potential to severely

contaminate any oceanic fields if not suitably accounted for. A primary aim of this project is to design a suite of routines that comprehensively remove these large magnitude signals, whilst retaining the integrity of the oceanic signal that remains. Ideally, this entire procedure should be as automated as possible, whilst allowing occasional updating of databases as new data are released. This in turn will allow the generation of large datasets with little effort, which can be used by myself or others to study ocean generated magnetic signals with the understanding that contamination from larger magnitude sources will be minimal.

- Some areas of ocean geomagnetism have received attention in recent years, one major study area being global tides. Early work [Tyler et al., 2003] highlighted that the magnetic field associated with global tidal flow can be rigorously isolated from within the satellite magnetic record. As a consequence of this earlier work, another aim of this project has been to further it, with a view to parameterising tidal signatures in the form of a tidal magnetic field model, derived solely from satellite magnetic observations. While tidal magnetic fields are already considered in many current field models [Maus et al., 2006], the predictions used to correct for tidal flow are not derived from magnetic data, but derived numerically from ocean circulation and ocean/sediment conductivity models [Maus and Kuvshinov, 2004]. While this approach does not appear to have any detrimental effects on current field models and has been shown to correlate well with satellite magnetic data [Tyler et al., 2003], a tidal approximation derived from magnetic data would be desirable. There are many potential benefits of such an aim. The first, relevant to the geomagnetic community, being that an accurate representation of tidal fields would be invaluable when attempting to understand the finer details of other magnetic sources, for example small scale lithospheric fields (both continental and oceanic). Secondly, as previously discussed, tides are notoriously difficult to monitor in the polar regions where sea ice prevents the use of many traditional ocean monitoring techniques. However, the magnetic field generated by flow beneath the ice sheets is transmitted through the ice without interference, potentially allowing polar tidal fields/flows to be monitored.

- The global ocean is a complex system and so tides are not the only oceanic process to generate a magnetic signature. In order to study such signals in detail, an accurate prediction of tidal contributions must be derived. However, as this is already an aim of this thesis, it is planned to use these tidal predictions to produce tide free magnetic datasets. Using these datasets, it is hoped it may be possible to study several lower magnitude signals in detail for the first time. These smaller magnitude signals range from small, localised processes, to global scale flows, in both periodic and non periodic settings, which would otherwise be largely overprinted by tidal signals. By studying flow features such as these, it may be possible to gain a greater understanding of the global oceans and how they relate to other environmental topics, such as global heat distribution, chemical transport and the current hot topic of global warming.

By fulfilling these aims, I hope to provide a base for other studies of this kind, whilst also giving key insights into specific flows within the ocean system. Ideally, this research will also be of future use and interest to both the geomagnetic and oceanographic communities.

The structure of this thesis attempts to address each aspect of the research within it in a logical sequence beginning with chapter 2, which outlines the various data sources used within this research and the their treatment with regards to pre-analysis preparation. Chapters 3 to 5 contain the bulk of the research contained within this thesis. Each chapter has been structured to be self contained, with all relevant information about that particular study being discussed within the chapter itself. Chapter 3 focuses on work conducted to isolate magnetic signatures due to a localised, periodic circulation in the Argentine Basin (southern Atlantic ocean). Moving up in scale, chapter 4 discusses research carried out to study global tides and their magnetic counterpart, including work undertaken to parameterise this particular field source in a magnetic field model. Moving onto non periodic flows, chapter 5 details a study attempting to identify oceanic Rossby waves in the magnetic record for the first time. Following this will be a final chapter in which the results from earlier chapters are discussed and their implications for future study outlined, followed by suggestions of future research opportunities within this topic that others may wish to investigate and a discussion about the impact of upcoming satellite missions on future research.

Chapter 2

Data Generation

The preparation of data is always of extreme importance when conducting scientific research, but given the magnitude ratio between unwanted signals and those we wish to study, the preparation of data in this case is paramount. While other studies prepare data by isolating the most suitable observations via some form of data selection, when studying oceanic magnetic fields this approach alone is not sufficient to achieve a truly robust result.

This chapter introduces the various data used to conduct the research within this thesis, along with reasoning for its inclusion. This will be followed by detailed descriptions of the preparation methods used to enhance the presence of ocean magnetic fields in these datasets above contributions from other sources within the geomagnetic system.

2.1 Magnetic Field Data

In the years since the introduction of continuous magnetic field observation, numerous forms of magnetic data have been developed. However, not all forms of magnetic data are appropriate for the work contained in this thesis, with only ground observatory and satellite data sources fulfilling the requirements of temporal continuity (observatory) and long term, global scale coverage (satellite). The following section of this chapter will introduce these datasets in detail, discussing the merits and limitations of each, along with reasons for its inclusion.

2.1.1 Observatory Data

In many recent global scale studies, magnetic observatories have been overlooked in favour of more spatially comprehensive satellite data. However, were it not for magnetic observatories, many of today's more advanced observation methods would not exist, and in many cases observatories are still the optimum way to observe the geomagnetic field. Their importance is further illustrated by their growth in numbers over the years, evolving from a solitary site in 1833 to a global network of over 100 observatories distributed across the globe.

In an effort to increase collaboration between sites and improve comparability of data between observatories, networks such as INTERMAGNET have been established in recent years (in the case of INTERMAGNET, between 1987 and present), the distribution of which can be seen in figure 2.1. What becomes clear when this map is studied is the bias in obser-

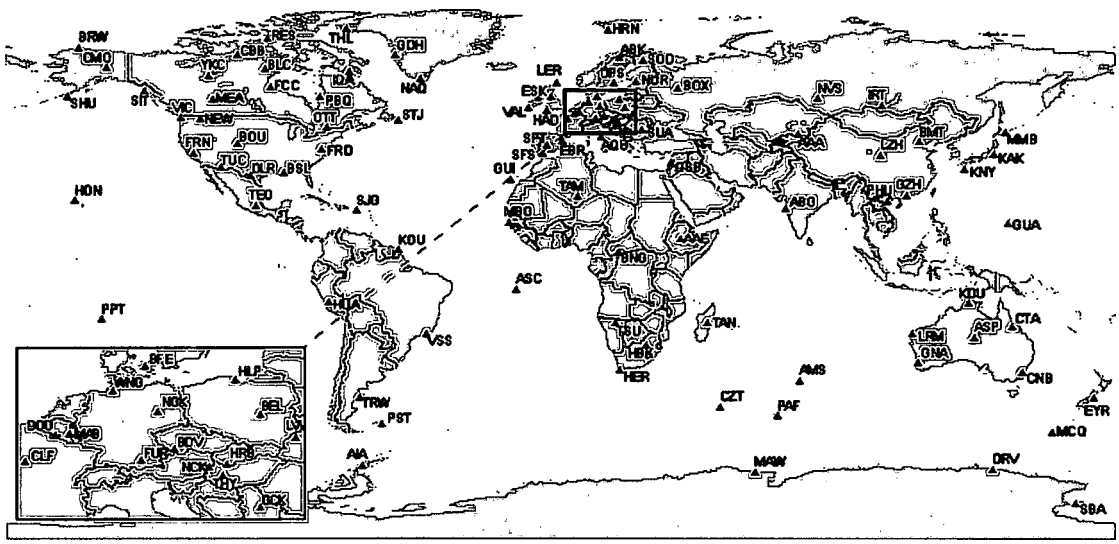

Figure 2.1: The global INTERMAGNET observatory network. *From www.intermagnet.org*

vatory density in favour of the northern hemisphere (the reasoning behind such a disparity between the two hemispheres can be explained primarily by the positions of most observatory contributing nations). This uneven distribution can be expanded further, with the US and Europe containing many northern hemisphere sites. The disparity becomes even more severe if we include the ocean, with only a few island based observatories occupying this vast region, although in recent years some short term ocean floor observations have been made [Lilley et al., 2004]. While this issue almost certainly influences global scale studies, introducing biases towards the northern hemisphere (unless accounted for by data selection), the distribution of observatories becomes insignificant when sites are considered on a regional or site by site basis (as in this work).

While magnetic observatories suffer from issues relating to spatial resolution, the accuracy and temporal resolution of observatory data is extremely high. This is primarily due to the stability of the recording instrumentation and that being ground based, observatories typically avoid some of the external field effects that can contaminate satellite data. In recent years, many observatories have also introduced autonomous systems, reducing human error and increasing sampling rate to 1 minute. The combination of such factors means that magnetic observatories are still useful and in some circumstances are the only data source available for some studies, examples being the investigation of secular variation and geomagnetic jerks (both of which originate in the core). While advances in satellite data processing have allowed such features to be resolved using satellite data [Olsen and Mandea, 2007], this represents a tentative first step and observatory data is still widely used for studies

requiring long, stationary time series.

Observatory data is available in two formats, XYZ and DHZ (both are equally usable as the magnetic field can be calculated from any of several elements, and also require identical processing). The observatory data used in this research was formed as a combination of both data formats, using both 1-minute and hourly sampling, downloaded from *ftp.dmi.dk*, although the observatory data section of this site has since been replaced by a BGS (British Geological Society) run site (*www.wdc.bgs.ac.uk*).

2.1.2 Satellite Data

While systematic, continuous measurements of Earth's magnetic field have been made for many years in the form of permanent observatories, marine voyages, paleomagnetic sampling and aeromagnetic surveys, none of these observation methods allowed for continuous monitoring of the geomagnetic field on a global scale. The only way to achieve this goal was to go into orbit. However, such an aim is ambitious given the technical and financial requirements of such a project. Initial attempts at satellite observations were made during the POGO missions (1965-71), but were limited due to operational issues and the presence of only a scalar magnetometer on board the satellites (leading to issues of Backus effect in the resulting data).

Eventually, technology caught up with the human imagination and the first dedicated vector magnetic observation satellite was launched in 1979 in the form of MAGSAT (1979-80). With its vector and scalar magnetometers, along with a star camera for attitude approximation and near polar orbit, MAGSAT finally gave geomagnetists what they craved; accurate, reliable geomagnetic observations with near global coverage, although only in a dawn/dusk orbit, limiting the number of investigations MAGSAT data could be used for. Unfortunately, MAGSAT remained operational for only a few short months and after its decommissioning no new satellites emerged, returning observations of the geomagnetic field exclusively to Earth's surface. For the next 19 years, researchers remained frustrated by the lack of truly global magnetic data. However, with the launch of Ørsted in 1999 and the CHAMP and SAC-C satellites that quickly followed, researchers found themselves with three satellites orbiting Earth simultaneously and the international decade of geopotential research had begun. The greatly increased data volume, coupled with extremely accurate instrumentation, meant that geomagnetism had truly entered the satellite era for the first time. Initially with only short operational periods planned, these three satellites have all greatly exceeded initial expectations, still delivering high quality near real-time data more than seven years after launch.

The introduction of long term satellite field observation has had a profound effect on all aspects of geomagnetism, the most noticeable of these being the widespread introduction of main field models (e.g., CHAOS, CM4, IGRF, etc). Prior to the launch of recent satellites,

derivation of such models was heavily reliant on early POGO and MAGSAT data, combined with large volumes of ground based observatory data [Sabaka et al., 2002] and as such was at risk from the effects of the observatory based spatial biases outlined previously. Occasionally, historical magnetic records were also used and due to their timespan produced very useful models for studying core dynamics. However, the introduction of modern satellites has allowed extremely detailed field models to be derived (Sabaka et al. [2004] & Olsen et al. [2006b]) and so a great deal has been learnt about the geomagnetic field from these models. The introduction of high quality satellite data has also allowed the study of more specific field sources with unprecedented accuracy, for example the detailed lithospheric field [Maus et al., 2007a].

Due to the global nature of this research, the use of satellite data is essential. However, given the magnitude of ocean magnetic fields it is vital that only the most accurate data is used. Therefore all the satellite data discussed within this thesis is from the three newest satellites, Ørsted, CHAMP and SAC-C with a brief introduction of each below.

Ørsted: After the success of MAGSAT the expectations placed on its successor were high, a burden that fell on the organising committee of the Ørsted mission. Formed as a collaboration between the Danish Meteorological Institute (DMI) in Copenhagen and numerous research, technology and industry partners, Ørsted was launched into orbit in 1999, nineteen years after the decommissioning of MAGSAT and has since provided researchers with more than eight years of high quality magnetic measurements, even though mission lifetime was only planned to be a mere 14 months. However, vector measurements are no longer available from Ørsted and data released at present are strictly scalar only. It is this extremely long time series which attracts many researchers to use Ørsted data in their work, particularly studies that investigate the geomagnetic field's temporal evolution (e.g secular variation).

The technical instrumentation on board Ørsted varies little from that which would eventually find its way onto CHAMP, consisting of fluxgate and Overhauser magnetometers for vector and scalar (plus calibration) observations respectively and a star camera for instrument orientation, all capable of one second sampling. The only major difference between Ørsted's technical capabilities and those of CHAMP is Ørsted's lack of a second star camera, introducing errors in the two directions lying perpendicular to the sole camera's boresight direction when determining satellite attitude and transforming observations from a satellite reference frame to a conventional co-ordinate system (see Olsen et al. [2000]).

Unlike both the CHAMP and SAC-C satellites that followed, Ørsted flies in an elliptical orbit and so at launch its altitude varied between 500km and 850km (in an effort to keep the satellite away from the troublesome lower F region of the ionosphere). The spatial distribution of Ørsted data over the course of several days can be seen in figure 2.2. DMI in Copenhagen are responsible for the maintenance of the satellite along with

the processing and calibration of observations, which are easily downloaded from the Ørsted section of *ftp.dmi.dk*.

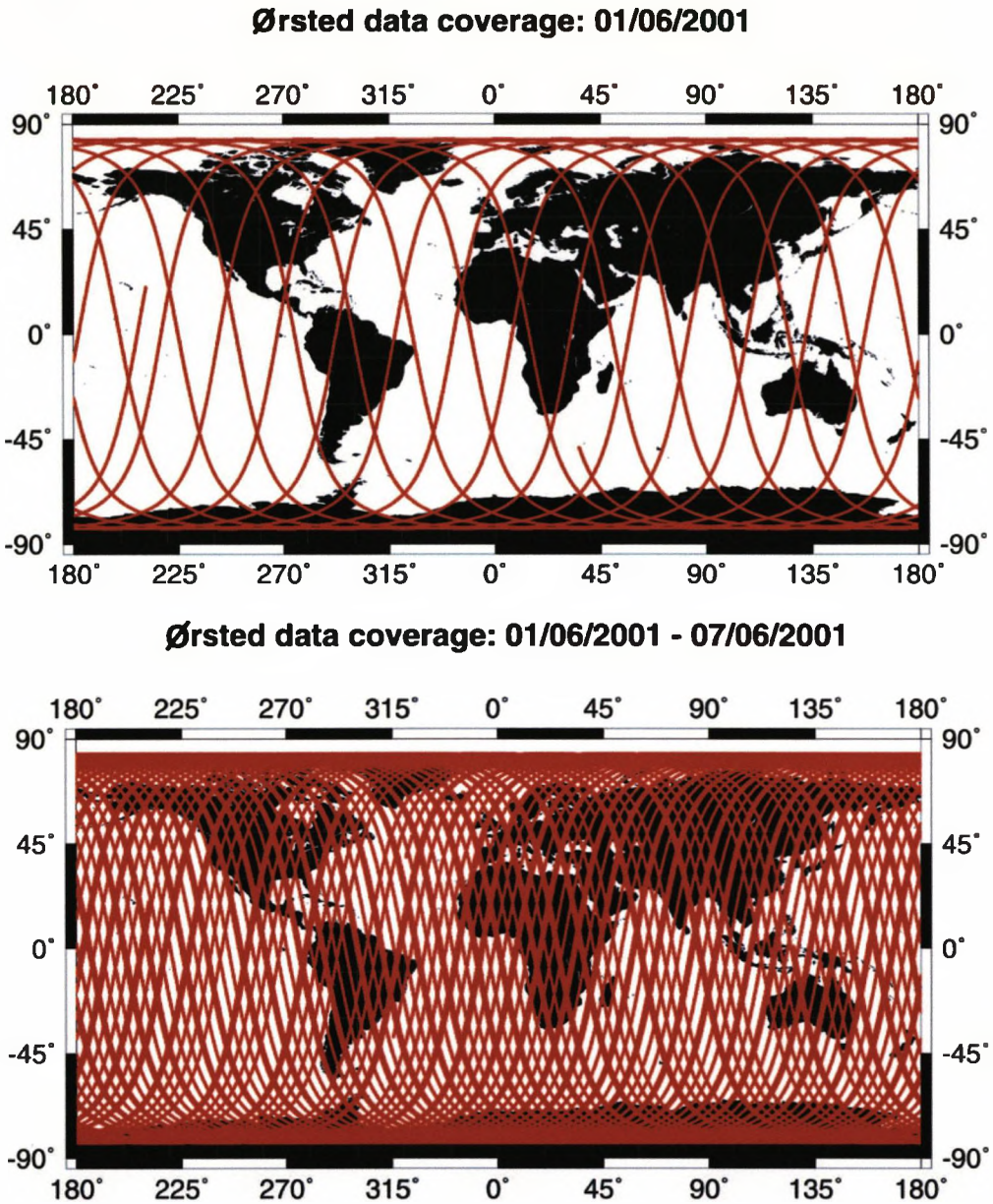

Figure 2.2: The spatial distribution of Ørsted data. The top panel shows data from a single day, while the lower panel shows orbit evolution over the course of seven consecutive days.

CHAMP: Although Ørsted was the first modern magnetic satellite to enter orbit, CHAMP is perhaps the most widely used in research. Conceived in 1994 and launched in 2000, CHAMP (CHAllenging Mini satellite Payload) has provided scientists with high quality vector and scalar magnetic data (with near global coverage), in near real time for over seven years. A collaboration between the German Space Agency (DLR) and GFZ in Potsdam, along with several industry partners, CHAMP also provides high quality gravity data along with observations of other atmospheric/ionospheric variables

used in other areas of scientific research. Post launch, the upkeep and processing of CHAMP and its data are the responsibility of the GFZ data centre, which also acts as the location for data retrieval (*www.gfz-potsdam.de*). CHAMP was launched to an initial altitude of 454km to guarantee the desired mission lifetime of 5 years, whilst also satisfying the scientific requirements of the mission. However, CHAMP is still providing high quality data 7 years later after several altitude manoeuvres conducted to counteract the effect of atmospheric drag on the satellite. Currently, the satellite has an altitude of $\sim$ 350km and is the lowest flying magnetic satellite in orbit, one of the major reasons why CHAMP data is so popular for research (due to the radial decay of the geomagnetic field, a low satellite altitude is always desirable).

Global coverage is achieved courtesy of an almost circular, drifting, near polar orbit (87^{o} inclination). Therefore, CHAMP is able to sample much of the Earth in only a short period of time (see figure 2.3). An orbit which drifts through local time has a large advantage over the alternative dawn-dusk sun-synchronous orbit, as many of the planned applications of CHAMP data have time varying components with periods of less than a day and so a dawn-dusk orbit (as used in the MAGSAT mission) would hamper these analyses.

While a favourable orbital configuration gives CHAMP an early advantage over other satellites, its magnetic instrumentation is also more than adequate. Equipped with one Overhauser magnetometer for scalar field measurements and two Fluxgate magnetometers for measuring the full vector field, CHAMP is capable of making sustained field observations with a sampling frequency of 1 Hz. However, two of the most important components of the instrumental setup for CHAMP are the star cameras which monitor attitude on board the satellite. As discussed previously, field observations on board satellites are typically made with respect to an instrumental system of co-ordinates. However, this reference frame is of limited use when conducting scientific research. Therefore, a system must be implemented which allows measurements made by the satellite to be transformed into a user friendly co-ordinate system (typically NEC or spherical). To achieve this the attitude of the satellite must be known as accurately as possible. While Ørsted has only one star camera for orientation, CHAMP has two cameras on board, meaning that while other satellites can determine attitude accurately in only one direction, CHAMP is able to determine satellite attitude and therefore conduct observation transformation equally in all three orthogonal directions.

SAC-C: While CHAMP and Ørsted are the most widely used of the current magnetic satellites, another satellite was also launched into orbit (although it no longer transmits data). SAC-C, a collaboration between NASA, DMI and the Argentine Commission on Space Activities (CONAE), is unique in the current satellite era of geomagnetism in that it only ever provided scalar measurements of the Earth's magnetic field (due to a technical malfunction). This simple technical point is one of the major reasons why SAC-C data is often used in a supplementary role when carrying out research.

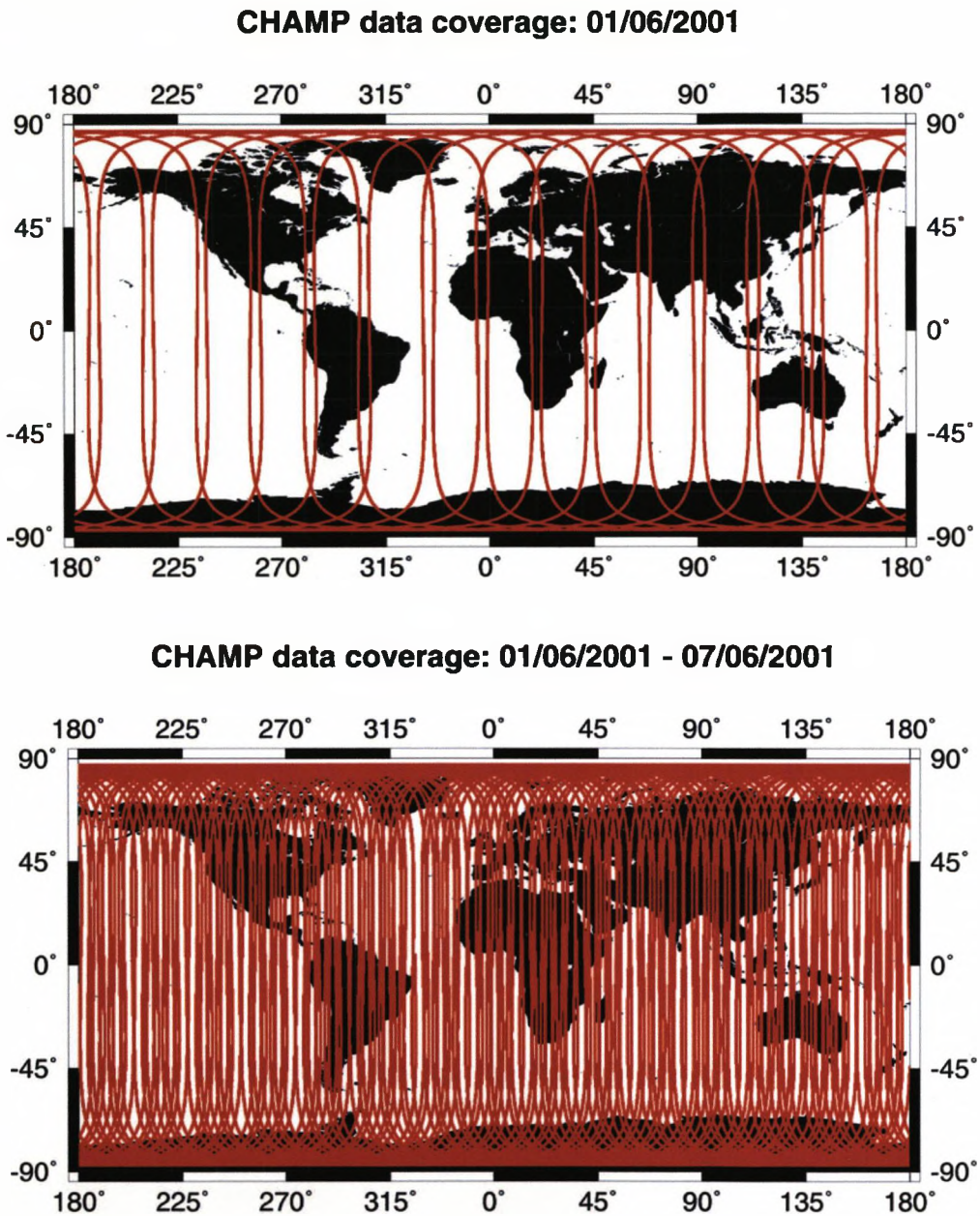

Figure 2.3: Plots of CHAMP data coverage. The upper panel shows data coverage during a single day, while the lower panel shows coverage after a week of CHAMP orbits.

However, in my research I have seen SAC-C as an extremely useful data source and so have integrated data from the start of the mission until the end of 2004 into much of the work within this thesis.

The SAC-C satellite was launched in November 2000 to an initial altitude of ~700km, very similar to that of Ørsted, although SAC-C flies in a sun-synchronous circular orbit with a 98.2° inclination. Figure 2.4 illustrates an example of SAC-C coverage over a short period, along with the development of this orbital pattern into global coverage.

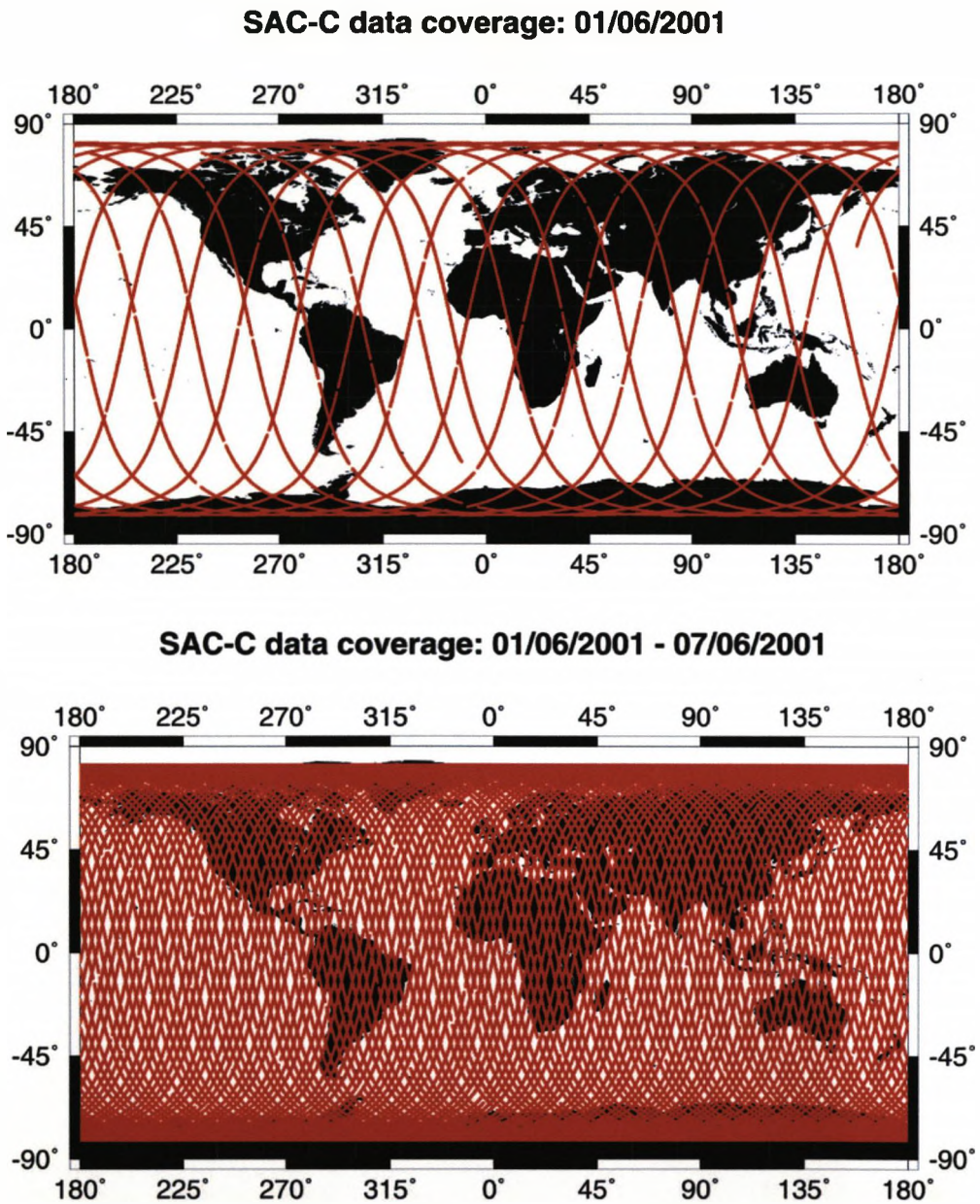

Figure 2.4: SAC-C orbital coverage. The upper panel represents the orbital path of the satellite during one day, while the bottom panel illustrates the temporal evolution of these tracks over a week.

While the instrumentation on board SAC-C may be lacking functional vector capabilities, the scalar measurements from the Helium magnetometer on board are still extremely accurate, and like CHAMP and Ørsted have a 1 second sampling rate. It is worth noting however, that all SAC-C data must be calibrated against a reference field model (derived using CHAMP and Ørsted data), meaning that SAC-C data would have no use without the CHAMP and Ørsted missions. Interestingly, in the same way that CHAMP and Ørsted have outlived their planned lifetimes, the SAC-C magnetometer was also operational for far longer than the year it was originally designed for.

The technical and orbital details of satellite data are often non-trivial and while some characteristics remain consistent between satellites, others vary dramatically. Therefore, this section will be concluded with a summary table (table 2.1) containing the defining characteristics of each satellite used in this research.

Summary Table of Satellite Characteristics					
Satellite	**Launch Year**	**Planned Lifetime**	**Still Working**	**Data Range Used**	**Launch Altitude (km)**
CHAMP	2000	5 Years	Yes	2001-2005	450
Ørsted	1999	14 months	Yes	1999-2005	500 → 850
SAC-C	2000	12 months	No	2001-2004	700
Summary Table of Satellite Characteristics cont.					
Satellite	**Vector Obs.**	**Sample Rate**	**Star Cameras**	**Repeat Orbit**	**Multi Discipline**
CHAMP	Yes	1 Sec	2	Short Periods	Yes
Ørsted	Yes	1 Sec	1	Short Periods	No
SAC-C	No	1 Sec	1	Yes	Yes

Table 2.1: A table to summarise the basic characteristics of the 3 satellites that provided data for the research within this thesis.

2.2 Preparation Methods

As previously outlined, the manner in which magnetic data are prepared prior to analysis is crucial to maximise the potential of a positive result. This section outlines the various methods used throughout this research to prepare observatory and satellite records for the various analyses discussed hereafter.

2.2.1 Main Field Model Subtraction

Due to the small relative magnitude of ocean induced fields to those from the core ($\sim$ 50,000nT), it is necessary to reduce the influence of these larger magnitude sources in the data we analyse. Currently, the preferred method of achieving this is main field model subtraction. While it may initially seem counter productive to employ such a technique in order to preserve a signal, this approach uses the weakness of main field models to our advantage. A model of the geomagnetic field can only predict the field sources it parameterises and it is this limitation that is used here. The core field and its secular variation are extremely well parameterised in recent models, along with approximations of lithospheric and external fields. However, while core and lithospheric fields are modelled with confidence, those from external sources are less certain, due to the particularly complex physics of the system, leading to the parameterisation of most external fields as noise sources rather than as field sources. However, most recent models do attempt to model external fields in a far more realistic manner than previously attempted (Sabaka et al. [2004], Olsen et al. [2006b]). As a result, the most significant field source yet to be parameterised in main field models is the flowing ocean. Therefore, given the accuracy of current models when predicting core and lithospheric fields (and to an extent external fields), by making predictions of our data using a main field model and subtracting it from observations, we are able to greatly reduce the effect these much larger magnitude sources have on the data used.

Here, the modelling process that forms the basis of all of the main field models used in this research is introduced. Unlike other models (Tsyganenko [2002a,b]) which are derived by representing the physics of each model source as a series of mathematical equations calibrated against observations, the field models used in this research are derived solely from magnetic observations. The method used to derive these models has its underpinnings in the concept that the geomagnetic field can be represented as a series of potential fields that satisfy Laplace's equation. The solution to Laplace's equation can be written as a series of trigonometrical functions and associated Legendre functions. If one of these trigonometric functions is translated onto a spherical geometry, the resulting function is a spherical harmonic, with any potential field being described by a series of linearly combined spherical harmonics and their Legendre functions. Therefore, if a series of spherical harmonics can be found, the chosen potential can be predicted anywhere within the potential sphere. This is achieved via the process of least squares inversion, a mathematical method that links observations with the governing equations of a system, in this case the equation for a potential field ($\mathbf{V}$) represented as a spherical harmonic series (see equation 2.1),

$$\mathbf{V} = a \sum_{n=1}^{N} \sum_{m=0}^{n} (g_n^m \cos m\phi + h_n^m \sin m\phi) \left(\frac{a}{r}\right)^{n+1} \mathbf{P_n^m}(\cos\theta) \tag{2.1}$$

where g_n^m and h_n^m are the Gauss co-efficients being found and $\mathbf{P_n^m}$ the associated Legendre Functions. θ is co-latitude, ϕ is longitude, r is the radius of the observation point from the

centre of the Earth, while a is the radius of the Earth (6371.2 km), N is the maximum degree of the expansion and n and m are the degree and order (respectively) of the spherical harmonic being found.

Graphically, each spherical harmonic can be thought of as a 2D standing wave wrapped onto a sphere, with its maximum amplitude equal to that of its associated Gauss co-efficient, with its complexity being determined by its degree and order. While the degree represents the total number of nodal lines on the harmonic's surface (a nodal line being a line of zero amplitude on the surface of the harmonic), the order represents the number of sectoral nodal lines on its surface (a sectoral nodal line falls along a line of constant longitude, while a zonal nodal line follows a line of constant latitude). By varying the number of zonal and sectoral nodal lines, an infinite number of spherical harmonics can be constructed (of varying complexity). Figure 2.5 illustrates this visually and for a more detailed discussion of spherical harmonics and their relevance to geomagnetism see Langel [1987].

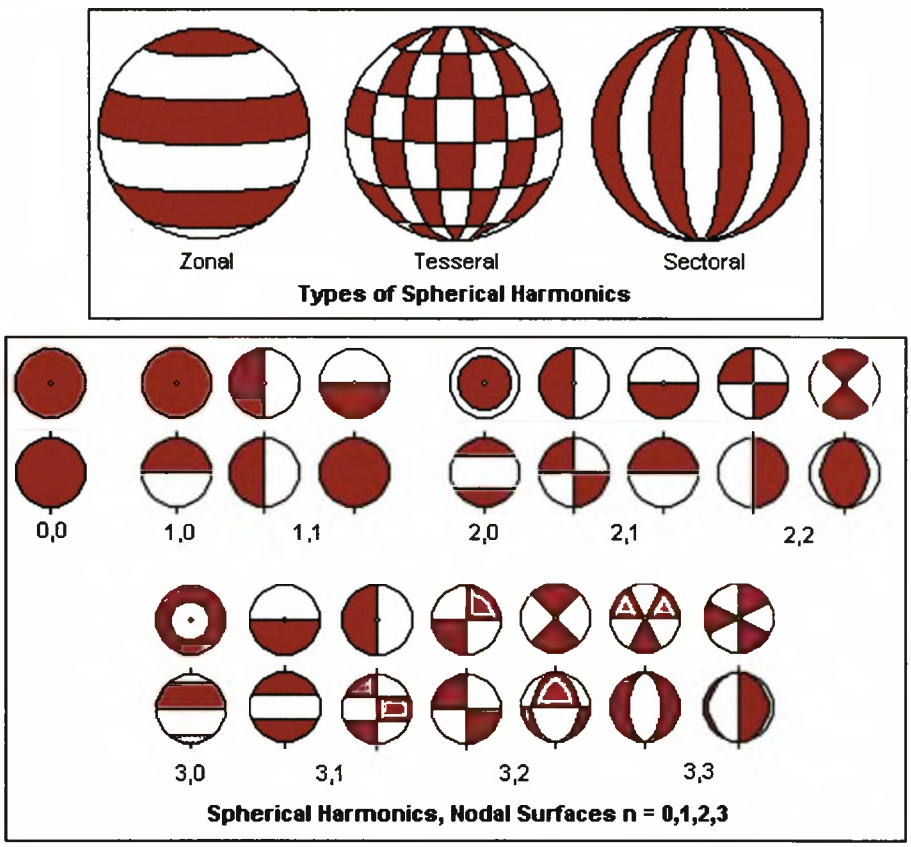

Figure 2.5: Schematic diagrams of several spherical harmonics. The upper panel displays the three types of spherical harmonic, while the lower panel illustrates all possible harmonic configurations for degrees 0 to 3 (plots are shown in both polar and equatorial projections). Note that when harmonic order ≥ 1, each harmonic can be rotated by 90° around an axis parallel to the Earth's rotational axis. This second harmonic corresponds to the h_n^m co-efficient from equation 2.1, with the un-rotated harmonic corresponding to the g_n^m co-efficient for that degree and order. *From www.du.edu*

The Earth's magnetic field evolves through time, not only as a consequence of combining sources, but also within each source (for example, secular variation of the core field). For the models considered here, temporal evolution is controlled by making lower degree Gauss co-efficients time dependent, fitting temporal evolution of input data to a series of B-splines.

As previously introduced, it is possible to reconstruct the geomagnetic field at a particular location and time by reforming equation 2.1 using appropriate values of θ, ϕ, r and time, along with the Gauss co-efficients representing each field source (derived via inversion of a given dataset). While all three field models used in this research share the same method of derivation, this is where most similarities end. In most cases the sources parameterised in each model vary, along with the manner in which parameterisation is conducted. More importantly, the data used to derive two field models are never the same and because input data has a direct control on the resulting model, field models will always vary to some extent unless identical input data is used.

It is easy to see that the defining characteristics of magnetic field models can vary widely and as a result, the determination of an appropriate model to use in an analysis can be difficult. To aid this process, table 2.2 provides summary information of each model considered in this thesis, accompanied by a relevant reference publication.

Summary Details of CO2003, CM4 and CHAOS field models			
Model Name	**CO2003**	**CM4**	**CHAOS**
Validity Period	2000 - 2001	1960 - mid 2002	1999 - 2006
Static Field	N = 29	N = 65	N = 50
Secular Variation	N = 13	N = 13	N = 15
Secular Acceleration	N/A	N/A	N/A
Input Data	CHAMP (08/00-12/01) Ørsted (08/00-12/01) SAC-C (01/01-12/01) Obs. data (98-00)	CHAMP (08/00-07/02) Ørsted (03/99-07/02) MAGSAT POGO Obs. data (60-00)	CHAMP (00-05) Ørsted (99-05) SAC-C (01-04)
Total Parameters	1121	8863	25243
More Details	Holme et al. [2003]	Sabaka et al. [2004]	Olsen et al. [2006b]

Table 2.2: Summary table detailing the characteristics of the 3 main field models used throughout this thesis.

Before the process of main field model subtraction can begin, raw data must undergo several stages of pre-processing preparation. These stages involve the re-assignment of all data to a common reference time, in this case all data are shifted and given an observation time in modified julian days post 2000.0, with data before this being assigned negative times. To

aid processing automation, all remaining data are also given a common data format.

The final stage of pre-processing before the removal of a field prediction is only applied to satellite data, separating observations into half orbits (single pole to pole track). At this point the subtraction of the chosen main field model takes place. This processing phase involves reading the positional co-ordinates and observation time of each data point into a forward modelling code. These values are then combined with the model co-efficients of the chosen field model to reconstruct equation 2.1 and produce a field prediction. At this stage, the predicted field is subtracted from the original observation and the residual written to an appropriate output file. It is important to note that input data are assessed on a point by point basis irrespective of data source and satellite data are only split into individual tracks to facilitate a secondary along track filtering process. However, even with the removal of a main field model, given that external sources are not understood as well as others, coherent external field signals remain in model residuals, meaning that additional data processing is required to prevent contamination of any oceanic signals.

2.2.2 Additional Along Track Filtering

While the current generation of main field models attempt to represent the geomagnetic field as accurately as possible, no model is perfect. Some field sources are neglected entirely during model parameterisation, but more concerning are the inaccuracies found in predictions of the ones that are parameterised. While un-modelled sources are easier to analyse, as in the case of the ocean, partially modelled sources are much more difficult to account for during further analysis of residual data. It is this issue which brought about the inclusion of additional filtering of residuals after main field subtraction, as some external field signal tends to be left unaccounted for in model residuals used in this work, even when the most recent field models are used. When we consider that many oceanic processes operate with similar frequencies to those active in the external field region (oceanic & ionospheric tides for example), this issue clearly must be addressed.

However, the effects of un-modelled external fields are not limited to ocean analyses and so filtering of this type has been used before in other areas of geomagnetism, often as a processing tool applied to data before field model derivation (see Maus et al. [2006] & Maus et al. [2007a]). Along track filtering has also been used in several high profile studies in recent years as a means of reducing external noise contamination in data whilst retaining the signal being investigated and is being used for a similar purpose here.

The filter used to approximate and remove these un-modelled external fields, specifically those from the magnetosphere, takes the form of a high-pass filter which when extended to a physical space takes the form of a degree 2 limited spatial filter. The filter is chosen to have these characteristics in order to maximise high latitude external noise reduction, whilst minimising damage to signals from other sources. Notably, the filter is always solved on

a track by track basis, hence why all satellite data are split into individual tracks before subtraction of a main field model. The reason for this track by track derivation lies in how quickly external fields vary in space and time. Given that the filter is only solved to degree 2, the inclusion of multiple data tracks spread across the globe would not allow the accurate modelling of the spatial structure within each track or globally, as the filter does not have the spatial resolution required to capture the full detail of such a spatially variable system. The same effect applies if we consider how multiple tracks over the same region vary with time. As the filter does not account for temporal variability, we again risk producing a badly fitting filter if multiple satellite tracks are used in one derivation. Therefore, to produce the closest fitting filter possible for all data, the filter must be re-derived individually for each track. In the case of observatory data the filtering process is not applied, as observations are made well away from the external field source region, where any contamination will be much less significant than in satellite observations which are often made within the source region itself, giving rise to a much higher level of contamination.

The method used to derive the filter is very similar to that used when formulating main field models, only on a much simpler basis. The filtering process begins by reading the data from a half orbit into an inversion routine. At this point, we invert the data to solve for a degree 2 spherical harmonic potential that best represents the un-modelled magnetospheric fields still present in our residual data. The filter is then reconstructed for each data point and subtracted from the input series. An example of this along track filtering can be seen in figure 2.6.

Counter-intuitively, only data between $\pm 50^{o}$ latitude are included in the filter formation, while the filter itself is applied to data of all latitudes. An explanation for this becomes more obvious if we look again at figure 2.6. At high latitudes, residual field amplitudes are significantly higher than those near the equator. If these high latitude data were included in the formation of the filter, because the filter is only derived to degree 2, the higher amplitude polar data would dominate filter magnitudes at all latitudes, rendering any data at low latitudes of little use, removing the relevance of filtering entirely. How, though, can we apply a filter derived using low latitude data to data recorded at high latitudes? This situation is analogous to using globally distributed data with a large data gap when deriving a global model. By using spherical harmonics to represent our field, the data we do include act to control the model where data are omitted, as spherical harmonics are continuous functions and so can span a data gap (although we have less confidence in our solution here). The same applies here, the low latitude data we use to derive our filter allow us to produce a filter that extends from pole to pole. While we may not have complete control over the filter at high latitudes, it is deemed better to have a filter that under fits the data at high latitudes, rather than a filter which destroys clean data near the equator.

While along track filtering can be seen to remove large scale unwanted signals from analysis data, this approach is not always appropriate. The difficulties of such an approach arise from

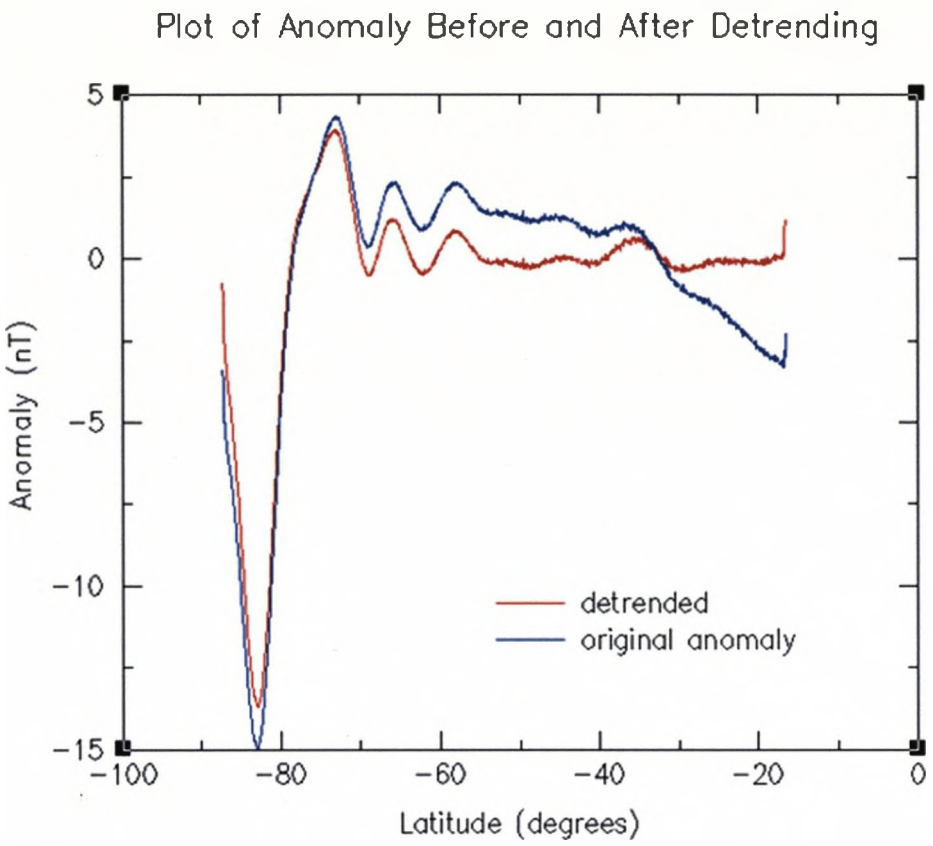

Figure 2.6: An example of noise reduction in magnetic residuals using along track filtering. In this example, scalar observations from CHAMP have been pre-treated with a CO2003 main field model subtraction prior to filtering.

the concept that the harmonic ranges of different field sources will overlap, making it easy to remove signal from one source while trying to filter out another. It is this concept which leads to our filter being limited to degree 2, as magnetospheric fields have a tendency to exhibit large spatial scales. By limiting the filter to low degree, we attempt to minimise the removal of ocean signal, whilst maximising the removal of external contamination. While the removal of some ocean signal is an undesirable, but inevitable outcome, it is deemed more beneficial to have filtered data which have have some oceanic signal removed than have oceanic signals swamped by un-modelled external fields, as would be the case if this filtering was not conducted. For most uses, including the isolation of ocean tidal fields, this filtering approach is an adequate method to address the problem of external contamination. However, in the case of tidal modelling, using this filtering approach only allows the verification of the existence of tidal signals in magnetic data, comparing results against filtered numerical estimates of the full tidal field (calculated using ocean circulation models). Therefore, to produce a model of the full tidal field using magnetic data it is important that input data are unfiltered, while still accounting for unmodelled external fields by other means. The manner in which this is achieved will be discussed in chapter 4.

2.2.3 Repeat Track Isolation

While along track filtering has been used to address the issue of un-modelled magnetospheric fields, additional un-modelled static fields remain in analysis data. To rectify this, repeat tracks are identified in filtered satellite data in an effort to reduce the influence of these un-modelled static contributions. Note that due to their static nature, all ground observatory data are technically repeat observations, although require no further processing and so are omitted from this discussion.

Repeat orbits occur when two orbits from a given satellite, with a small temporal separation pass over very similar ground paths, typically specified as a longitudinal separation at the equator. In the case of the satellites used in this research, all three show some repeat orbit behaviour. While CHAMP was not launched into a repeat orbit configuration, in an effort to retain the altitude of the satellite and extend mission lifetime, CHAMP has had its altitude periodically boosted, resulting in brief periods of repeat orbits. We can identify these periods graphically by plotting the longitude of each satellite orbit equator crossing against the time of the crossing, with periods of repeat orbits represented as periods of time where equator crossings align to preferred longitudes (see figure 2.7). The situation is much the same for Ørsted, also exhibiting a sporadic repeat orbit distribution. SAC-C on the other hand was launched into a permanent repeat track orbit and so has provided repeat orbit data for the whole of its operational lifetime (see figure 2.7). However, the exact criteria for repeat orbit acceptance vary from satellite to satellite. For the purposes of this work, criteria for all three satellites were chosen to have an equator separation of 0.5° longitude, with CHAMP using a temporal track separation of $\leq$ 2 days, Ørsted $\leq$ 10 days and SAC-C $\leq$ 16.5 days. Isolation of repeat orbits is achieved by noting the longitude and time of equator crossing of each satellite track. Repeat orbit pairs are identified by comparing these figures against the same values for all other orbits. Any orbit pairs which fall within the relevant criteria are put forward for further processing.

Once a series of orbit pairs have been identified, it remains to produce a usable dataset. The most important fact to note when compiling a repeat orbit dataset is that satellite data is recorded at regular temporal intervals, not at regular latitudinal intervals. This means that simply subtracting the first point of one track from the first point of its pair track is unacceptable and erroneous. Therefore, repeat orbit pairs are processed by taking the first point of one orbit and searching its pair track for any point that lies within $\pm 0.03^{\circ}$ latitude of the first observation. Importantly, this limit of acceptable latitudinal separation is approximately half the typical distance between consecutive observations within a track, meaning that only one observation will ever be found to match each starting observation. Note that this latitudinal separation is relatively small, meaning that spatial differences between observation pairs should be minimal. Once a matching pair of observations has been identified, a simple difference between the two observations is calculated. Unfortunately, this does mean that final data volumes are reduced by approximately half. The time and position

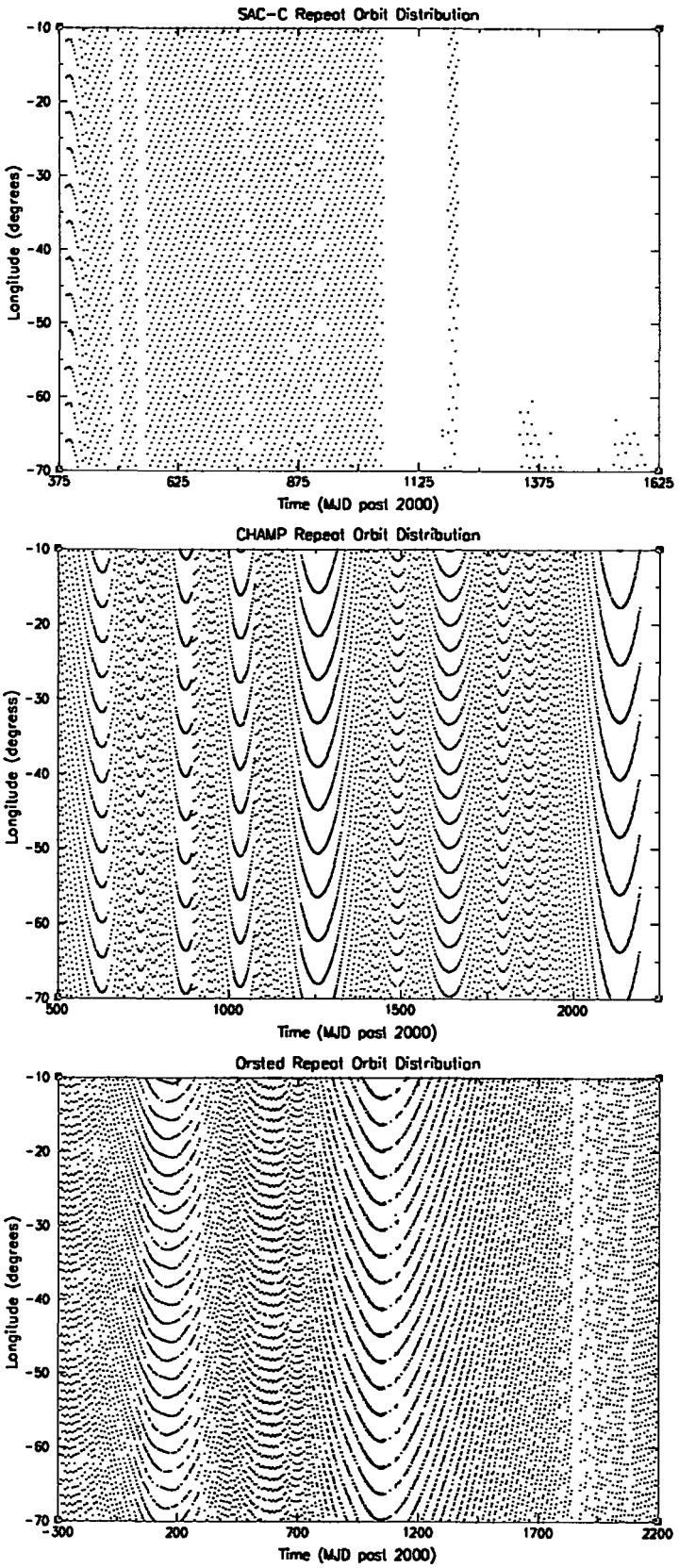

Figure 2.7: The temporal distribution of repeat tracks available in SAC-C (top), CHAMP (centre) and Ørsted (bottom) satellite datasets.

of repeat observations are then set as the intermediate values between the time and position of the original observations. A visual explanation of this process can be seen in figure 2.8. One point to bear in mind when using this approach is that no adjustments are made to repeat observations to account for long period changes between observations within a pair. However, as linear secular variation has already been accounted for during the subtraction of a main field model, this effect should be a consideration rather than a concern.

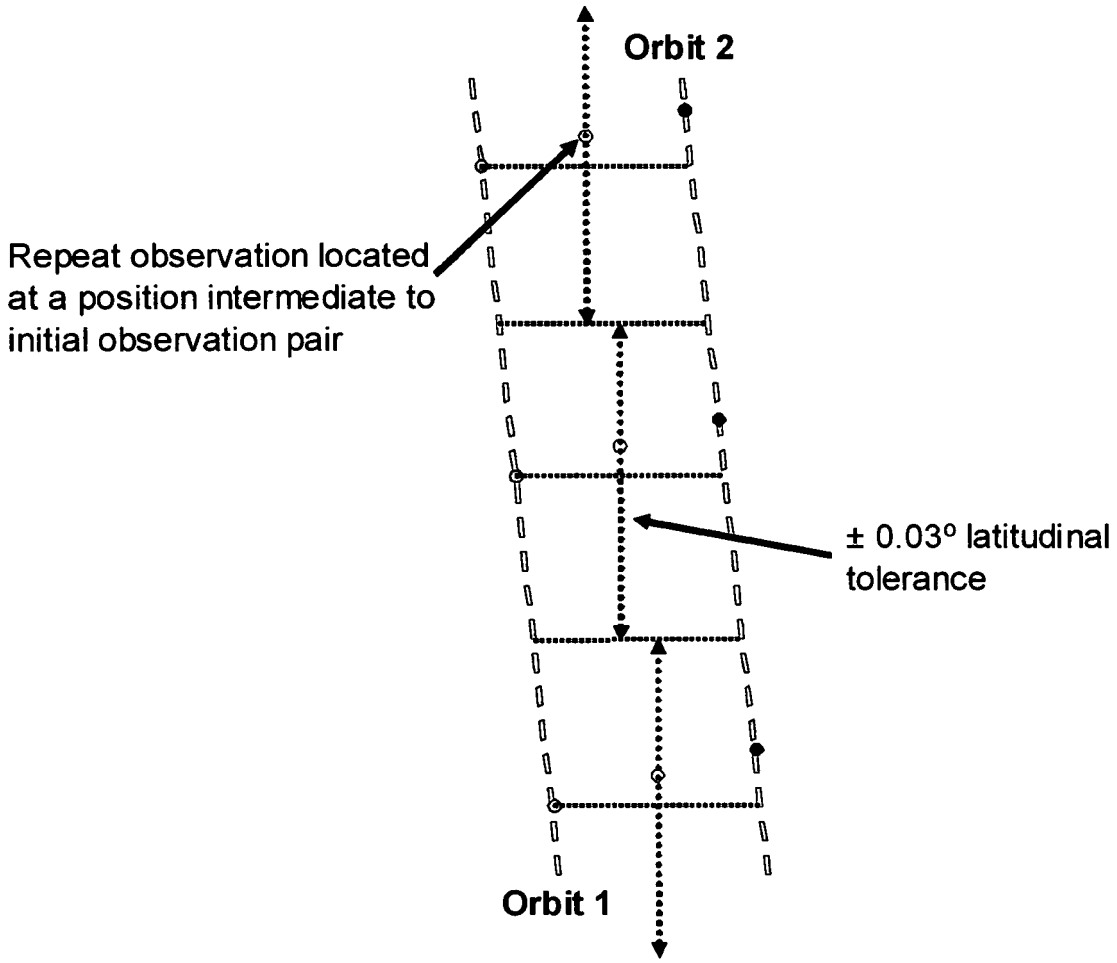

Figure 2.8: A schematic illustration of the methodology applied to satellite data pairs when producing datasets of repeat orbit observations.

The effect this processing has on data is to remove any signal that has been static across the repeat period of the satellite, leaving the temporally varying signal much of this research is attempting to isolate undamaged, making repeat track isolation a useful tool on this occasion. However, dangers are present when utilising repeat orbit data in analysis, especially if the target signal of an analysis has a period close to the repeat period of the satellite being used. The effect this would have would be to remove much, if not all of the target signal, even though the target signal is temporally varying. This effect is introduced because both tracks of the repeat pair will show a similar phase of the periodic signal, giving the impression of a static signal. As a result, a range of signal periods that can be studied with confidence using

repeat orbit data from each satellite should be determined. Graphical representations of this process can be seen in figures 2.9 & 2.10. These plots indicate the amplitude of synthetic repeat orbit data (with a maximum signal amplitude of ± 1.0) over a range of signal periods for each of the temporal track separations outlined previously. While figure 2.9 assumes that periodic signals take a simple sinusoidal form, figure 2.10 makes the assumption that periodic signals take the form of a double positive peak signal, with two equally spaced, equal magnitude peaks per signal period (this form is potentially relevant for the use of this data within the Argentine basin study discussed in chapter 3). While this is a subjective approach (the cutoff level of acceptable residual amplitude is not fixed), a reasonable range of viable study periods can be given for each satellite; CHAMP: 3-30 days , Ørsted: 11-150 days & SAC-C: 17-250 days. It must be noted that in all 3 cases these datasets can be used on signals with periods shorter than the temporal track separation of that satellite, although analyses must be undertaken with extreme caution, as lower period harmonics of the track separation used will also result in a removal of all signal at that period, and so is not advised.

However, while determining a useable bandwidth for each repeat orbit dataset is a useful exercise, for the purposes of this thesis the only periods which need to be considered are those of signals studied using repeat orbit data. Therefore, the only period to be considered is $\sim$ 24.8 days, the period identified in TOPEX altimeter data over the Argentine basin and the subject of a detailed magnetic analysis in chapter 3 (work on global tides and oceanic Rossby waves do not involve the use of repeat orbit satellite data). Therefore, to determine whether the use of repeat orbit data from all 3 satellites is valid for this analysis, more synthetic tests have been conducted. On this occasion, a signal of fixed 24.8 day period is analysed using the three repeat orbit temporal track separations identified earlier in this discussion. Once again, signals take both simple sinusoidal and double peak forms to ensure test results are robust using several signal forms. The results of this test can be found in figure 2.11, showing that while repeat track processing results in a reduction of 24.8 day signal amplitude when considering CHAMP repeat orbit data (to $\sim$50% of their original values), in some circumstances (when using Ørsted & SAC-C data) residual amplitudes can be larger than those of the original time series (due to the phase difference between satellite passes within a repeat orbit pair). Therefore, while reductions in signal amplitude can be expected when using repeat orbit datasets throughout the work contained within this thesis, reductions are not considered significant enough to warrant the exclusion of these datasets from analyses and so are available to use throughout.

2.2.4 Post Subtraction Data Selection

Observations of the geomagnetic field can vary greatly over short periods due to the influence of factors external to the Earth causing large fluctuations in the strength of the Earth's external magnetic field. In an effort to give a measure of magnetic activity on short time scales, numerous magnetic indices are derived (using ground observatory data) for selecting

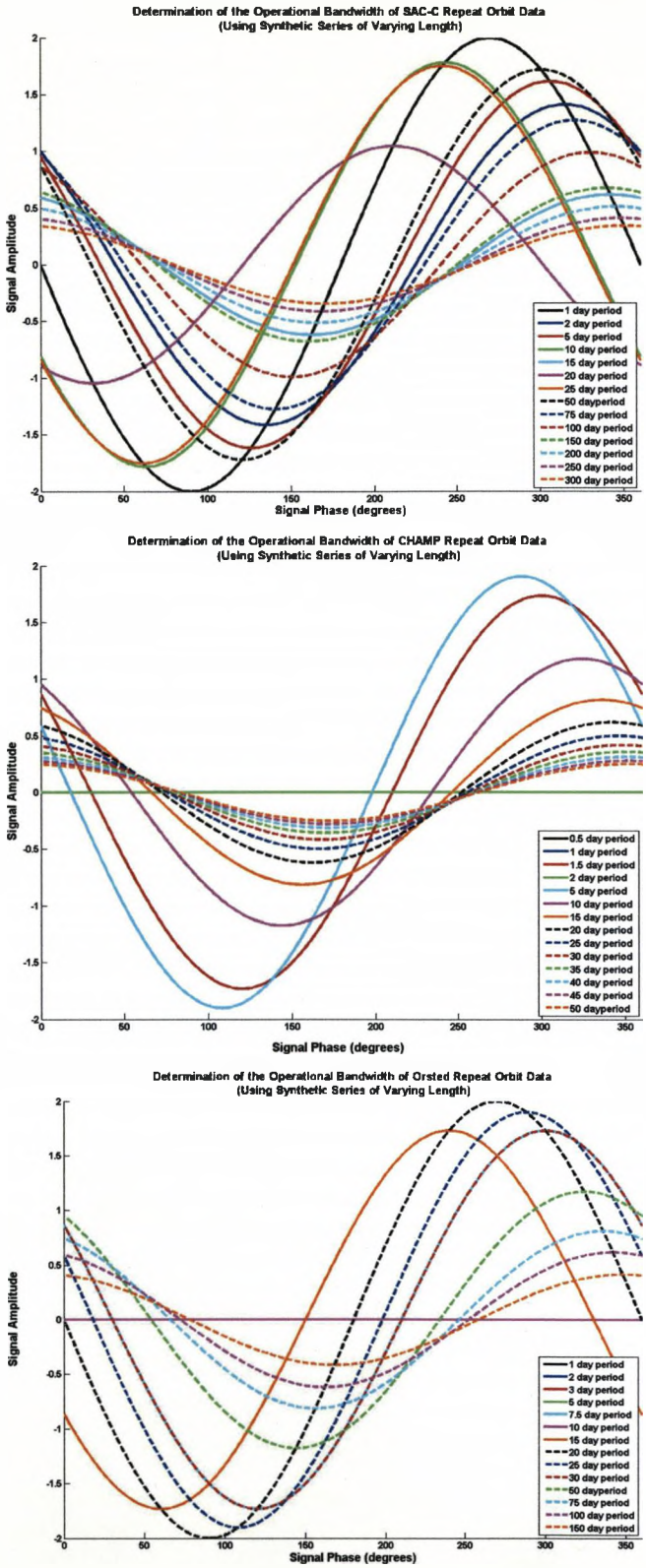

Figure 2.9: Plots highlighting the operational bandwidth of satellite repeat orbit magnetic data (top: SAC-C, middle: CHAMP & bottom: Ørsted), determined using simple synthetic signals of varying period (assuming periodic signals take a simple sinusoidal form) and realistic repeat track temporal separations.

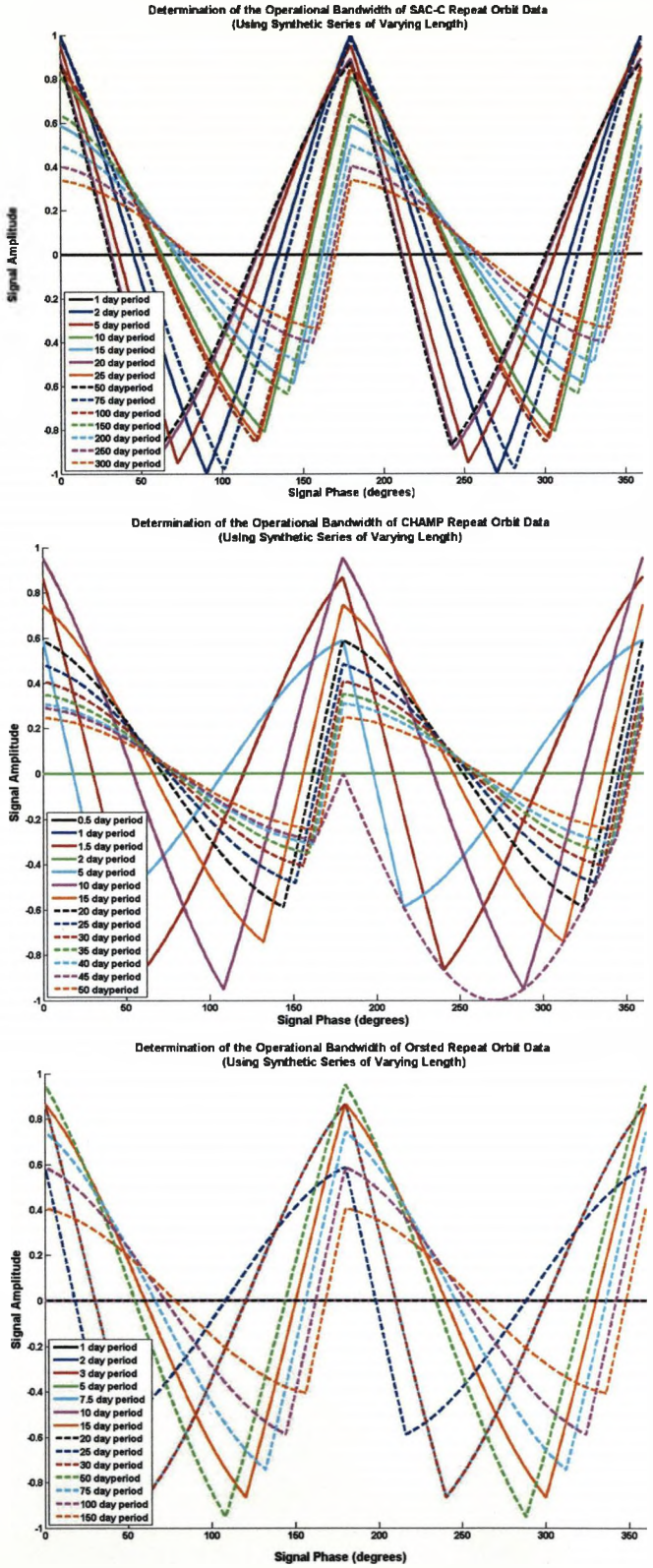

Figure 2.10: Plots highlighting the operational bandwidths of satellite repeat orbit magnetic data (top: SAC-C, middle: CHAMP & bottom: Ørsted), determined using simple synthetic signals of varying period (assuming periodic signals take the form of a double positive peak signal) and realistic repeat track temporal separations.

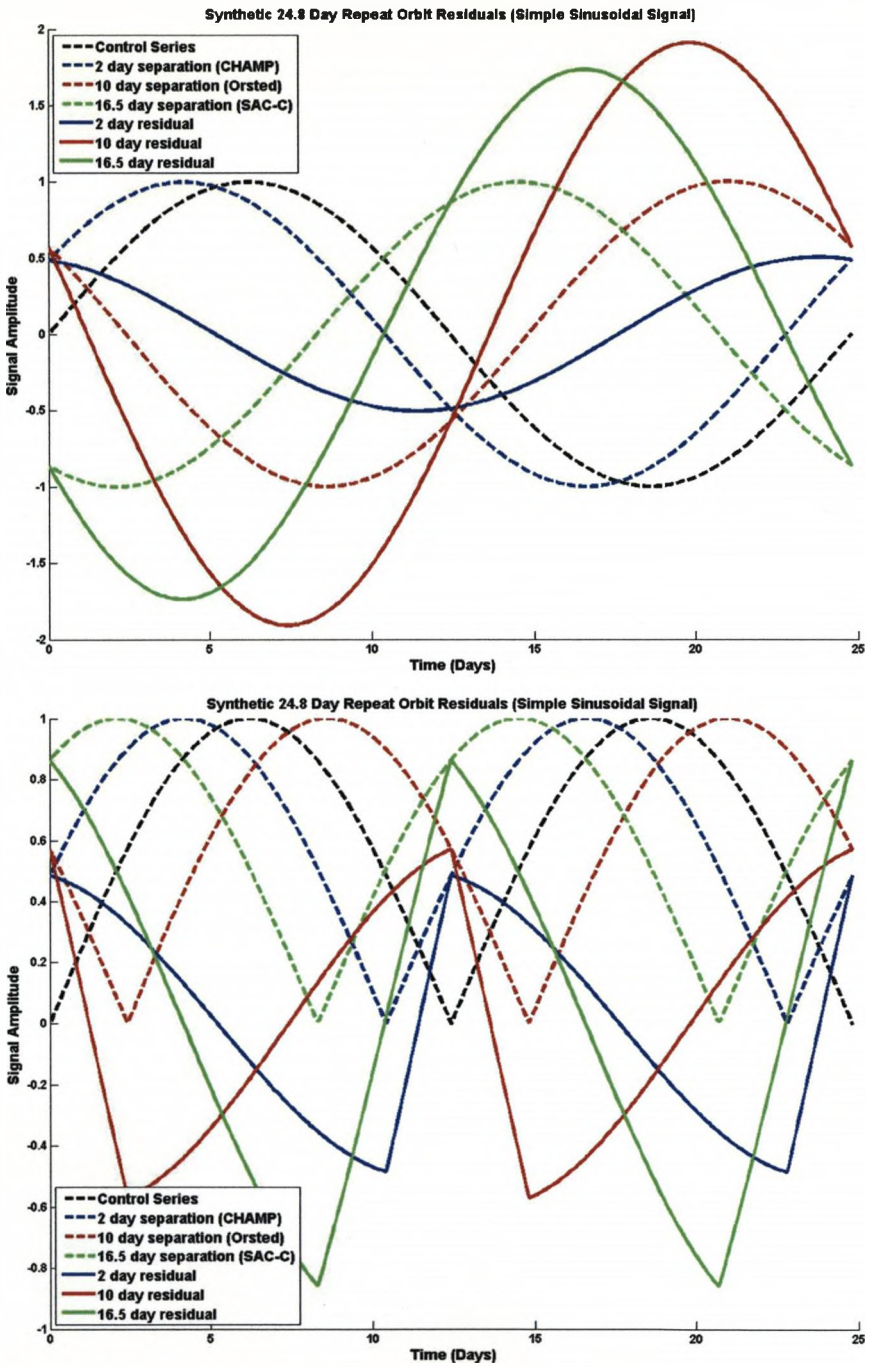

Figure 2.11: Synthetic repeat orbit data residuals, generated to simulate the behaviour of realistic temporal track separations (from CHAMP, Ørsted & SAC-C) when investigating a $\sim$ 24.8 day period signal emanating from the Argentine basin. The upper panel displays residuals generated using signals with a standard sinusoidal form (as seen in TOPEX altimeter data over the region), while the lower panel assumes the target signal takes the form of a double positive peak signal (possibly more realistic when considering magnetic data).

'quiet' data for use in further analysis and the derivation of field models. The work discussed here is no different and so in an attempt to remove the influence of any remaining noisy observations caused by active external fields, a comprehensive data selection process has been conducted on the data used within this thesis. Here, data selection involves a combination of both magnetic indices and temporal and positional constraints to achieve the desired outcome. What follows is an introduction to each of the criteria included in the data selection process used in this research. However, the specific configuration of criteria cut-offs varies from study to study (to achieve the desired result) and so a detailed outline of each configuration will be given where appropriate.

Kp Index: The Kp index is recognised as one of the easiest ways to assess geomagnetic field disturbance at a given time. Available from 1932 to present with 3 hour resolution, the Kp index is derived using data from a small network of mid latitude ground observatories, using a weighted average of K-indices (a measure of the horizontal field strength and declination) and increases from 0 (representing a very quiet field) to 9 (representing a very disturbed field). Although the cut-off level in data selection can vary from study to study, in most cases authors tend to choose values towards the lower end of the Kp scale, as a small number of highly active data can very quickly ruin a large analysis. On the other hand, some studies use a much higher Kp cut-off (5-7), the desired effect being to only remove the effect of geomagnetic storms, allowing the study of a higher percentage of field behaviours.

Dst/dt Index: Traditionally, the Dst index was used in data selection as a direct proxy for ring current strength, in a similar way to Kp being used as a storm time indicator (although Dst is measured in nT rather than a unitless scale), with large negative values of Dst corresponding to a stronger ring current. However, due to the strong correspondence between ring current strength and the Dst index, the ring current is one of the more comprehensively parameterised external field sources in most recent main field models and so Dst alone is not as useful as a selection criteria as previously thought.

However, the ring current also has an effect internally in the Earth in the form of induced fields. These secondary induced fields are generated as the ring current varies in strength through time, inducing electric currents and the associated magnetic fields in the conductive interior of the Earth, with increased induced field strength relating directly to increased temporal variability of the ring current. At the present time, to parameterise these induced fields in field models, accurate knowledge of the Earth's internal conductivity structure must be known as well as solving for the complex magnetic diffusion equations these fields are governed by. Unfortunately, none of the main field models utilised during this research comprehensively account for externally driven, internally induced fields in their parameterisation and so must be accounted for by some other means. However, because induced field strength is heavily reliant on how rapidly

the ring current varies, we can use the temporal derivative of the Dst index as a proxy for how rapidly the ring current varies. Therefore, by selecting data recorded during low Dst/dt conditions, it is possible to minimise the effect externally induced fields have on final analysis datasets.

Additional Criteria: Although not strictly a magnetic index, but certainly driven by magnetic considerations, several temporal criteria are also included in the selection of data. The most restrictive of these criteria is a local time window imposed on all observations. As external fields are typically most active during the day (due to an increased amount of incoming solar radiation), I restrict selection to data recorded between 1800hrs and 0600hrs local time (at the location of observation). However, it is well known that during particular periods of the year, high latitude regions experience 24hr sunlight or darkness. To address this I apply an additional criteria that data above $\pm 60^{\circ}$ magnetic latitude are only accepted during six month segments which will vary between northern and southern hemispheres and correspond to periods of permanent darkness (local winter).

Another criteria is also included, which until recently was not a mainstay criteria in data selection. Work by Ritter and Lühr [2004] highlighted that rather than using traditional polar cap magnetic indices (although they are used briefly in chapter 4), the use of interplanetary merging electric field measurements is a more reliable measure of high latitude magnetic field activity, and so this criteria replaces the use of polar cap indices in most of the work presented in this thesis. Note that the merging electric field values used in this research span the period 2000.0 - end 2005 and were provided by Dr. Emma Woodfield.

As already discussed, the exact configuration of selection criteria varies from study to study, however this process generally reduces total data volume available for analysis by a significant percentage. We can see why this is the case if we examine how the magnetic indices used in the data selection process vary with time. Figure 2.12 shows the temporal variation of Kp, Dst/dt and interplanetary merging electric field selection criteria used in this research.

2.3 Summary

This chapter has introduced the basic data preparation methods that underpin the research contained within this thesis, along with the principal data sources these methods have been applied to. This discussion has shown with appropriate examples, that simple techniques such as main field model subtraction and suitable additional filtering, are capable of producing datasets ideally suited to the study of ocean generated magnetic fields. The discussions contained in the chapters that follow illustrate how the datasets formed using the techniques outlined here can be used (in conjunction with additional analysis methods) to study a wide range of ocean flow processes.

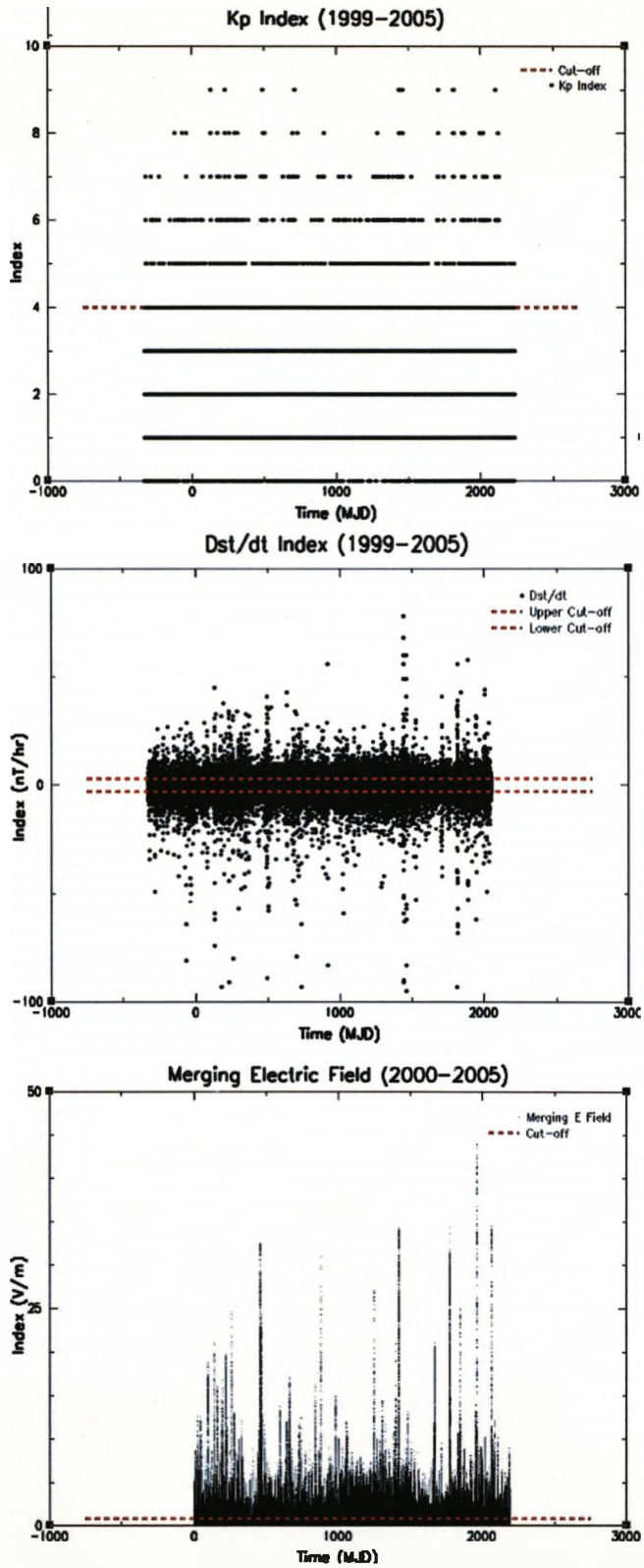

Figure 2.12: Plots showing the temporal variability of Kp (top), Dst/dt (centre) and interplanetary merging electric field (bottom) selection criteria, while red dashed lines indicate typical cut-off values.

Chapter 3

An Investigation of Local Scale Ocean Flow: The Argentine Basin

3.1 Introduction

Previous research undertaken to investigate the magnetic fields generated as a consequence of ocean flow has traditionally been limited to the study of global scale processes. In contrast this chapter presents results from a study designed specifically to identify the magnetic fields associated with localised ocean flows, using satellite and observatory datasets prepared using the methods outlined in chapter 2. In conjunction with these standard datasets, additional data analysis methods are used to identify the magnetic field associated with a localised circulation in the Argentine Basin. Prior to this study, such a circulation had been observed using both satellite altimeter and ocean bottom pressure measurements. While this study aims to understand how a magnetic signal may relate to a localised flow source and its temporal evolution, it is but a tentative first step towards using magnetic field observations as a means to monitor, observe and understand small scale ocean flow processes globally.

This study will begin with an introduction to the Argentine basin and the circulation within its limits, as understood from an oceanographical viewpoint, along with the magnetic field morphologies produced as a result of circulation. This will be followed by a detailed description of the additional techniques required to conduct the analysis, along with the results and considerations of potential complications related to this work. The chapter will conclude with a discussion of study results and their implications, both in terms of understanding the circulation within the Argentine basin and the effect this analysis may have on the future study of localised flow processes.

3.2 Analysis Locality

The localised circulation identified as the target of this study is located in the Argentine basin, situated in the southern Atlantic ocean, to the North-East of South America's southern tip.

The basin also lies to the North of Drake passage, an ocean channel that separates South America from Antarctica and forms part of the ACC (Antarctic Circumpolar Current), one of the largest ocean circulations on Earth. Figure 3.1 highlights the basin's geographical context.

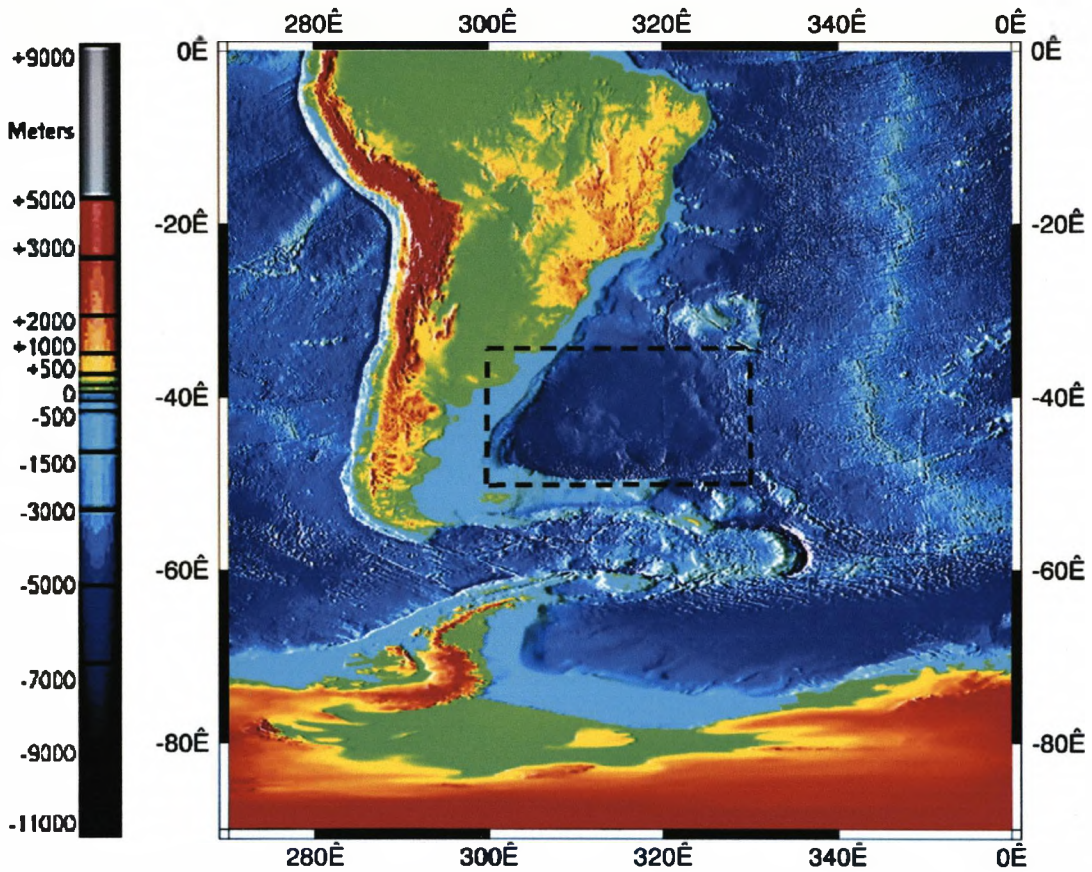

Figure 3.1: ETOP02v2 global relief data (combined satellite topography and bathymetry) of the Southern Atlantic ocean (an approximate Argentine basin boundary is indicated by a black dashed line). Note the basin has an average depth of $\sim$ 5-7km with steep Eastern and Southern flanks and shallow boundaries to the West and North. A sea mount (Zapiola Rise) in the centre of the basin plays an important dynamical role, although this bathymetric feature is not easily visible in this image. *Image has been modified from a global map at ngdc.noaa.gov*

This location is ideal as we have prior knowledge of the circulation and its flow properties from oceanographic studies, as well as the data used to form that knowledge, with which the results of this study can be compared. This circulation also has the advantage of a large mass transport compared to other circulations of this type, which is not only beneficial regarding the amplitude of magnetic signal it may generate, but also explains the large interest from the oceanographic community.

3.3 Motivation from Oceanography

Due to its proximity to the ACC, this is not the first study to focus on flow within the Argentine basin, with early oceanographic work providing many of the circulation's flow characteristics, without which identification of the circulation from within a noisy magnetic dataset would be extremely difficult.

The spatio-temporal characteristics that describe flow within the Argentine basin have been well determined by several recent oceanographic studies. Fu et al. [2001] used TOPEX/ POSEIDON satellite altimeter data recorded between 1992 and 1997, re-gridded using gaussian weighted interpolation (a similar process is used in this study and so a detailed description is provided in §3.5.3), to calculate a frequency spectrum of data central to the basin and also generate maps of their basin wide spatial variability (see figure 3.2). As a result, the authors were able to identify a feature with a circulation period of $\sim$ 25 days that exhibits a dipolar surface configuration and anti-clockwise rotational sense. The same group verified these results using a more sophisticated complex empirical orthogonal function (CEOF) analysis (descriptions of the EOF/CEOF methods are given in §3.5.2), the details of which can be seen in figure 3.3. Finally, using pressure measurements taken at two locations on the basin floor, Hughes et al. [2007] were able to reaffirm the findings of Fu et al. [2001] using an entirely different oceanographic dataset.

The physical dimensions of the circulation were also outlined by Fu et al. [2001], suggesting a horizontal scale of $\sim$ 1000km and a peak to trough surface amplitude of $\sim$ 10cm. However, Tai and Fu [2005] suggest that due to the sampling of TOPEX/POSEIDON data, the surface amplitude given by Fu et al. [2001] may be under-estimated and be nearer to 20cm.

While the spatial and temporal characteristics of a circulation are very important when attempting identification, it is also vital to determine the flow regime of the system, as this has a large influence on mass transport, thus having a direct influence on the potential of the system to generate an identifiable magnetic signature. Fu et al. [2001] suggest that the temporal and spatial characteristics of this circulation can be adequately explained by the solution to a linearised barotropic potential vorticity equation. This suggestion is further validated using the work of Harkema and Weatherly [1989]. Using current velocities calculated (by Harkema and Weatherly [1989]) from current meters distributed throughout the basin water column, Fu et al. [2001] were able to determine the frequency content of the velocity profile in both clockwise and anti-clockwise directions, identifying a 25 day, anti-clockwise rotating mode (see figure 3.4). Due to its penetration to the bottom of the water column (a result also found by Hughes et al. [2007]), this result provides further evidence for the operation of a dominant barotropic, rather than baroclinic mode in the Argentine basin. This detail is particularly important as when combined with the surface amplitude and horizontal length scale already discussed for this particular circulation, mass transports ranging from 50Sv to 200Sv (in extreme conditions) can be generated (although some spread between studies

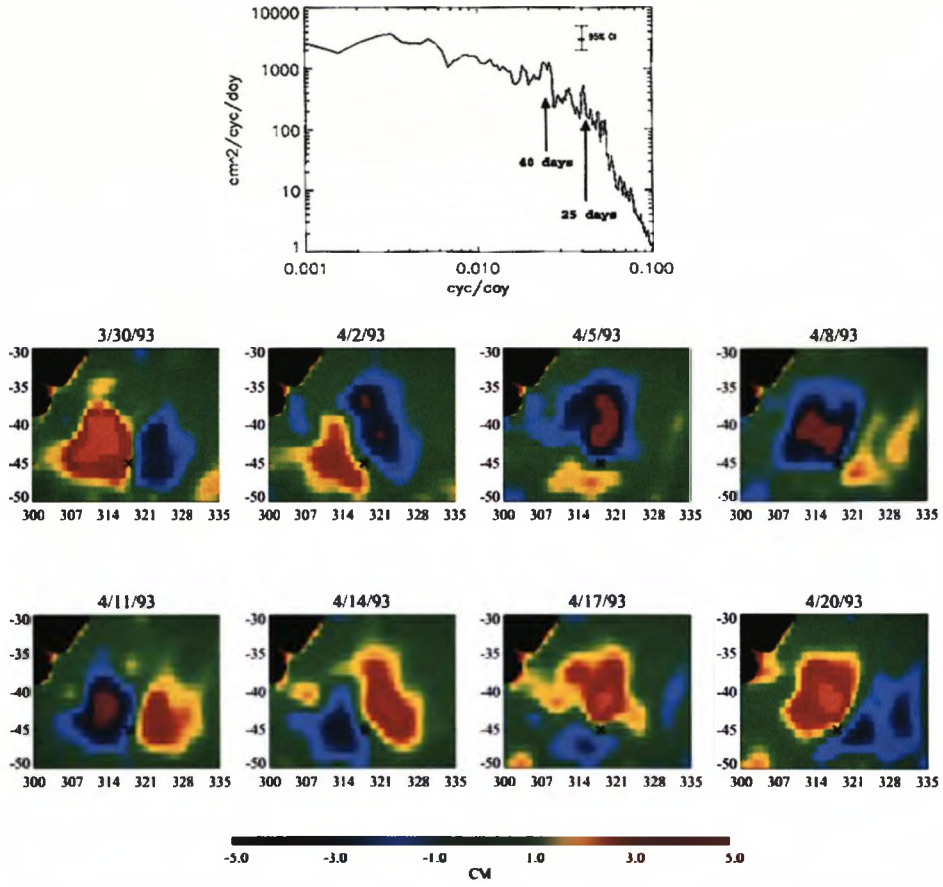

Figure 3.2: Data analysis from Fu et al. [2001]. Upper panel shows a frequency spectrum calculated using re-gridded TOPEX/POSEIDON altimeter data from within a 4° lat x 10° long window centred on 42°S, 316°E. The lower panel displays a series of snapshots of the re-gridded altimeter data (with a temporal separation between images of 3 days), that indicate the presence of an anti-clockwise propagating wave feature, centred over the Zapiola Rise (indicated by an X in each plot).

does exist). (N.B. Oceanic mass transports are typically measured in Sverdrups (Sv), where $1\text{Sv} \equiv 10^6\text{m}^3\text{s}^{-1}$ of fluid movement.). Assuming that flow geometry and ambient magnetic field directions are favourable, such a mass transport should generate a magnetic field of detectable magnitude in both observatory and satellite records.

Unlike the dynamical parameters of the system which vary slightly from study to study, the generation mechanism of this circulation is widely agreed upon. The Argentine basin lies within a very complex oceanographic region and with its proximity to the ACC and Brazil and Falklands (Malvinas) currents (arriving from the North and South respectively), this region is a highly active area of current convergence. It is this convergence of several key currents that is thought to generate an eddy field observed around the basin periphery (see figure 3.5) which subsequently excites the large scale, anti-cyclonic barotropic circulation this study attempts to identify. This hypothesis has been supported by extensive ocean modelling (see Hughes et al. [2007]), where it has been shown that a barotropic circulation model cannot

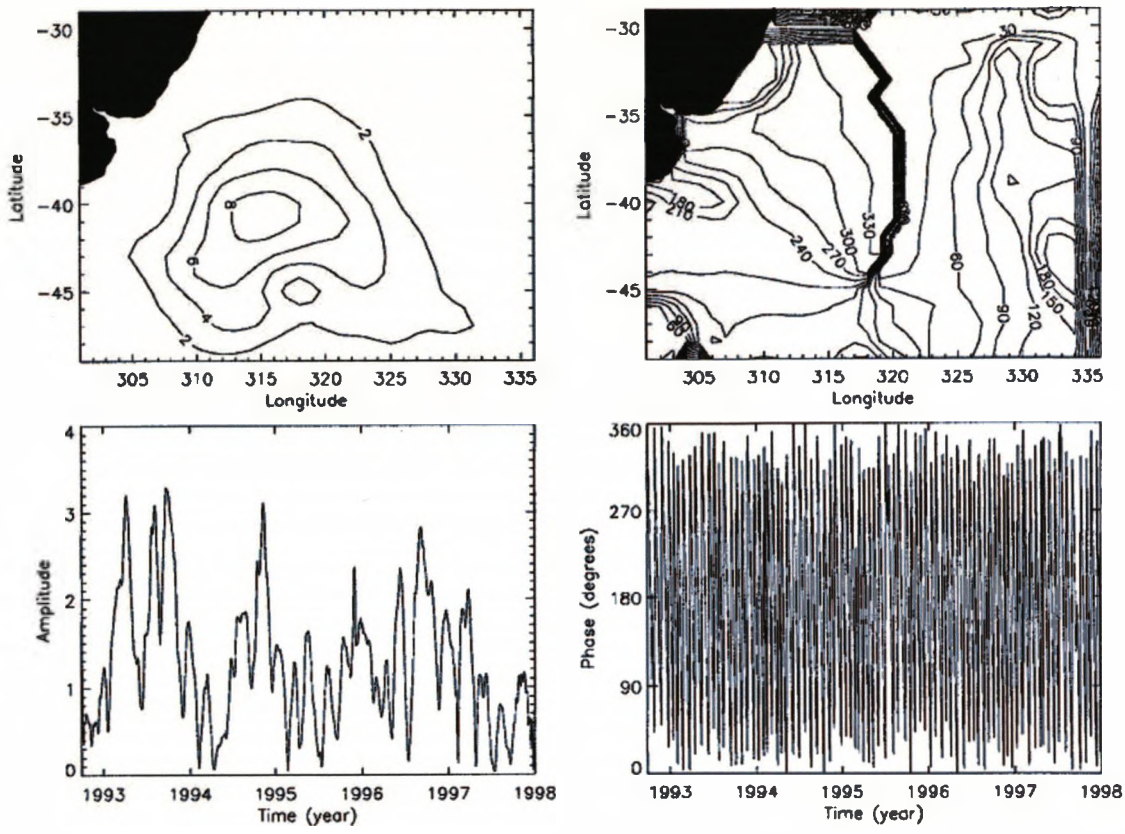

Figure 3.3: Results of a CEOF analysis from Fu et al. [2001]. The upper left panel: the spatial distribution of mode amplitude (in cm). Lower left: the temporal evolution of mode amplitude. Upper right: map of circulation phase (in degrees). Lower right: temporal evolution of circulation phase (in degrees). Note that the map of phase indicates a similar rotational sense to the plots in figure 3.2, with the amphidrome of the mode centred around the Zapiola Rise.

reproduce the flow observed in the field, irrespective of physical parameters such as bottom friction. However, using a baroclinic circulation model, complete with realistic eddy field, the cyclone is well reproduced, suggesting that the target barotropic circulation is heavily excited by baroclinic eddy interactions around the basin edge.

3.4 Time Dependent, Secondary Magnetic Field Morphologies

Using the flow characteristics outlined in §3.3, time dependent magnetic field morphologies generated as a consequence of Argentine basin circulation can be constructed. Due to the work of Harkema and Weatherly [1989], Fu et al. [2001] & Hughes et al. [2007], two distinctly different, yet closely linked field morphologies can be determined (see figure 3.6). The first is tied to the bulk 25 day rotation of the Argentine basin water column (taken as from the basin floor up to mean sea level). Assuming that ocean conductivity and rotational flow

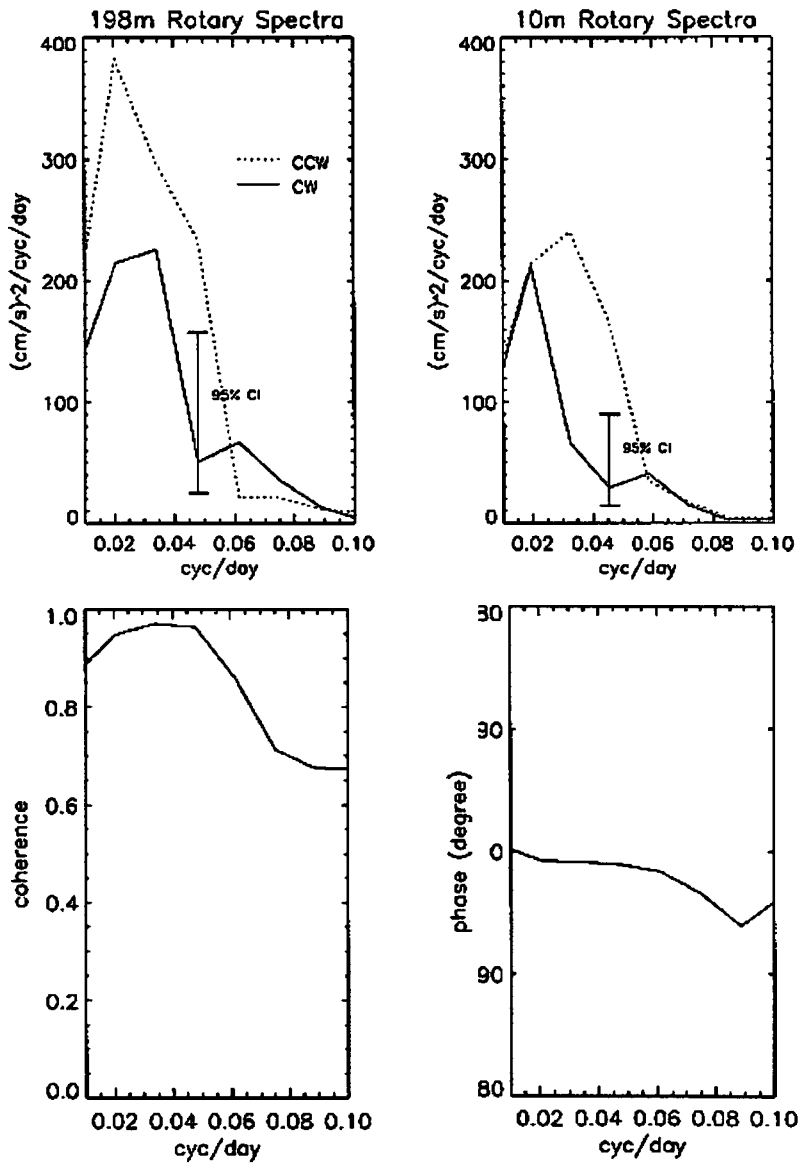

Figure 3.4: Rotary frequency spectra derived using velocity records from Harkema and Weatherly [1989] (shown in Fu et al. [2001]). The upper panels show frequency spectra of current velocities 10m (right) and 198m (left) from the basin floor. The lower panels illustrate plots of coherence between the anti-clockwise components of the upper panels, with coherence amplitude on the left and phase on the right.

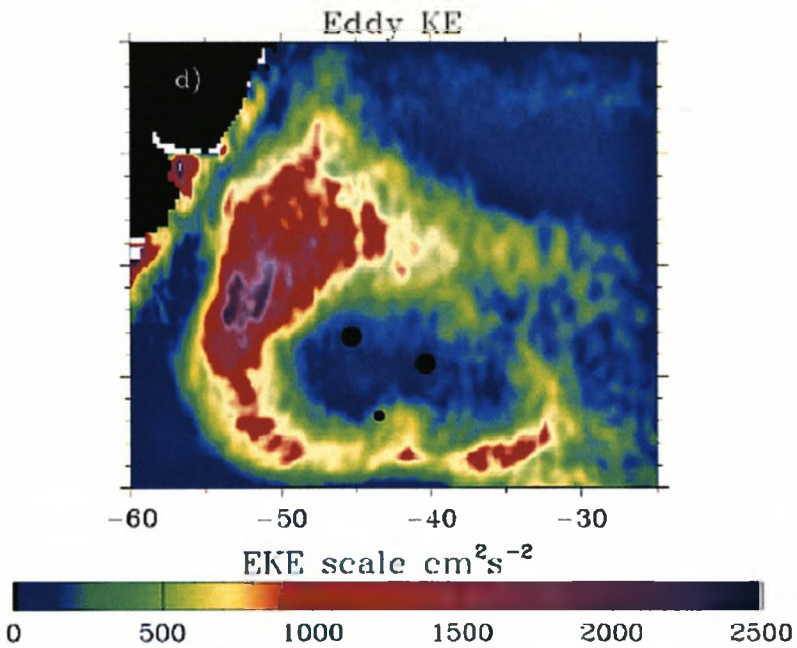

Figure 3.5: Eddy kinetic energy across the Argentine Basin. Black dots in the image correspond to bottom pressure recorder (discussed earlier in this chapter) locations, with the larger dots representing retrieved recorders and the smaller dot corresponding to a lost instrument. *Taken from Hughes et al. [2007], although original map is from Ducet et al. [2000]*

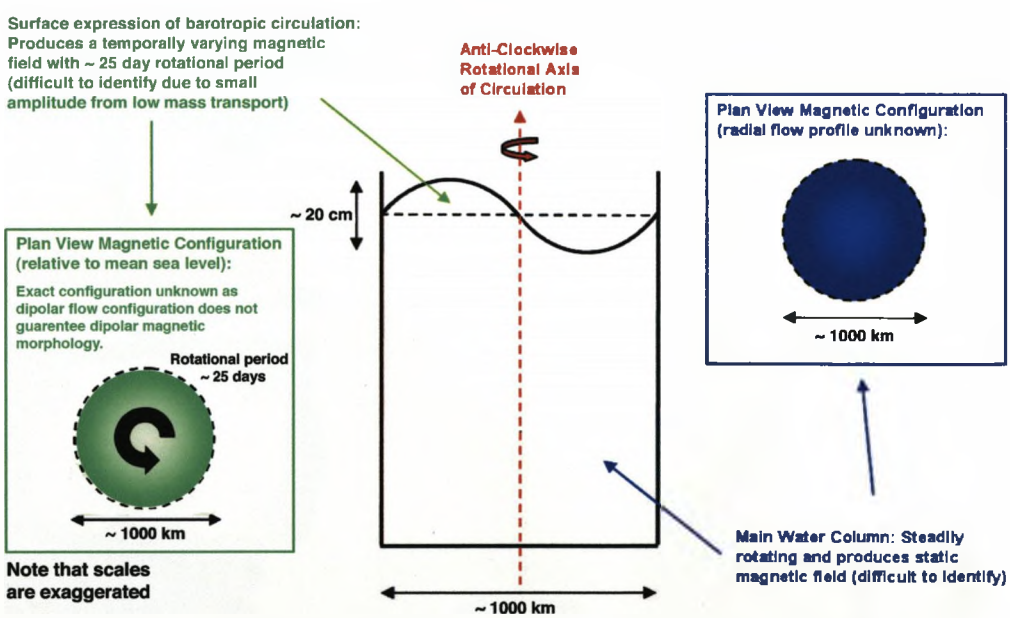

Figure 3.6: A schematic diagram of the various magnetic field morphologies thought to arise from circulation within the Argentine basin.

velocity remain constant locally (unlikely to hold in reality), this signal will remain static through time, generating a patch of magnetic amplitude, centred over the Zapiola Rise, that coincides with the rotational area of the basin (in figure 3.6 this region is assumed circular for simplicity). Unfortunately, the signal is made difficult to identify as a detailed bulk fluid velocity distribution of the basin is not known. The second field morphology is linked to the surface expression of the target barotropic circulation (the rotating surface height anomalies identified by Fu et al. [2001] and shown in figure 3.2). While the forcing for this particular secondary field displays a definite dipolar configuration, without extensive forward modelling (assuming a detailed flow distribution could be obtained), an accurate magnetic morphology is difficult to determine and a matching dipolar magnetic signature is not a certainty. However, unlike in the case of bulk water column rotation, the magnetic field generated by the dipolar surface expression of this circulation will propagate, with a rotation most likely to be centred on the Zapiola Rise in the centre of the basin. The period of this rotation should match that of the oceanic forcing at $\sim$ 25 days. Therefore, it is this second magnetic field morphology that represents the clearest opportunity to identify this circulation in the magnetic record, although due to the uncertainty in its detailed spatial configuration, great care must be taken during analysis.

3.5 Analysis Methodology

This section discusses the analysis methods employed during this investigation, giving details of each approach and reasons for its use.

3.5.1 Harmonic Modelling

Given the complex spatial structure of the geomagnetic field in this region, the easiest flow parameter to test from this system is its $\sim$ 25 day rotational period. However, as observatory data are often non-continuous and satellite data, by their very nature cannot be continuous, Fourier techniques are difficult to implement and so an alternative approach is sought.

Adopting an approach used by Tyler et al. [2003] and Maus and Kuvshinov [2004] (while analysing tidal magnetic signals), a 3 parameter function:

$$M = M_o + M_r \cos(\omega t) + M_i \sin(\omega t) \tag{3.1}$$

is fitted to observations, where M is the unknown magnitude of a harmonic signal, at a frequency ω and time t (in days past the year 2000), consisting of a static component M_o and two time varying components, $\cos(\omega t)$ and $\sin(\omega t)$, with magnitudes M_r and M_i respectively. (Note that M_r and M_i are both real numbers and not real and imaginary components as stated in some studies. Instead, M_i is merely 90° out of phase with M_r, therefore the combination of the two can reconstruct any temporally varying signal for a given ω.). Signal

power at a frequency ω can be represented by $(M_r^2 + M_i^2)$, although signal leakage from neighbouring frequencies must be taken into account.

To determine the parameters of equation 3.1, the system is solved using generalised least squares inversion. Initially, equation 3.1 must be rewritten in a more general form:

$$\gamma = \mathbf{A}.\mathbf{m} \tag{3.2}$$

where γ is a data vector of length p, $\mathbf{m}$ is a vector of model parameters with length q and $\mathbf{A}$ is the operations matrix with dimensions $p \times q$. In this case, these variables have the following assignments:

$$\mathbf{m} = \begin{pmatrix} M_o \\ M_r \\ M_i \end{pmatrix}$$

$$\gamma_\mathbf{i} = M\left(t_i\right)$$

$$\mathbf{A_{i1}} = 1$$

$$\mathbf{A_{i2}} = \cos\left(\omega t_i\right)$$

$$\mathbf{A_{i3}} = \sin\left(\omega t_i\right)$$

where ω, t, M_o, M_r and M_i are as for equation 3.1. Pre-multiplying equation 3.2 by $\mathbf{A^T}$ provides the generalised least squares inversion formalism:

$$\left(\mathbf{A^T A}\right)^{-1}.\mathbf{A^T}\gamma = \mathbf{m} \tag{3.3}$$

where $\mathbf{A^T}$ is the transpose of the operations matrix $\mathbf{A}$, with dimensions $q \times p$. To achieve a well determined solution $p \gg q$, although the accuracy of solutions will always be limited by the simplification of a non-trivial system into only 3 model parameters. Also note that all input data are assumed to have equal uncertainty. While realistic error estimates on input data would be desirable, it is not thought that the results presented here would change to first order as a result and so have been omitted. Once equation 3.3 is solved using Cholesky decomposition, signal power can be calculated and a simple frequency spectrum derived by re-solving equation 3.3 for a range of frequencies.

Synthetic Tests: To test the limitations of this method, numerous synthetic datasets, each configured to simulate a particular aspect of real observatory and satellite observations, have been generated and analysed.

The first aspect of real data to be tested synthetically is time series length. Therefore, synthetic datasets with lengths between 1 and 20 years and a signal period of 28 days have been generated. The lengths of these series were chosen to replicate typical

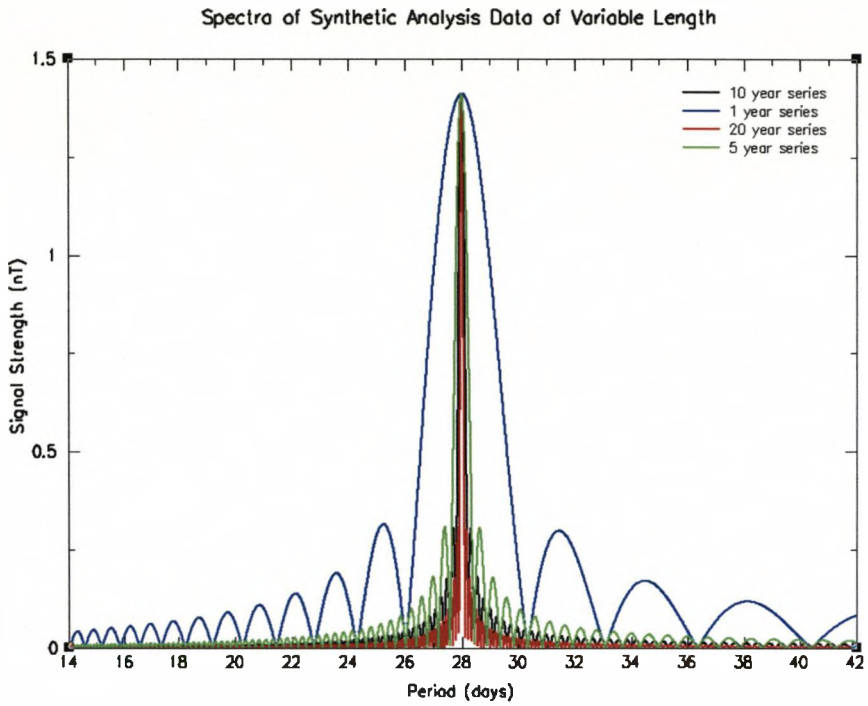

Figure 3.7: Synthetic test results, highlighting the importance of series length when considering the ability of harmonic modelling to cleanly isolate a signal at a given frequency.

series lengths available from ground and satellite records; figure 3.7 shows the resulting spectra. Clearly, series far shorter than most observatory or satellite records are capable of identifying a single 'perfect' signal. However, obvious differences between the spectra are evident. While main peak power does not vary with series length, main peak width and side lobe prominence (both peak power and spectral width) all increase with decreased length, indicating that extremely short series are more prone to inaccurate, unstable solutions and more likely to suffer the effects of signal leakage into neighbouring frequencies.

However, whether series length is the control here is uncertain. Indeed, it is plausible that the ratio of signal frequency to series length is the main control, rather than just series length. This hypothesis is tested, replacing a set frequency and variable series length, with a set series length of 10 years and varying target frequencies between 1 week and 1 year, with the aim of achieving superior results with higher frequency signals (favourable frequency/series length ratio). The resulting spectra are shown in figure 3.8. Indeed upon inspection this appears to be the case, with higher frequency signals displaying superior signal isolation, confirming that frequency/series length ratio is likely the dominant control here. However, given that this study targets only a single frequency, series length remains the dominant factor.

Having determined that synthetic time series far shorter than the real data used in this study still resolve 'ideal' signals, other aspects of real data must be tested, the

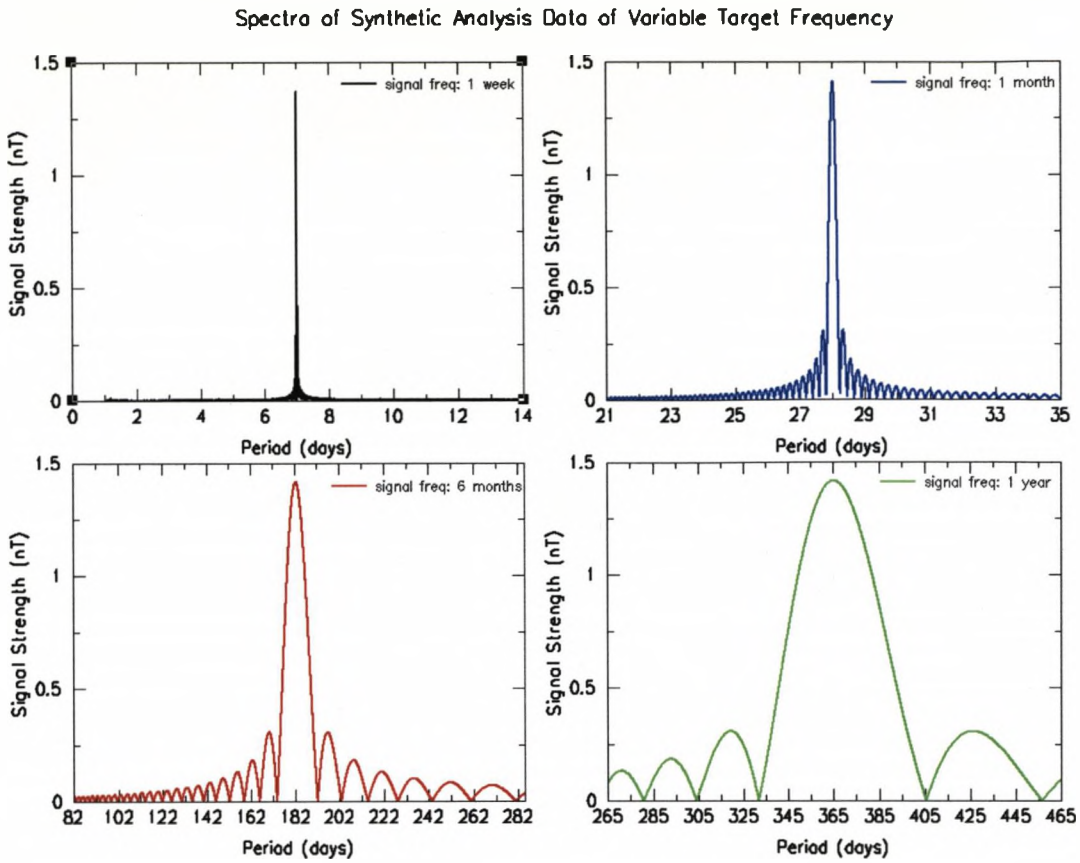

Figure 3.8: Plots illustrating the effect of target frequency on the harmonic modelling method. Upper left panel: spectrum with target frequency of 1 week. Upper right panel: spectrum with frequency of 4 weeks. Lower left panel: spectrum with 6 month target frequency. Lower right spectrum: spectrum of series with a 1 year target frequency.

first of these being the differentiation of signals with similar frequencies from within a single series. This will be particularly important in other areas of this thesis, where this method is used to separate and identify numerous tidal constituents (chapter 4). In this case, a combination of three signals is used to create the test series, in one case having a period separation of 0.5 days and the other 1 day. In both cases the central period is 25 days (to replicate the setting of this study) and series are generated with both 5 and 10 year lengths (although no obvious difference is seen between the two). Spectra of these series can be seen in figure 3.9 and demonstrate that even with lower sampling rates (1 hour), multiple signals separated by only 0.5 days in their period can be easily identified, suggesting the additional complexity of multiple signals, in this synthetic setting at least, does not affect the efficiency of the approach a great deal, although in reality the effects of non-trivial sources may be greater.

The effect of sampling rate on signal identification is clearly evident in figure 3.9, with a lower rate resulting in poorer signal isolation. However, to investigate frequency dependent effects, three synthetic series have been generated, all with 10 year length

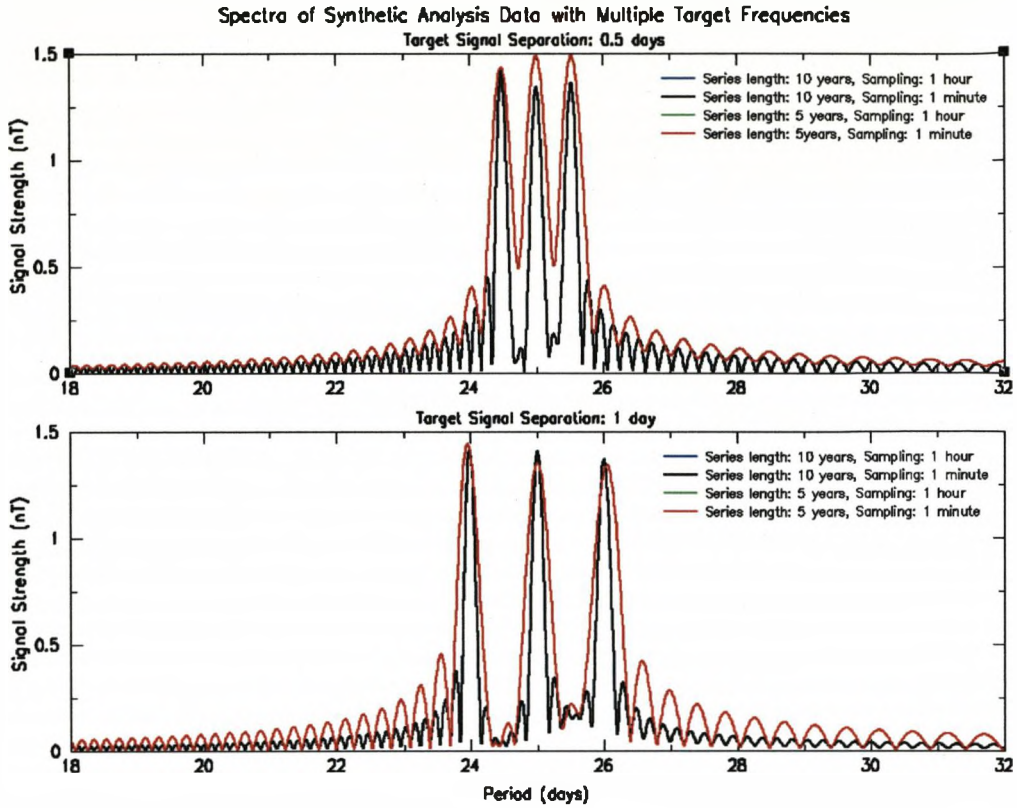

Figure 3.9: Spectra of multi-frequency synthetic data. Upper panel: frequency separation of 0.5 days. Lower panel: frequency separation of 1 day.

and 28 day target period, but with minute, hourly and daily sampling rates. Note that the one second sampling of satellites has not been included, as this faster rate will always provide a superior result and therefore does not require testing. Inspecting the resulting spectra (figure 3.10), frequency dependent variations clearly exist between the various sampling rates, with clear differences only present at lower periods where anomalous strength is present in spectra derived using hourly and daily sampled series. These anomalous solutions are most likely to be the result of an inadequate number of observations per signal period, a problem more prominent at higher frequencies. Such a lack of observations reduces the number of constraints on the inversion solution, therefore anomalously high amplitudes can be assigned at a non target period, without incurring significant data misfit. However, at the periods considered in this study such an effect is not evident and so the use of observatory data (with a lower sampling rate) seems valid.

All the above tests have used continuous series; however, the real data used in this study is often non-continuous (particularly satellite data). Therefore, the final test of this method is to identify a signal at a given period using non-continuous synthetic series. Four such series have been created, each with 10 year duration and hourly sampling. The first two series replicate un-realistic data discontinuities, one including

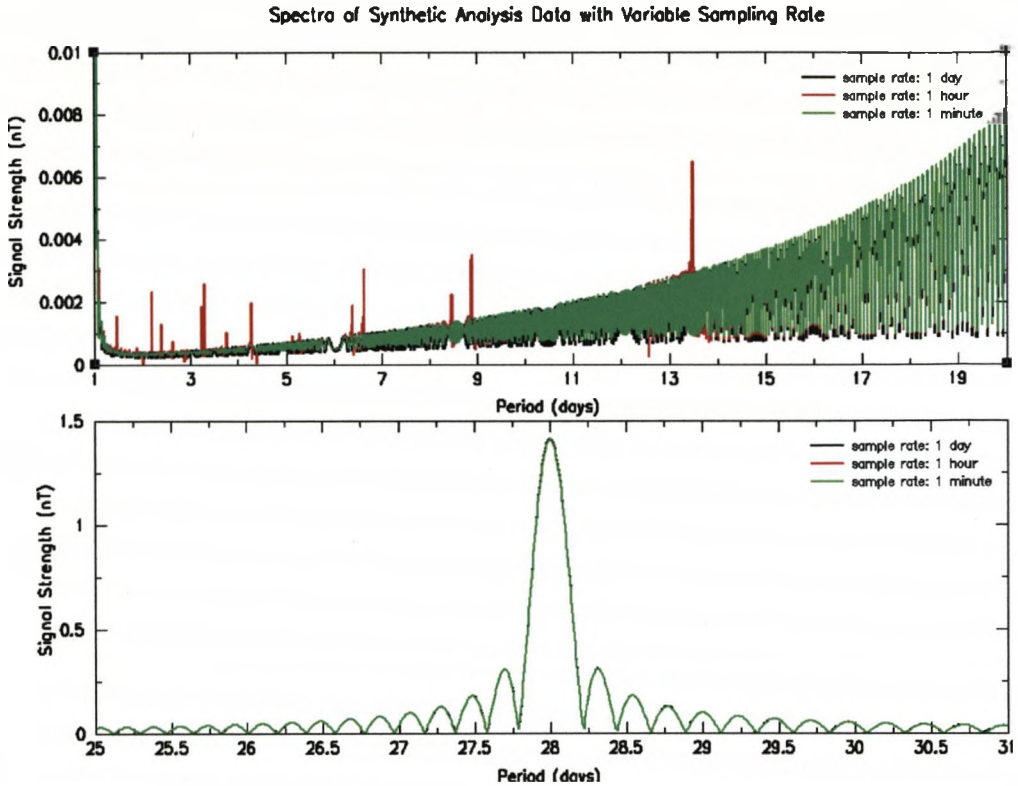

Figure 3.10: Spectra derived from synthetic series with differing sampling rates of 1 hour, 1 minute and 1 day. The upper panel (focused on lower periods) highlights anomalous differences in spectra derived using lower sampling, while uniformity between spectra is achieved at the target period (lower panel).

a single six month gap in the middle of the series, the other featuring 5 one month gaps distributed evenly throughout (see upper row of figure 3.11). Studying the spectra of these series in the upper panel of figure 3.12, only marginal differences in their side lobe characteristics are found when compared to a continuous equivalent, while signal peak characteristics remain consistent with the continuous case. The final two series attempt to be more realistic, replicating typical observatory and satellite data. While the observatory series is near complete, with only occasional data gaps on the order of a few days and a single prolonged gap to simulate a period of extended in-operation (for either technical or operational reasons), the satellite series is much more sparse with only brief periods of near continuous data (to replicate a satellite studying a localised region, as in this case). These series and their corresponding frequency spectra can be seen in the lower panels of figures 3.11 & 3.12 respectively. While the spectrum of the observatory-like series is very similar to the continuous reference (due to its near continuous nature), the satellite-like spectrum differs greatly. While main peak characteristics (power & width) remain consistent with the continuous reference, side lobe behaviour is far more chaotic, generally with higher power and greater width. This is also the first test to show side lobes whose strength does not systematically decrease

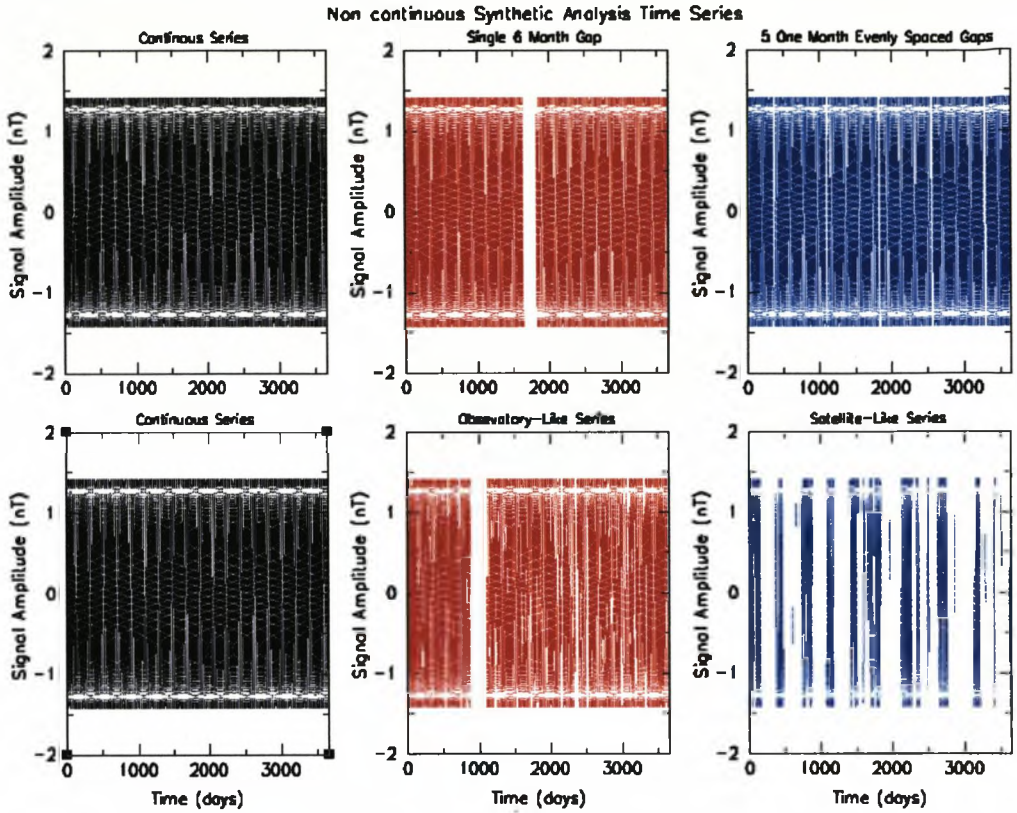

Figure 3.11: Plots of the time series used in figure 3.12. The upper row contains unrealistic series with a continuous reference. The lower row contains a continuous reference (left), an observatory like series (centre) and a satellite like series (right).

away from the main peak, the most likely reason for behaviour such as this being that across extensive data gaps model fit cannot be constrained, allowing the assignment of anomalous magnitudes at non signal periods (without a significant misfit penalty). However, the main signal peak remains clearly identifiable; therefore, the method is still considered valid.

This extensive testing has shown that harmonic modelling is indeed a suitable method to study the frequency content of magnetic records, although prior knowledge of the target frequency may be useful, particularly when dealing with satellite observations. However, all of these tests do assume that the target signal is statistically stationary in both its magnitude (i.e., the amplitude of the signal does not vary in time, through random sporadic forcing, or the presence of periodic forcing fluctuations) and position. It is hoped that due to the successful identification of this circulation in other studies, these assumptions may hold sufficiently to obtain a positive circulation identification.

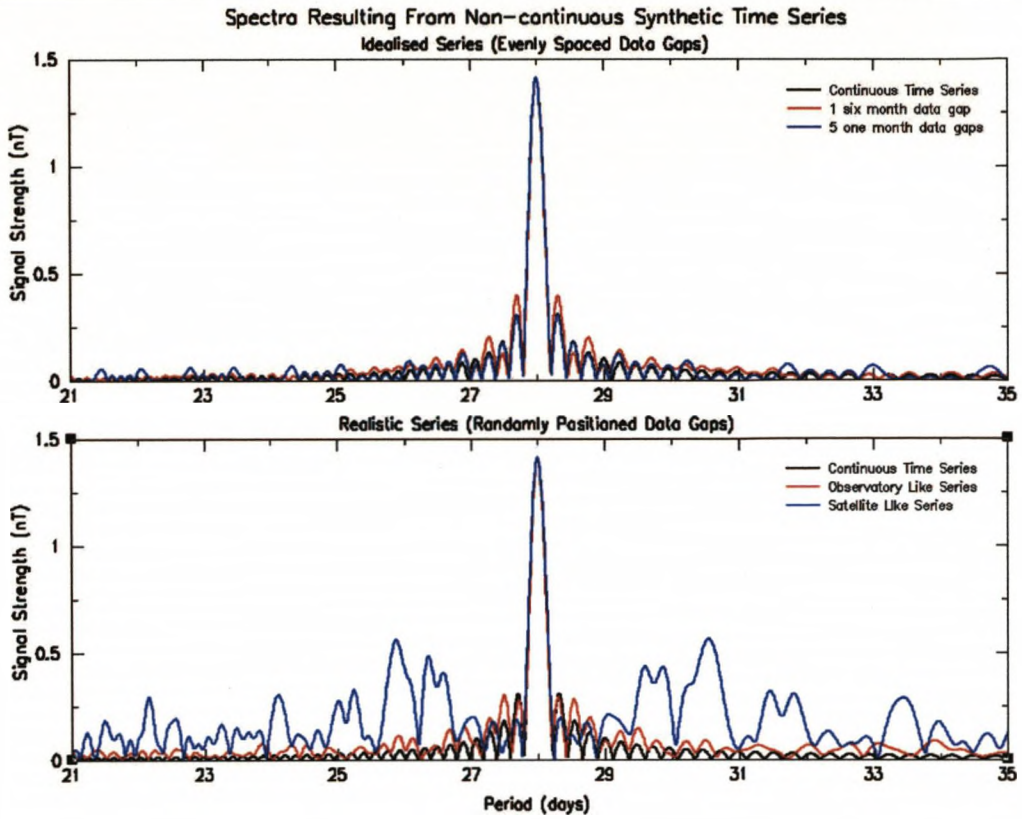

Figure 3.12: Spectra derived from non-continuous synthetic series. The upper panel contains spectra of series with evenly distributed data gaps. The lower panel contains spectra from more realistic series designed to replicate satellite and observatory series. Note that both panels also contain an equivalent continuous spectra for reference.

3.5.2 Empirical Orthogonal Functions (EOFs/Complex EOFs)

It is often very difficult to isolate the contribution of a particular field source from the ambient background. Empirical orthogonal functions, or EOFs, are widely used in many areas of scientific research to improve signal isolation and are used in this study for the same reason (for detailed information see Preisendorfer [1988] & Björnsson and Venegas [1997]).

In any multi-dimensional system variability exists in every dimension. EOFs represent that variability as a series of orthogonal functions, with each successive mode accounting for as much of the remaining variance (after the removal of all variance previously allocated to earlier modes) in the system as possible, with the total number of modes being equal to the dimension number of the system (equal to the number of input series). The temporal evolution of each mode is derived by transforming the input time series into the direction of the mode in question. Figure 3.13 shows a simple two dimensional example of how EOF modes are assigned.

From this generic base, EOFs can be applied to many physical systems, in this case to fit observatory and satellite magnetic data. In the case of observatories, the resulting EOFs

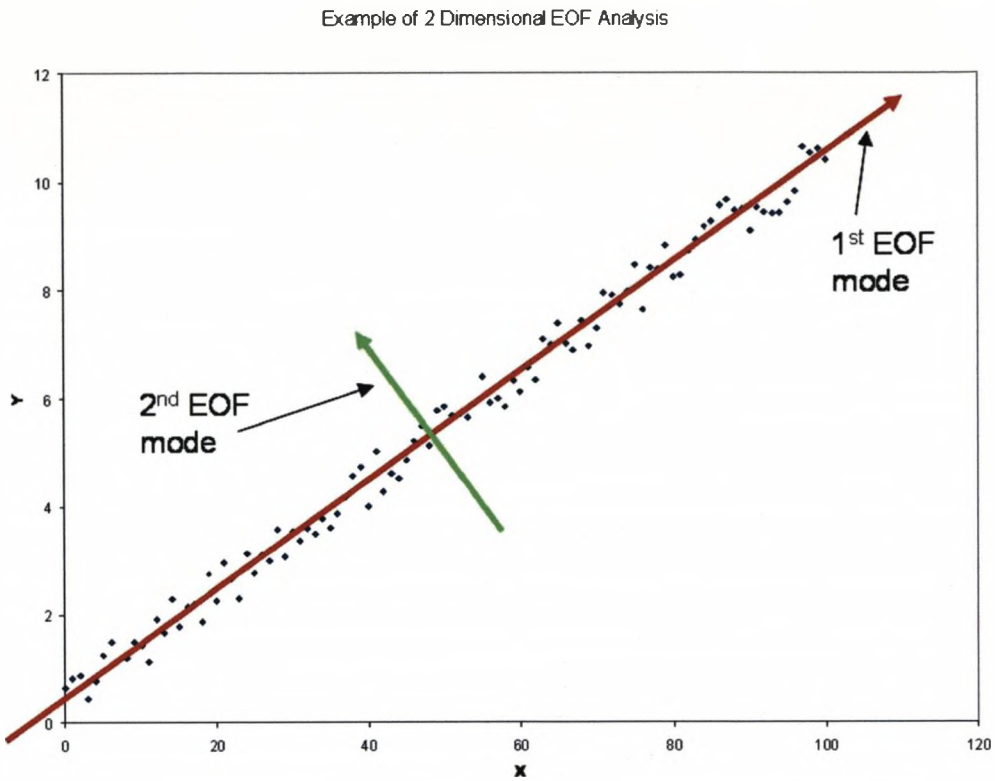

Figure 3.13: A schematic illustration of a 2D EOF analysis.

are identical to those in figure 3.13, with the addition of a 3rd orthogonal mode. As such, we can consider these modes as a rotational alignment of the original vector field to the direction of maximum variance remaining in the system, with each mode being represented as a unit vector describing its orientation relative to the X, Y & Z axes. The expansion time series (temporal variation) for the modes are calculated by multiplying each element of the unit vector with the corresponding input vector component series. When analysing satellite observations, while the expansion series of a mode continues to represent its temporal evolution, the mode itself alters context, as each input time series now represents magnetic field evolution at a different spatial grid node. (Note that this application of EOFs requires uneven satellite observations to be reduced onto a regular 3D data grid [see §3.5.3 for details].). Therefore, each mode can be considered as a map that describes the spatial structure of the data variance (magnetic field) the mode accounts for.

While standard EOFs are useful in static systems, they are often of limited use in a spatial context where positional translation and rotation are common (standard EOFs can only identify amplitude variations). In order to identify such variability, the standard EOF approach is extended into a complex regime, where each CEOF mode and expansion series pair have both real and imaginary components. As such, these 4 components can be combined to describe the spatio-temporal variability of the chosen input data. This approach is ideal for this study, as in principle this method can identify the rotational signals that Argentine

basin circulation is expected to produce.

However, it is important to note that both EOFs and CEOFs are only a statistical tool, used to split data into individual modes of variability. Therefore, it is ill-advised to interpret any EOF/CEOF mode in a physical sense until its context within the system has been determined. Signals also rarely separate cleanly, often with multiple signals contributing to a single mode and single signals contributing to many modes. As such, multiple modes from one analysis may have to be considered simultaneously.

3.5.3 Gaussian Weighted Data Re-Gridding

The semi-irregular distribution of satellite magnetic data often poses difficulties when studying the spatial variability of the geomagnetic field. To investigate such variability, data can be relocated onto a regularly spaced 3D spatio-temporal grid, an approach used on numerous occasions previously (for example Cipollini et al. [1997], Fu et al. [2001] & Tai and Fu [2005]). To produce the grid, at each grid node all data that fall within a designated search window are gaussian weighted according to their spatial and temporal separation from the node in question, with more distant observations given a lower weighting. The mean of these weighted observations is allocated to the node and the process repeated across the grid. By altering node spacing and search window dimensions this approach can be applied to numerous scenarios; examples in this thesis being the study of localised ocean circulation (see §3.7.3) and the identification of oceanic Rossby waves in the satellite magnetic record (see chapter 5).

3.6 Observatory Analysis

3.6.1 Analysis Data

In this analysis, data from three observatories have been used to investigate the presence of circulation related signals in the ground based geomagnetic record. Port Stanley (PST [1994-2005]), the primary dataset, is situated on the Falkland Islands only a few hundred kilometres South of the Argentine basin. Data from Port Stanley is complemented by series from Vernadsky, previously known as Faraday/Argentine Islands (AIA [1990 - 2005]), situated to the South West of PST and Neimgk, Germany (NGK [1990.8 - 2005]). NGK data have been included in the analysis to identify the presence of any global signals in PST & AIA records. All datasets use full vector format (X, Y & Z) hourly mean values. A map displaying the positions of PST, AIA & NGK relative to the Argentine basin and each other can be seen in figure 3.14. Note that prolonged periods of data loss at all 3 observatories have resulted in uneven series lengths (see figure 3.15); therefore shortened, even length series have been used in the primary statistical and EOF analyses that follow (the results of equivalent statistical and EOF analyses, conducted using full length series can be found in Appendix A).

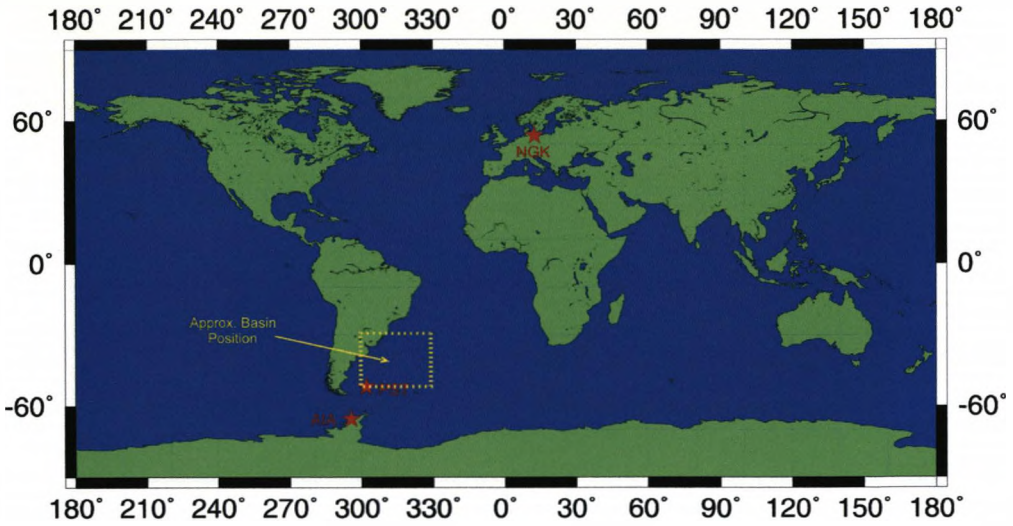

Figure 3.14: A map displaying the geographic locations of observatories used in the analysis of Argentine basin flow.

Prior to analysis, to ensure that the preparation of raw observations (CM4 model subtraction) has not introduced additional signals, frequency spectra of both raw and residual series are shown in figure 3.16, where as expected no additional signals are found.

As in most geomagnetic studies, the effects of unwanted external fields are controlled by selecting data using magnetic activity criteria: Kp $\leq$ 4- and Dst/dt $\leq \pm$3.0nT/hr. These moderate limits were chosen to minimise data loss, whilst reducing the effects of extreme external events. The effect of this reduction on the rms (root, mean, square) and standard deviation of observations can be seen in table 3.1, where in most cases a marginal reduction in statistical values is seen (any exceptions may be due to the removal of low amplitude data points not adversely affected by external events).

Data Type			R.M.S			Standard Deviation		
Station	**Selected**	**Filtered**	**X**	**Y**	**Z**	**X**	**Y**	**Z**
PST	no	no	122.689	39.707	223.073	19.79	37.156	13.234
		yes	1.736	1.178	1.684	1.599	1.176	1.13
	yes	no	123.179	38.92	223.715	19.179	36.492	13.082
		yes	1.741	1.146	1.675	1.582	1.143	1.094
AIA	no	no	296.013	70.753	561.747	29.224	31.552	45.773
		yes	3.229	1.496	3.907	2.787	1.454	2.356
	yes	no	296.822	69.023	561.703	29.593	31.175	44.979
		yes	3.196	1.459	3.879	2.746	1.421	2.322
NGK	no	no	235.507	28.542	38.163	19.282	23.503	14.379
		yes	2.022	1.245	1.521	1.532	1.242	1.507
	yes	no	235.422	27.586	38.248	18.656	22.62	13.612
		yes	2.029	1.214	1.457	1.509	1.214	1.437

Table 3.1: Basic rms & standard deviation statistics for all Argentine basin observatory analysis time series

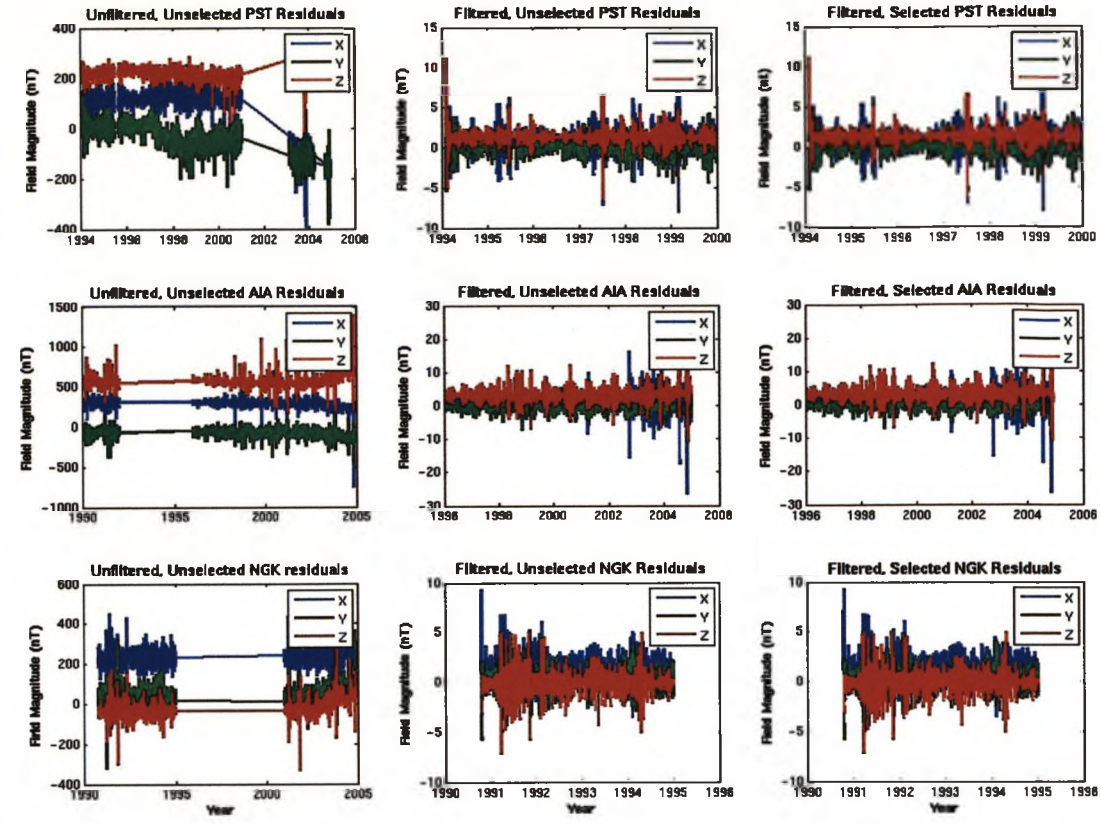

Figure 3.15: Plots of the unselected, unfiltered residuals (left) and filtered residuals, both unselected (centre) and selected (right) used in both statistical and EOF analyses of observatory data. PST data are found in the upper row, AIA in the centre and NGK in the lower row.

Post data selection, to improve comparability between the results of this analysis and those of oceanographic equivalents (e.g., Fu et al. [2001], Hughes et al. [2007]), both selected and unselected observatory series are filtered using a bandpass filter with a 10 - 30 day pass band. To ensure no adverse effects due to filtering are present, both filtered and unfiltered series are analysed. Note that filtering data requires a continuous series; to achieve this any data gaps are filled using linear interpolation.

3.6.2 Statistical Analysis

I begin by plotting the direction of the observed magnetic field vector from PST (see figure 3.17). Ideally, the presence of a rotating flow within the region of observation, should result in a slight rotational deflection of the ambient magnetic field vector, due to the additional contribution made by its secondary magnetic field (the rotational frequency of the deflection should match that of the oceanic circulation). However when figure 3.17 is examined, while rotation of the field vector is present, considerable additional complexity makes determination of the period and origin of the rotation difficult. The frequency content of these time series (see figure 3.18), also displays no clear peaks at $\sim$ 25 days, although slight broadband

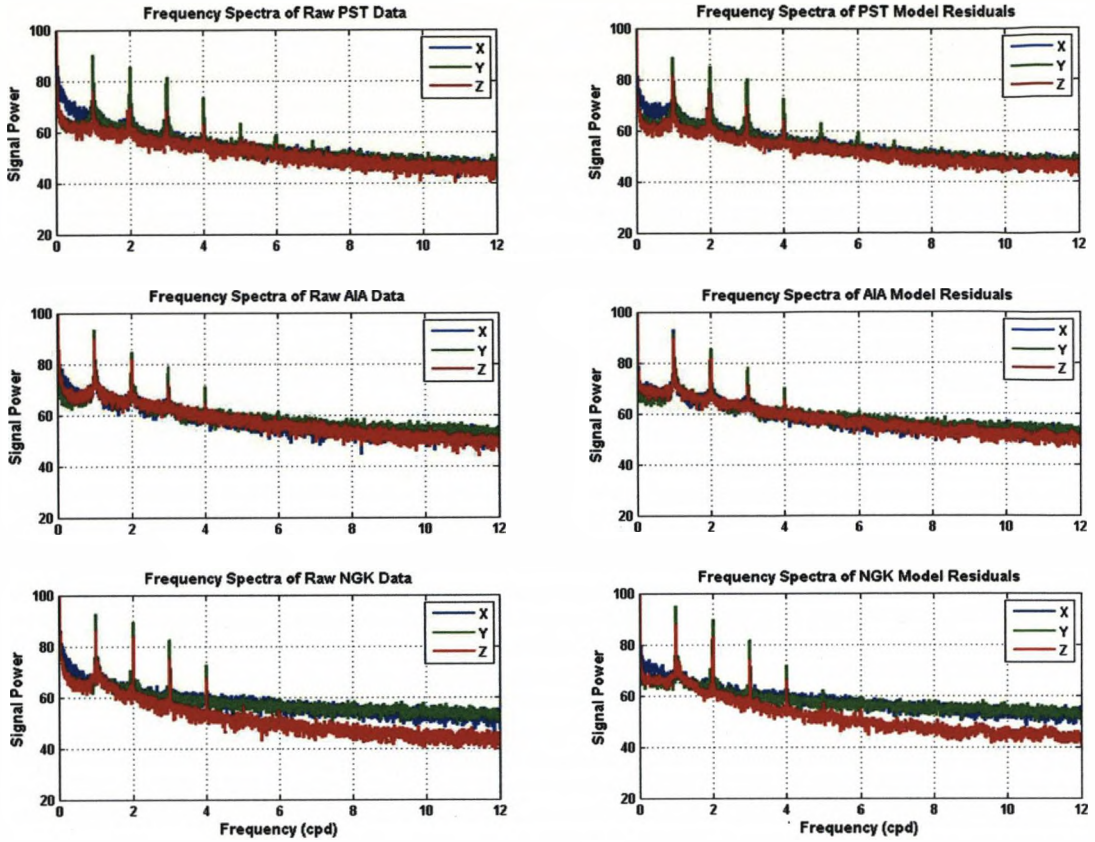

Figure 3.16: Frequency spectra of observatory time series [top: PST, centre: AIA, bottom: NGK], pre (left) and post (right) CM4 subtraction. Spectra show no indication of artificial signal introduction.

amplifications are seen in the spectra of some field components. Recent work by Weijer et al. [2007a,b] suggests that the Argentine basin is the site of several coincident modes of variability, each operating at a different frequency. While this hypothesis validates the discrepancy in operational frequencies found by Fu et al. [2001] & Hughes et al. [2007], it also suggests a reason for the broadband amplifications between 15 and 30 days found in many of the spectra in figure 3.18. However, multiple persistent modes would produce several distinct peaks in the relevant frequency spectra and given that such signals are not observed in figure 3.18, it suggests that either each individual mode must be sufficiently short lived to reduce its peak definition, or more likely that the magnetic counterparts to these modes are not recorded clearly in PST observations.

To advance this analysis, magnetic records are studied in conjunction with a CEOF mode from Hughes et al. [2007] (identified using TOPEX/POSEIDON data), an extension of the Fu et al. [2001] CEOF mode shown in figure 3.3. In this case, pre-processed TOPEX/Poseidon SSH anomaly data from the period 1993-2004 (in the region 30°-50°S & 300°-335°E), manipulated onto a uniform $1^{\circ} \times 1^{\circ}$ data grid are used to calculate the resulting CEOF mode, which is very similar to that of Fu et al. [2001] only over a longer time span. The comparison begins with the derivation of frequency dependent coherence between magnetic series from

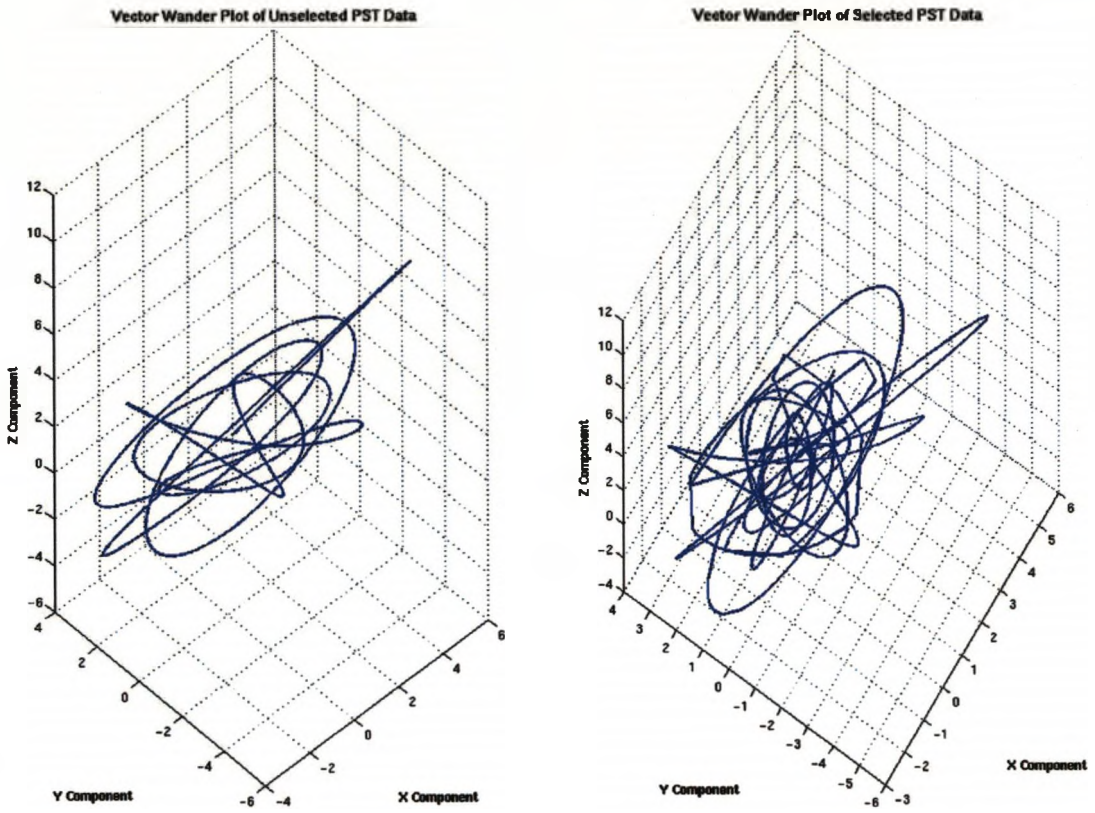

Figure 3.17: Vector wander plots of selected and unselected PST series. Both series are filtered to reduce noise from non target frequencies. The plots span 100 days of the observatory record, $\sim$ 4 full circulation periods.

PST & NGK and the previously mentioned CEOF mode (using a series from the centre of the basin at 40°S, 43°W), with the resulting spectra shown in figure 3.19. Studying this figure, no clear signal is identified in PST coherence at the operational frequency identified previously (Fu et al. [2001], Tai and Fu [2005] & Hughes et al. [2007]), again indicating that the magnetic counterpart to Argentine basin circulation is not clearly recorded in PST data. However, some minor signals are present in both PST & NGK coherences at $\sim$ 25 days (the previously identified operational frequency), indicating the possible presence of a weak global scale overprinting field in these series (see §3.8 for proposed sources). Note that in all cases coherence estimates are below the 95% significance level indicated, casting doubt over the origins of any signals found.

Finally, maps of correlation between the same CEOF mode and both PST and NGK magnetic series (see figures 3.20 & 3.21) illustrate that while spatial correlations involving PST data closely resemble the spatial distribution of circulation phase highlighted in figure 3.3, very similar correlations are also found when using NGK data, like many results from this statistical analysis, hinting at the presence of a global overprinting signal. However, it must be noted that due to the very nature of this analysis, given that the CEOF mode in question represents SSH signals that are symmetric about the centre of the Argentine basin, points

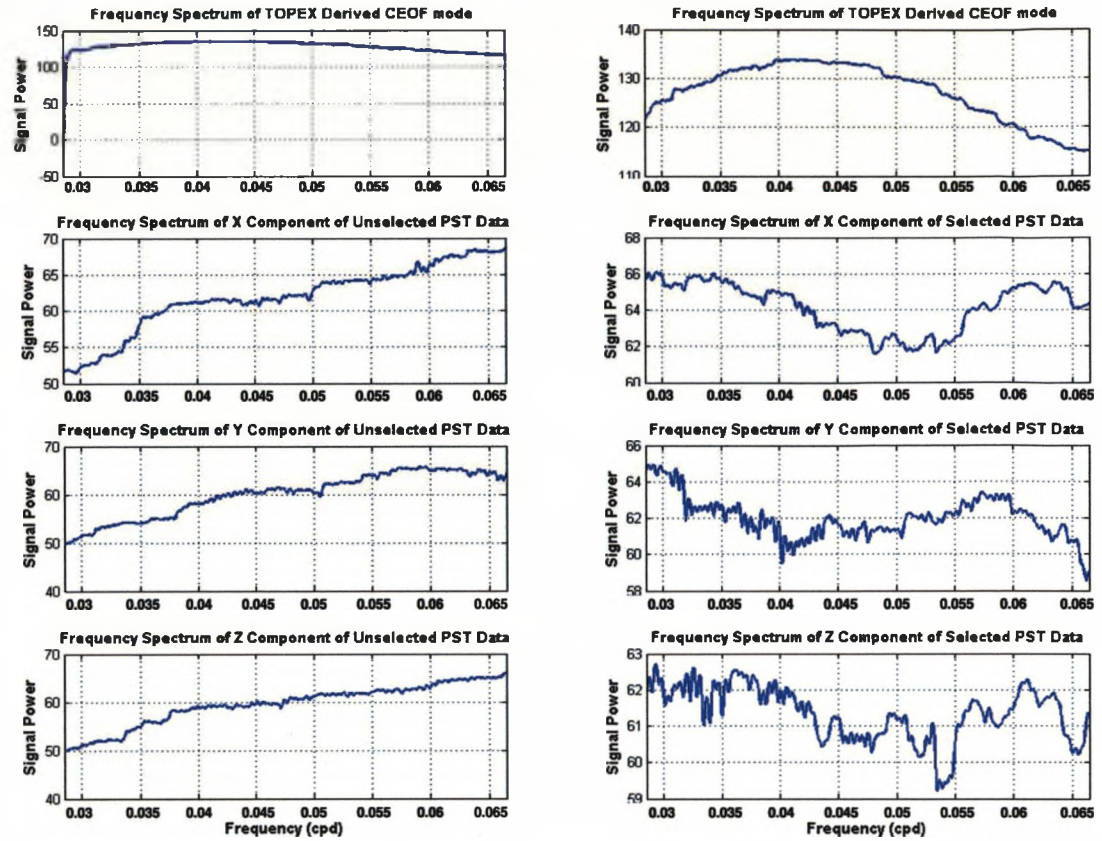

Figure 3.18: Frequency spectra of PST observatory data used in this study (within the frequency range of the target circulation). The frequency content of the CEOF mode derived by Hughes et al. [2007] is also shown for comparison. Note that the sampling rate of magnetic series have been reduced to 3 days to match that of the CEOF mode.

directly across the basin will always be out of phase. Therefore, while points on one side of the basin may be positively correlated to magnetic data, those on the other side will be anti-correlated, falsely giving the impression that magnetic data are correlated to the Hughes et al. [2007] CEOF mode. Even so, in both cases correlation co-efficients rarely exceed ± 0.1 and in many cases are not statistically significant across the basin (at the 95% level), suggesting that any proposed links between magnetic records and the Hughes et al. [2007] CEOF mode may be weak.

3.6.3 Harmonic Analysis

The observatory data used in these analyses have been shown to be non-continuous (figure 3.15). However, all of the statistical analyses conducted thus far require complete series, introducing the need for gap interpolation, a process that if used excessively could have a negative effect on the isolation of periodic signals. To remove the need for interpolation and the detrimental effect it may have on data, PST, AIA & NGK series used previously (selected and unselected) are re-analysed in their original, unfiltered (to prevent further

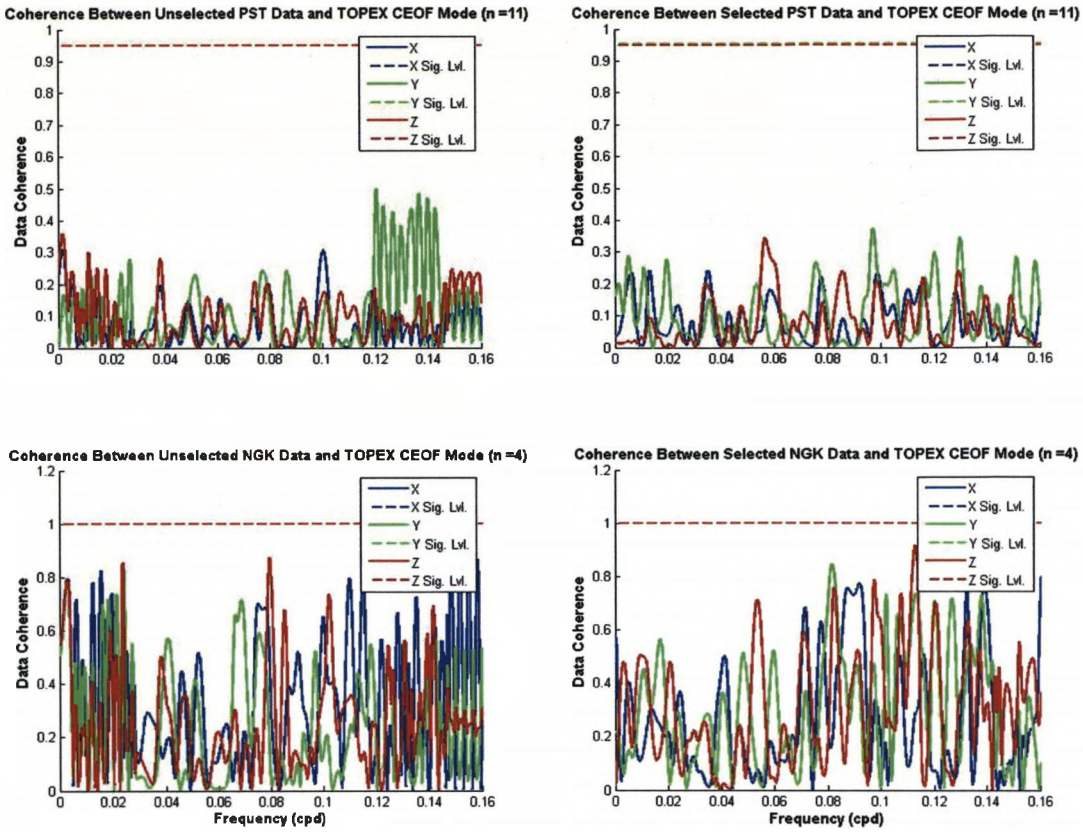

Figure 3.19: Plots of coherence between PST (upper row) & NGK (lower row) magnetic observatory series and the CEOF mode of Hughes et al. [2007] at [40S, 43W]. 95% significance levels for each magnetic component are marked in panels as dashed lines of appropriate colour, while degrees of freedom (n) used to calculate these levels are shown in the title of each panel.

interpolation) form using the harmonic modelling approach discussed in §3.5.1. Note that unlike previously, both 1 minute and hourly sampled data are analysed (synthetic testing in §3.5.1 indicates that larger data volumes tend to provide more accurate and stable solutions when using this method). As before, NGK series are analysed to gauge the extent of signal localisation at PST & AIA. Figures 3.22 & 3.23 display the results. Note that to determine the directionality of any identified signals, individual X, Y & Z series have been analysed along with those of scalar field magnitude.

Clearly, the results of this analysis are far from the ideal spectra produced when testing this method, with the effects of noise and multiple signal sources making a positive signal identification much more difficult. Encouragingly, when considering spectra of NGK series, no prominent signals are found at ~ 25 days (when compared to neighbouring frequencies), suggesting a lack of any strong 25 day signal at this location. Considering spectra derived using AIA series, whilst minute sampled data are not available at this site, peaks in spectra derived from hourly records are far more prominent above neighbouring frequencies than those from equivalent NGK series (data selection increases this prominence further), with

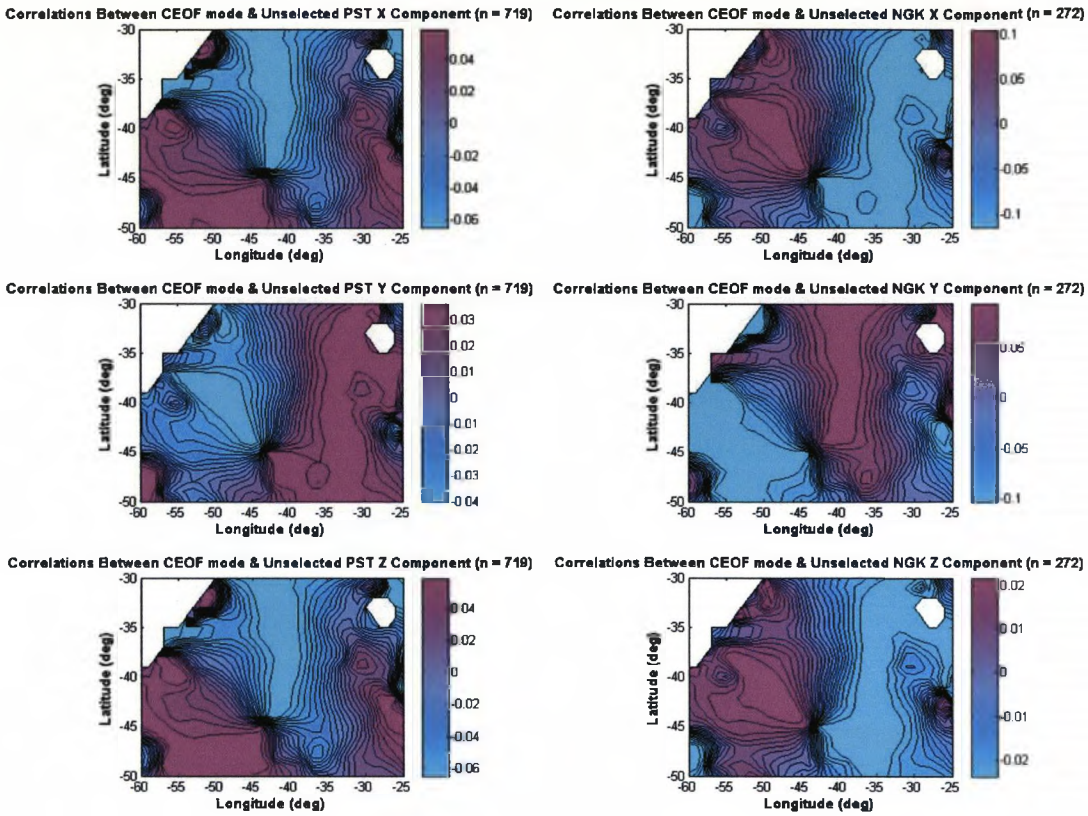

Figure 3.20: Maps of correlation between filtered, unselected magnetic observatory data from PST (left) & NGK (right) and the CEOF mode of Hughes et al. [2007], with the X component occupying the top row, Y on the central row and Z on the bottom row. Locations of statistically significant correlations (at the 95% level) are shown as white crosses, with the degrees of freedom available to determine significances (n) shown in the title of each panel.

several clearly displaying periods of $\sim$ 25 days (see figure 3.23), although there is some variation in dominant signal period between vector components. Such a variation may be the result of several contributing factors, with uncertainties within the harmonic modelling method, the presence of multiple operational modes within the basin [Weijer et al., 2007a,b] and distance of AIA from the Argentine basin, all being plausible explanations.

The most encouraging results are found in spectra of PST series, where a clear peak can be seen in the spectra of most vector components (both selected and unselected), at a frequency of $\sim$ 24.8 days. While side-lobes are present, they clearly appear to be secondary to the main peak (lower amplitude and a systematic decrease in amplitude away from the main peak). This operational frequency can be validated if the time series from the Fu et al. [2001] CEOF mode, used in earlier coherence calculations is applied to the same harmonic modelling approach (see figure 3.24). This spectrum presents a clear operational frequency of 24.8 days, suggesting that the signals found in PST spectra may have their origins within the Argentine basin.

Unlike NGK & AIA series, PST data experiences a distinct and consistent decrease in am-

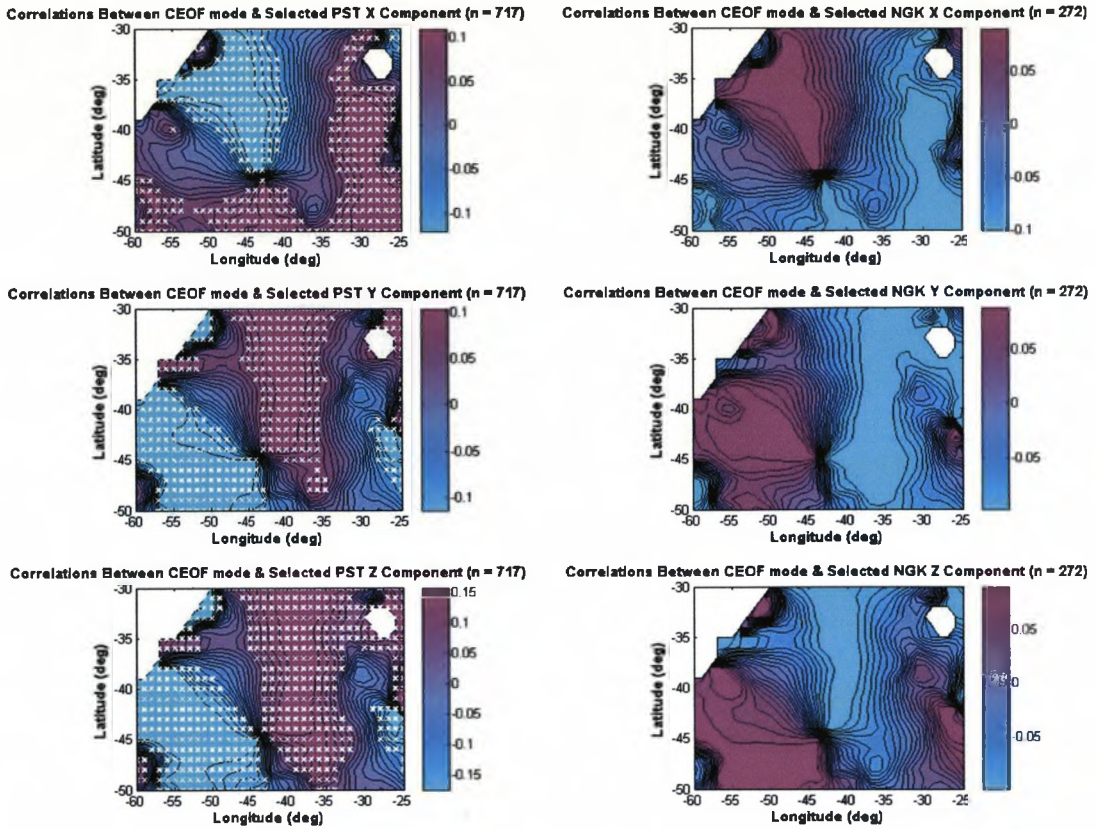

Figure 3.21: Maps of correlations between filtered, selected magnetic observatory data from PST (left) & NGK (right) and the CEOF mode of Hughes et al. [2007], with the X component occupying the upper row, Y on the central row and Z on the lower row. Locations of statistically significant correlations (at the 95% level) are shown as white crosses, with the degrees of freedom available to determine significances (n) shown in the title of each panel.

plitude of all 3 vector components between 1997 and 1998 (see figure 3.15). However, as the Y component exhibits the strongest 24.8 day signal, spectra of Y component data before and after this shift have been calculated to ensure the signal in figure 3.22 is not an artifact of the shift itself (see figure 3.25). This figure clearly illustrates that the shift in field amplitudes is not responsible for the signal peak found in figure 3.22, as although less defined (due to a decreased number of complete cycles within each data segment), both spectra indicate 24.8 day content.

Curiously the same signal is not dominant in spectra of minute sampled, selected PST records. Here a new signal dominates, with a slightly longer operational period of $\sim$ 27.5 days, the source of which is somewhat confusing. A simple hypothesis is that data selection has in some way preferentially enhanced a different mode of operation from within the basin. However, logically such an explanation is tenuous at best, especially when the same signal is completely absent in the corresponding unselected spectrum. An alternative hypothesis is that the selection process has acted to simplify the complicated contributions from the external magnetic field, preferentially highlighting one particular source (possibly the screening

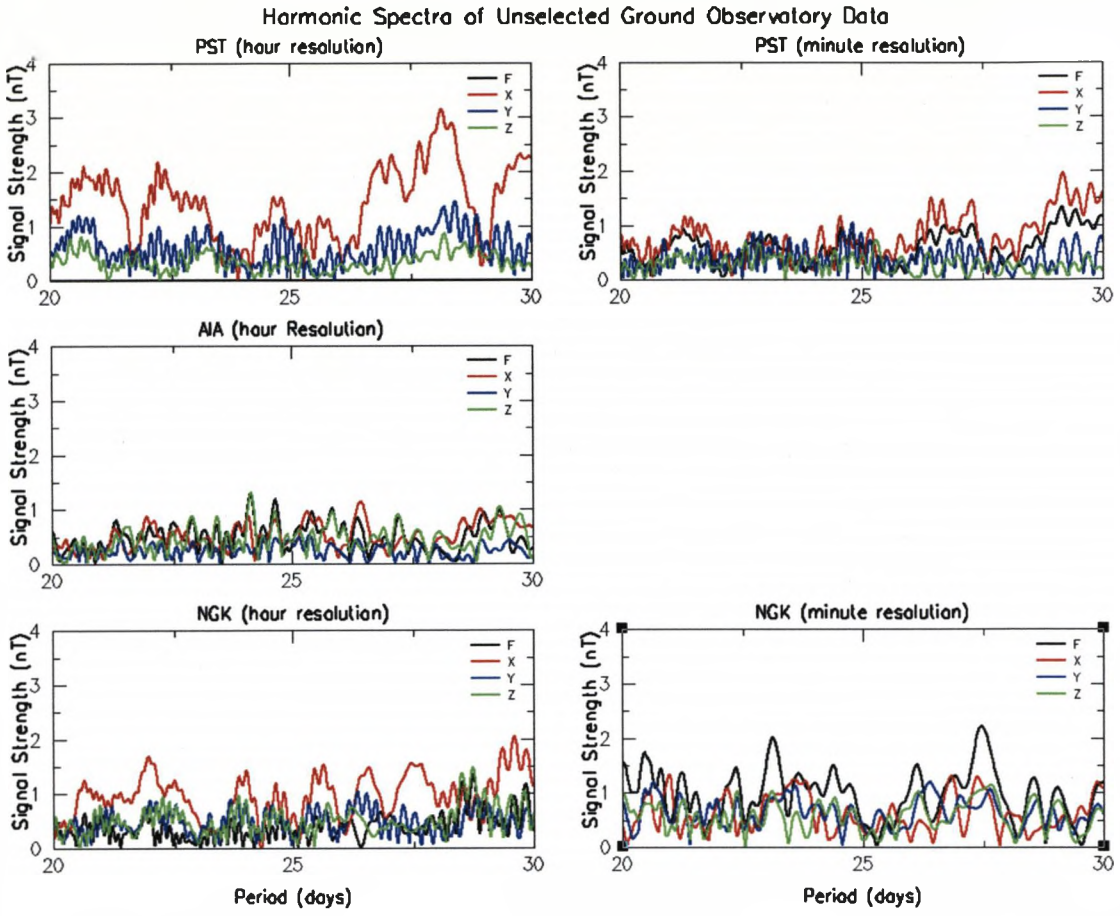

Figure 3.22: Frequency spectra of unselected observatory series, derived using harmonic modelling. Spectra of hourly sampled data are on the left and minute sampled data on the right. PST spectra are found in the upper panels, AIA spectra in the central panels and NGK spectra in the lower panels.

signal that has proved troublesome in this analysis) above others (the concept is explained graphically in figure 3.26). Such a hypothesis cannot, however, explain the anomalous increase in amplitude of this signal seen between unselected (figure 3.22) and selected (figure 3.23) spectra and therefore this signal may merely be a product of the harmonic modelling approach used, combined with highly non-continuous series (tests in §3.5.1 indicate such results), although even this hypothesis is uncertain.

3.6.4 EOF Analysis

It is inevitable, regardless of pre-processing, that contributions from numerous sources remain in the time series studied throughout this analysis. It has already been shown that any magnetic field generated in the Argentine basin is very difficult to isolate from the ambient background. To improve the separation of these signals, both single and dual station EOF analyses of PST, AIA & NGK series are conducted (the physical context of such an analysis

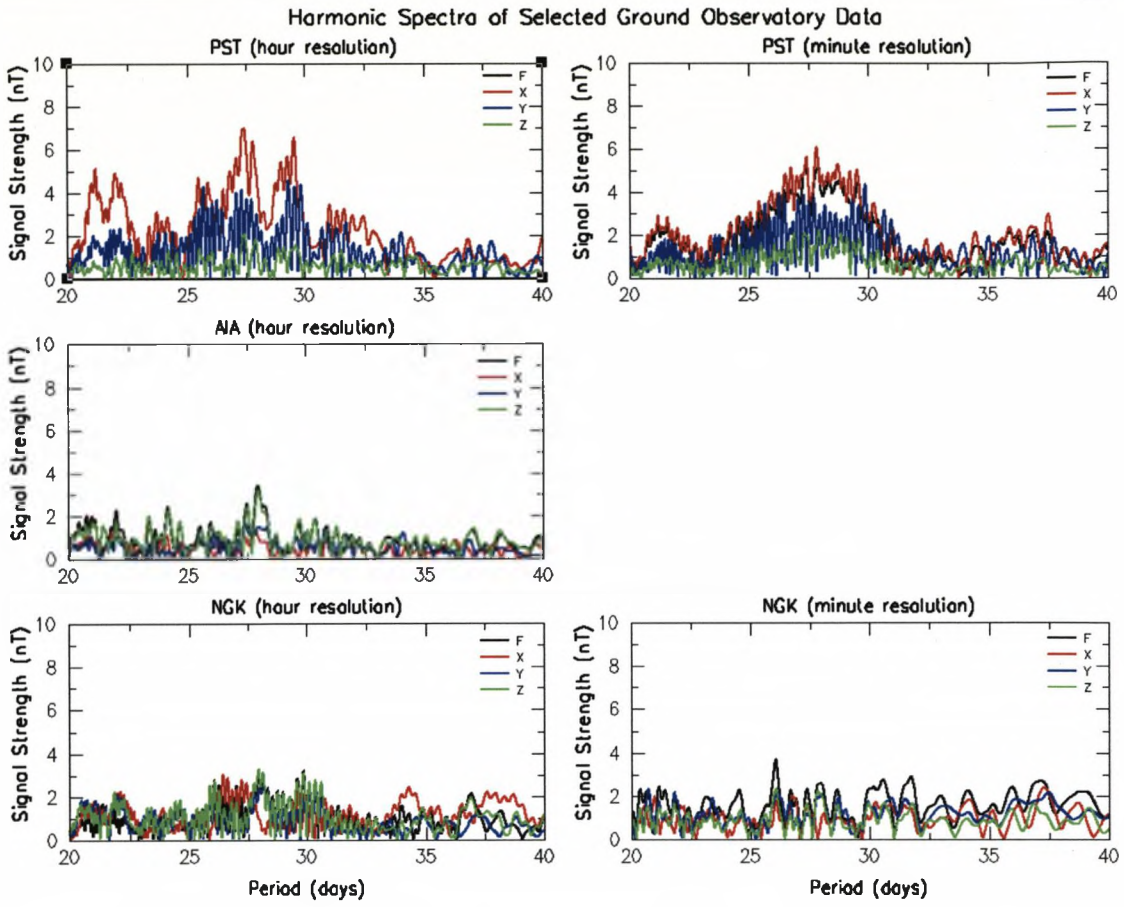

Figure 3.23: Frequency spectra of selected observatory series, derived using harmonic modelling. Spectra of hourly sampled data feature in the left hand column and minute sampled data in the right hand column. PST spectra are located in the top row, AIA in the centre and NGK in the bottom row.

is discussed in §3.5.2).

The first stage of this EOF analysis takes place in a single station configuration, using unselected and selected, hourly sampled, filtered data from PST and NGK. The data from each station are analysed individually and the resulting EOF statistics given in both tabular and graphical form in table 3.2 and figures 3.27 & 3.28 respectively. Studying each mode (both direction and expansion series) of these analyses, it is evident that identification of similar signals using mode direction alone is difficult (as data variance will be assigned differently in each case). However, frequency spectra of each expansion series may highlight any signal with a period similar to that expected from the Argentine basin (see figure 3.29). Note that as all data used in the EOF analyses are bandpass filtered, only content between 0.33 cpd (cycles per day) and 0.1 cpd is to be considered (content outside of this range, most likely 'ringing' as a result of the filtering process, should be ignored). Ideally, the analyses would have split the complex input series enough to identify any signs of signals generated within the basin. However, none of the spectra in figure 3.29 exhibit any dominant frequency,

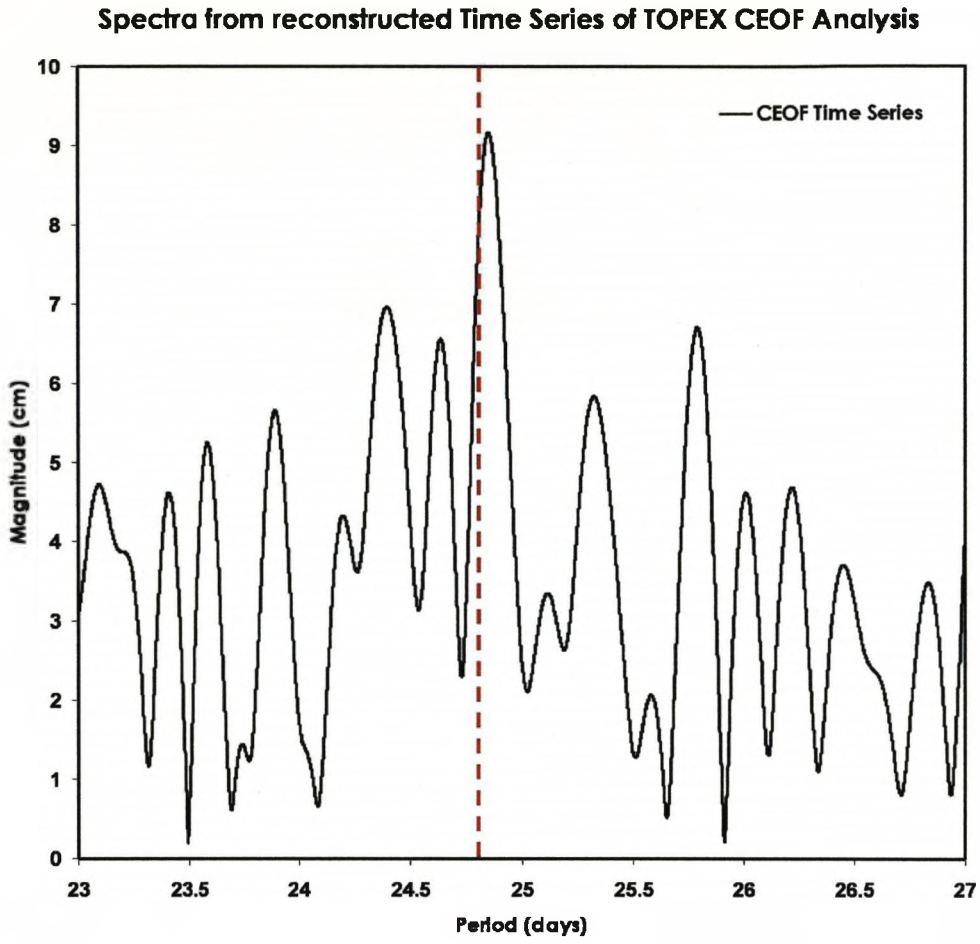

Figure 3.24: A frequency spectrum of the CEOF mode time series described by Hughes et al. [2007]. The red dashed line indicates the operational period identified in PST records (see figures 3.22, 3.23 & 3.25).

	PST filtered EOFs			NGK filtered EOFs		
	1st	**2nd**	**3rd**	**1st**	**2nd**	**3rd**
X	-0.8613 (-0.8615)	0.0218 (0.0169)	-0.5076 (-0.5075)	-0.7455 (-0.7439)	0.3254 (0.3297)	-0.5816 (-0.5813)
Y	-0.0344 (-0.0381)	0.9943 (0.9945)	-0.1011 (0.0977)	0.3061 (0.3032)	-0.6080 (-0.6087)	-0.7326 (-0.7332)
Z	-0.5069 (-0.5063)	-0.1045 (-0.1035)	0.8556 (0.8561)	0.5920 (0.5956)	0.7242 (0.7217)	-0.3537 (-0.3528)
% var	62.17 (62.19)	26.62 (26.62)	11.21 (11.9)	52.87 (52.91)	31.15 (31.05)	15.98 (16.0)

Table 3.2: Single observatory EOF mode statistics. Statistics of modes calculated using selected data are in brackets.

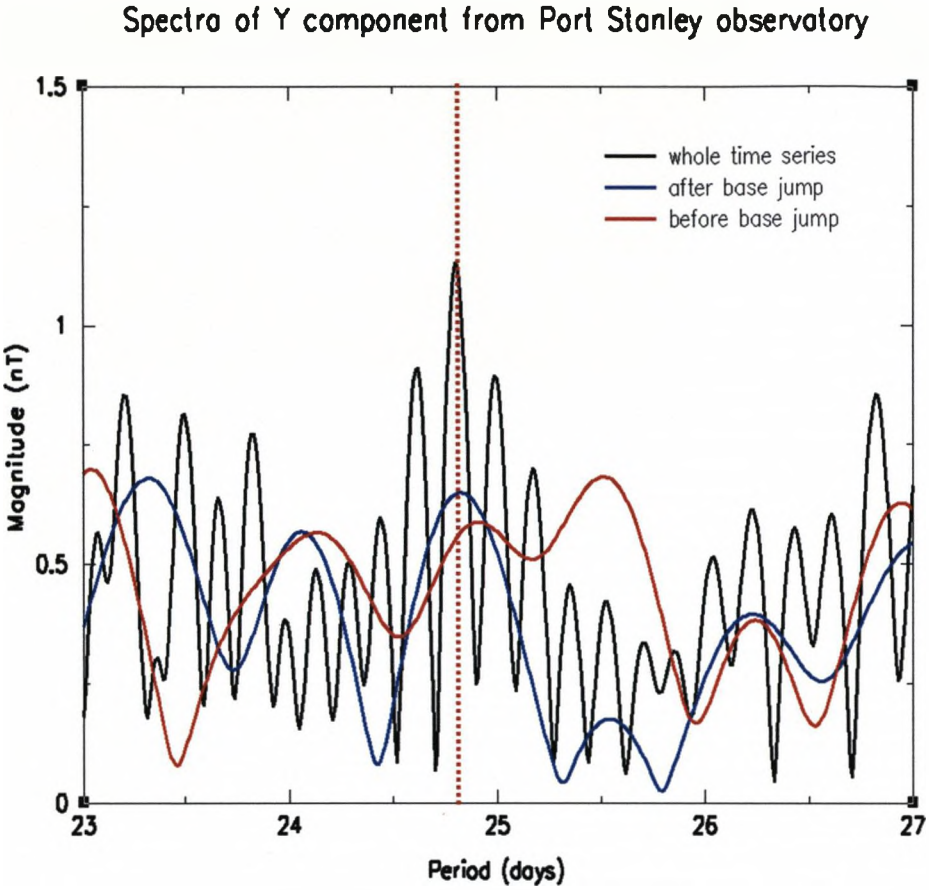

Figure 3.25: Spectra of Y component PST data, before and after the systematic decrease in field values between 1997 and 1998 (the spectra of the whole series is also plotted for reference). Note that the unselected data used to derive these spectra have 1 hour sampling.

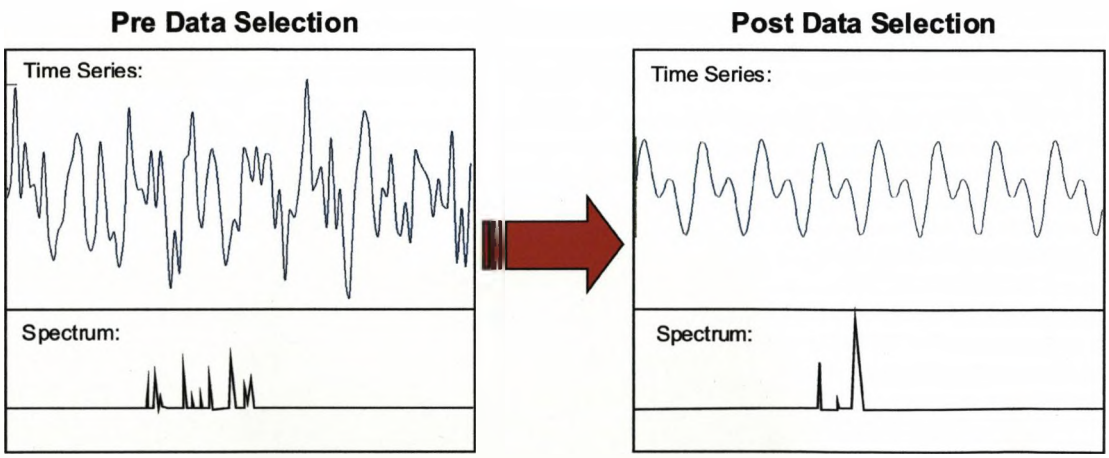

Figure 3.26: A schematic diagram illustrating the concept of complex signal simplification via data selection.

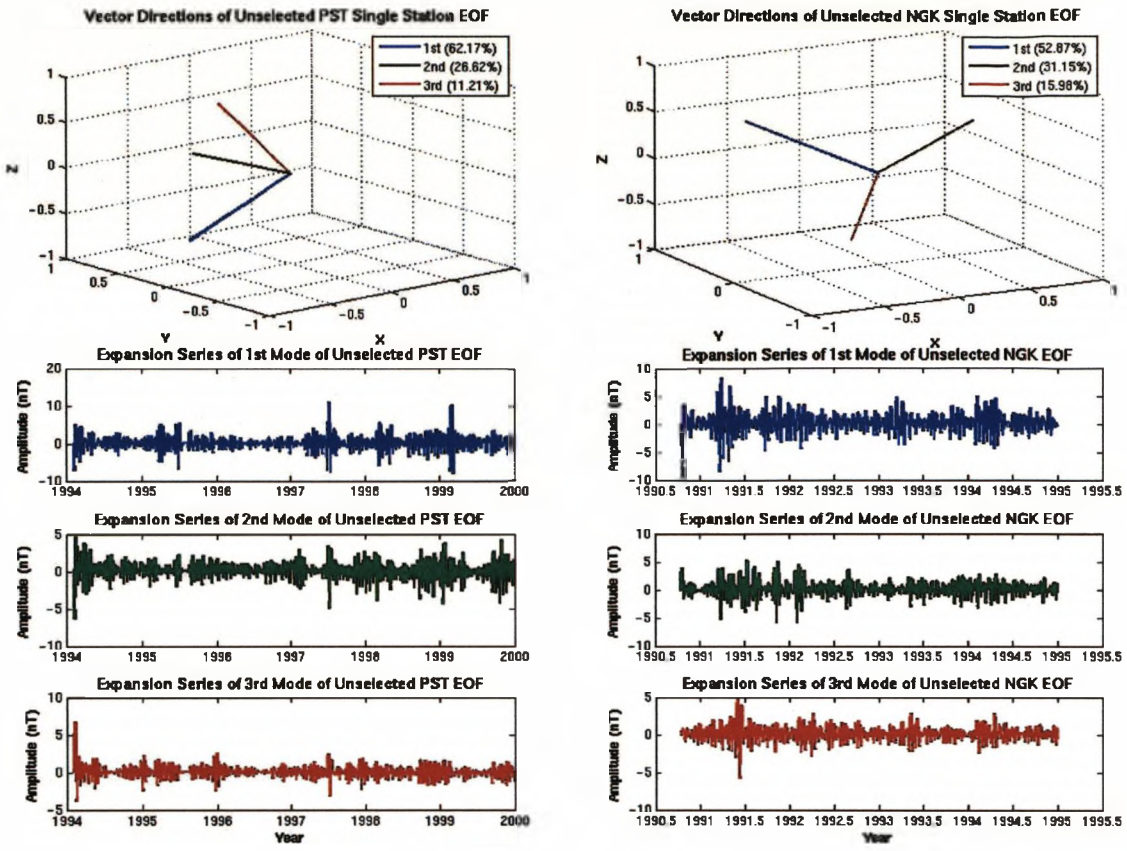

Figure 3.27: Graphical results of single station EOF analyses of unselected PST and NGK data. Mode directions are shown in the upper half of the figure (PST on the left, NGK on the right). The lower half of the figure displays the expansion time series of each mode (PST on the left, NGK to the right).

certainly not at ~ 0.04 cpd ($\sim$ 25days). The only clear feature, visible in all spectra, is a broadband peak between the two band stop frequencies used in the filtering process.

An alternative approach to the single station EOF is to use multiple stations in the same analysis, in this case using PST and AIA series, the aim being to study the directional structure of the two datasets while considering their combined variance. In this case, the analyses attempt to find a single mode from within the six calculated that exhibits both a strong Z component at PST and a weak contribution in the Z direction at AIA (the configuration one would expect to see as the result of a circulation within the Argentine basin). The results of the subsequent analyses can be found in figures 3.30 & 3.31 and table 3.3. Frequency spectra of the expansion series shown in figures 3.30 & 3.31 can be found in figure 3.32. Whilst the first 5 modes do not display the required configuration, the 6th mode of both analyses fit the required criteria, with a Z direction unit vector contribution of -0.634 at PST and only -0.0084 at AIA. However, aspects of the theory behind EOFs do raise concerns regarding the validity of this result, in addition to the rather small 1.29(1.29)% variance the mode accounts for. Theory states that if an input system contains n input series, then $(n-1)$ of the n solution modes are freely determined. However, the final mode

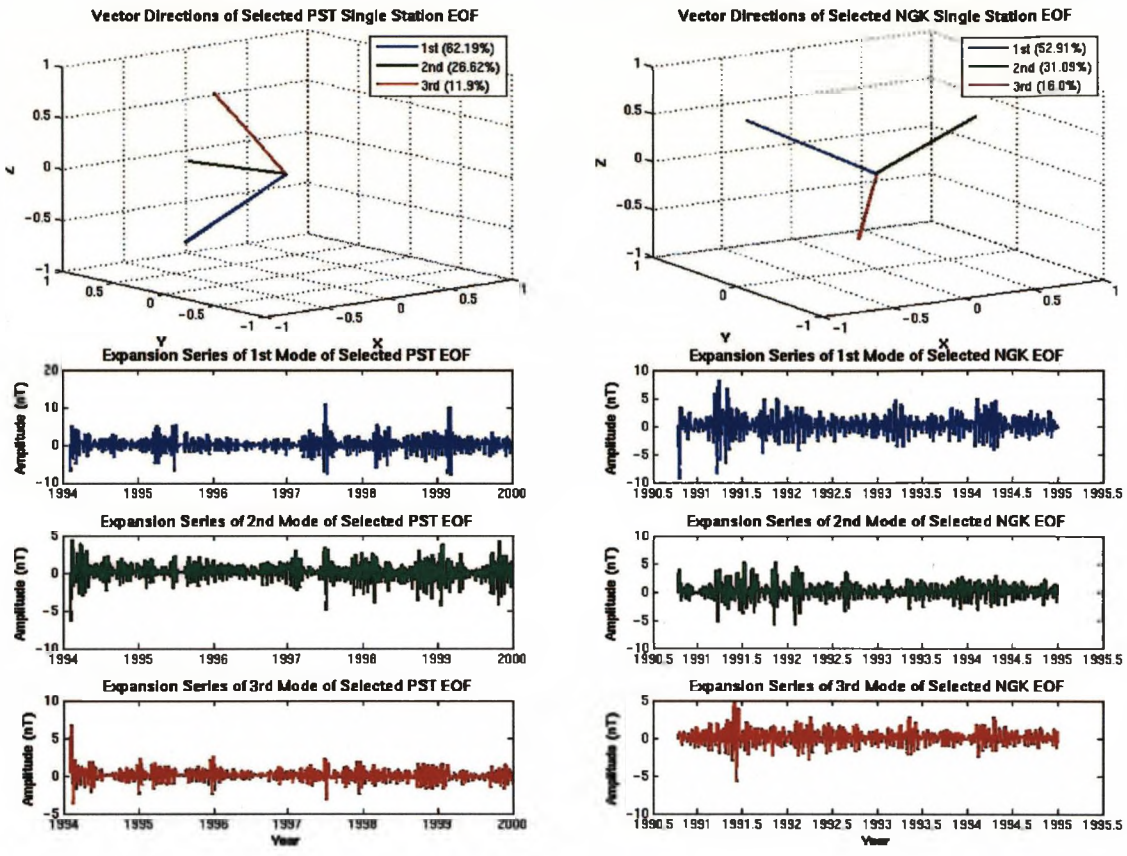

Figure 3.28: Graphical results of single station EOF analyses of selected PST and NGK data. Mode directions are shown in the upper half of the figure (PST on the left, NGK on the right). The lower half of the figure displays the expansion time series of each mode (PST on the left, NGK to the right).

is forced into the direction orthogonal to all others and is assigned all the data variance not accounted for previously. This would indicate that although the 6th mode in both dual station analyses (unselected and selected) has the directional configuration desired, it may be purely coincidental that this occurs and the small percentage of variance these modes explain may support this hypothesis. Unfortunately, the spectra from figure 3.32 do not provide any further insight. Very much like the spectra derived during single station analyses (see figure 3.29), the only dominant signal present in all spectra is a broadband signal that spans the pass band frequencies of the applied filter. This lack of any dominant spectral signal, combined with identical selected data mode statistics, again poses the question of whether the observatory data used in these analyses contains any signal generated by circulation within the Argentine basin.

Before conducting this analysis, it was thought that observatory data would provide the ideal opportunity to identify the magnetic signal associated with circulation in the Argentine basin. However, the results of the analysis have been far from conclusive. While some highlight potentially localised signals with the required 24.8 day period (see figures 3.22, 3.23 & 3.25 and table 3.3), many based on correlations between observatory data and an altimeter derived

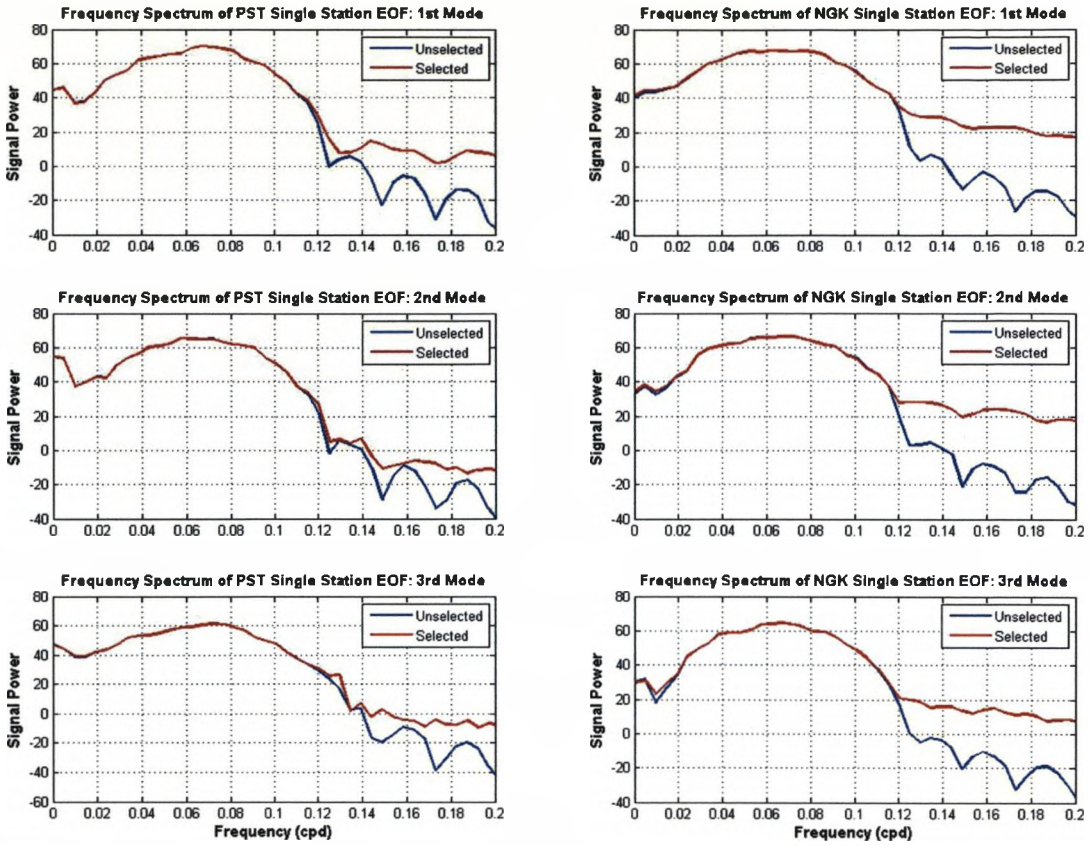

Figure 3.29: Frequency spectra of expansion time series derived during PST and NGK single station EOF analyses (PST on the left, NGK on the right). Spectra of expansion series derived using unselected data are shown in blue and those using selected data in red.

	1st	2nd	3rd	4th	5th	6th
PST X	0.4730 (0.4731)	-0.4886 (-0.4888)	0.4291 (0.4289)	-0.2592 (-0.2589)	0.0712 (0.0710)	0.5303 (0.5303)
PST Y	-0.0984 (-0.0983)	-0.5424 (-0.5424)	-0.4281 (-0.4281)	0.0779 (-0.0793)	-0.7087 (-0.7086)	0.0677 (0.0676)
PST Z	0.2809 (0.2808)	-0.1968 (-0.1975)	-0.0598 (-0.0601)	-0.6308 (-0.6306)	0.0122 (0.0118)	-0.6934 (-0.6934)
AIA X	0.1565 (0.1567)	-0.2007 (-0.20)	0.5706 (0.5708)	0.5922 (0.5923)	-0.1927 (-0.1922)	-0.4710 (-0.4710)
AIA Y	-0.2852 (-0.2850)	-0.6117 (-0.6114)	-0.2278 (-0.2277)	0.2164 (0.2169)	0.6589 (0.6592)	-0.1076 (-0.1075)
AIA Z	0.7628 (0.7628)	0.1179 (0.1186)	-0.5016 (-0.5014)	0.3624 (0.3622)	0.1458 (0.1461)	-0.0084 (-0.0084)
% var	53.0 (53.02)	23.43 (23.42)	10.63 (10.63)	7.83 (7.81)	3.81 (3.81)	1.29 (1.29)

Table 3.3: Statistical table for dual observatory EOF analyses. Statistics of modes derived using selected data are shown in brackets.

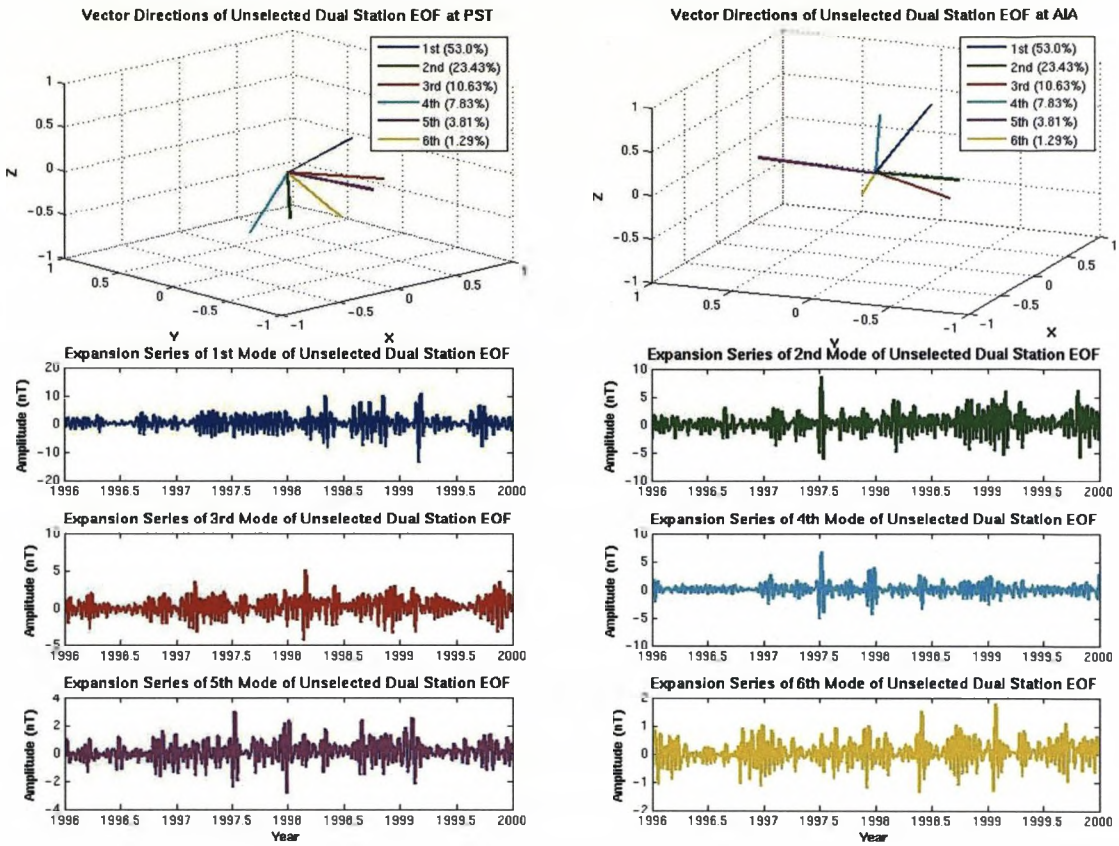

Figure 3.30: Results of an unselected dual observatory EOF analysis. The top half of the figure illustrates vector directions for all six modes at both PST (left) and AIA (right). The bottom half of the figure shows the expansion time series of the 6 modes identified.

CEOF mode [Hughes et al., 2007] (that represents basin circulation), indicate the presence of a global scale overprinting signal in both PST and NGK datasets. In an effort to separate this signal from any oceanic contributions and determine if one or both are a consequence of the methods applied here, the next section of this chapter will investigate this system from a satellite perspective.

3.7 Satellite Analysis

3.7.1 Analysis Data

§3.6 highlighted the difficulty found when attempting to separate numerous signals from within a single time series when the spatial characteristics of those signals could not be explored. This section uses the advantageous position of satellite magnetic data to study both the temporal and spatial variability of signals generated as a consequence of localised ocean circulation within the Argentine basin.

For the purposes of this investigation, CHAMP (2001 → 2005) and Ørsted (1999 → 2005)

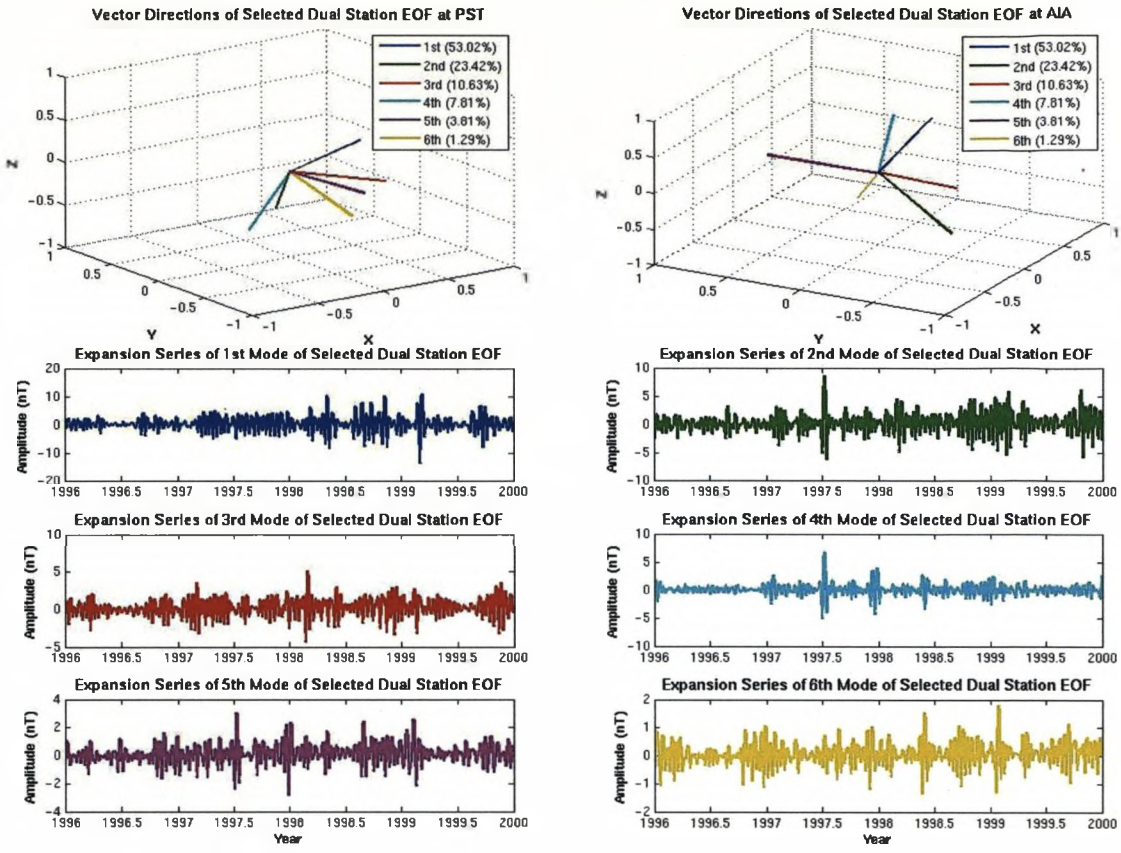

Figure 3.31: Graphical results of a dual station EOF analysis conducted using selected PST and AIA data. The upper half of the figure illustrates the direction of each of the 6 modes determined at both PST (left) and AIA (right). The lower portion of the figure shows the corresponding expansion series.

scalar and vector data and SAC-C (2001 $\rightarrow$ 2004) scalar data, pre treated in accordance with the data preparation methods outlined in chapter 2 have been included in the analysis. Data are also selected using the following criteria; local time: 1800 $\rightarrow$ 0600 hrs, Kp $\leq$ 4- ($\leq \pm 60^{o}$ magnetic latitude), Dst/dt $\leq \pm 3.0$nT/hr (at all latitudes) & Merging electric field $\leq$ 0.8 V/m ($\geq \pm 60^{o}$ magnetic latitude). Note that at magnetic latitudes greater then $\pm 60^{o}$ data are also selected according to season, with data recorded during the summer months in each hemisphere (period of near constant sunlight in polar regions) being discarded. Post data selection, all datasets are subject to repeat track selection (see §2.2.3). To determine the effect of each processing stage on analysis results, a dataset is generated for each combination of the outlined processing stages (see table 3.4). Note that SAC-C vector datasets are unavailable for analysis (in any form) due to the absence of vector observations from the SAC-C spacecraft. In addition, due to the combination of limited repeat orbit availability and data selection, no selected, repeat orbit datasets are available from Ørsted. Similarly, selected, vector repeat orbit data are not available from CHAMP.

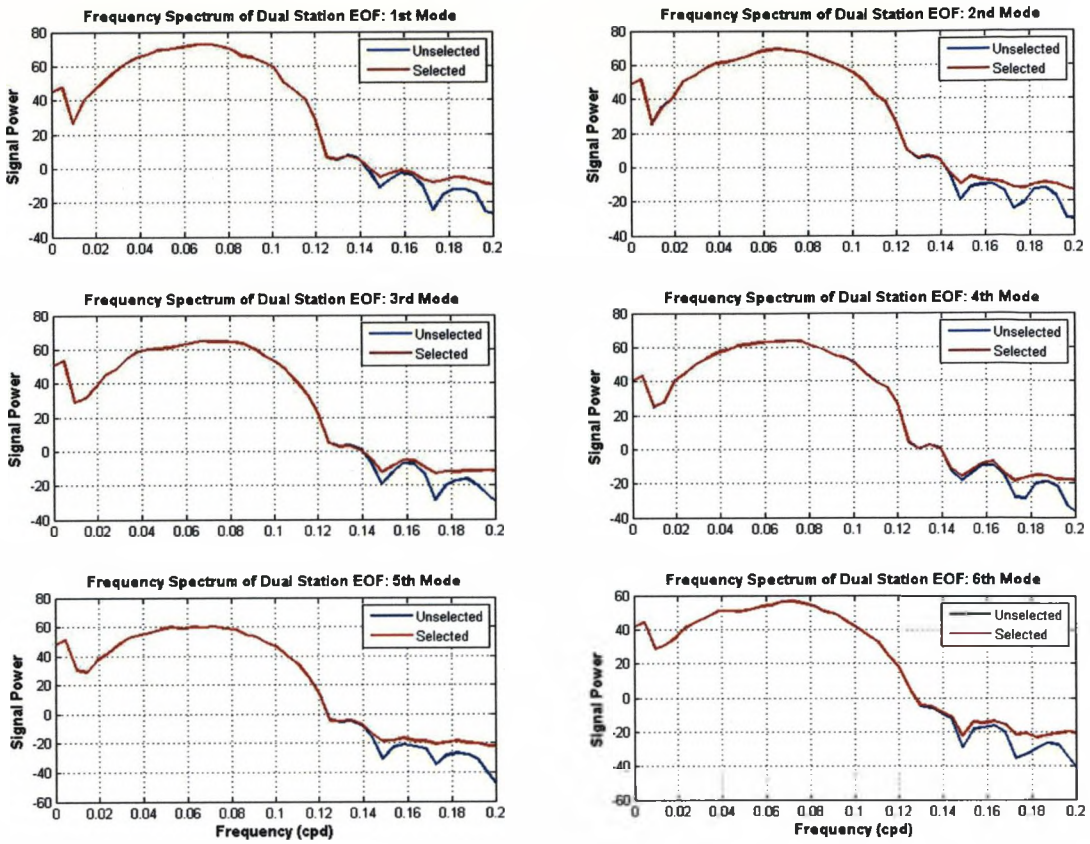

Figure 3.32: Frequency spectra of expansion series displayed in figures 3.30 & 3.31. Spectra derived using unselected data are shown in blue and those derived using selected data in red.

Data Type			CHAMP	SAC-C	Ørsted
Unselected	Scalar	Standard	✓	✓	✓
		Repeat	✓	✓	✓
	Vector	Standard	✓	X	✓
		Repeat	✓	X	✓
Selected	Scalar	Standard	✓	✓	✓
		Repeat	✓	✓	X
	Vector	Standard	✓	X	✓
		Repeat	X	X	X

Table 3.4: Summary table of the satellite datasets used to study Argentine basin flow. Ørsted, CHAMP and SAC-C data are used, both in selected and unselected forms. Datasets can also take the form of standard residuals or repeat orbit data.

3.7.2 Harmonic Analysis

The first stage of this analysis involves the determination of a target field morphology. Using the morphologies outlined in §3.4 as a base, the signals discussed there can be adapted for use with this approach. Due to the time-averaged nature of this method, the rotating field morphology discussed in §3.4 should produce a ring of positive signal power when equation 3.1 is solved for periods of ~ 25 days.

The body of this satellite analysis involves applying harmonic modelling (§3.5.1) to the datasets in table 3.4. Prior to modelling, each dataset is split into small regional blocks with dimensions of 10^o longitude $\times 5^o$ latitude. This allows the spatial variability of the data to be explored, preventing the destruction of spatially varying signals by simultaneous inversion of all data. The splitting is conducted across the basin within the following boundaries; $-65^o \rightarrow -15^o$ longitude and $-20^o \rightarrow -60^o$ latitude. This configuration can be seen more clearly in figure 3.33.

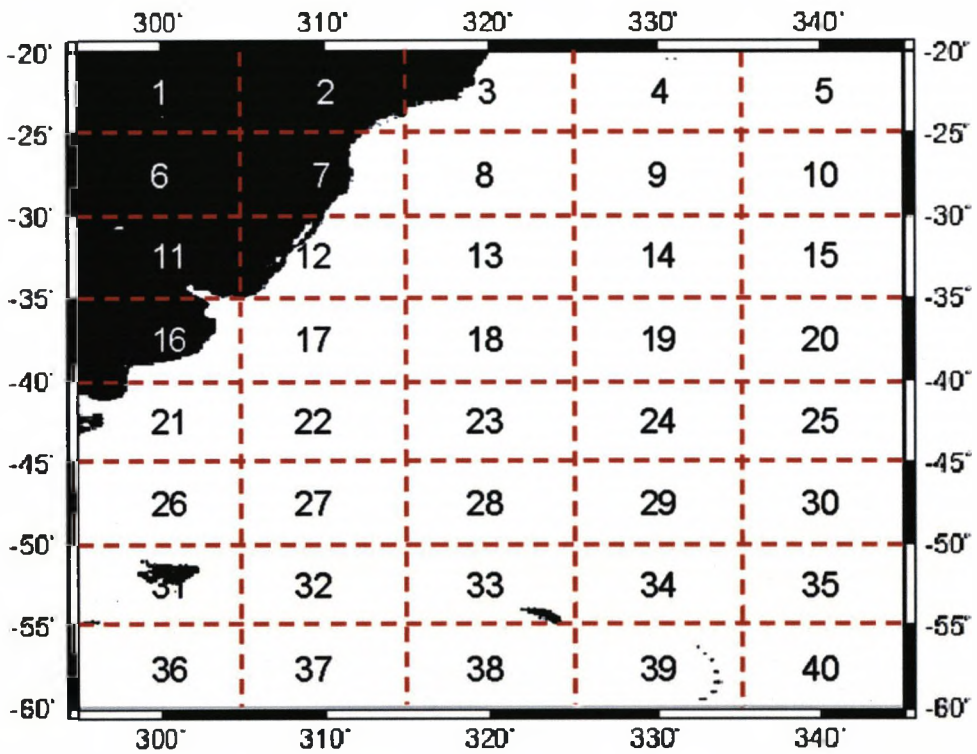

Figure 3.33: A schematic diagram of the initial data splitting configuration used for satellite harmonic analysis.

Once each dataset is split, each block of data is analysed with the harmonic modelling methodology described in §3.5.1. Spatial maps of the resulting spectra are formed by selecting the maximum amplitude of each spectrum between the periods of 24.4 & 25.2 days and translating that value to its corresponding location within the basin. This period range is chosen to match the operational periods identified in figures 3.22, 3.23, 3.24 & 3.25. The

window width is chosen to allow variation in operational frequency across the basin, whilst reducing the probability of contamination from non-oceanic sources. The final maps are shown in figures 3.34, 3.35, 3.36, 3.37 & 3.38. Upon inspection, many of these maps are dominated by unexplained high latitude variability (most likely due to unmodelled external fields), with very little spatial variability at lower latitudes near the Argentine basin. However, some maps do exhibit low latitude spatial patterns, although in the case of most Ørsted derived maps, these signals appear to be data related, consistent N-S trending stripes of anomalously high or low amplitude (see figures 3.36 & 3.37). Of those images that exhibit neither extreme high latitude variability or suspected data related signals, the majority are derived from CHAMP data (figures 3.34 & 3.35), not surprising given the lower altitude of this satellite. While these few examples exhibit the most likely oceanic signals of all the maps generated, as is the case with all these images, very little can be understood from them due to their extremely poor spatial resolution.

To solve this problem, higher resolution maps of the same datasets are generated and shown in figures 3.39, 3.40, 3.41, 3.42 & 3.43. These higher resolution images replace the previously used 10^{o} longitude $\times$ 5^{o} latitude grid with a finer 2^{o} longitude $\times$ 2^{o} latitude mesh. However, to retain sufficient data volume in each cell to acquire a stable solution (the reason for the original grid), a $5^{o} \times 5^{o}$ selection window (centred on each grid node) is implemented, with the overlap between neighbouring cells providing additional confidence in the solution of each cell. Unfortunately, due to the reduced dimensions of the selection window used to generate these maps, some datasets (repeat orbit datasets in particular) do not have sufficient data density to produce a stable solution in some cells and so are omitted. Notably, the variability displayed in these maps differs markedly from image to image. However, as in the low resolution case, several maps (derived using unselected CHAMP scalar residuals and numerous Ørsted datasets) display spatial distributions very similar to those in figures 3.36 & 3.37, taking the form of anomalously high or low amplitude N-S trending lineations, thought to be a result of the harmonic modelling methodology used. As all data are assumed equally noisy, only a few anomalous values are required to skew a solution to the extent seen in these images. Application of an upper magnitude limit when splitting data is not employed, as while this may reduce the influence of the lineations, true magnetic signals may also suffer from artificially reduced magnitudes. In addition to the N-S trending lineations already noted, unusual spatial patterns are also identified in maps derived from CHAMP repeat orbit data (see figure 3.40). This apparent checkerboard configuration is not observed in any other images and its source is uncertain (although again it may be data related), although this signal would certainly not appear to have its origin in the Argentine basin and so is of little concern.

However, several images (see figure 3.44) do show signals that conform to the field morphology outlined at the start of this sub-section. However, whether these signals are diagnostic of circulation in the Argentine basin is debatable as they are very weak ($\leq$ 1 nT) and their proximity to the noisy higher latitudes means it is difficult to determine their lower

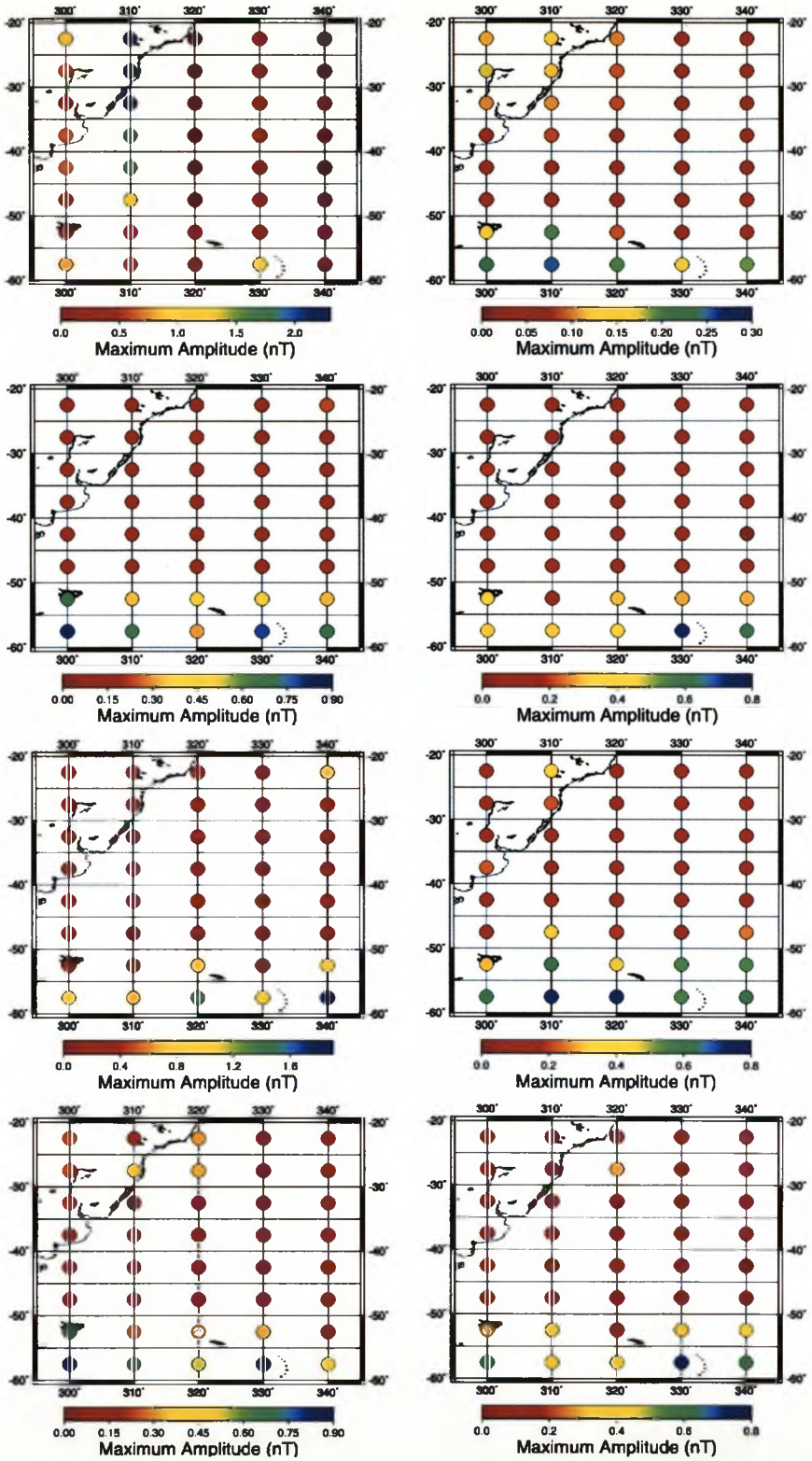

Figure 3.34: Maps of signal amplitude generated using standard CHAMP residuals. Maps on the left are generated using unselected data and those on the right using selected data. Maps on the upper row were derived using scalar data and those on the 2nd, 3rd and 4th rows use X, Y and Z vector components respectively.

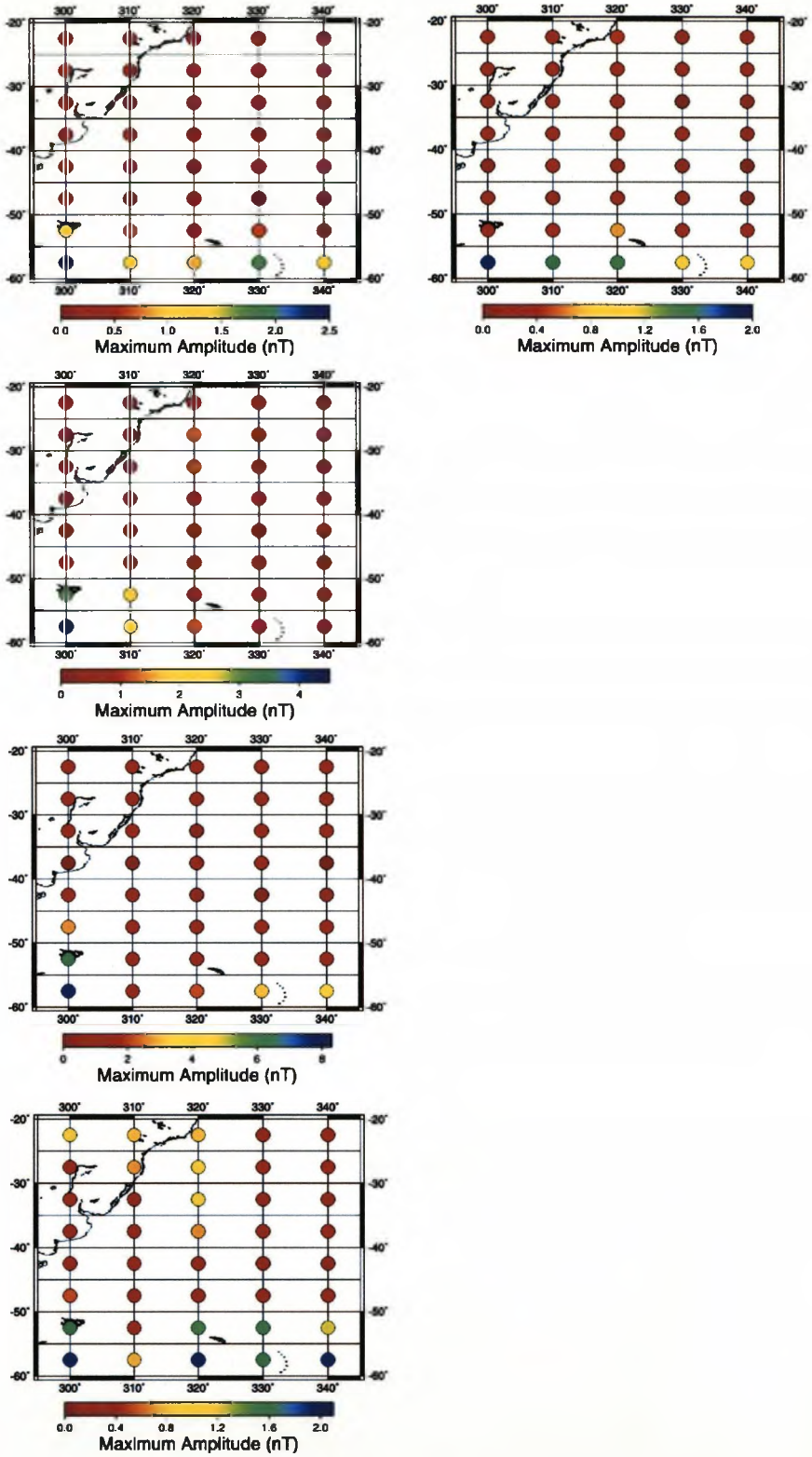

Figure 3.35: Maps of signal amplitude generated using CHAMP repeat observations. Maps on the left are generated using unselected data and those on the right using selected data. Maps on the upper row were derived using scalar data and those on the 2nd, 3rd and 4th rows use X, Y and Z vector components respectively. Note that 3 panels on the right hand side of the figure are empty due to a lack of repeat vector data from CHAMP.

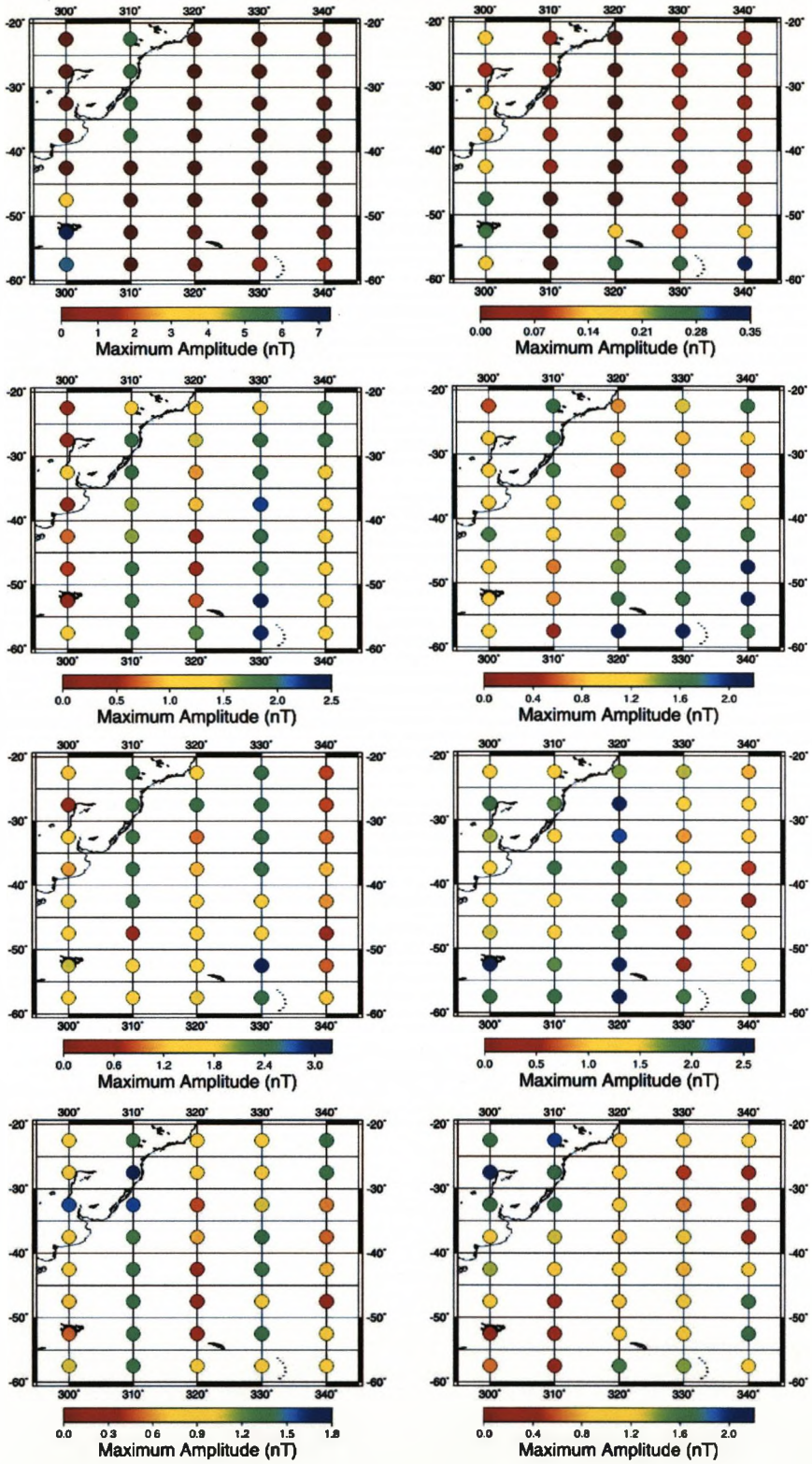

Figure 3.36: Maps of signal amplitude generated using standard Ørsted residuals. Maps on the left are generated using unselected data and those on the right using selected data. Maps on the upper row were derived using scalar data and those on the 2nd, 3rd and 4th rows use X, Y and Z vector components respectively.

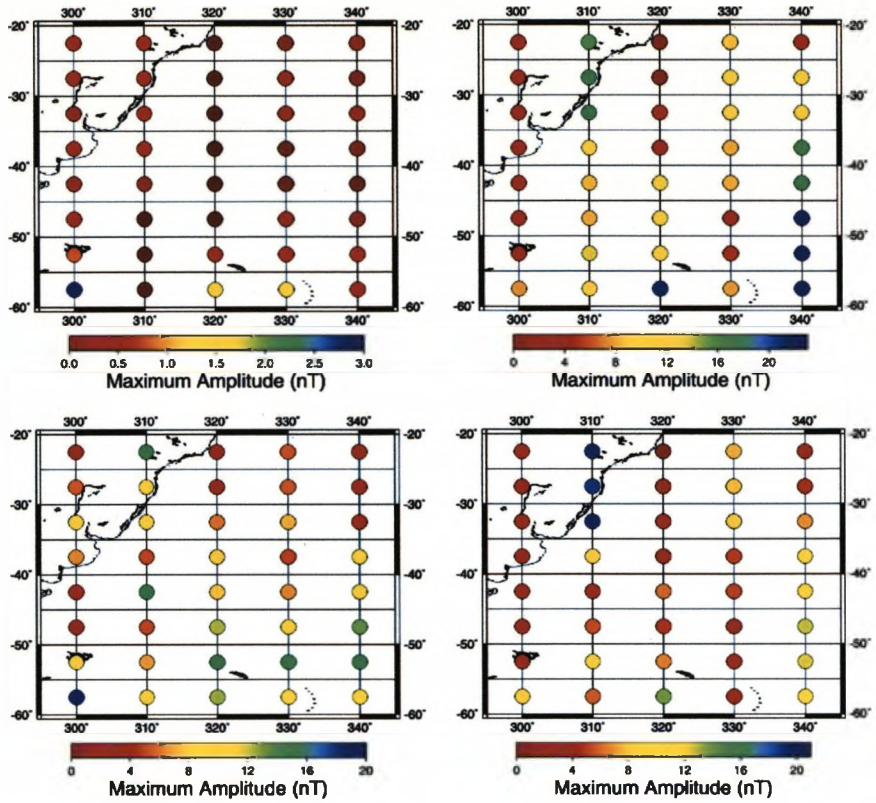

Figure 3.37: Maps of signal amplitude generated using unselected Ørsted repeat observations. The upper left map is derived from scalar data and the upper right map using X component data. The lower left image is derived using Y component data and the lower right map using Z component data.

termination point. While they may follow the bathymetric contour plotted in figure 3.44, they may easily continue to the South, being masked by the much higher amplitudes of unmodelled external contributions, and so determining the origin of the signals shown in figure 3.44 is difficult.

3.7.3 EOF/CEOF Analysis

Due to the limited success of the satellite harmonic analysis in §3.7.2, EOF and CEOF analyses of CHAMP and SAC-C unselected scalar residuals are conducted (Ørsted data are omitted due to poor performance in the previous harmonic analysis) in an effort to separate the various signals in operation within this region. Prior to analysis, basic CHAMP & SAC-C datasets are manipulated into 3D spatio-temporal data grids in accordance with the method outlined in §3.5.3. In this case grids have node dimensions of $1^o \times 1^o \times 2$ days and search window dimensions of $8^o \times 8^o \times 8$ days. Note that the temporal lengths of the two grids are different, as both datasets experience prolonged periods of data loss. Therefore while both grids have a start date of 800 julian days after the year 2000, the CHAMP grid terminates on julian day 2150 and the SAC-C grid on julian day 1040. However, both grids should have

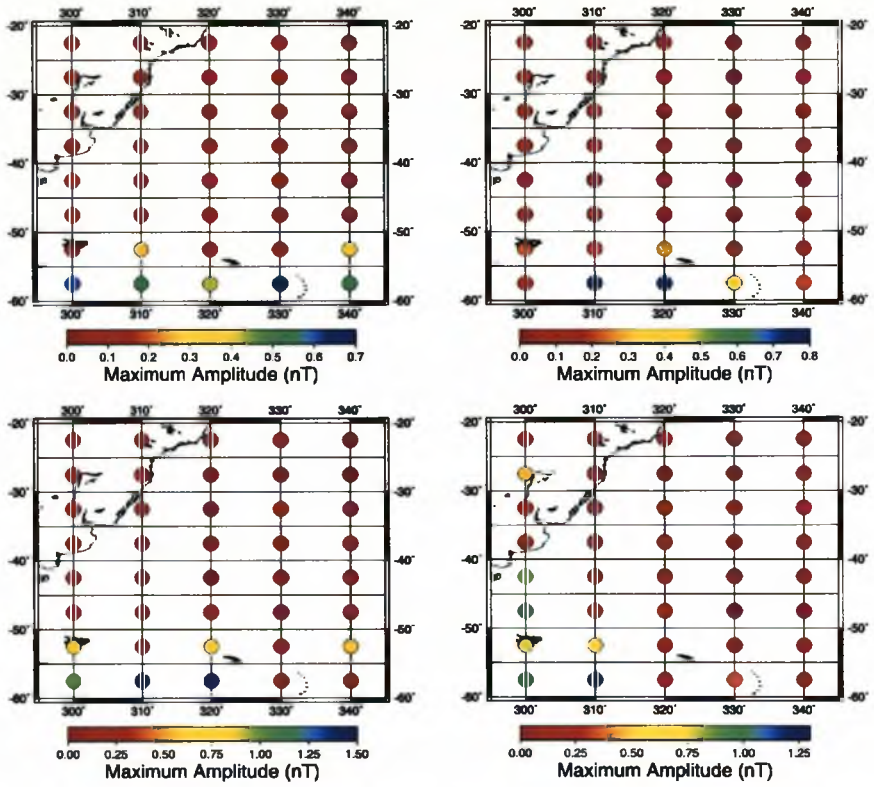

Figure 3.38: Maps of signal amplitude generated using unselected (left) and selected (right) SAC-C data. Maps derived using standard scalar residuals occupy the upper row and those in the lower row using repeat observations.

sufficient temporal length to resolve signals with temporal characteristics similar to those thought to be generated in the Argentine basin.

EOF Results: As already stated, EOF analyses of satellite data introduce the potential to investigate both the spatial and temporal behaviour of a system and in this case, mode configurations anticipated from these analyses are as outlined in §3.4. However, as standard EOF methods cannot isolate propagating behaviour within a single mode, the second configuration identified in §3.4 should be spread across several modes, with the position of the rotating target field morphology moving around the basin with each successive mode. Only when all the relevant EOF modes are reconstructed in unison will propagating variability evolve. In addition, the static field generated by bulk water column rotation may also be identified (within a single or several modes). However, a lack of propagation will make the signal difficult to differentiate from the background.

It is clear from figure 3.45 (a plot of variance distribution for both EOF analyses) that as a technical exercise the analyses have been successful, with no single mode accounting for an excessive amount of variance and with assigned variance decreasing smoothly with each additional mode. However, when the resulting modes are analysed, very little evidence of the field morphologies described in §3.4 is found, with only two

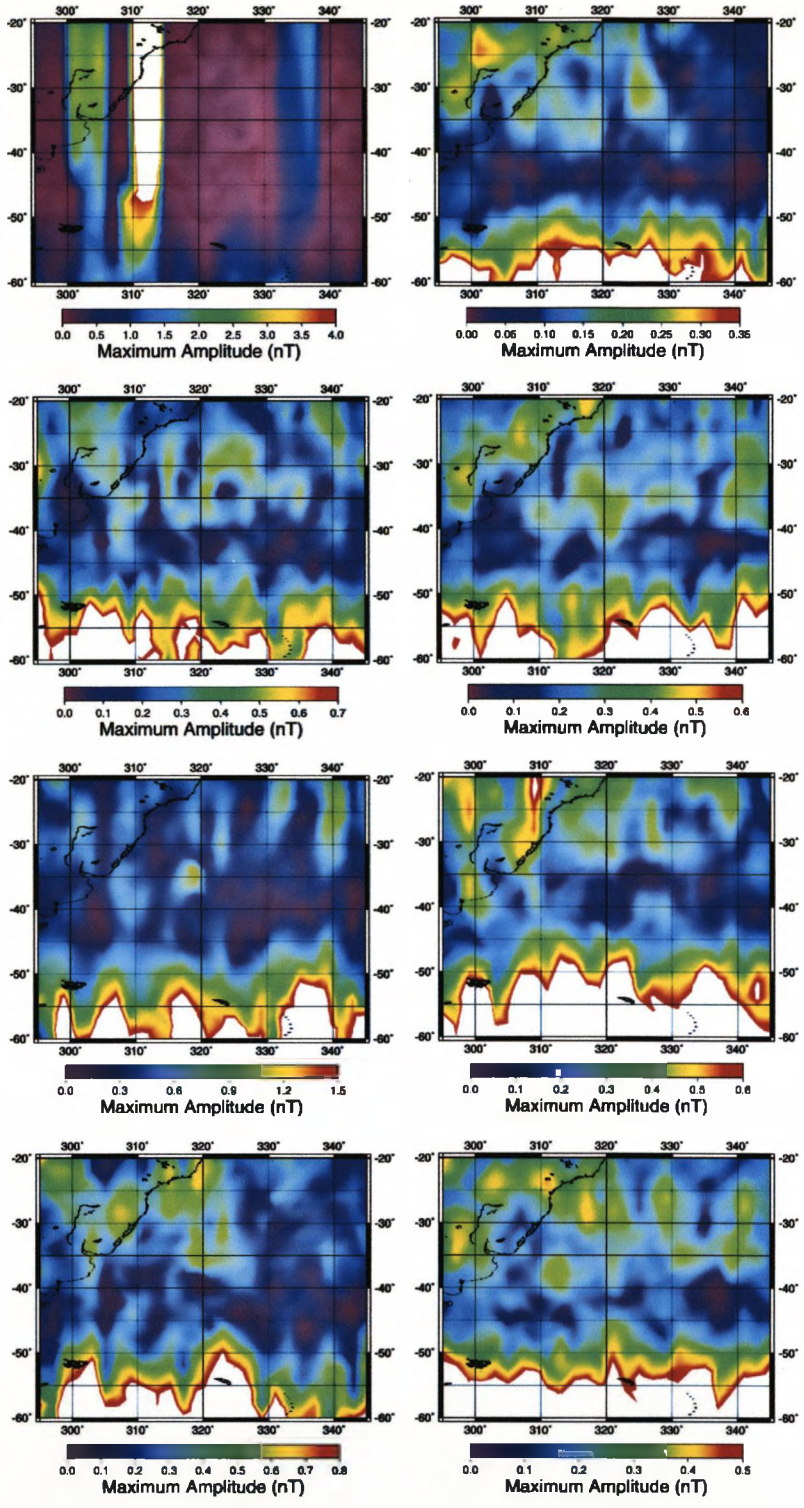

Figure 3.39: High resolution signal amplitude maps, generated using standard CHAMP residuals. Maps in the left hand column were formed from unselected data and those in the right hand column using selected data. The images in the upper row of the figure were generated using scalar residuals, and the 2nd, 3rd and 4th rows using X, Y and Z vector component data respectively.

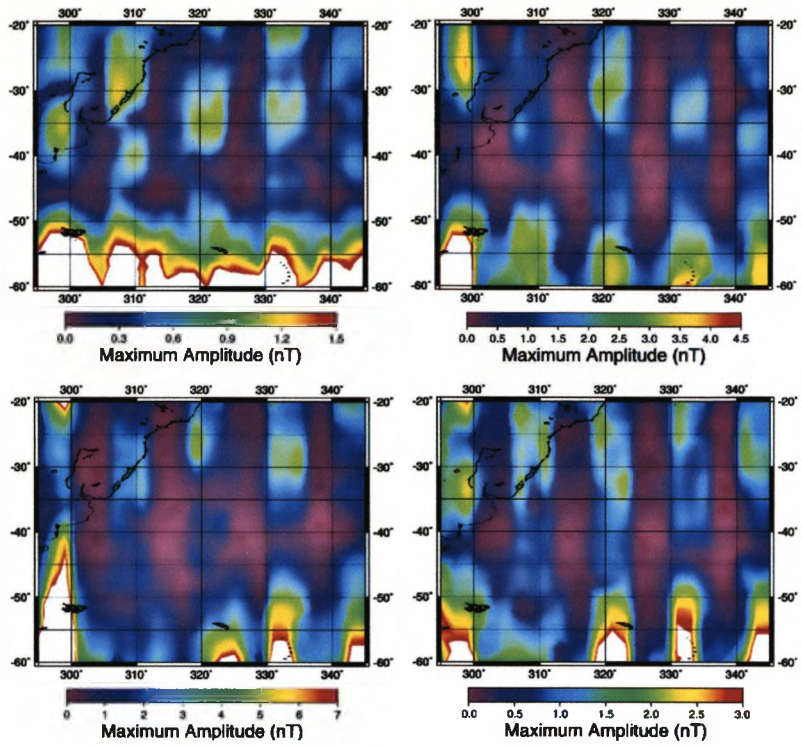

Figure 3.40: High resolution signal amplitude maps, generated using unselected CHAMP repeat data. The upper right panel has been formed using scalar data, the upper right formed using X component vector data. The lower left and right hand panels were generated using Y component and Z component data respectively.

of the top 25 CHAMP modes and one of the top 25 SAC-C modes exhibiting even faint signs of the expected spatial variability (the details of these modes can be seen in figures 3.46, 3.47 & 3.48 respectively.) While all three modes display frequency content at ~ 0.04 cpd (~ 25 days) in their expansion series, in all three cases content at other frequencies is more prominent. Also, in all three modes only a single small magnetic anomaly (increased or decreased field amplitude relative to the background) is identified, although none are overly distinctive when considered against the remaining background variability in each mode, raising doubts over the source of these signals. These concerns are re-enforced if we consider that the position of the sole amplitude patch is consistent in each mode, which in conjunction with a lack of counterpart modes, suggests these modes merely highlight activity from another source, inconveniently located over the Argentine basin. What these EOF analyses do highlight is that even in a satellite setting, identification of oceanic signals such as the ones studied here is extremely difficult, largely due to the inability of standard EOFs to cleanly identify low amplitude propagating signals within a noisy dataset.

CEOF Results: To address the limitations of standard EOFs, CEOF (complex empirical orthogonal functions) analyses have been conducted,using the 3D spatio-temporal CHAMP & SAC-C data grids used previously in EOF analyses. The advantage of

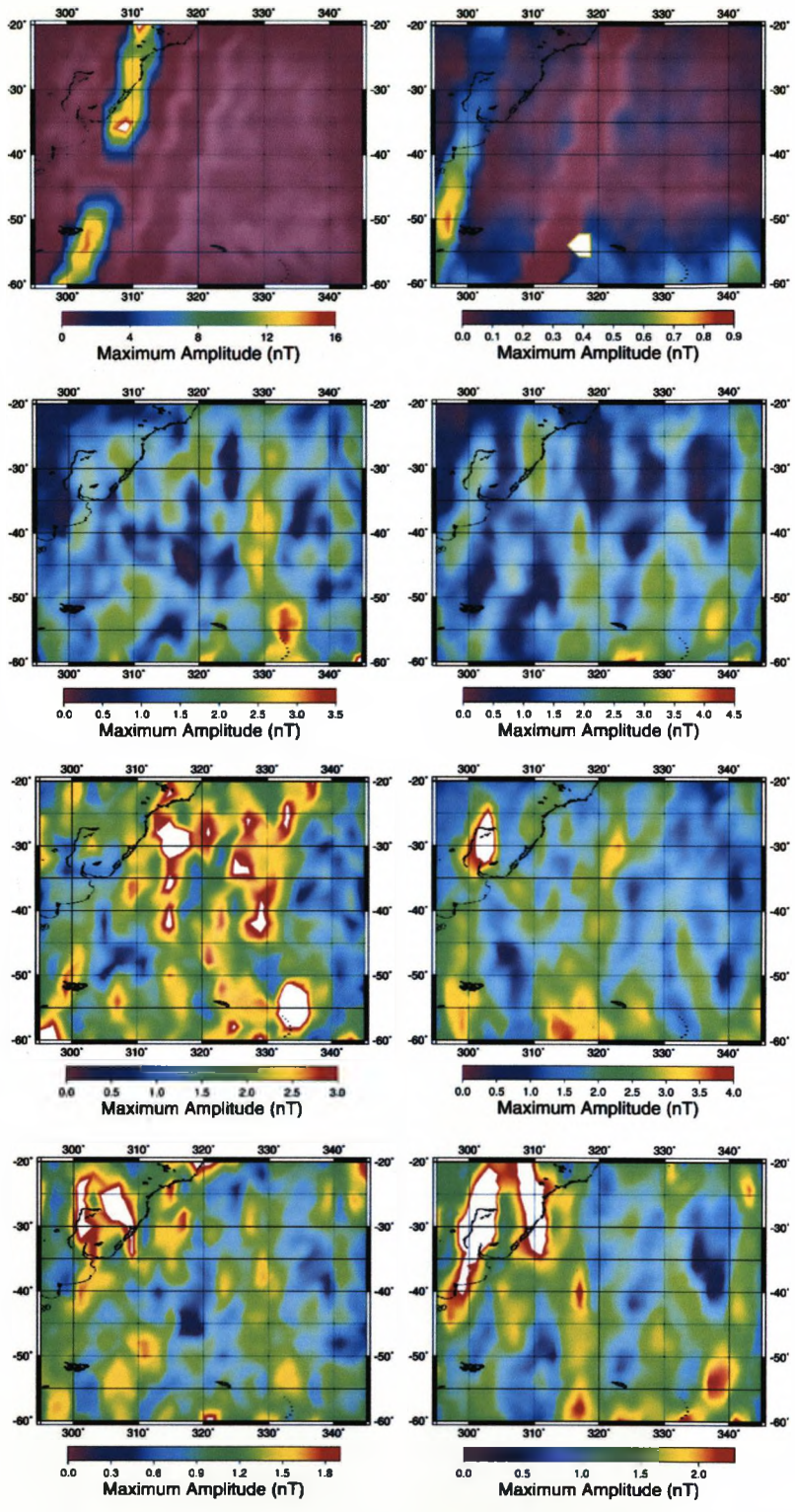

Figure 3.41: High resolution signal amplitude maps, generated using standard Ørsted residuals. The maps in the left hand column were formed using unselected data and those in the right hand column using selected data. The images in the upper row of the figure were generated using scalar residuals, and the 2nd, 3rd and 4th rows using X, Y and Z vector components respectively.

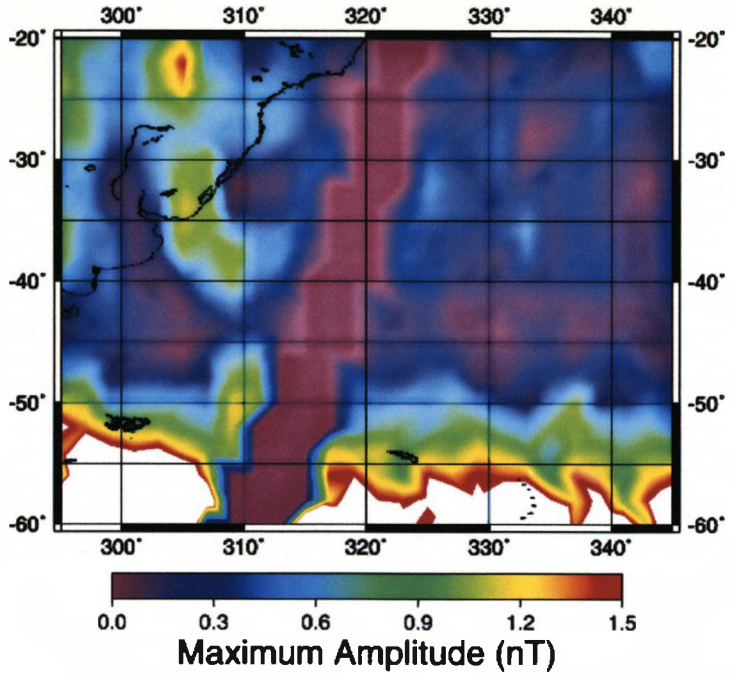

Figure 3.42: A high resolution signal amplitude map, generated using Ørsted unselected, scalar repeat orbit data. Vector data are not represented due to a lack of acceptable observations.

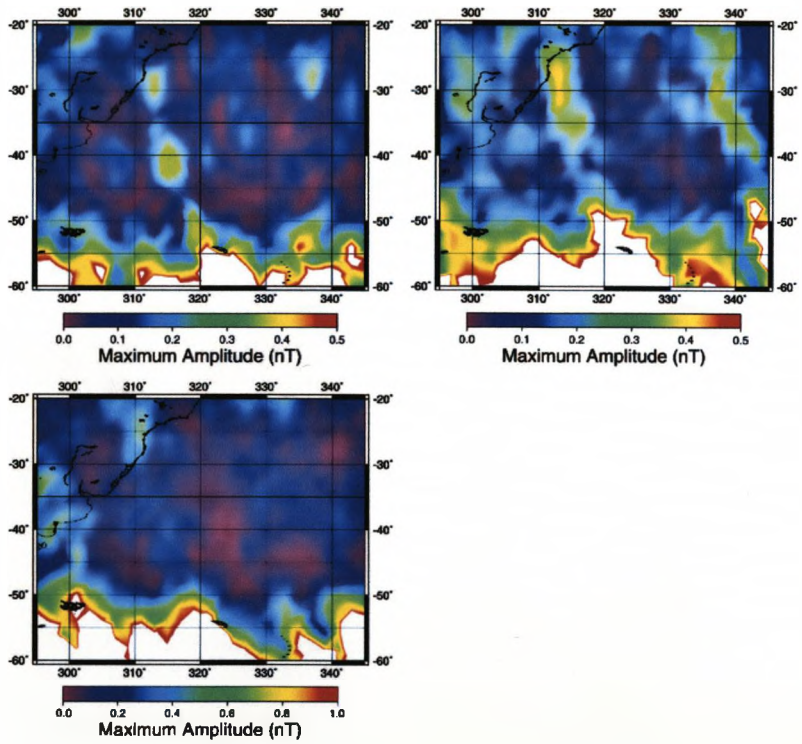

Figure 3.43: High resolution signal amplitude maps, generated using data from the SAC-C satellite. The map in the upper left hand panel has been generated using unselected scalar residuals and the map in the lower left hand panel using unselected repeat observations. The upper right image is derived using selected scalar residuals.

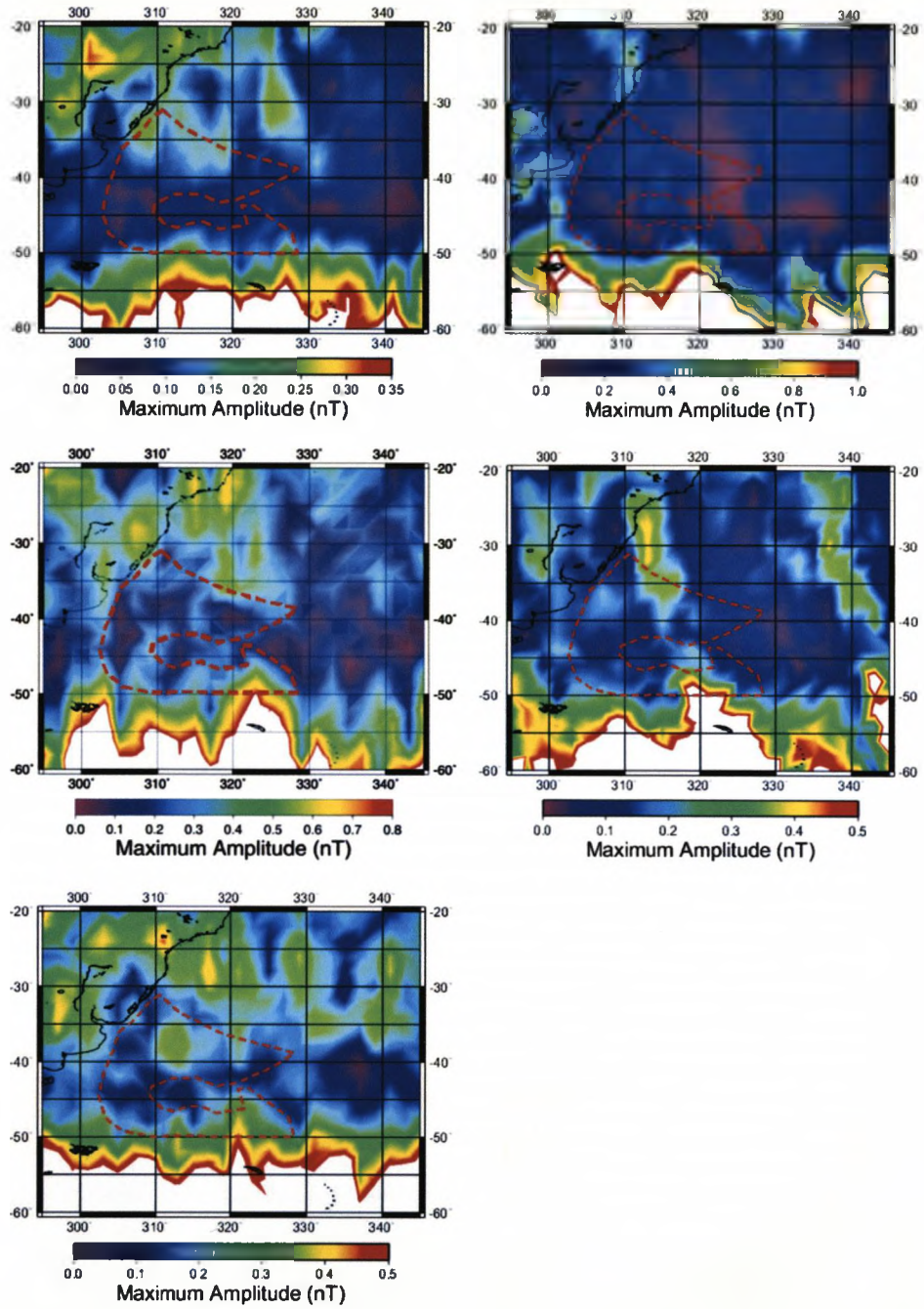

Figure 3.44: High resolution signal amplitude maps derived using CHAMP (left) and SAC-C (right) data. In the left hand column, the top map has been derived using selected scalar residuals, the central map using unselected Z component residuals and the bottom image using selected Z component data. In the right hand column, the top image has been derived using unselected scalar repeat data and the lower image using selected scalar residuals. All maps have been overlayed with the 2km bathymetric contour (as shown in Hughes et al. [2007]) to highlight the presence of weak magnetic signals around the basin edge.

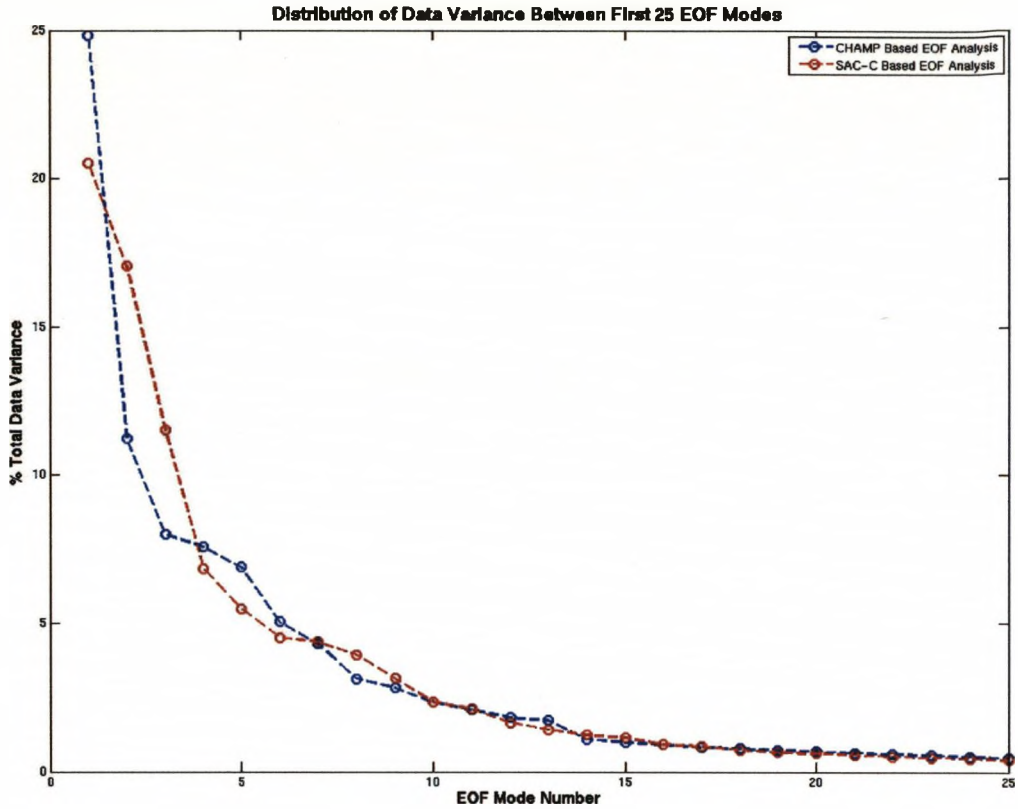

Figure 3.45: Variance distributions of CHAMP and SAC-C spatial EOF analyses (as a function of EOF mode number).

CEOFs over standard EOF methods being the capacity to identify propagating and rotating patterns within a dataset and assign that variability to a single CEOF mode, making it an ideal method for this circumstance. The added complexity of CEOFs does mean that depending on whether static single mode maps or temporal reconstructions are being considered, expected signal morphologies will differ. When considering a single static map, field configurations should be as the second field morphology outlined in §3.4, with the same spatial morphology appearing in both real and imaginary maps of the mode, albeit with the morphology of the imaginary map being 90° out of phase (rotated in this case, around a centre somewhere near the Zapiola rise) with respect to the real counterpart map. Frequency spectra of both expansion series should also display peaks at ~ 0.04 cpd ($\sim$ 25days). When the temporal reconstruction of a mode is considered, the same configuration as that found in the static case and §3.4 is expected, although here the configuration should rotate around the Zapiola Rise (45°S, 45°W), propagating in an anti-clockwise sense, completing a single revolution approximately every 25 days, making the configuration easier to differentiate from the ambient background.

When the resulting CEOF modes are evaluated, very few of the first 25 modes in either CHAMP or SAC-C analyses exhibit the required static configuration, although

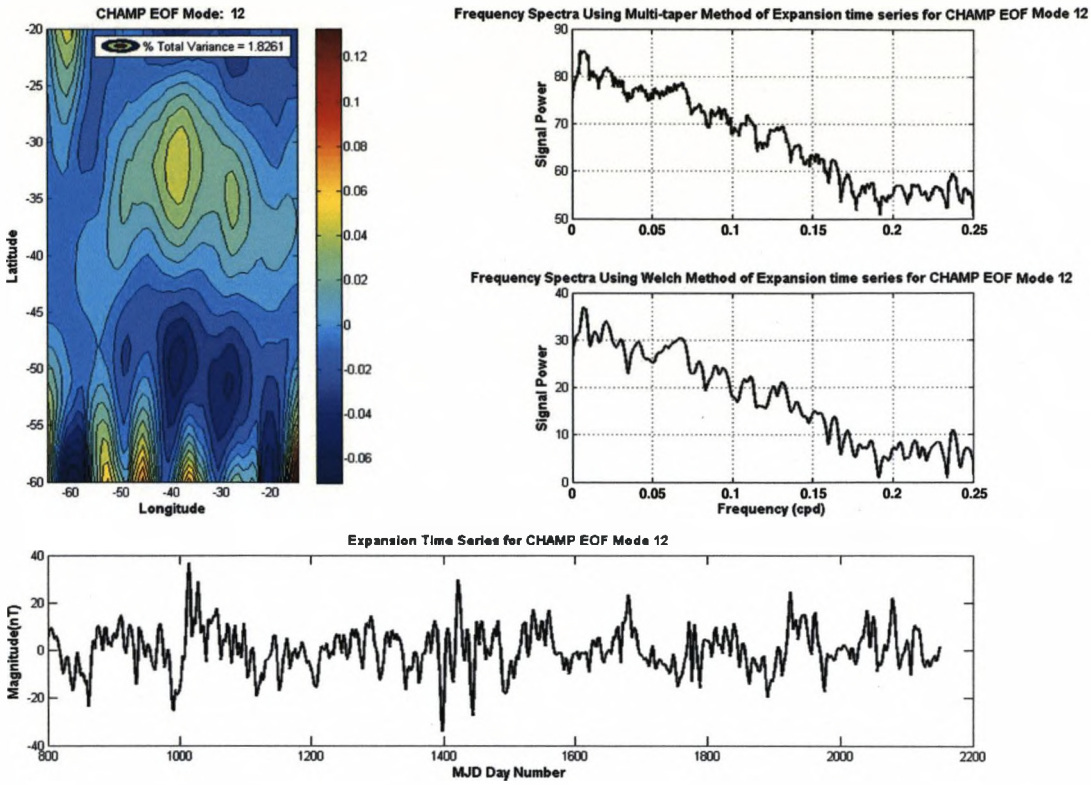

Figure 3.46: Detailed results of the 12th EOF mode from the CHAMP based, spatial EOF analysis (the mode accounts for ~ 1.8 % total data variance) . The upper left map highlights the spatial variability of the mode with the two smaller panels in the upper right corner of the figure showing the frequency content of the expansion time series displayed across the bottom of the image (calculated using two different methods).

those that do to some extent are shown in figures 3.49, 3.50, 3.51 & 3.52, with the variance distribution of both analyses shown in figure 3.53 (again both analyses have proved successful as a technical exercise). However, when the frequency spectra of these modes are examined, only the mode shown in figure 3.49 displays a peak in frequency anywhere near the required 0.04 cpd (25 days) (although not at precisely 0.04 cpd), while all others show either weak or absent content. This lack of sufficient frequency content in most modes, combined with amplitude distributions not too dissimilar from the ambient background, indicate that identification of propagating features is still difficult when using CEOFs, or more pessimistically that no circulation based signals are present in these datasets.

To make any signs of rotational movement in these modes clearer, temporal reconstructions of all the modes derived in these CEOF analyses were generated. However, while many of the reconstructed modes rotate, very few display spatial configurations similar to that outlined at the beginning of this analysis, with the number reducing further if the position of the rotational centre is considered (Note that as CEOF analyses can isolate a rotating signal within a single mode, a limited number of target modes is not overly concerning.). Of the fifty mode reconstructions considered (25 using CHAMP

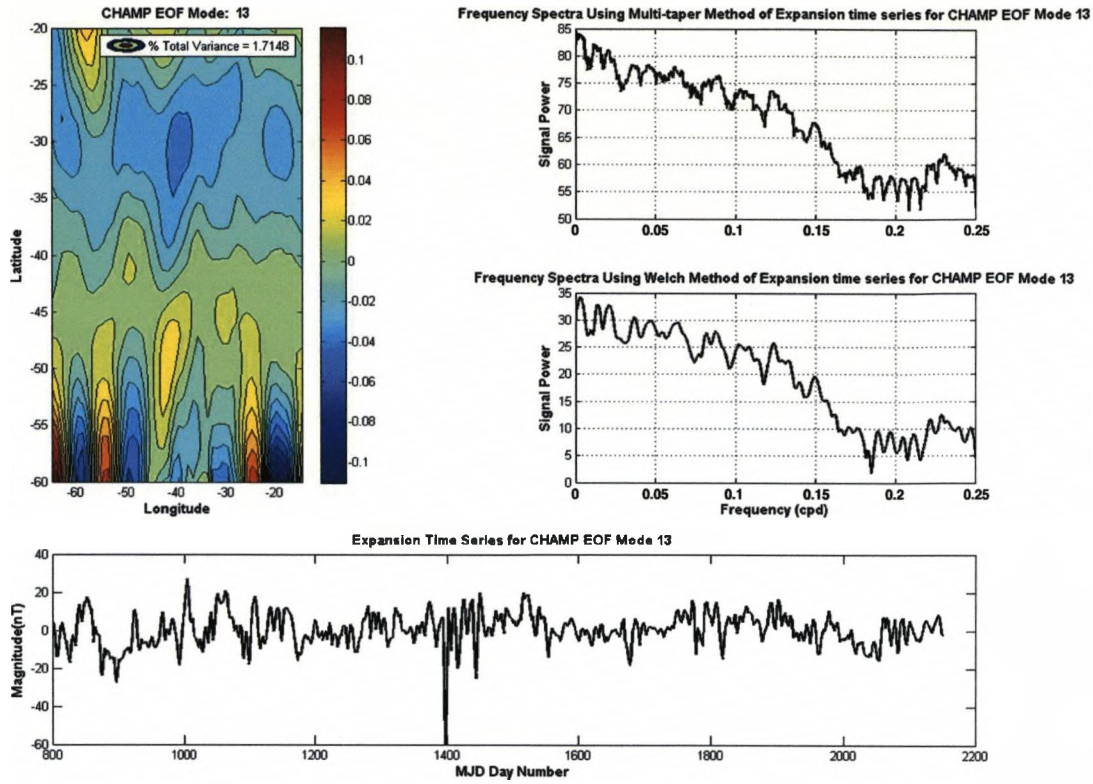

Figure 3.47: Detailed results of the 13th EOF mode from the CHAMP based, spatial EOF analysis (the mode accounts for ~ 1.7 % total data variance) . The upper left map highlights the spatial variability of the mode with the two smaller panels in the upper right corner of the figure showing the frequency content of the expansion time series displayed across the bottom of the image (calculated using two different methods).

data, 25 using SAC-C data), only the 10th mode of the CHAMP based analysis (considered previously in figure 3.49) displays a rotation with the correct spatial structure, rotational sense (anti-clockwise) and position of rotational centre (at 45°S, 45°W - the Zapiola Rise). Rotation of this mode is displayed as a series of snapshots (with 2 day temporal separation) in figure 3.54. However, the frequency characteristics of this mode are less than ideal with only a small contribution at 0.04 cpd. The mode also accounts for only $\sim 2.5\%$ data variance (this is not surprising given the localised nature and relatively small amplitude of this signal) and has a maximum amplitude of 0.5 nT, a value that given the mass transport of this system could easily be greater given the correct magnetic conditions. As such, these CEOF analyses have failed to provide the definitive evidence of localised circulation generated magnetic fields it was hoped they would produce.

This extensive analysis has attempted to improve on results acquired during the analysis of observatory data (§3.6), using records from the Ørsted, CHAMP and SAC-C spacecraft. It was hoped that the spatial and temporal characteristics of these data could be explored and evidence of localised oceanic circulation found in the satellite magnetic record. Using

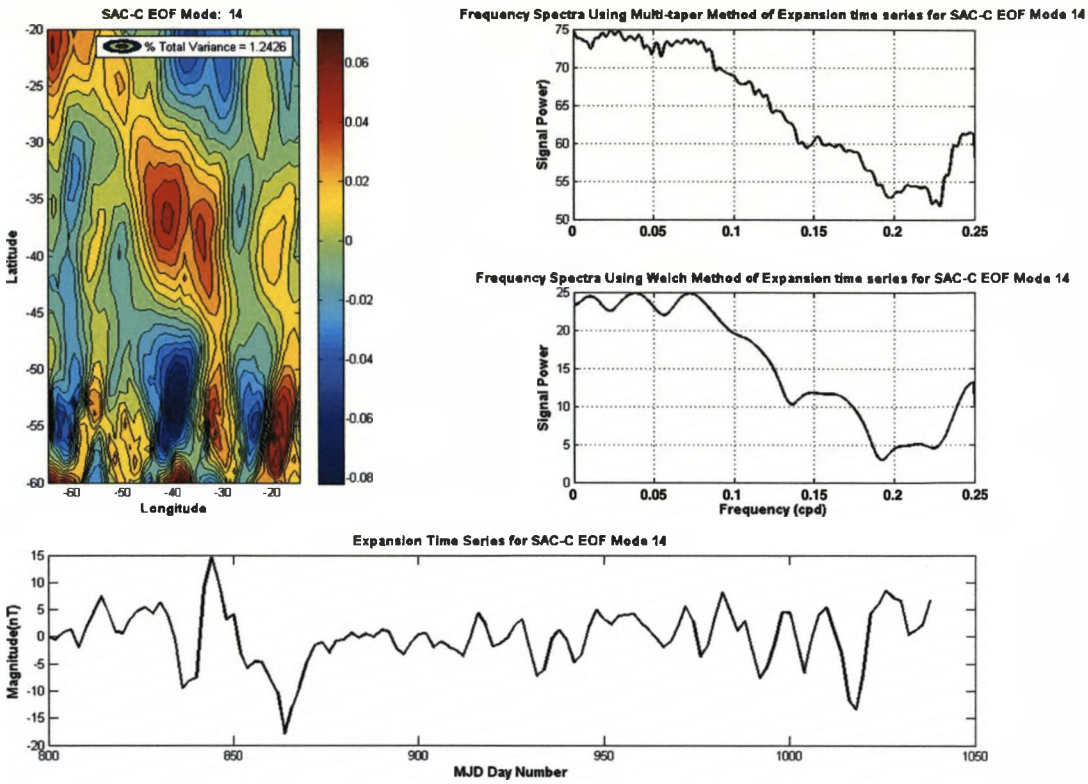

Figure 3.48: Detailed results of the 14th EOF mode from the SAC-C based, spatial EOF analysis (the mode accounts for $\sim 1\%$ total data variance). The upper left map highlights the spatial variability of the mode with the two smaller panels in the upper right corner of the figure showing the frequency content of the expansion time series displayed across the bottom of the image (calculated using two different methods).

harmonic modelling and statistical tools such as EOF and CEOF analysis, further evidence supporting the hypothesis of locally induced secondary magnetic fields, as a result of oceanic circulation has been found (for example, the presence of rotating variability in results of a CEOF analysis of CHAMP data (figure 3.49)). However, very much like the observatory analysis in §3.6, many of the results exhibit small magnitudes (often less than 1 nT), while also contributing very little to the total data variance of the system (EOF/CEOF analyses), and so only provide brief glimpses of potential oceanic behaviour, complicated and diminished by the effects of other signals.

3.8 Complications

Throughout this study, many results have appeared to be dominated by large scale, non-oceanic signals. This discussion aims to identify potential sources for these signals, and also discuss why circulation within the Argentine basin may not generate a magnetic field of the magnitude suggested previously.

During this study, the most widely contaminated results have been those linked to PST and

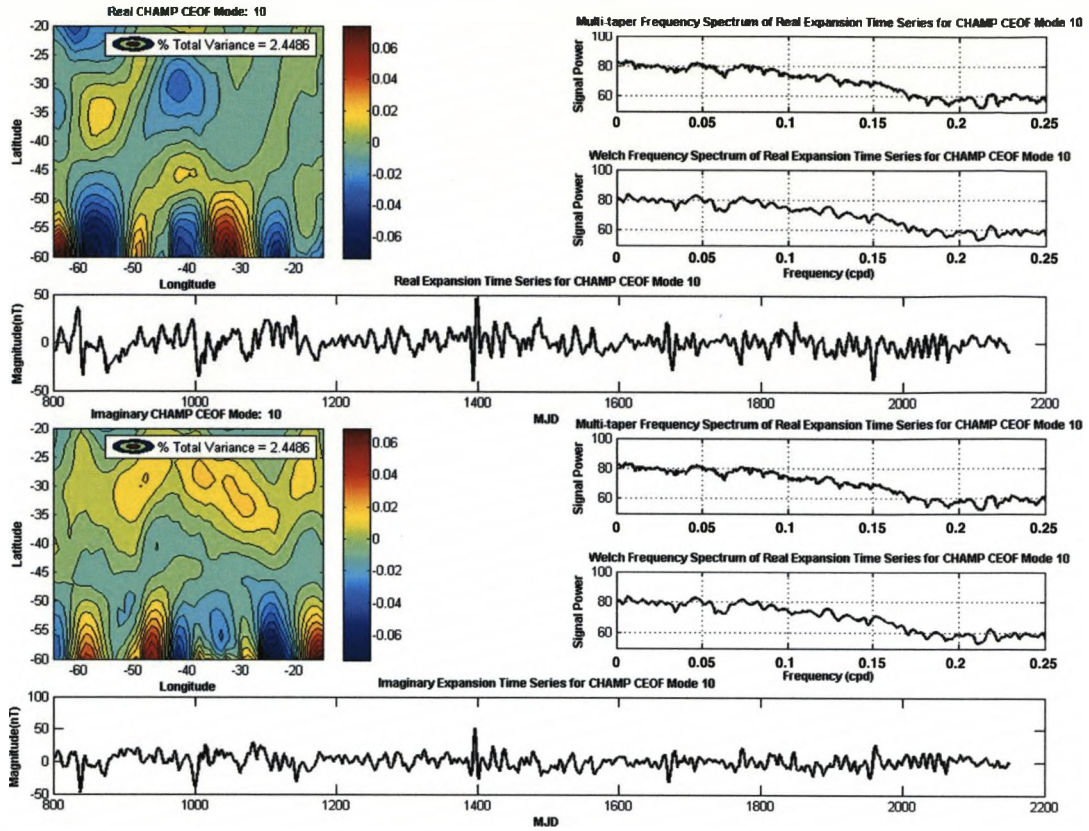

Figure 3.49: Detailed information relating to the CHAMP CEOF analysis (10th mode). The figure can be split into the upper and lower halves, with the upper half describing the real component of the mode and the lower half describing the imaginary component. The maps in the upper left corner of each half describe the spatial structure of the mode, while the two small plots in the upper right corner of each half display the frequency content of the expansion time series shown across the bottom of each half of the image.

NGK data, with large scale similarities between the analysis results of these two distant datasets (spatial correlations in particular) suggesting the presence of a global scale $\sim$ 24 day signal (this operational period is obtained from calculations of coherence between PST & NGK series, shown in figures 3.55 & 3.56) in both time series. As subtraction of the CM4 field model has already removed contributions from most internal field sources, potential sources for this signal that are external to the Earth are sought.

It was first noted by Lesur et al. [2005] that a particular external field source (probably located somewhere in the magnetosphere) produces a temporally varying magnetic field, with a period of $\sim$ 25 days, that is captured well in IMF By (Y component of the interplanetary magnetic field) records. While some field models use IMF By series to parameterise this field, the CHAOS and CM4 field models used in this study do not. Therefore, this field is likely to contribute to the magnetic residual data analysed in this study. To eliminate or confirm this field as a potential source of the global scale target, the harmonic modelling of §3.5.1 has been applied to IMF By time series to generate the frequency spectra shown in

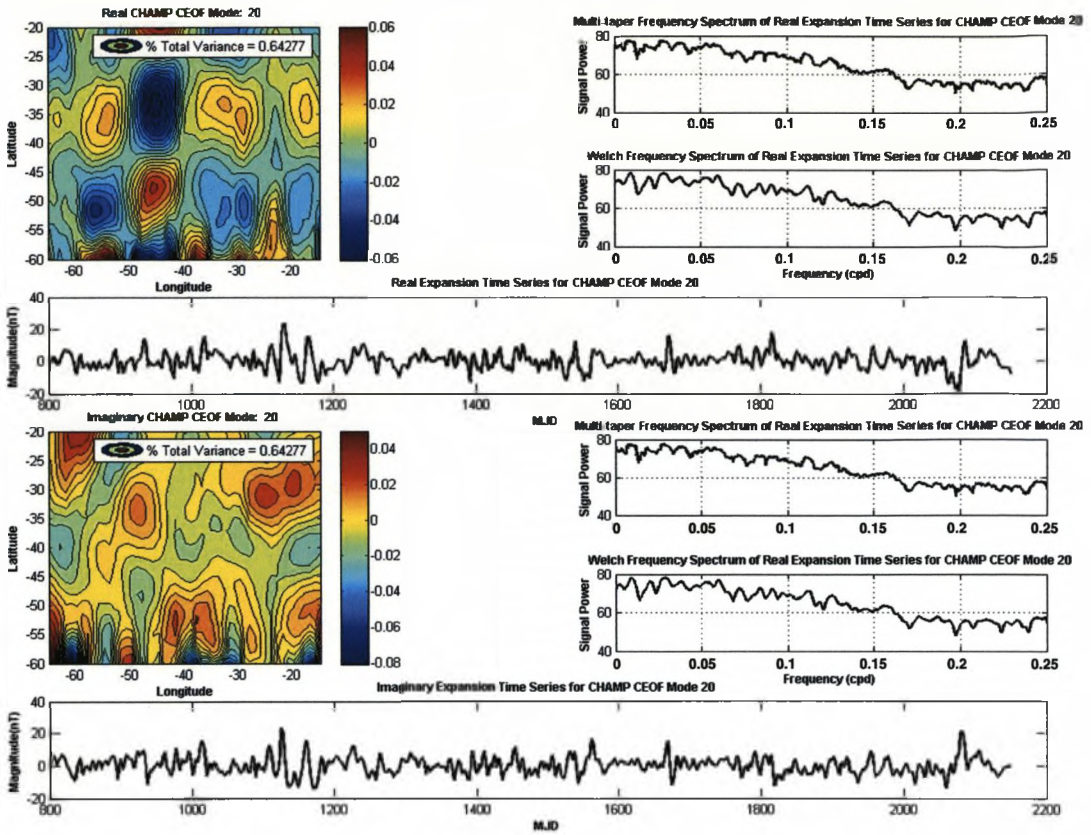

Figure 3.50: Detailed information relating to the CHAMP CEOF analysis (20th mode). The figure can be split into the upper and lower halves, with the upper half describing the real component of the mode and the lower half describing the imaginary component. The maps in the upper left corner of each half describe the spatial structure of the mode, while the two small plots in the upper right corner of each half display the frequency content of the expansion time series shown across the bottom of each half of the image.

figure 3.57. Interestingly, the large scale signal peaks in these spectra shift through time, and while spectra from 1999 and 2003 do show some signal between 24 and 25 days, when a spectrum of the full time series is considered no such signal is evident, suggesting that these small side lobes are present as a result of the short input series and their proximity to a main peak at slightly longer periods. Therefore, as this field appears not to have a frequency that matches that of the global scale target signal, another source must still be identified. Such a source may be found in the monthly rotation of the Sun. Just like the Earth, the Sun rotates about its own rotational axis, in this case taking $\sim$ 25 days to complete a single revolution (although due to the gaseous composition of the Sun, its rotational velocity decreases at high solar latitudes). This rotation means that from the reference frame of the Earth, the solar wind flux, so influential on the strength of the Earth's external magnetic field, will fluctuate on a global scale with an $\sim$ 25 day period, as sunspots and other solar surface phenomena rotate into and out of the line of sight between the Sun and Earth. Importantly, at the present time, this signal is not formally parameterised in the CHAOS & CM4 field models, although this periodicity of external magnetic field strength will affect the magnetic

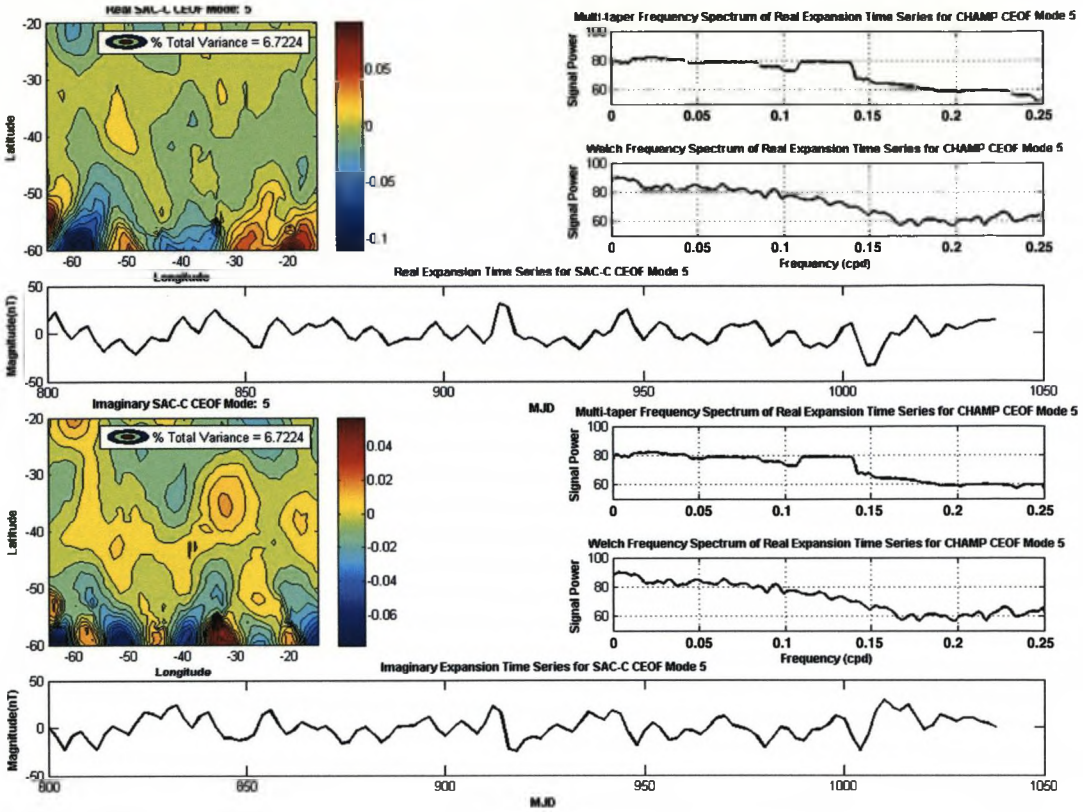

Figure 3.51: Detailed information relating to the SAC-C CEOF analysis (5th mode). The figure can be split into the upper and lower halves, with the upper half describing the real component of the mode and the lower half describing the imaginary component. The maps in the upper left corner of each half describe the spatial structure of the mode, while the two small plots in the upper right corner of each half display the frequency content of the expansion time series shown across the bottom of each half of the image.

indices that are used in the general external field parameterisations of CHAOS & CM4. This transfer of magnetic field strength into magnetic indices at a period of $\sim$ 25 days can be seen in figure 3.58. However, while various forms of the Dst index are used in the parameterisation of external fields in main field models, the likelihood of perfect parameterisation is low and the Kp index is rarely used in external field parameterisations in any way. Therefore, it is conceivable that some of the magnetic field variability generated due to solar rotation may remain in the magnetic records used in this study, producing the desired global scale masking signal and also possibly explaining the anomalous signal seen in figure 3.23.

Finally, throughout this study many of the signals being identified as being potentially oceanic in origin, have suffered from very low magnetic amplitudes when compared to those expected (several nT) as a result of circulation mass transport estimates from oceanographic literature (for example Fu et al. [2001], Tai and Fu [2005] & Hughes et al. [2007]). However, when the expected field morphologies outlined in §3.4 are examined, a clear separation of magnetic contributions can be seen. Given that a high percentage of mass transport in the Argentine basin generates a static magnetic field (5-7km of water column depth compared

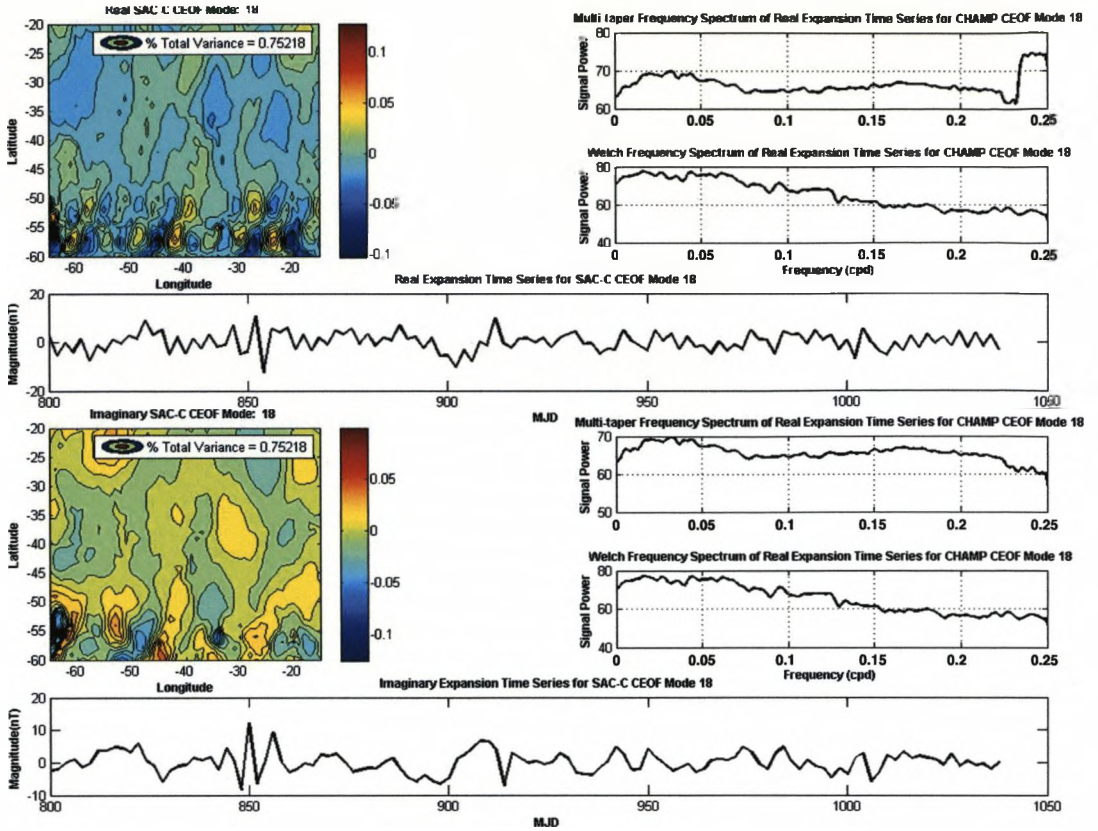

Figure 3.52: Detailed information relating to the SAC-C CEOF analysis (18th mode). The figure can be split into the upper and lower halves, with the upper half describing the real component of the mode and the lower half describing the imaginary component. The maps in the upper left corner of each half describe the spatial structure of the mode, while the two small plots in the upper right corner of each half display the frequency content of the expansion time series shown across the bottom of each half of the image.

to $\sim$ 20cm peak to trough surface amplitude), a similarly large percentage of magnetic field amplitudes predicted from mass transport estimates could contribute to this static field, leaving its rotating counterpart (the main focus of this study) with the significantly reduced magnitudes observed throughout this investigation. However, these reduced magnitudes may also be heavily influenced by the incompatibility of geostrophic flows (responsible for most of the flow in the Argentine basin) with the main axial dipole of the Earth's magnetic field (responsible for the largest secondary fields). In the horizontal plane, geostrophic flows are constrained by the following expression;

$$\nabla_H \left(\mathbf{u} \cos\theta\right) = 0 \tag{3.4}$$

where the horizontal gradient (∇_H) of a function $\mathbf{u}\cos\theta$ (where $\mathbf{u}$ is representative of the geostrophic flow in question and θ is colatitude) equals zero. However, if the motional induction equation (equation 1.5) is also considered in the horizontal plane, the resulting forcing term;

$$\nabla_H \left(\mathbf{u} B_{rmain}\right) \tag{3.5}$$

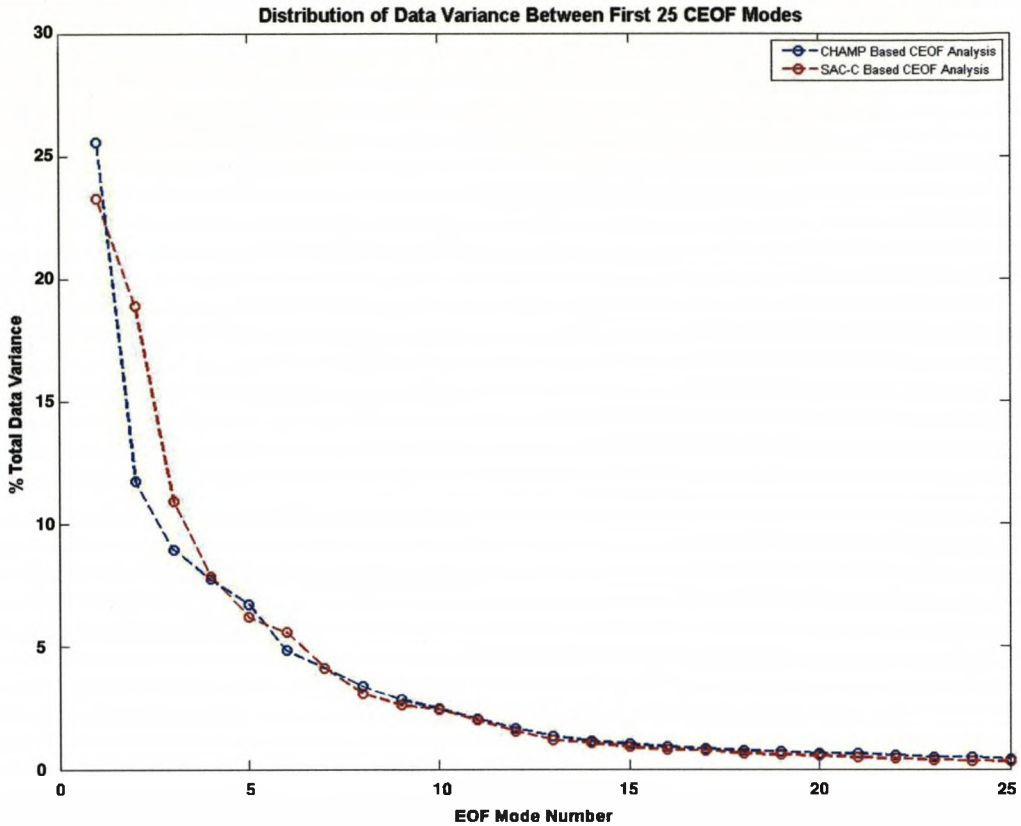

Figure 3.53: Distribution of data variance as a function of CEOF mode number, from CHAMP & SAC-C spatial CEOF analyses.

(where B_{rmain} is the ambient radial [predominantly dipolar] magnetic field and $\mathbf{u}$ is the flow from equation 3.4) states by definition that if B_{rmain} has a dependence in $\cos\theta$ (as in the geostrophic case), the flow will be unaffected by the dipole magnetic field when generating a secondary magnetic field, resulting in a much lower secondary field magnitude, as induction from geostrophic flow is limited to the use of weaker non-dipole magnetic field components, while ageostrophic flow interacts with the axial dipole (this concept and its associated equations are also introduced and discussed by Chulliat and Hulot [2001] & Chulliat [2004] within the setting of core flow modelling). However, in this case the ratio of non-dipole to dipole magnetic field strength ($\sim$ 10%) is expected to be larger than the ageostrophic/geostrophic flow ratio ($\sim$ 3% - 5%), meaning that geostrophic flow should still dominate any magnetic fields generated in this scenario. In either case, due to the limited magnetic field/flow configurations available, the magnetic fields generated in the Argentine basin will be smaller than those predicted from mass transport estimates alone.

3.9 Discussion

The results presented in this chapter have often shown potential oceanic content, although frequently appear to be influenced by coherent global scale signals (figures 3.20 & 3.21), that

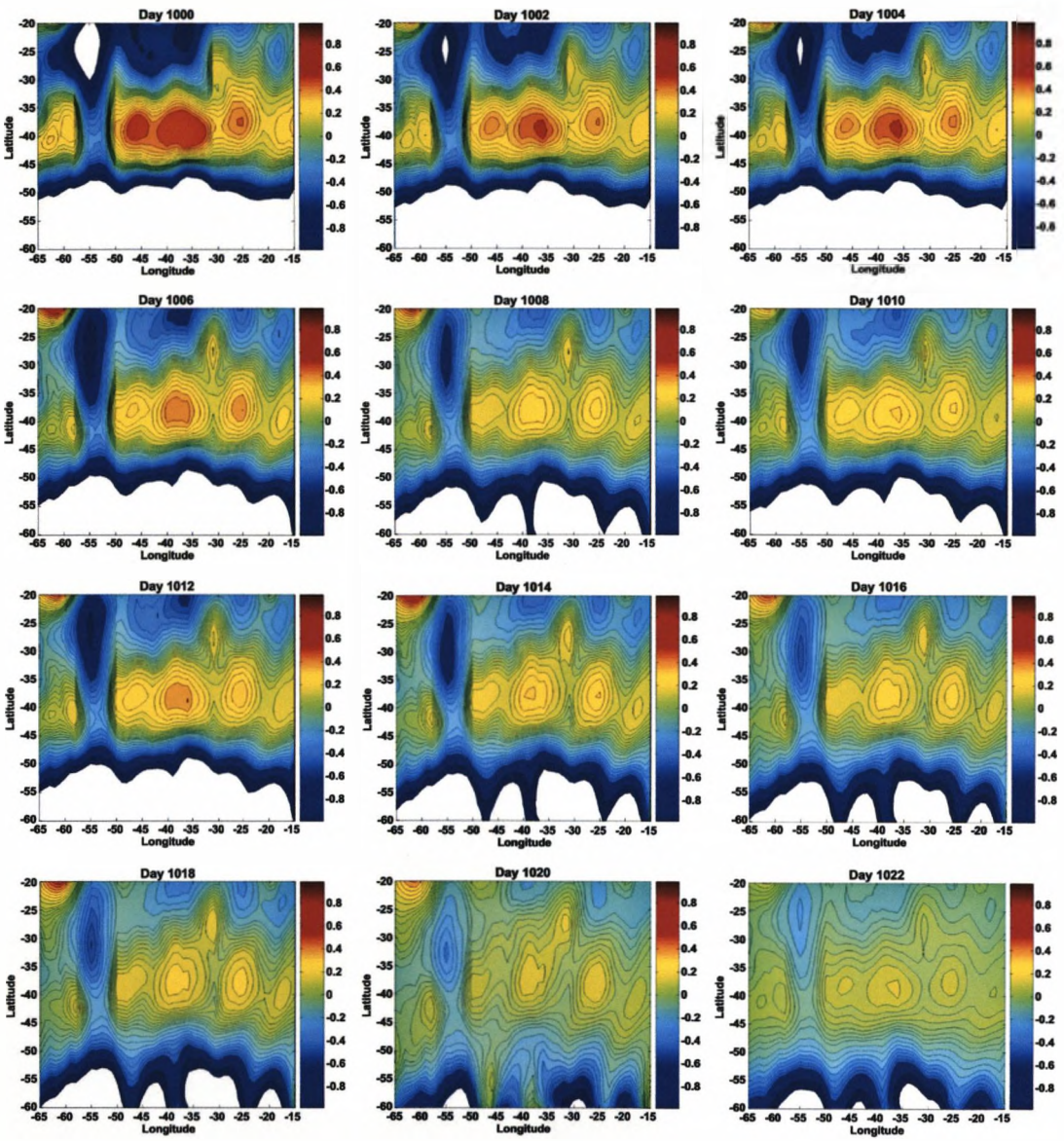

Figure 3.54: Snapshots of the 10th CHAMP CEOF mode reconstruction. The temporal separation between images is 2 days and spans a total period of 22 days, slightly under one rotational period of the target signal.

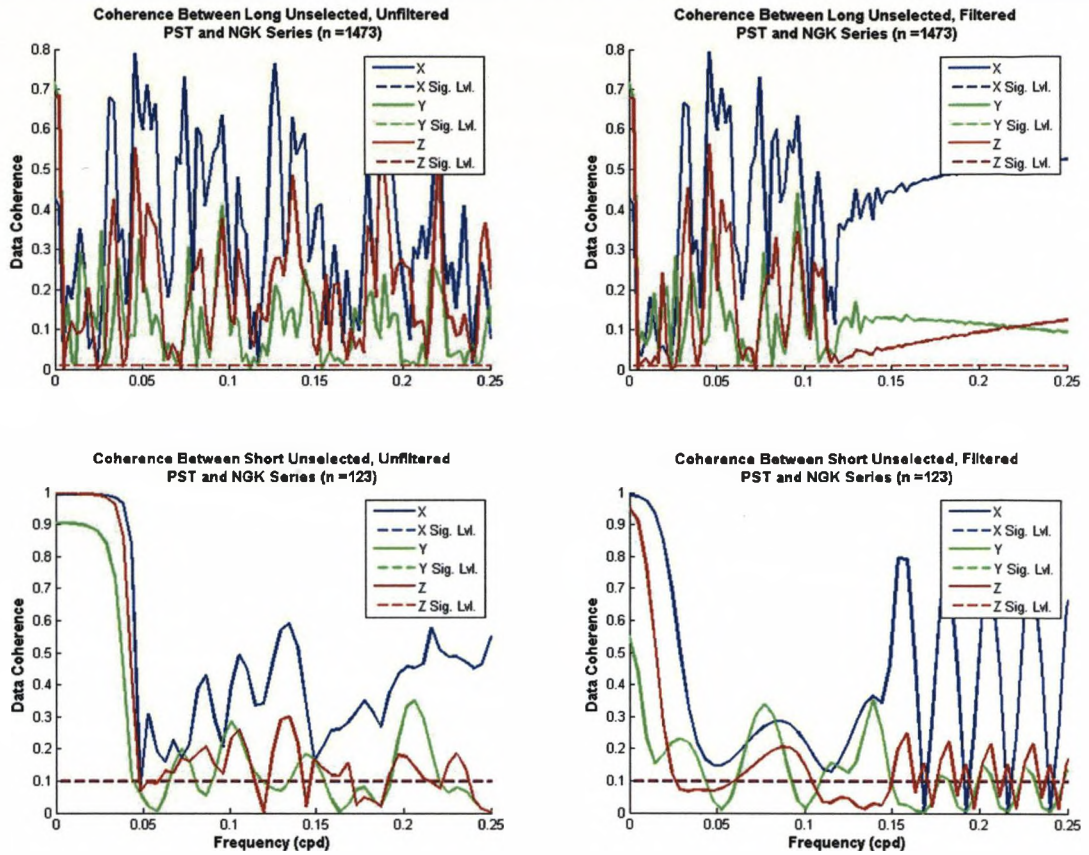

Figure 3.55: Plots of coherence between unselected PST and NGK time series. 95% significance levels for each magnetic component are marked in panels as dashed lines of appropriate colour, while degrees of freedom (n) used to calculate these levels are shown in the title of each panel.

due to the prior removal of main field models are most likely to originate in regions external to the Earth. Investigation of this additional field has ruled out the periodic magnetospheric field that maps into IMF By records (see figure 3.57), but has suggested a possible source as the monthly rotation of the Sun about its own axis, a mechanism that would produce a field fluctuation with the required period, whilst also having the potential to be embedded in the magnetic data used in this study.

Even without the influence of this additional signal, evidence of localised, circulation driven magnetic fields has been sparse, often appearing at close to noise level (for example see table 3.3). However some results, for example those in figures 3.22 & 3.23 do show distinct signal content at the required frequency, on a localised basis with the correct vector directionality, suggesting there is indeed a magnetic field associated with circulation in the Argentine basin present in magnetic records. If this is the case, why do many of the results found have such small field amplitudes, when mass transport estimates from oceanographic literature are large, which should translate into relatively large magnetic field magnitudes ($\sim$ several nT)? Upon further investigation, it becomes clear that oceanic flow within the basin may

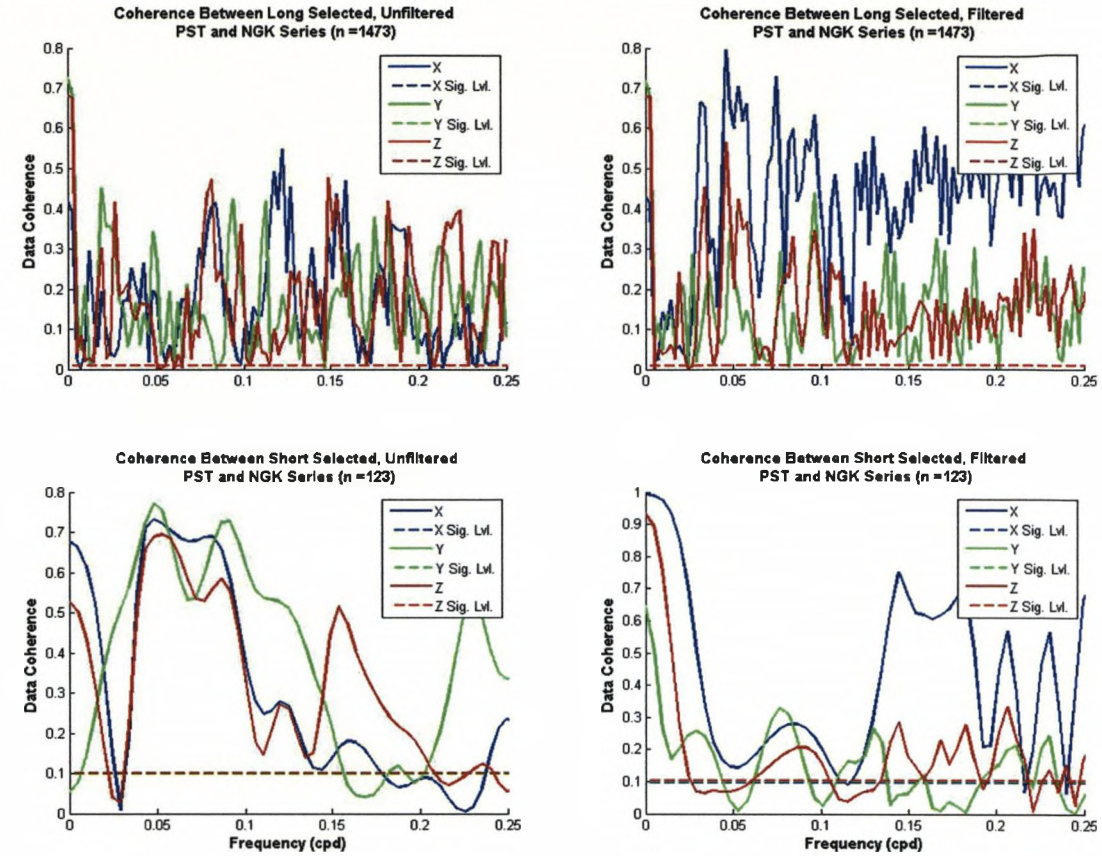

Figure 3.56: Plots of coherence between selected PST and NGK time series. 95% significance levels for each magnetic component are marked in panels as dashed lines of appropriate colour, while degrees of freedom (n) used to calculate these levels are shown in the title of each panel.

generate two different magnetic signatures, one much larger in amplitude than the other. Unfortunately, the larger of the two fields will be static and so very difficult to identify from background noise, especially at this mid to high latitude. The second field, which arises due to the sea surface anomalies (relative to mean sea level) that propagate/rotate around the basin (figure 3.2) and are generated by the barotropic circulation within it, will produce the rotating magnetic field desired, although due to the small peak to trough amplitude of the surface height anomalies ($\sim$ 20cm compared to 5-7km of the basin water column) a large magnitude magnetic field will not be produced (compared to its static counterpart, generated by main water column rotation), potentially explaining the small magnetic contributions identified during this study.

3.10 Summary

In this chapter, various data processing techniques have been employed, using both ground and satellite based magnetic records, to identify the presence of locally generated oceanic

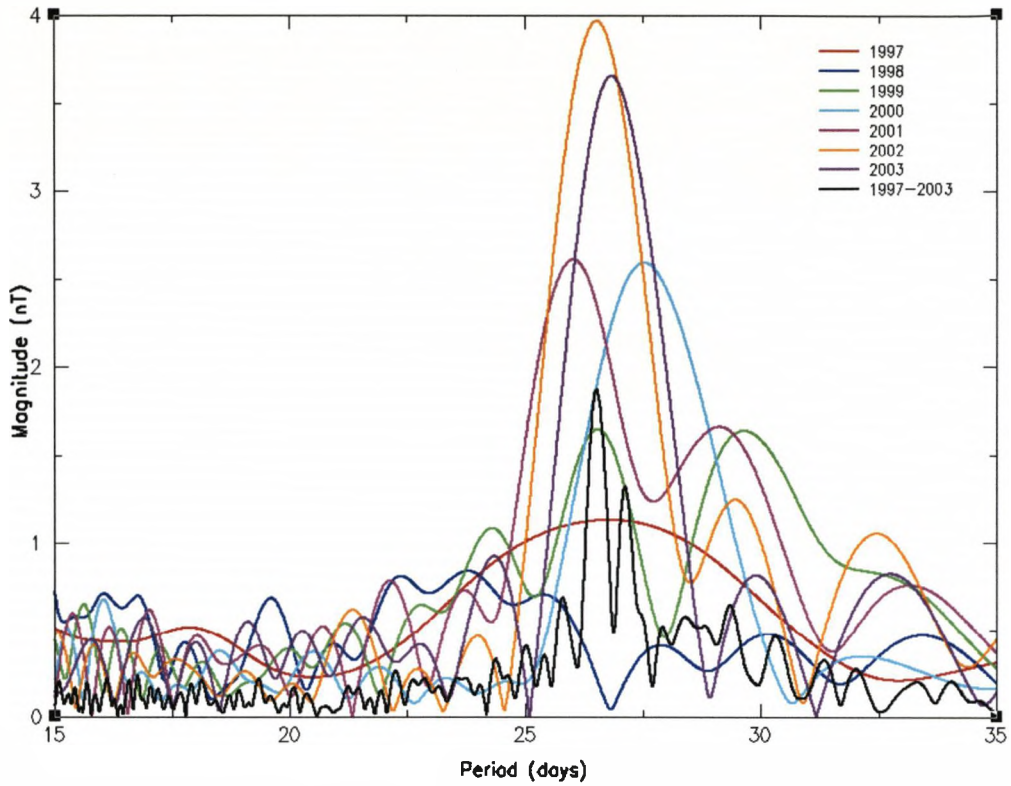

Figure 3.57: Frequency spectra of IMF By records.

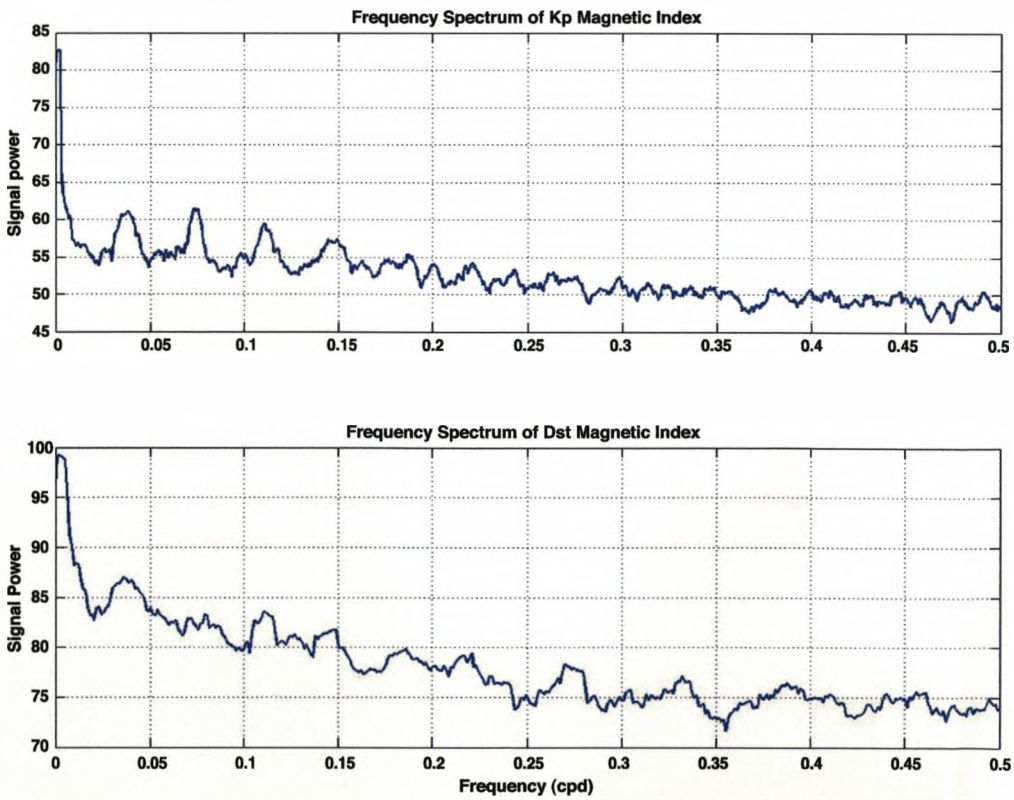

Figure 3.58: Frequency spectra of Kp (top) and Dst (bottom) magnetic indices.

magnetic fields emanating from the Argentine basin. Unfortunately, many of the results have been compromised by additional global scale masking signals and low magnetic amplitudes. However, possible explanations for these complications, both geomagnetic and oceanographic have been suggested where appropriate. In summary, localised ocean circulation would appear to possibly generate magnetic fields detectable at both ground level and satellite altitude, although in this case results are tantalisingly positive, yet frustratingly disappointing. However, in other cases where global masking signals are not present and more favourable circulation dynamics are in place, a more positive outcome may result, although such investigations should be undertaken with a great deal of caution.

Chapter 4

Modelling of Global Scale, Multi-Constituent Tidal Fields

4.1 Introduction

In this chapter, the focus shifts from periodic flow on a localised basis, to flow on a global scale. Ocean tides represent an ideal target, as their strict periodicity make them a relatively easy flow to study and large magnitude make them one of the most significant periodic flows in the oceanic domain, illustrated by extensive prior investigation from both oceanographic [Egbert et al., 1994, Ponchaut et al., 2001] and geomagnetic [Tyler et al., 2003, Maus and Kuvshinov, 2004] viewpoints.

However, previous magnetic research of ocean tides tends to follow a similar path, taking the form of numerical predictions of tidally generated fields, validated using ground [Maus and Kuvshinov, 2004] and satellite [Tyler et al., 2003] magnetic records. Unfortunately, while these studies identify tidal magnetic signals, they do not provide estimates of the full tidal field, as observations are often filtered (potentially removing tidal signal) prior to analysis. This investigation attempts to rectify this, firstly by re-affirming the results of Tyler et al. [2003], before deriving a multi-constituent, tidal vector magnetic field model.

The chapter begins with an introduction to ocean tides, after which the findings of the study (both technical details and results) are presented. The chapter concludes with a discussion of these findings and their possible implications for the future study of tidal magnetic fields as a whole.

4.2 Ocean Tidal System

Ocean tides are the hydrodynamic response of the global oceans to astronomical forces and account for over 80% of all sea-level variations (Ponchaut et al. [2001]); however, the tides we observe arise due to modifications (due to real world effects) of idealised tidal forcing.

Tides (oceanic or solid Earth) arise due to gravitational interactions within the Earth - Sun - moon system (described mathematically in Gill [1982]). Using the Earth - moon system as an example (although all subsequent arguments are equally valid for the Earth - Sun system), the Earth and moon orbit together around their joint centre of mass ($\sim \frac{1}{4}$ of the way from the Earth's surface to its centre), with the gravitational attraction of the moon on the Earth providing tidal driving forces. However, the manner in which their generation is explained differs depending upon the reference frame being considered.

In a stationary frame, the moon exerts a radially dependent gravitational force on the Earth. However, to retain Earth - moon orbit, net force must be zero at the Earth's centre and so all gravitational forces are re-calibrated accordingly, subtracting the gravitational force at the Earth's centre. As a result, the radial dependence of gravity leads to a residual tidal force everywhere on Earth except at its centre, the distribution of which can be seen in the upper panel of figure 4.1.

Alternatively, in a rotating frame tidal forces arise due to imbalances in gravitational (towards moon) and centrifugal (away from the Earth -moon centre of mass) forces across the Earth. Due to the orbit of the Earth about the joint Earth - moon centre of mass, centrifugal forces are generated to maintain orbit (by equalling gravitational attraction at the Earth's centre of mass). However, while centrifugal forces typically vary radially from the centre of rotation, in this circumstance because the Earth is rigid, all points on and in it experience the same centrifugal force (that at the Earth's centre of mass), with the resulting imbalance between the two forces everywhere in Earth but at its centre, producing the tidal force distribution shown in the lower panel of figure 4.1.

Note that irrespective of the way in which the system is viewed, the response to tidal forces always consists of two 'bulges' aligned to the Earth - moon line, with two smaller inward facing forces that lie perpendicular. Therefore, if the Earth were draped in a global ocean of uniform depth, its surface would adjust to match the distribution shown in figure 4.1. When Earth rotation is considered, because the positions of tidal forces are locked, as the Earth rotates the ocean surface continually adjusts, producing the periodic rise and fall in sea level associated with ocean tides. While figure 4.1 shows the configuration of the M2 and O1 lunar tides, numerous other tidal constituents exist, each with a period equal to a periodic forcing within the Earth - Sun - moon system (e.g., the MF (fortnightly) lunar tides or semi-diurnal (12 hours) S2 and diurnal (24 hours) P1 solar tides).

While tides are simple in an ideal environment, when applied to a realistic Earth, fluid dynamical effects complicate them, a primary effect being tidal lag (the time between theoretical and actual high tide), a problem caused by limited wave speeds in realistic ocean basins. Due to their wavelength, tides propagate as shallow water waves, whose speed (c) is governed by;

$$c = \sqrt{g.h} \tag{4.1}$$

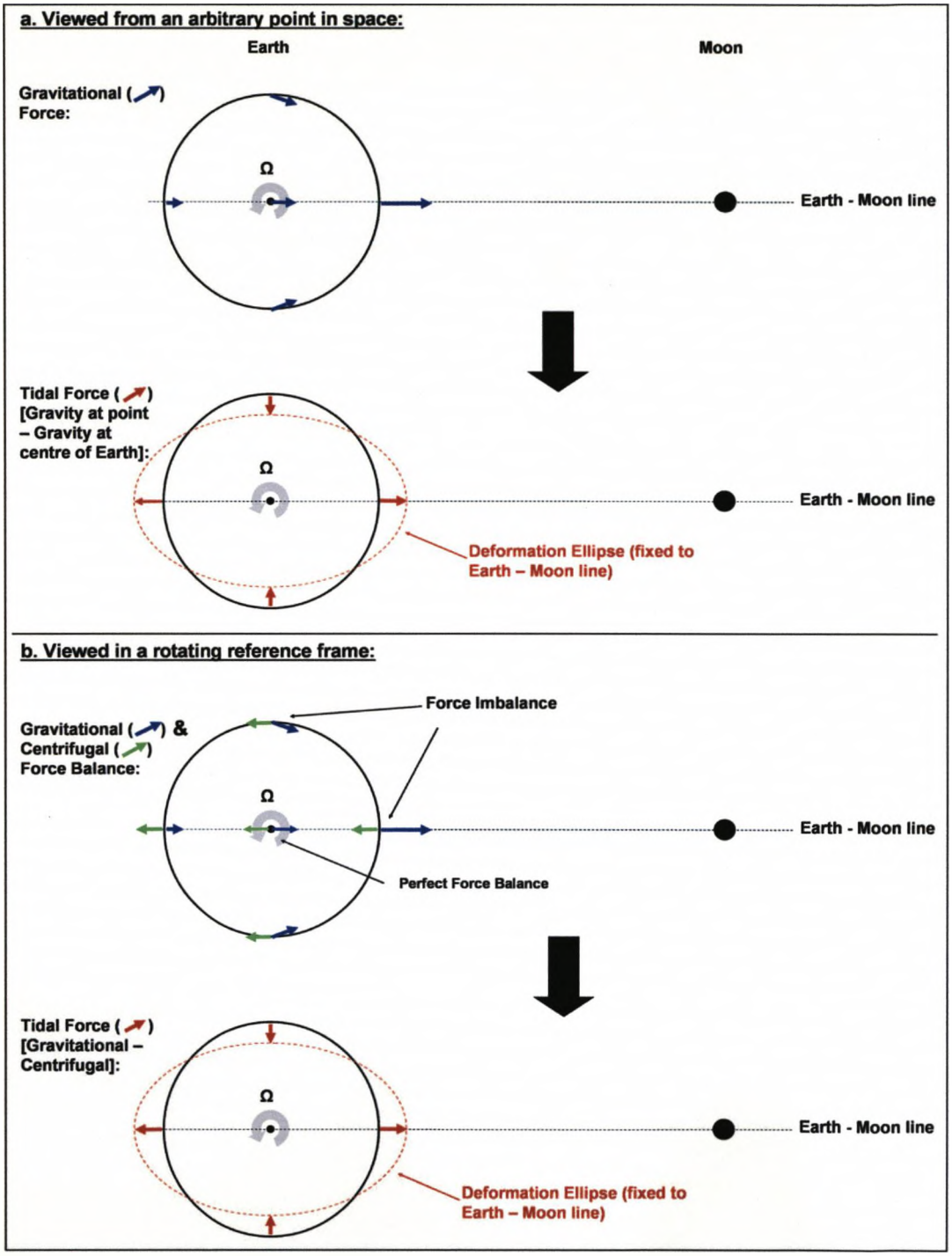

Figure 4.1: A schematic diagram illustrating the details of tidal (in this case lunar) forcing (viewed from the North pole), considered in both stationary (Panel a) and rotational (Panel b) reference frames. Note that the direction and magnitude of all the forces (arrows) shown are greatly exaggerated.

where g is gravitational acceleration and h is water depth. While the Earth rotates at very high speed ($\sim$ 450 ms^{-1} at the equator), tides cannot travel as quickly (to achieve such speeds, ocean basins $\sim$ 22 km deep are required) and so lag behind.

However, basin geometry and coriolis forces (equation 5.2) have a much greater effect on tidal flow. In a similar manner to Rossby waves (chapter 5), fluid moving on a rotating body tends to be deflected (in a direction perpendicular to that of the fluid motion) by coriolis forces that arise due to rotation. Therefore, ideal zonal flow is disrupted, a problem compounded by continental land-masses which act as physical barriers to zonal flow. Therefore the tides adjust, replacing long wavelength zonal flow with a series of smaller scale amphidromic systems (an ocean basin dominated by the circulation of a single confined rotary wave). Within each system, the tide (now represented as a tidal Kelvin wave) circulates around the basin boundary, with a rotational period equal to the period of the ideal tide from which it was derived. The spatial configuration of each system is determined by basin geometry, with the destructive interference of a tidal Kelvin wave (as it circulates) determining the amphidromic point of the 'cell' (wave interference may require several amphidromic points within one cell). The amphidromic point is one of the most important features within a cell, as not only is tidal amplitude zero here (and increases radially outwards), but it is also the point from which all co-tidal lines emerge. Co-tidal lines delineate positions of identical tidal phase (the stage of the tide in hours after high tide (usually relative to Greenwich), or degrees between 0° and 360° (a full tidal cycle)) within each cell. Note that for each tidal constituent, a unique distribution of amphidromic cells and co-tidal/co-range (lines of constant tidal amplitude) lines exist. Figure 4.2 shows a typical example of reconfigured tides, derived by assimilating TOPEX/POSEIDON altimeter data into a modelling framework constructed using theoretical oceanographic considerations (equations of fluid motion, etc).

It is of little surprise that this topic is researched so heavily (ocean tides still represent one of the largest sources of signal noise in oceanographic datasets). However, even though these signals are visually complex, their high magnitude, largely barotropic flow regime (although interactions with bathymetry do introduce a small baroclinic component) and strict periodicity mean that when investigating more dominant constituents (e.g., M2, K1, S2 and O1 among others), the magnetic fields they generate are clearly identifiable [Tyler et al., 2003, Maus and Kuvshinov, 2004].

4.3 Simple, Single Mode (M2) Tidal Isolation

In this section simple tidal isolation exercises are presented, along with an introduction to the methodologies that underpin all the results presented in this chapter.

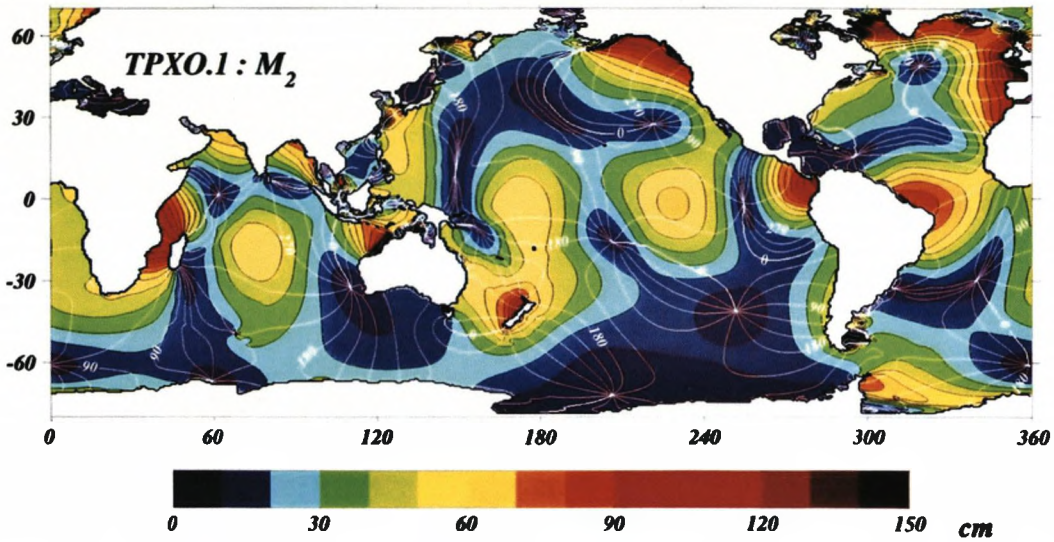

Figure 4.2: A model of the M2 tidal constituent derived using TOPEX/POSEIDON data (*from Egbert et al. [1994]*). The image displays the reconfiguration of global tides into smaller amphidromic cells. Tidal amplitude is shown as shaded contours, tidal phase by white co-tidal lines (30° intervals).

4.3.1 Harmonic/SHA (Spherical Harmonic Analysis) Methodology

The methodology used throughout this chapter is very similar to that used by both Tyler et al. [2003] and Maus and Kuvshinov [2004]. Previous work, both outside (Tyler et al. [2003], Maus and Kuvshinov [2004]) and more specifically within this thesis (chapter 3), has shown that the methodology adopted here is stable when used in conjunction with magnetic observations and that reliable results can be obtained.

The methodology itself consists of two distinctly different yet interlinked parts, each of which is detailed here. The first aspect of the methodology is very similar to that used in chapter 3 (detailed in §3.5.1), where a three parameter harmonic function (equation 3.1) is fitted to data via generalised least squares inversion (equation 3.3). The application of the method is similar to that used in both §3.7 and Tyler et al. [2003], where satellite magnetic observations are used to study the spatial characteristics of a target. However, unlike when using stationary data (§3.6), in this situation observations cannot be applied as full datasets, as tidal signals vary across the globe. Therefore, it is necessary to split datasets into smaller spatial blocks, each of which is applied to the harmonic fitting procedure individually to prevent contamination from neighbouring cells. The result is a series of grids, each one representing the spatial distribution of a single parameter from equation 3.1 across the study region (see figure 4.3). This figure clearly shows there is a trade off between solution resolution and stability when using this method. Unfortunately, no optimum pixel resolution exists (as the characteristics of the data being used have a large effect on the optimum resolution), explaining the difference between the 5° latitude × 5° longitude pixel resolution used in work presented throughout this chapter and the 6° latitude × 10° longitude

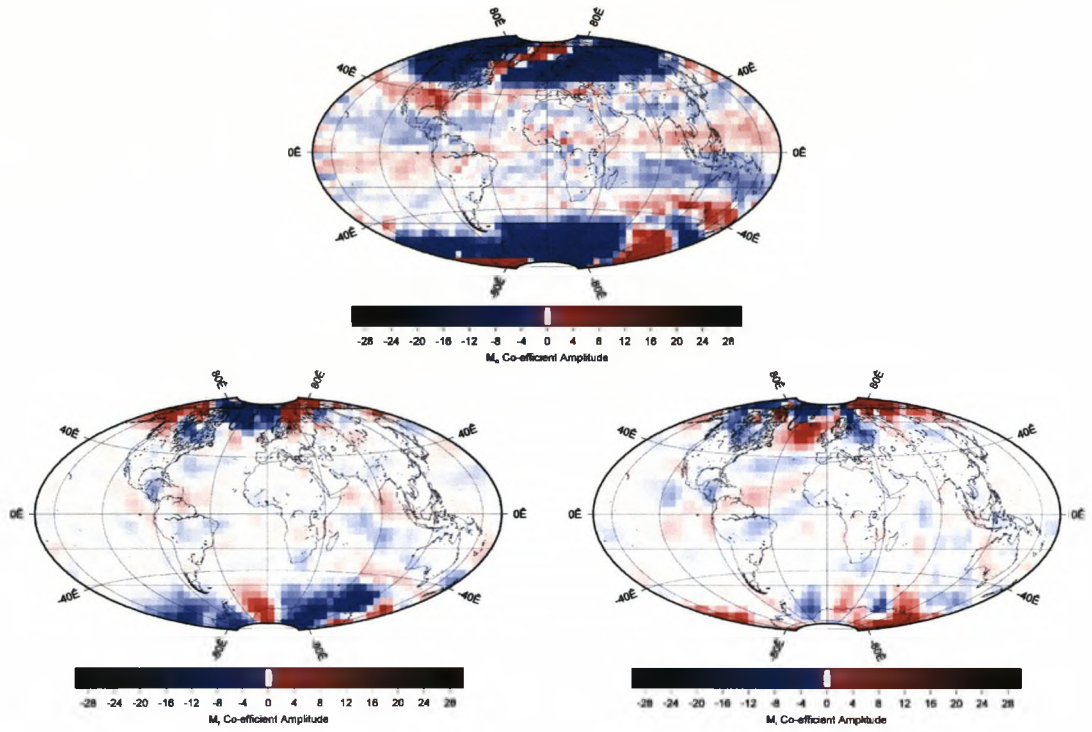

Figure 4.3: Global distributions (between $\pm 87.5^{o}$ latitude) of parameters from equation 3.1 (using the M2 tidal frequency), derived using CHAMP selected scalar observations. Each pixel (5^{o} latitude $\times$ 5^{o} longitude) corresponds to the parameter amplitude defined using data within the pixel.

resolution used by Tyler et al. [2003]. Note that this resolution difference may explain many of the small scale differences found when the two analyses are compared (see §4.3.2 for a more in-depth discussion).

However, the method's assumption that all data within a pixel are measured at the same location within it (in terms of latitude, longitude and also altitude) is clearly un-realistic. While horizontal uncertainty can be controlled to an extent by pixel resolution, the assumption of uniform altitude is more difficult to control, the only solution being to limit studies to the use of a single satellite source (as CHAMP, Ørsted & SAC-C all have differing mean altitudes); therefore, all fits are limited to data from a single satellite dataset.

Secondly, if left in a discrete form, solutions are extremely difficult to analyse. Therefore, to use solutions further (i.e. to compare with those of Tyler et al. [2003]) they must be expanded on a basis of continuous functions. To allow this, a second aspect of the harmonic modelling methodology is introduced, where the discrete grid of a chosen harmonic parameter (M_o, M_r or M_i) is expanded into a continuous function (consisting of a series of spherical harmonics (equation 2.1)) that can be calculated at any location within the study area. The effect of this processing can be seen in figure 4.4. It should be noted that the images shown in this figure have been damped to produce a smooth solution (low model norm or roughness) whilst modelling the input data as closely as possible (low misfit). An appropriate damping

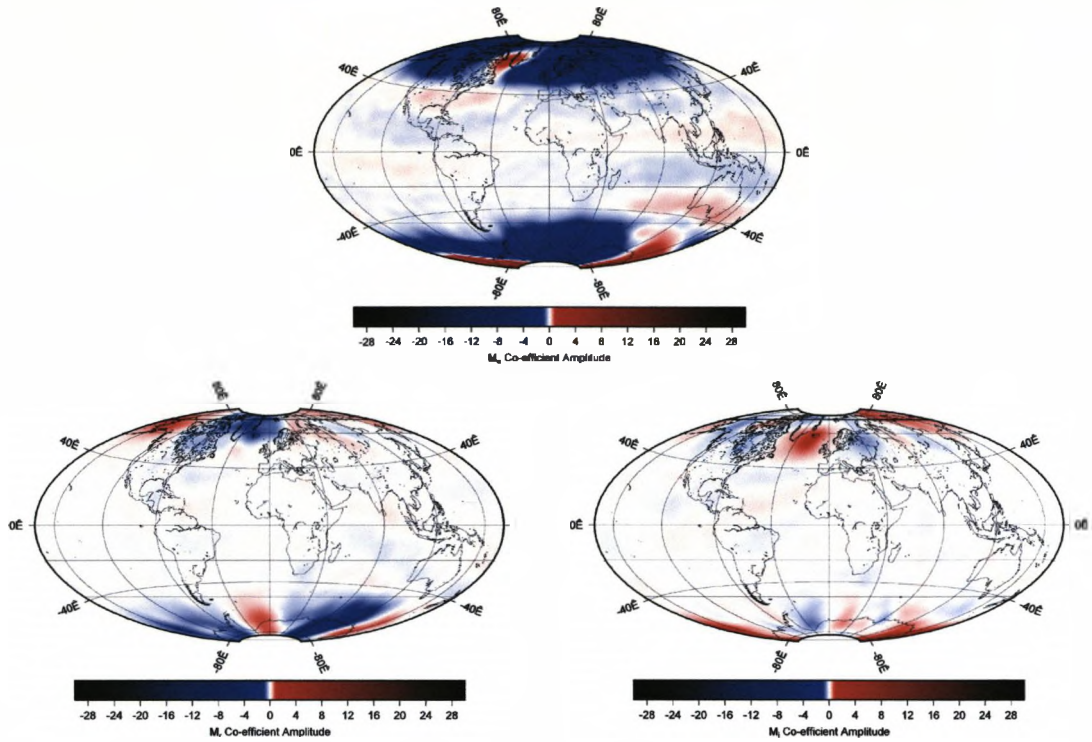

Figure 4.4: Spherical harmonic expansions of co-efficient grids shown in figure 4.3 (up to spherical harmonic degree 30). A damping parameter of 50 has been applied to reduce small scale variability.

parameter is selected using a trade off curve (see figure 4.5). It should also be noted that in all the model solutions presented throughout this chapter, damping is implemented at the Earth's surface (as this is the source region for the target fields) in the form of a Lagrange multiplier, applied to each element of the normal equations matrix $\mathbf{A^T A}$ (from equation 3.3). Also, in order to find the optimum balance between model misfit to input data and model complexity/smoothness (these models attempt to minimise the least squares misfit, i.e. an L2 norm), the level of damping increases as a function of spherical harmonic degree (as increased power in higher degree spherical harmonic terms can lead to a low model misfit at the cost of an overly complex and possibly unrealistic model solution). By applying damping more heavily to higher degree terms, a more delicate balance between misfit and complexity can be found and the most appropriate damping parameter for the situation determined.

As noted in chapter 3, the effect of anomalously high amplitude data on a solution can be drastic. Here, such effects are reduced through iterative modelling (a process also required when modelling a vector field using scalar data), a process which involves inverting a system of model equations until the model converges (model misfit stabilises), rejecting outlying data with each iteration. Once an initial solution is found (using all data) the standard deviation of misfit between data and model is calculated. All data that lie beyond a given cut-off are rejected and the remaining data inverted again. The process is repeated, comparing the current model with all the original data (because a rejected point may become valid later on)

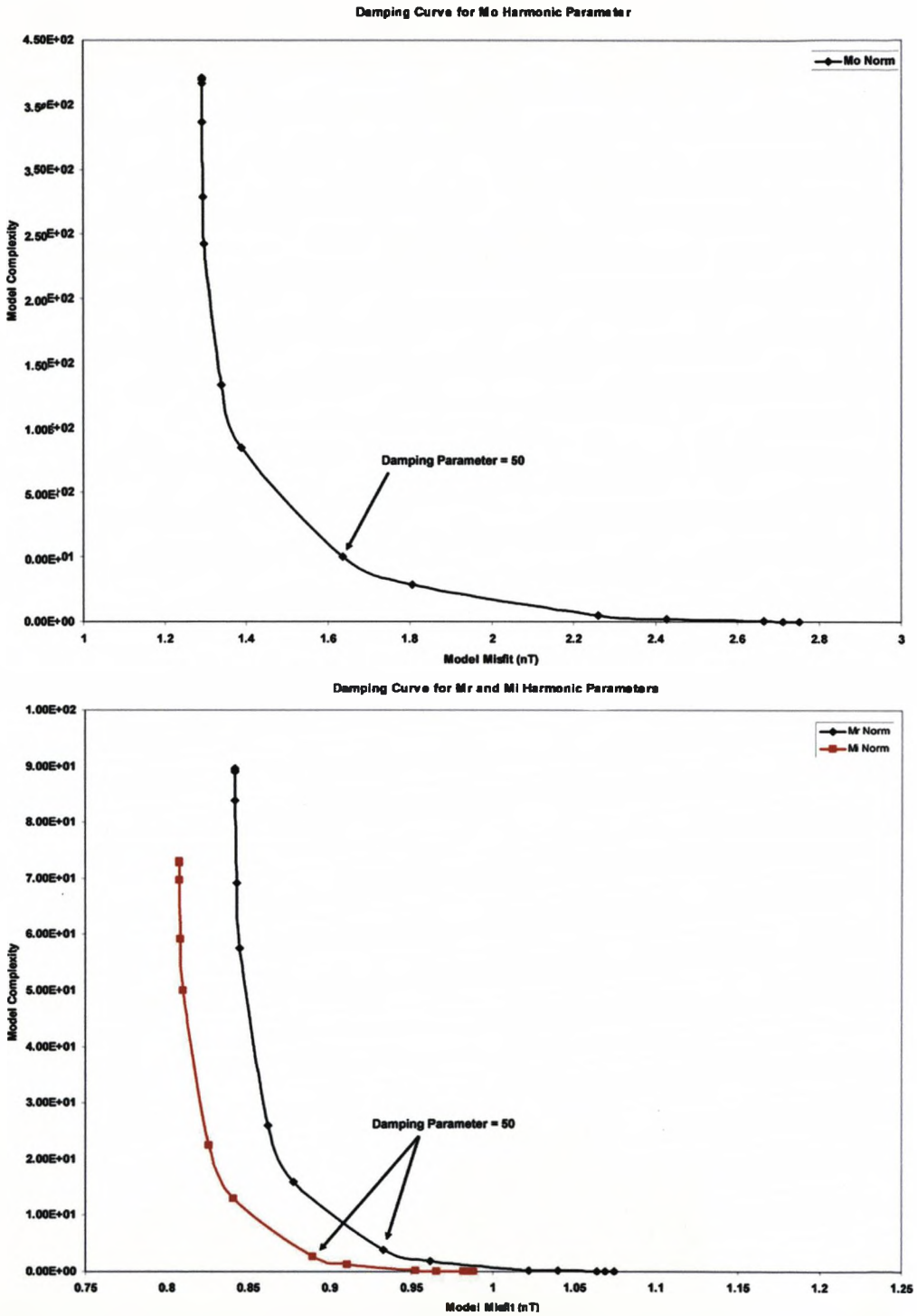

Figure 4.5: Trade off curves generated as part of spherical harmonic expansions derived from discrete parameter grids shown in figure 4.3. The ideal damping parameter is chosen as the value which balances model misfit and complexity (i.e. the 'knee' of the curve).

until a stable solution is reached. The effects of iterative modelling are shown in figure 4.6. Here, data are modelled through six iterations, three with a 5σ cut-off and three with a 3σ

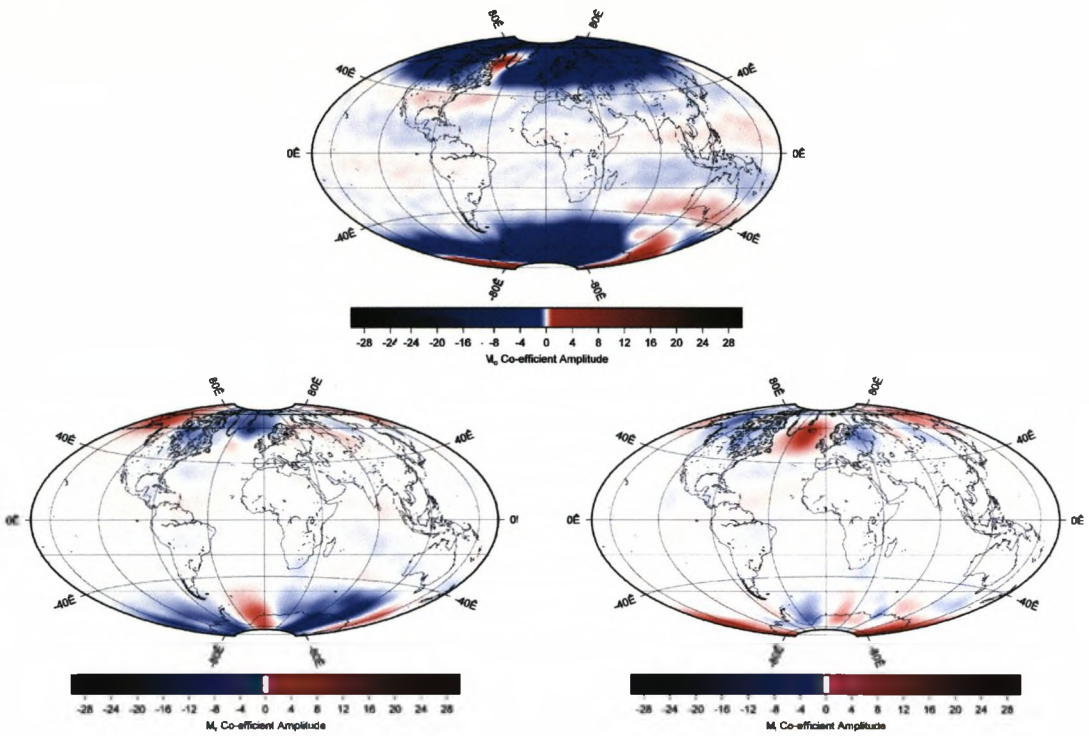

Figure 4.6: Iteratively derived spherical harmonic approximations of the discrete parameter grids shown in figure 4.3.

threshold. Note that because the data used is relatively quiet (with few or no anomalously high or low magnitude observations), stability is achieved quickly and little difference is seen between standard and iterative results.

4.3.2 Low Latitude Scalar Tidal Approximation, [Tyler et al., 2003]

This sub-section presents a comparison of Tyler et al. [2003] with results generated using the methodology outlined in §4.3.1. The analysis is conducted to ensure that the methodology used provides (along with the data used) results comparable with those of others, ensuring that any further work conducted using this approach has a sound methodological base.

Specific Data Requirements:

As in Tyler et al. [2003], this analysis uses CHAMP scalar satellite observations (pre-processed in accordance with chapter 2), therefore all solutions investigate the tidal field lying in the direction of scalar observation. Data are selected using the criteria; Kp $\leq$ 2+ (at all latitudes), Dst/dt $\leq \pm 3.0$ nT/hr (at all latitudes), PCn $\leq \pm 0.2$ (at latitudes $\geq 60^{o}$N) & local time: 1800 $\rightarrow$ 0600. Here, the removal of day time observations attempts to reduce the effects of tidal signals from external fields. However, this

cannot guarantee a 100% reduction and the possible presence of these signals within results must be considered. Data are further reduced in number by a latitude restriction of $\pm 50^{o}$ (also applied by Tyler et al. [2003]), before being applied to the methodology outlined in §4.3.1.

Analysis Results and Comparison with Prior Investigations:

Spherical harmonic representations of M_r and M_i parameters (from equation 3.1) at low latitudes are shown in figure 4.7, along with corresponding plots from Tyler et al. [2003]. Clearly, there are a great deal of similarities between the studies. Firstly,

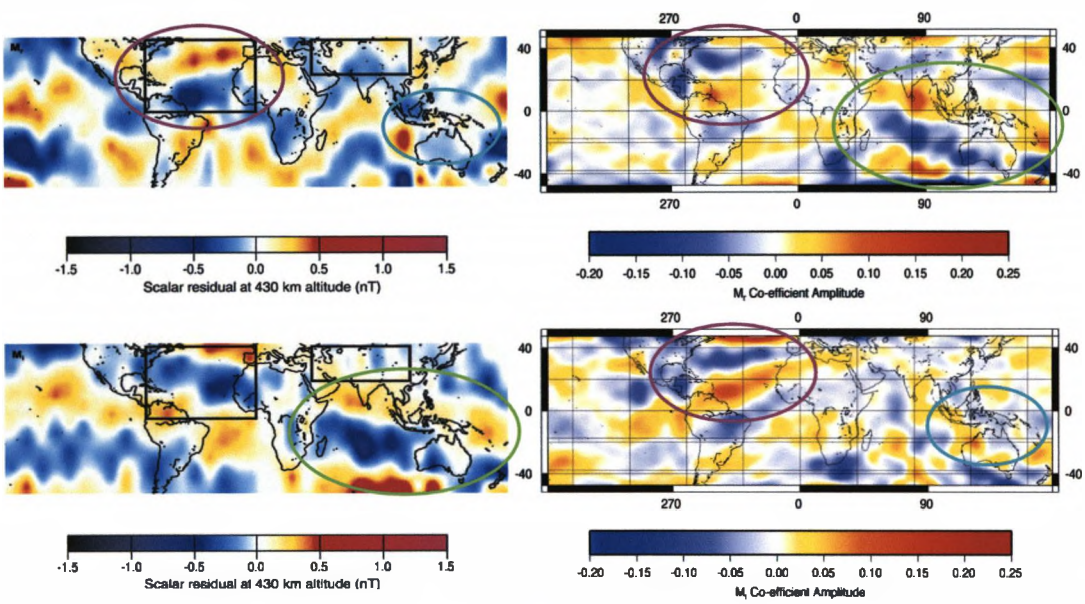

Figure 4.7: A comparison between the earlier results of Tyler et al. [2003] (left) and M2 tidal isolations (right), derived to spherical harmonic degree 30 (damping: 50) using CHAMP selected scalar observations. Expansions of M_r and M_i parameters are placed in the upper and lower rows respectively. Green, magenta and cyan ellipses identify similar spatial features found in both studies. Note that the black boxes shown in Tyler et al. [2003] should be ignored as they apply to an aspect of the Tyler et al. [2003] analysis that is not replicated here.

signal amplitudes are comparable, although this analysis consistently under-estimates those of Tyler et al. [2003] (possibly a consequence of more stringent selection criteria). However, the main similarity lies in the spatial scales of signals ($\sim 10^{o} \rightarrow 20^{o}$ in N-S direction), with the results of this analysis also exhibiting the mainly zonal structures identified by Tyler et al. [2003]. Specifically, the two studies show very similar spatial structure in three regions; the Pacific and North Atlantic oceans and over the Americas. However, while the studies seem comparable, the configurations of the M_r and M_i parameters in each case seem confused, a problem caused by the time zero used in each case. Time zero is the position within a time series that acts as the origin for the $(M_r)\cos(\omega t)$ and $(M_i)\sin(\omega t)$ functions (from equation 3.1) modelled in these

analyses. By changing the position of the time zero point, the harmonic content within analysis data can be shifted from one harmonic parameter to another, a process shown graphically in figure 4.8. As the time zero position used by Tyler et al. [2003] is

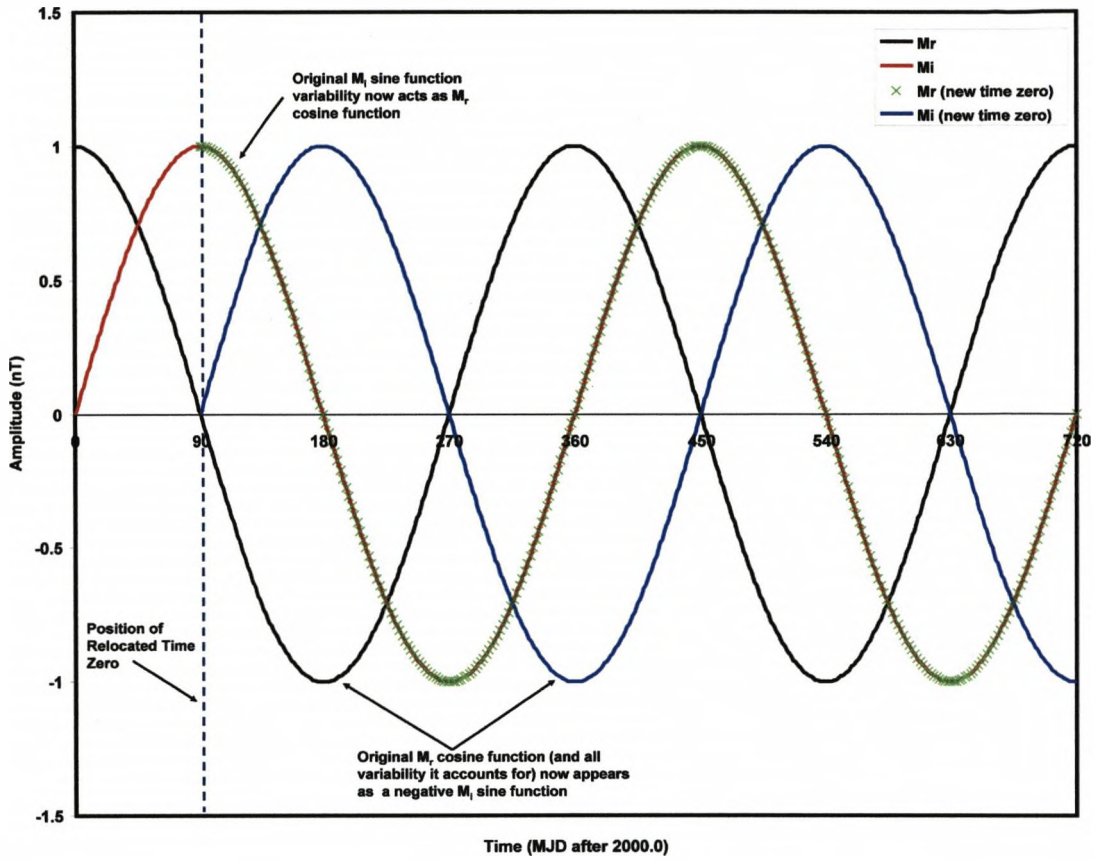

Figure 4.8: An illustration of the effect of time zero position in harmonic modelling.

unknown, the same point cannot be used here (note that while time zero position affects the detailed configuration of the M_r and M_i parameters, the total tidal field predicted remains constant, therefore for predictive purposes time zero position is unimportant). However, taking differences in time zero position into consideration, the large amount of comparability between the two analyses illustrates not only that the method used here is suitable for the investigation of ocean tides, but also validates the work of Tyler et al. [2003].

4.3.3 High Latitude Scalar Isolation

While tides are a well understood oceanic phenomena, understanding of their behaviour at the poles is severely limited, as sea ice restricts access to surface observations whilst also acting to screen satellite monitoring. This lack of understanding extends to geomagnetism where, although tidally generated magnetic fields are clearly identifiable at low latitudes, their identification towards the poles has never been attempted using magnetic observations.

analyses. By changing the position of the time zero point, the harmonic content within analysis data can be shifted from one harmonic parameter to another, a process shown graphically in figure 4.8. As the time zero position used by Tyler et al. [2003] is

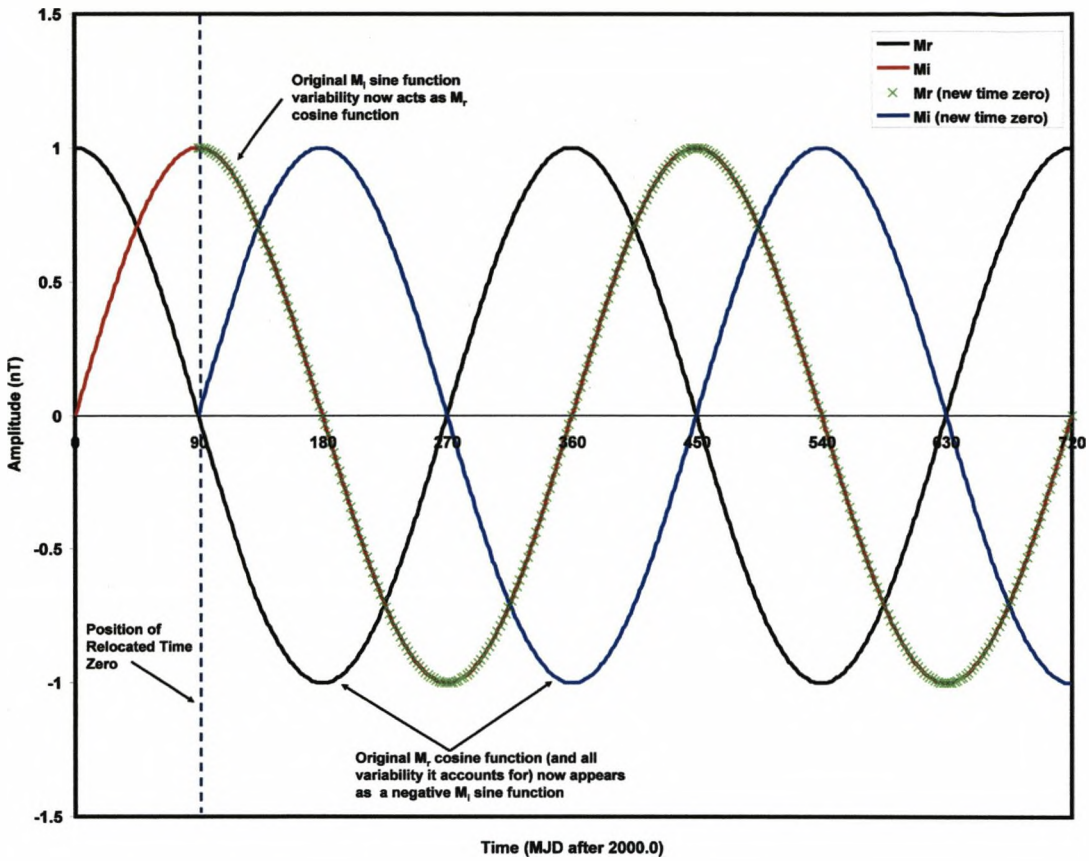

Figure 4.8: An illustration of the effect of time zero position in harmonic modelling.

unknown, the same point cannot be used here (note that while time zero position affects the detailed configuration of the M_r and M_i parameters, the total tidal field predicted remains constant, therefore for predictive purposes time zero position is unimportant). However, taking differences in time zero position into consideration, the large amount of comparability between the two analyses illustrates not only that the method used here is suitable for the investigation of ocean tides, but also validates the work of Tyler et al. [2003].

4.3.3 High Latitude Scalar Isolation

While tides are a well understood oceanic phenomena, understanding of their behaviour at the poles is severely limited, as sea ice restricts access to surface observations whilst also acting to screen satellite monitoring. This lack of understanding extends to geomagnetism where, although tidally generated magnetic fields are clearly identifiable at low latitudes, their identification towards the poles has never been attempted using magnetic observations.

This sub-section presents an attempt to identify polar tidal magnetic fields using the methodology identified in §4.3.1.

Specific Data Used and Ritter and Lühr [2004] Selection Criteria:

As in §4.3.2, this analysis uses scalar data from the CHAMP satellite and so is again limited to the investigation of tidal fields in the direction of the observations used. The CHAMP spacecraft is used as its low altitude means it is both close to the target source and at a distance from high altitude external fields, while scalar data is used as external fields have a tendency to affect vector measurements much more than scalar observations at high latitudes. Again, all observations follow the preparation guidelines established in chapter 2, in this case using CO2003 main field subtraction, together with along track filtering. The data selection employed is designed specifically with polar regions in mind (driven heavily by Ritter and Lühr [2004]), consisting of; Kp $\leq$ 2+, Dst/dt $\leq \pm$ 3.0 nT/hr, Interplanetary merging electric field $\leq \pm$ 0.8 V/m, Local time: 1800 hrs $\rightarrow$ 0600 hrs, Seasonal: October $\rightarrow$ March (N. Hemisphere) & April $\rightarrow$ September (S. Hemisphere), Latitude $\geq \pm 45^{\circ}$. As a final step, all remaining data are decimated, retaining the 15% of data with the lowest magnitudes.

Additional Modifications to Standard Methodology:

While data selection and reduction aim to reduce external effects, the result is a desperate lack of accepted data, with the $5^{\circ} \times 5^{\circ}$ discrete analysis cells used at low latitudes often containing insufficient data to obtain a stable solution (as cells are smaller at the poles). Therefore, latitude dependent data binning is implemented, with higher latitude cells having greater longitudinal extent. Figure 4.9 illustrates the distribution of the resulting cells across the northern hemisphere (note that cell distribution is identical in the southern hemisphere).

Results & Discussion:

The results of the analysis are shown in figure 4.10 (up to harmonic degree 30 with damping of 0.01), with the distribution of contributing cells displayed in figure 4.11. Note that green circles in figure 4.10 indicate the limit of validity of the solutions; beyond this line all fields should be considered with extreme caution (as they are unconstrained).

These solutions clearly show tidal signals with much higher amplitudes (often up to an order of magnitude) than at low latitudes. This, coupled with a lack of tidal field magnitude reduction around the southern pole when compared to the north (despite a reduced surface area of ocean here), suggests these high latitude tidal estimates are influenced to some extent by an alternate field source, most likely persistent external tidal fields. However, solutions show similar spatial scales to those at lower latitudes ($\sim 10^{\circ} \rightarrow 20^{\circ}$), suggesting signals may share a common source, while the effects of

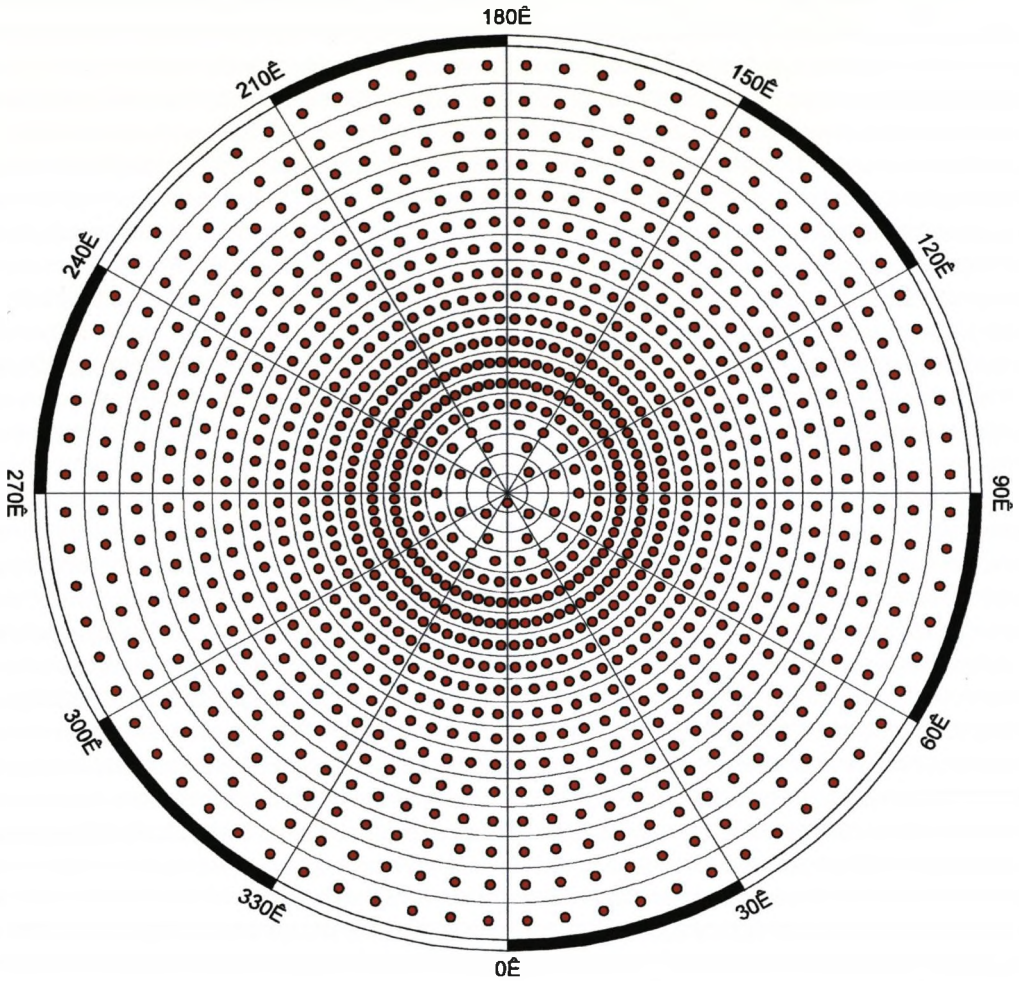

Figure 4.9: The latitude dependent cell distribution used to study high latitude tidal magnetic fields. Red dots represent cell centres, boundaries are placed half-way between neighbouring cell centres.

uneven cell distributions can also be seen, with the replacement of large scale consistent fields by unconstrained ringing that extends to lower latitudes. Spatial clarity also decreases towards the pole as a result of the latitude dependent binning employed, although without this step solutions may be of much poorer quality.

This section has presented preliminary investigations designed to test the validity of the harmonic modelling/spherical harmonic methodology and also investigate the ability of satellite magnetic data to resolve tidal fields in various locations around the globe. They have indicated that satellite magnetic data is perfectly capable of identifying tidal magnetic fields at both low and high latitudes (provided the correct data processing/selection precautions are taken), whilst also giving firm indications that the methodology used is sound and appropriate for further use. However, analysis of polar tides has indicated that while reasonable tidal isolation is achievable at high latitudes, the approach used here (strict data decimation and latitude dependent data binning) may not be appropriate for detailed investigation of

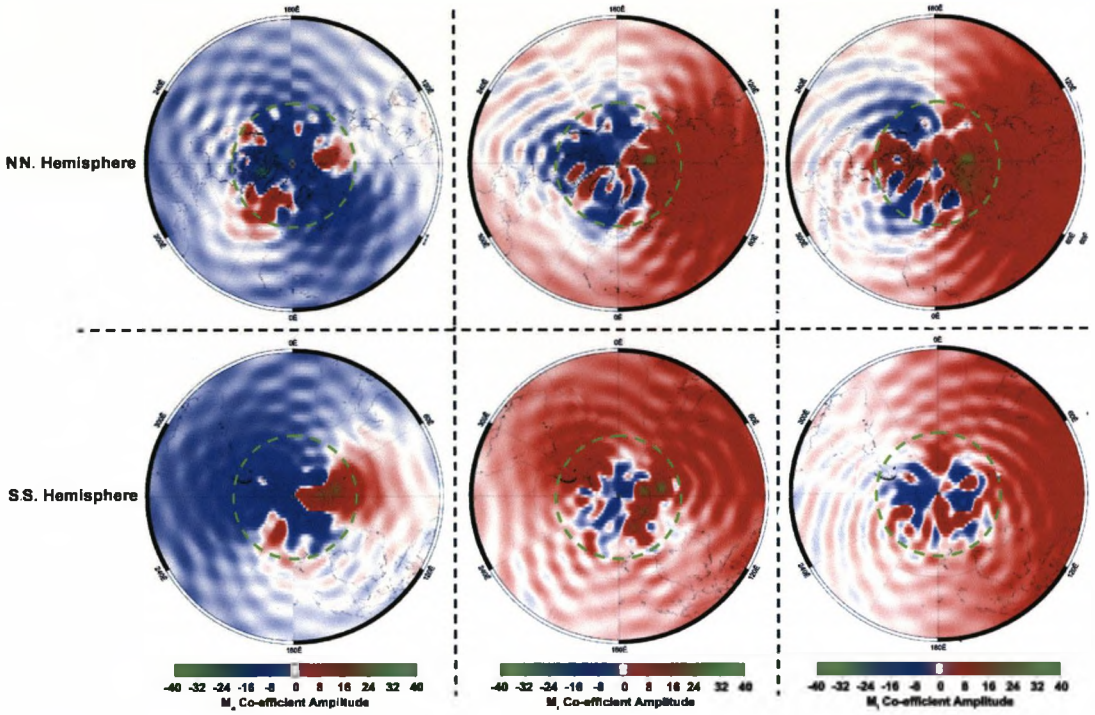

Figure 4.10: Spherical harmonic expansions of M2 north (upper row) and south (lower row) polar tides, derived using CHAMP selected scalar observations. Expansions of the M_o, M_r and M_i parameters are located in the left, centre and right columns respectively. Green dashed circles indicate the equator-ward limit of solution validity.

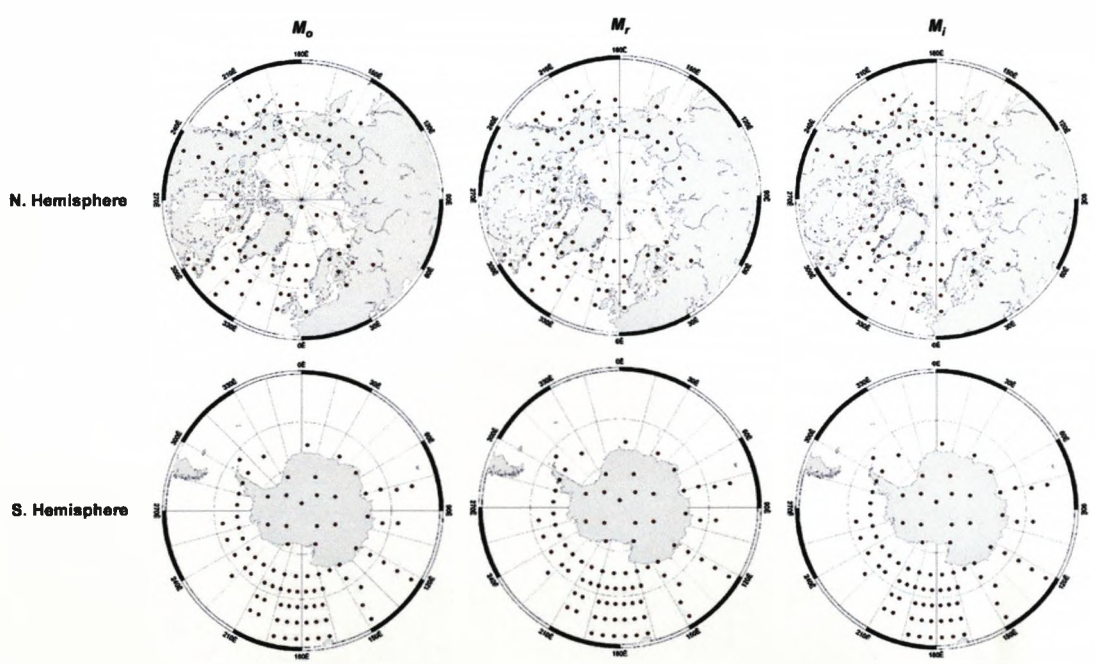

Figure 4.11: Cell distributions used to derive solutions shown in figure 4.10. Red dots indicate cell centres, boundaries lie half-way between neighbouring cell centres.

the polar regions. Therefore, the remainder of this chapter will focus on the progression of these analyses towards the derivation of a tidal vector magnetic field model.

4.4 Comprehensive, Vectorised Multi-Constituent Tidal Field Modelling

4.4.1 Integration of Multi-Constituent Tidal Behaviours Into a SHA Framework

While §4.3.2 & §4.3.3 implemented separate harmonic modelling and spherical harmonic expansion processing, this investigation fuses the two, replacing each of the model parameters in equation 3.1 with a set of spherical harmonics (equation 2.1), so that each tidal constituent is modelled as a pair of spherical harmonic series modulated by the frequency of the chosen tidal constituent, with an additional un-modulated series representing M_o. The resulting model formulation:

$$\begin{aligned}\mathbf{V}(\theta,\phi,r,t) = &\left(a\sum_{n=1}^{N}\sum_{m=0}^{n}(g_n^m\cos m\phi + h_n^m\sin m\phi)\left(\frac{a}{r}\right)^{n+1}P_n^m(\cos\theta)\right) + \\ &\left(a\sum_{n=1}^{N}\sum_{m=0}^{n}(k_n^m\cos m\phi + l_n^m\sin m\phi)\left(\frac{a}{r}\right)^{n+1}P_n^m(\cos\theta)\right)\cos(\omega_{M2}t) + \\ &\left(a\sum_{n=1}^{N}\sum_{m=0}^{n}(s_n^m\cos m\phi + q_n^m\sin m\phi)\left(\frac{a}{r}\right)^{n+1}P_n^m(\cos\theta)\right)\sin(\omega_{M2}t) + \end{aligned} \quad (4.2)$$

is solved using generalised least squares inversion. In this case, a scalar potential $\mathbf{V}$ is represented as the sum of individual potential fields, each consisting of a series of spherical harmonics, where g_n^m, h_n^m, k_n^m, l_n^m, s_n^m, and q_n^m are the gauss co-efficients to be found, a and t are Earth's radius and time, while r, θ and ϕ are geocentric spherical co-ordinates altitude, co-latitude and longitude respectively. ω (in this case denoted $M2$) is the tidal frequency of the constituent being modelled and P_n^m is the associated Legendre polynomial at degree n and order m, up to a truncation degree N. Advantages of this approach are three-fold; firstly, the positional averaging assumptions involved previously are removed, as each observation is included in the modelling framework individually, removing the need for discrete cells where all data are assumed positionally coincident. Secondly, the framework allows the inclusion of numerous data sources, as the spherical harmonic expansions used allow for radial variability. Finally, the method also allows for the inclusion of an infinite number of tidal constituents in a single inversion, with the addition of extra spherical harmonic series to equation 4.2 (although testing that is not shown here has suggested correlations between constituents are minimal and so in most cases tidal constituents can be modelled individually), and so this investigation presents a model of most major tidal constituents. Unfortunately, this method

does not account for temporal variability in tidal amplitude, something which may need to be addressed in the future.

4.4.2 Model Data & Additional Processing

Unlike previously, both scalar and vector data from all three magnetic satellites (SAC-C scalar: 2001 $\rightarrow$ 2004, CHAMP scalar and vector: 2001 $\rightarrow$ 2005, Ørsted scalar and vector: 1999 $\rightarrow$ 2005) are used in this analysis. Note that to reduce external field effects, scalar data are used above $\pm 60^{o}$ magnetic latitude; vector observations are used at magnetic latitudes below $\pm 60^{o}$. As before, all observations are processed according to chapter 2, although on this occasion CHAOS main field subtraction replaces CO2003 (as CHAOS produces field predictions to a much higher harmonic degree than CO2003, while external field parameterisation is also more sophisticated in CHAOS) and data are not along track filtered (as filter estimates will instead be used as data errors in the final tidal field model). Data selection is also changed slightly, using the criteria; Kp $\leq$4+ (at magnetic latitudes $\leq \pm 60^{o}$), Dst/dt $\leq \pm$ 3.0 nT/hr (at all latitudes), Interplanetary merging electric field $\leq$ 0.8 V/m (at magnetic latitudes $\geq \pm 60^{o}$), Local time: 1800 hrs $\rightarrow$ 0600 hrs and seasonal: local winter (October $\rightarrow$ March in N. hemisphere, April $\rightarrow$ September in S. hemisphere). Following selection, observations are re-sampled from 1 second to 1 minute to make input data volumes more manageable (1 minute sampling should be sufficient to model variations on tidal time scales). As a result $\sim$ 125,000 scalar observations and $\sim$ 880,000 vector triplets are used in the final model inversion.

However, the inclusion of any scalar observations introduces a non-linearity into the inversion (due to a lack of directional information) and so the solution must be obtained iteratively. While this iterative approach is technically sound, in practise it is inefficient, so an alternative means of treating scalar observations was sought. The solution was the re-configuration of scalar observations into vector triplets using CHAOS main field model predictions as a guide. The process, shown graphically in figure 4.12, involves using a unit vector generated from vector predictions of a scalar observation (provided by the CHAOS main field model) to transform the scalar observation into a vector triplet, linearising the model inversion and vastly improving inversion efficiency. The justification for this approach is based around the concept that the scalar residuals used as input data during this modelling process represent the component of the vector field residual that lies in the direction of the main field. As a result, scalar residuals lie in a direction parallel to the scalar observations from which they are derived. Therefore, a scalar residual can be transformed into its X, Y, & Z vector components by multiplying with a unit vector describing the directional properties of the initial scalar observation. In this instance, field direction estimates from the CHAOS main field model are considered accurate enough to provide a directional representation of each scalar observation, which can be used to produce a unit vector that describes the scalar observation's directional orientation. As each scalar residual lies in a direction parallel to that of its

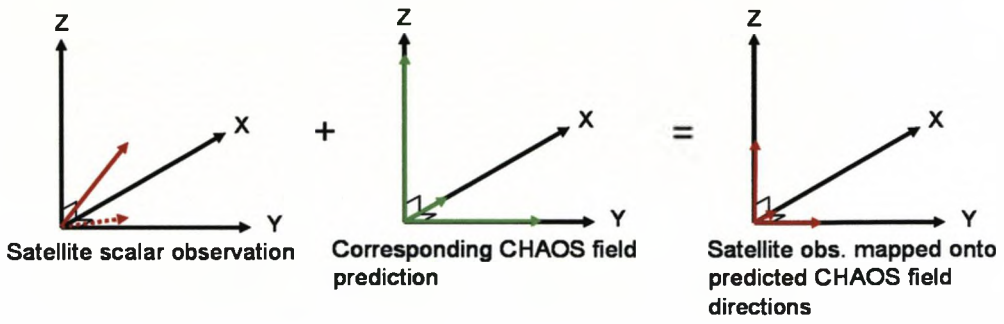

Figure 4.12: Images graphically illustrating the transformation of scalar observations into vector triplets, using CHAOS vector field predictions as a directional guide.

parent observation (according to the justification above), the unit vector describing observation direction also describes the direction of its scalar residual, allowing its decomposition into vector components (as shown in figure 4.12) prior to its use during this modelling effort.

4.4.3 Comprehensive Data Error Estimates

In any field modelling exercise, error estimates are essential, to act as both data uncertainties and weighting in the model inversion. In this case, three error estimates are used:

Standard Data Uncertainties:

A simple uncertainty of 3.0 nT is added to each component of every vector triplet. The error is isotropic and uncorrelated with both other vector components within the observation and with other observations. This uncertainty was initially derived as a latitude dependent error (calculated using the r.m.s of all data within a 5^{o} magnetic latitude band), although with the introduction of along track filtering as an error, this was no longer needed and so was replaced with an error that ensures that all observations are linked to some form of uncertainty (as all other error estimates can equal zero).

Along Track Filter Estimates:

Throughout this thesis along track filtering (§2.2.2) has proved an invaluable tool in reducing the influence of magnetospheric fields in analysis data. While in most cases (§4.3 included) this approach is sufficient, this is not the situation here due to the method's inability to distinguish between field contributions from various field sources. This means that in scenarios where the isolation of full field contributions are required, as is the case here, the subtraction of along track filters is not appropriate, as tidal contributions can be removed from data. To still use filter estimates in some form, this analysis instead implements along track filtering as a model error (typically ranging between 1-20 nT). In this way, filter estimates do not directly affect model data, but

can still have an influence, down weighting any vector component of an observation that has a particularly strong corresponding filter estimate. In this way the effects of unmodelled magnetospheric fields can in some way be controlled, while the resulting tidal field model retains a full tidal contribution.

Attitude Error:

The final model error takes the form of an attitude uncertainty that attempts to account for uncertainties in satellite orientation (determined by the on-board star camera(s)), as small errors in the orientation of the satellite translate into observations when they are converted from a spacecraft reference frame into spherical or NEC co-ordinates. The errors associated with satellite attitude are ψ, the angular uncertainty of a star camera's bore-sight direction and χ, the rotational uncertainty of the bore-sight about its axis. The positions of these uncertainties can be seen more clearly in figure 4.13. Note that the size of χ and ψ vary depending on the number of operational star

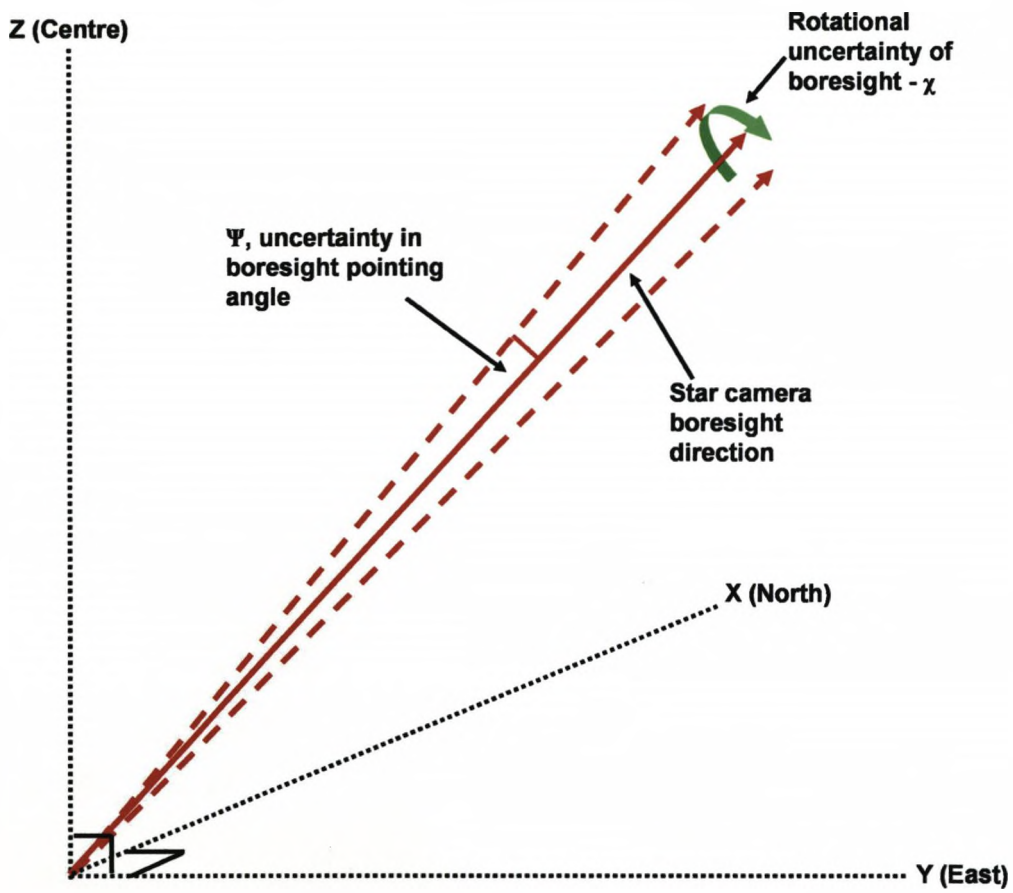

Figure 4.13: A schematic illustration of the angular arrangement of attitude errors ψ and χ around the bore-sight of a star camera on board a magnetic satellite.

cameras (as more star cameras reduce attitude uncertainty), meaning that χ and ψ vary between satellites and throughout their operational lifetime. While ψ remains constant with a value of 10 arcsecs, χ varies between 10 and 60 arcsecs (these values

of ψ and χ are only applicable to true vector data), with these angular uncertainties being converted into data errors by combining ψ and χ with the magnitude of the main geomagnetic field, producing final attitude errors ranging from $\sim$ 1 - 15 nT. Note that high latitude observations, obtained using the scalar to vector transformation shown in figure 4.12 are down weighted using large attitude errors (ψ and χ are both set to 10^{o}) to counteract the influence of any high amplitude external fields, and uncertainties in the CHAOS field model used during transformation. Importantly, attitude errors are correlated between vector components, although are still assumed uncorrelated with other observations. More details on attitude errors and their integration into a geomagnetic field modelling framework can be found in Holme and Bloxham [1996] & Holme [2000].

While error estimates are important, their integration into an existing modelling framework is crucial. For this investigation, a 3 $\times$ 3 error covariance matrix is constructed for each observation. Once all input data are considered, the final covariance matrix consists of a 3 $\times$ 3 block diagonal matrix (on account of the uncorrelated nature of errors between observations) $\mathbf{C_e^{-1}}$ which is integrated into equation 3.3 to form a new model formulation;

$$\left(\mathbf{A^T C_e^{-1} A}\right)^{-1} . \mathbf{A^T C_e^{-1}} \gamma = \mathbf{m} \tag{4.3}$$

where the variables $\mathbf{A}$, $\mathbf{A^T}$, γ and $\mathbf{m}$ are as in equation 3.3, but have new assignments;

$$\mathbf{m} = \begin{pmatrix} g_1^0 \\ g_1^1 \\ h_1^1 \\ \vdots \\ g_n^m \\ h_n^m \\ k_1^0 \\ k_1^1 \\ l_1^1 \\ \vdots \\ s_1^0 \\ s_1^1 \\ q_1^1 \\ \vdots \\ s_n^m \\ q_n^m \end{pmatrix}$$

$$\gamma_i = \begin{pmatrix} M_x(t_i) \\ M_y(t_i) \\ M_z(t_i) \end{pmatrix}$$

$$\mathbf{A_i^T} = \begin{pmatrix} X_{(1,0)}, & Y_{(1,0)}, & Z_{(1,0)} \\ X^g_{(1,1)}, & Y^g_{(1,1)}, & Z^g_{(1,1)} \\ X^h_{(1,1)}, & Y^h_{(1,1)}, & Z^h_{(1,1)} \\ \vdots & \vdots & \vdots \\ X_{(n,0)}, & Y_{(n,0)}, & Z_{(n,0)} \\ X^g_{(n,m)}, & Y^g_{(n,m)}, & Z^g_{(n,m)} \\ X^h_{(n,m)}, & Y^h_{(n,m)}, & Z^h_{(n,m)} \\ X_{(1,0)} \cos(\omega_{M2} t_i), & Y_{(1,0)} \cos(\omega_{M2} t_i), & Z_{(1,0)} \cos(\omega_{M2} t_i) \\ X^g_{(1,1)} \cos(\omega_{M2} t_i), & Y^g_{(1,1)} \cos(\omega_{M2} t_i), & Z^g_{(1,1)} \cos(\omega_{M2} t_i) \\ X^h_{(1,1)} \cos(\omega_{M2} t_i), & Y^h_{(1,1)} \cos(\omega_{M2} t_i), & Z^h_{(1,1)} \cos(\omega_{M2} t_i) \\ \vdots & \vdots & \vdots \\ X_{(n,0)} \cos(\omega_{M2} t_i), & Y_{(n,0)} \cos(\omega_{M2} t_i), & Z_{(n,0)} \cos(\omega_{M2} t_i) \\ X^g_{(n,m)} \cos(\omega_{M2} t_i), & Y^g_{(n,m)} \cos(\omega_{M2} t_i), & Z^g_{(n,m)} \cos(\omega_{M2} t_i) \\ X^h_{(n,m)} \cos(\omega_{M2} t_i), & Y^h_{(n,m)} \cos(\omega_{M2} t_i), & Z^h_{(n,m)} \cos(\omega_{M2} t_i) \\ X_{(1,0)} \sin(\omega_{M2} t_i), & Y_{(1,0)} \sin(\omega_{M2} t_i), & Z_{(1,0)} \sin(\omega_{M2} t_i) \\ X^g_{(1,1)} \sin(\omega_{M2} t_i), & Y^g_{(1,1)} \sin(\omega_{M2} t_i), & Z^g_{(1,1)} \sin(\omega_{M2} t_i) \\ X^h_{(1,1)} \sin(\omega_{M2} t_i), & Y^h_{(1,1)} \sin(\omega_{M2} t_i), & Z^h_{(1,1)} \sin(\omega_{M2} t_i) \\ \vdots & \vdots & \vdots \\ X_{(n,0)} \sin(\omega_{M2} t_i), & Y_{(n,0)} \sin(\omega_{M2} t_i), & Z_{(n,0)} \sin(\omega_{M2} t_i) \\ X^g_{(n,m)} \sin(\omega_{M2} t_i), & Y^g_{(n,m)} \sin(\omega_{M2} t_i), & Z^g_{(n,m)} \sin(\omega_{M2} t_i) \\ X^h_{(n,m)} \sin(\omega_{M2} t_i), & Y^h_{(n,m)} \sin(\omega_{M2} t_i), & Z^h_{(n,m)} \sin(\omega_{M2} t_i) \end{pmatrix}$$

where g_n^m, h_n^m, k_n^m, l_n^m, s_n^m and q_n^m are the gauss co-efficients to be found, M_x, M_y and M_z are vector components of a vector observation and the subscripted ω are the frequencies of the target tidal constituents. Note that in this instance, the configuration of $\mathbf{A^T}$ is shown instead of $\mathbf{A}$ as the orientation of $\mathbf{A}$ does not allow for the full matrix to be shown, while constants $X_{(1,0)}$, $X^g_{(1,1)}$, $X^h_{(1,1)}$, $X_{(n,0)}$, $X^g_{(n,m)}$, $X^h_{(n,m)}$, $Y_{(1,0)}$, $Y^g_{(1,1)}$, $Y^h_{(1,1)}$, $Y_{(n,0)}$, $Y^g_{(n,m)}$, $Y^h_{(n,m)}$, $Z_{(1,0)}$, $Z^g_{(1,1)}$, $Z^h_{(1,1)}$, $Z_{(n,0)}$, $Z^g_{(n,m)}$ and $Z^h_{(n,m)}$ represent how the various vector components of an observation (X, Y, & Z) relate to the scalar potential ($\mathbf{V}$) from equation 4.2;

$$\begin{aligned}
X_{(1,0)} &= \left(\frac{a}{r}\right)^3 \delta_\theta P_1^0(\cos\theta) && \Rightarrow X_{(n,0)} = \left(\frac{a}{r}\right)^{n+2} \delta_\theta P_n^0(\cos\theta) \\
X^g_{(1,1)} &= \cos(\phi)\left(\frac{a}{r}\right)^3 \delta_\theta P_1^1(\cos\theta) && \Rightarrow X^g_{(n,m)} = \cos(m\phi)\left(\frac{a}{r}\right)^{n+2} \delta_\theta P_n^m(\cos\theta) \\
X^h_{(1,1)} &= \sin(\phi)\left(\frac{a}{r}\right)^3 \delta_\theta P_1^1(\cos\theta) && \Rightarrow X^h_{(n,m)} = \sin(m\phi)\left(\frac{a}{r}\right)^{n+2} \delta_\theta P_n^m(\cos\theta) \\
Y_{(1,0)} &= 0 && \Rightarrow Y_{(n,0)} = 0 \\
Y^g_{(1,1)} &= \frac{\sin(\phi)\left(\frac{a}{r}\right)^3 P_1^1(\cos\theta)}{\sin\theta} && \Rightarrow Y^g_{(n,m)} = \frac{\sin(m\phi)\, m \left(\frac{a}{r}\right)^{n+2} P_n^m(\cos\theta)}{\sin\theta} \\
Y^h_{(1,1)} &= \frac{-\cos(\phi)\left(\frac{a}{r}\right)^3 P_1^1(\cos\theta)}{\sin\theta} && \Rightarrow Y^h_{(n,m)} = \frac{-\cos(m\phi)\, m \left(\frac{a}{r}\right)^{n+2} P_n^m(\cos\theta)}{\sin\theta} \\
Z_{(1,0)} &= -2\left(\frac{a}{r}\right)^3 P_1^0(\cos\theta) && \Rightarrow Z_{(n,0)} = -(n+1)\left(\frac{a}{r}\right)^{n+2} P_n^0(\cos\theta) \\
Z^g_{(1,1)} &= -2\cos(\phi)\left(\frac{a}{r}\right)^3 P_1^1(\cos\theta) && \Rightarrow Z^g_{(n,m)} = -(n+1)\cos(m\phi)\left(\frac{a}{r}\right)^{n+2} P_n^m(\cos\theta) \\
Z^h_{(1,1)} &= -2\sin(\phi)\left(\frac{a}{r}\right)^3 P_1^1(\cos\theta) && \Rightarrow Z^h_{(n,m)} = -(n+1)\sin(m\phi)\left(\frac{a}{r}\right)^{n+2} P_n^m(\cos\theta)
\end{aligned}$$

where a, r, θ, ϕ, n and m represent Earth radius, observation radius (altitude plus Earth radius), co-latitude, longitude and spherical harmonic degree & order respectively. Legendre functions (present elsewhere in equation 4.2) and their derivatives (with respect to co-latitude θ) are also included in the form of P and $\delta_\theta P$ respectively. Finally, error covariance matrix $\mathbf{C_e^{-1}}$ (in invariant form) is structured as;

$$\mathbf{C_e^{-1}} = \left[\mathbf{I}\left(\sigma^2 + \mathbf{B}^2\psi^2\right)\right] - \left[\mathbf{B}\mathbf{B}^{\mathbf{T}}\psi^2\right] + \left[\left(\chi^2 - \psi^2\right)\left(\hat{\mathbf{n}} \wedge \mathbf{B}\right)\left(\hat{\mathbf{n}} \wedge \mathbf{B}\right)^{\mathbf{T}}\right] + \left[\mathbf{B_e}\mathbf{B_e^T}\right] \quad (4.4)$$

where $\mathbf{I}$ is the identity matrix, $\mathbf{B}$ is the main geomagnetic field (as predicted by CHAOS), $\hat{\mathbf{n}}$ is a unit vector describing satellite attitude at the time of observation, σ^2 are the relevant isotropic data uncertainties, $\mathbf{B_e}$ is a vector of along track filter values and ψ and χ are the associated attitude errors, and excluding ψ and χ have the following assignments:

$$\mathbf{I} = \begin{pmatrix} 1 & 0 & 0 \\ 0 & 1 & 0 \\ 0 & 0 & 1 \end{pmatrix}$$

$$\mathbf{B} = \begin{pmatrix} B_x \\ B_y \\ B_z \end{pmatrix}$$

$$\hat{\mathbf{n}} = \begin{pmatrix} \hat{x} \\ \hat{y} \\ \hat{z} \end{pmatrix}$$

$$\sigma^2 = \begin{pmatrix} \sigma_x^2 \\ \sigma_y^2 \\ \sigma_z^2 \end{pmatrix}$$

$$\mathbf{B_e} = \begin{pmatrix} B_{ex} \\ B_{ey} \\ B_{ez} \end{pmatrix}$$

Solving this system of equations using generalised least squares inversion, model solutions shown in the following sub-section are found.

4.4.4 Model Predictions and Validation Against Previous Work

The first model results shown are those generated specifically to be compared with the work of Tyler et al. [2003] and are shown in figure 4.14 with corresponding power spectra shown in figure 4.15. Note that these solutions have been derived using along track filters as values to subtract from observations prior to modelling rather than as a model error and so are used to illustrate that the model framework, vector input data and other error estimates being used function properly. These models clearly show similar spatial features to those of Tyler et al. [2003] (in a similar manner to those in §4.3.2), particularly over the Indian/Southern

oceans, the Americas and the Northern Atlantic ocean, suggesting comparability between the two studies. However, while an earlier comparison (§4.3.2) consistently underestimated tidal amplitudes, here amplitudes are much higher and appear to be in line with those published previously, suggesting the lack of positional assumptions and rigorous error estimates used here may make this approach superior to the methodology outlined in §4.3.1 (when considering filtered tidal estimates). The lack of high degree power in spectra (figure 4.15) also suggests good model stability.

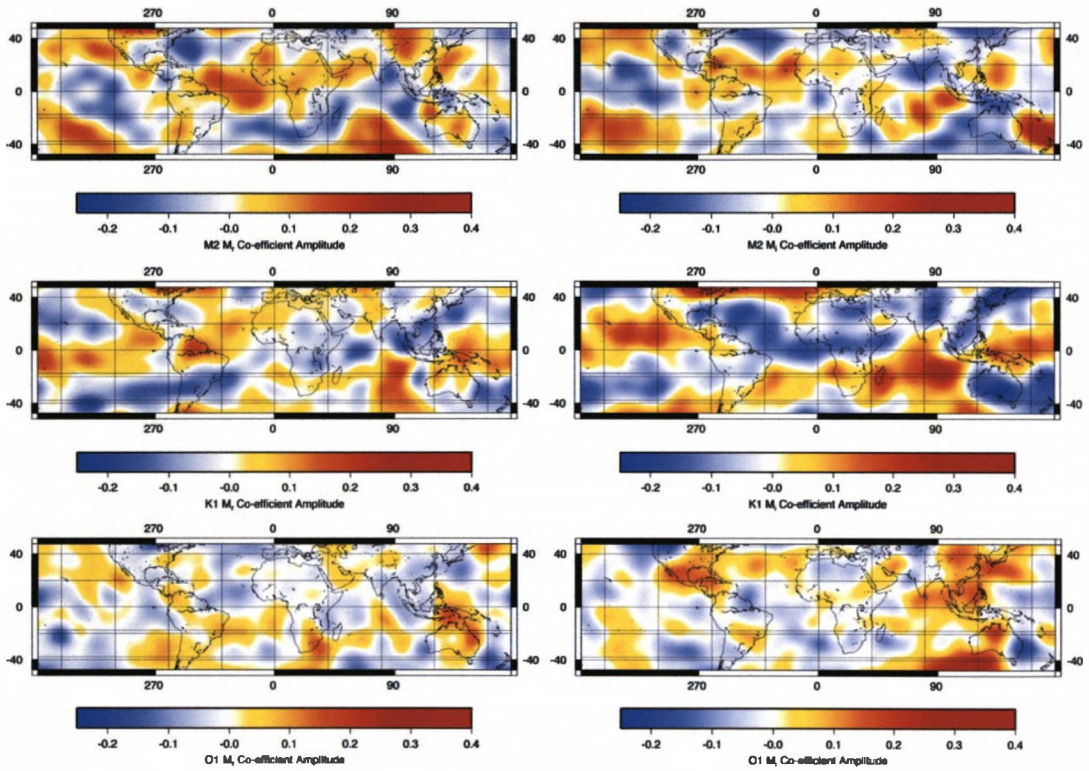

Figure 4.14: Model results (derived to harmonic degree 20 using a damping of 3.0) of M2 (upper row), K1 (centre row) and O1 (lower row) tidal constituents, generated using along track filtering as prescribed in chapter 2. Images corresponding to the M_r and M_i parameters from equation 3.1 are located in left and right hand columns respectively. Note that due to incompatible time zero points, M2 models shown cannot be directly compared with similar images from Tyler et al. [2003].

While comparisons with filtered fields are a useful tool, to fully investigate this model's potential it must be validated in its unfiltered form. Unfortunately, no magnetic studies are available for such comparisons and so numerically derived solutions are used instead. However, as most numerical solutions are accompanied by filtered observations, only two suitable validation targets were found, with each being addressed here. All solutions presented from this point are solved to spherical harmonic degree 30, with a damping parameter of 100.0.

Kuvshinov and Olsen [2005] (figures 4.16, 4.17 & 4.18):

Inspecting these comparative figures of M2, O1 and K1 tidal constituents (once again

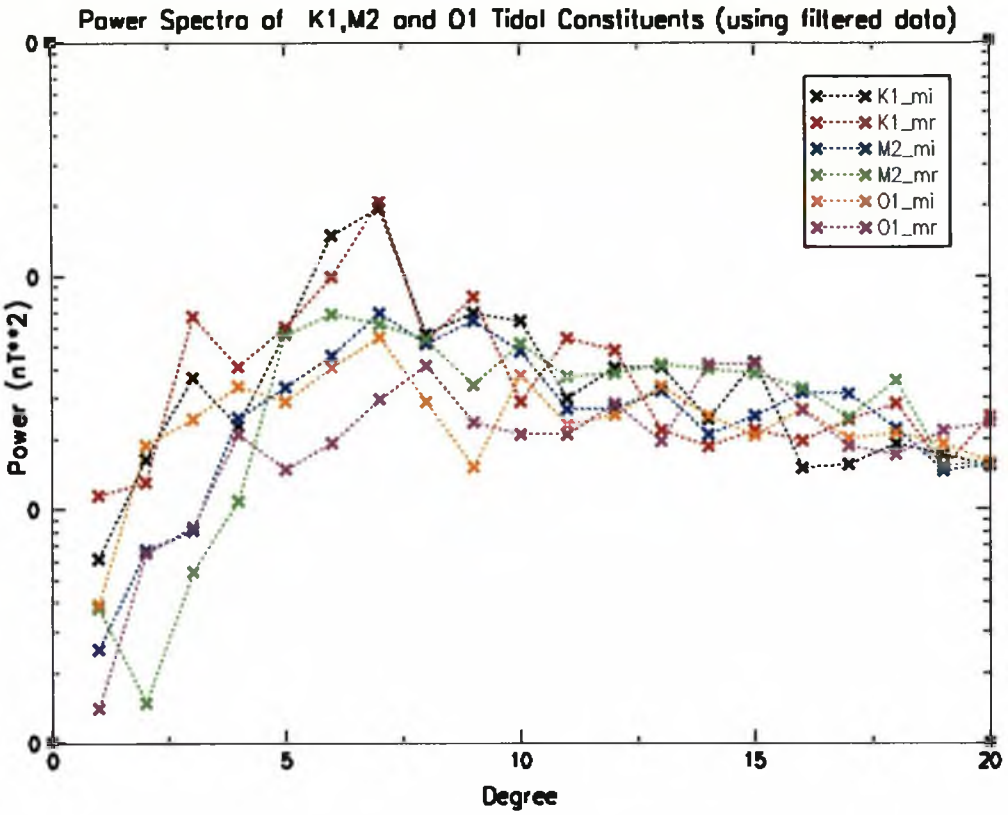

Figure 4.15: Power spectra of tidal models shown in figure 4.14.

projected as scalar anomalies in the direction of the main field) it is clear that few similarities exist between the numerical and observational solutions shown. Unfortunately, while M2 amplitudes are comparable, those of K1 and O1 are far higher than those derived numerically. Indeed no similarities can be seen in the K1 constituent, while both M2 and O1 show only minor spatial similarities (zonal Atlantic striping in M2 and consistently high positive amplitudes around South and East Australia in O1 M_i). However, the clear feature in these figures is the substantially higher levels of small scale noise present in observational solutions, with the presence of persistent high amplitude external signals being a likely explanation, as several anomalously high amplitude data points without adequate error estimates could easily introduce high amplitude, short wavelength variability into model solutions. Unfortunately, very few estimates of external tidal fields are available to verify this conclusion, with the work of Malin [1973] & McKnight [1995] suggesting M2 ionospheric tidal field estimates of 1 -5 nT, although these estimates are at ground level (observatories).

Maus and Kuvshinov [2004] (figures 4.19 & 4.20):

While model validations within the region of constraint are essential, it is interesting to investigate the behaviour of the model in unconstrained regions. Figures 4.19 & 4.20 display solutions of the radial field magnitude $\left(\sqrt{M_r^2 + M_i^2}\right)$ of M2, P1, N2, O1 and K1

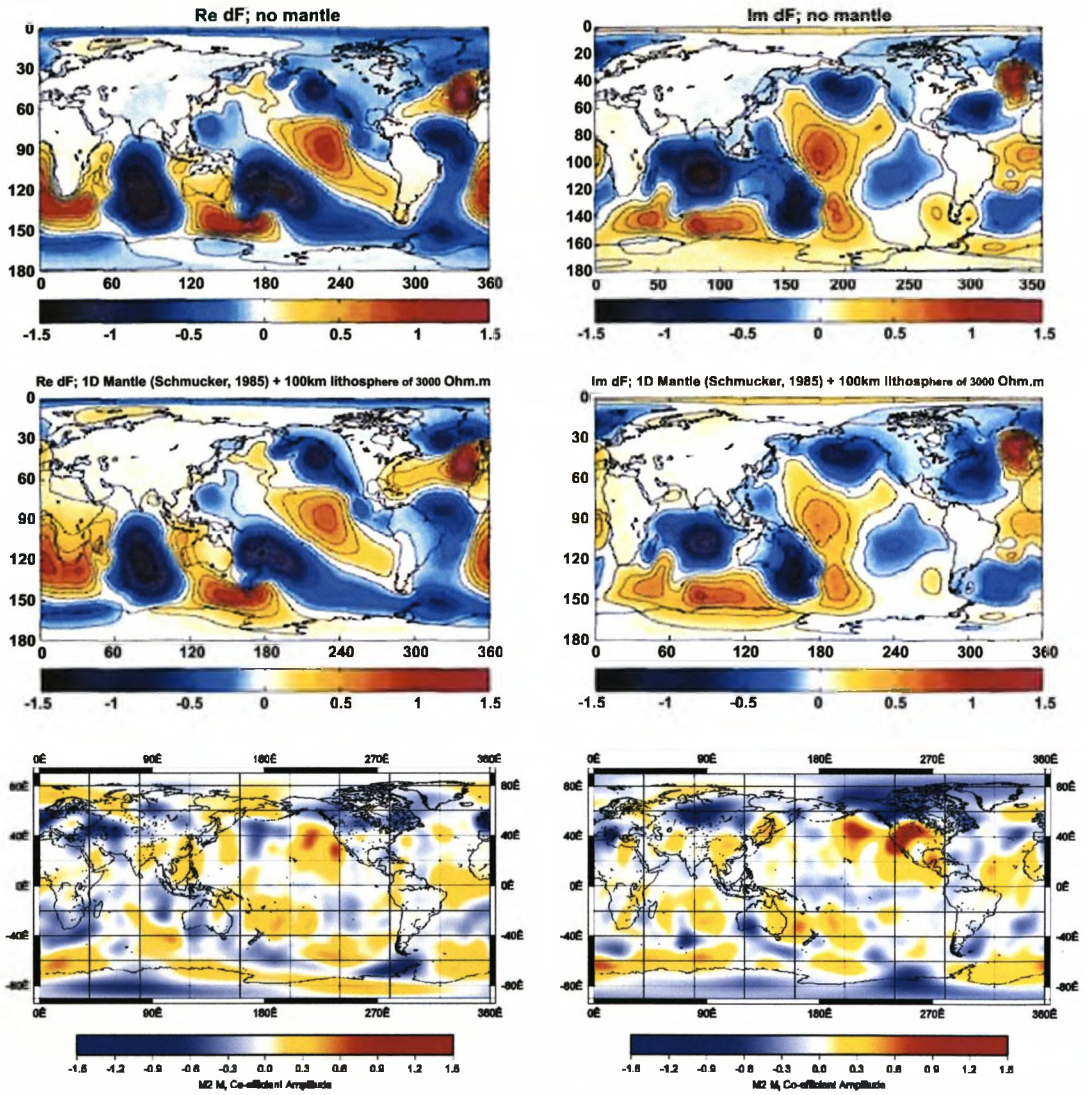

Figure 4.16: A comparison between numerical tidal predictions of the M2 tidal constituent from Kuvshinov and Olsen [2005] (upper 2 rows) and an equivalent from the model derived as part of this investigation (bottom row). M_r and M_i (or equivalent) parameters are shown in the left and right columns respectively, and all predictions are made at an altitude of 430 km. Note that Kuvshinov and Olsen [2005] predictions in the upper row are made assuming an insulating mantle while those in the centre row are made using a conducting mantle.

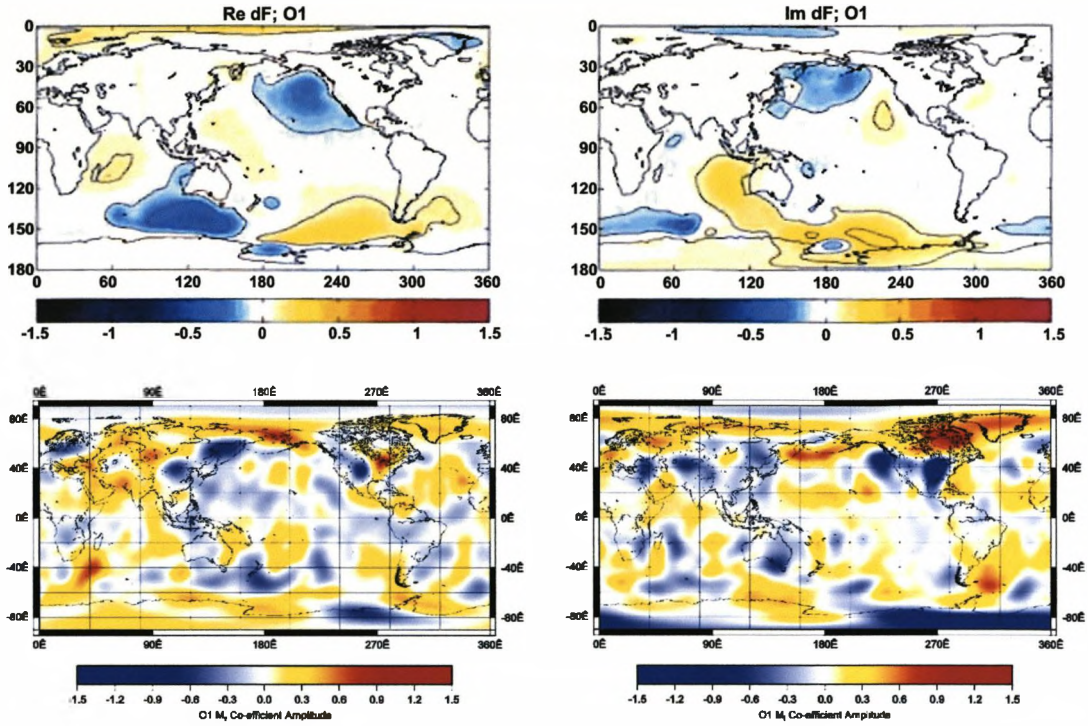

Figure 4.17: A comparison between numerical tidal predictions of the O1 tidal constituent from Kuvshinov and Olsen [2005] (upper row) and an equivalent from the model derived as part of this investigation (bottom row). M_r and M_i (or equivalent) parameters are shown in the left and right columns respectively. Note that all predictions are made at an altitude of 430 km.

tidal constituents at ground level, using both numerical (Maus and Kuvshinov [2004]) and observational (this model) solutions. Comparing the two, the radial stability of this model can be tested in a region not constrained by current volumes of model data. It is clear immediately that the observational solutions are unconstrained here, as all constituents suffer from highly overestimated tidal magnitudes and excessive amounts of small scale noise and ringing (assuming that the oceanically driven numerical estimates they are compared to are correct). Indeed the only similarity found is a zonal patch of amplitude along the Pacific equator in both P1 and K1 solutions, although even this spatial similarity suffers from an inflated magnitude. However, given that model solutions are controlled solely by observations, the highly variable solutions in figure 4.20 are no surprise when no ground observations are included in the current modelling effort.

These simple validation exercises have highlighted that while comparisons with studies conducted in a filtered environment are generally good and that this model represents a step forward in tidal field prediction, it is certainly not prefect. Therefore, future iterations of the model would appear to need more stringent data processing and improved error estimates to further reduce the influence of external tidal fields, while low altitude/ground observatory

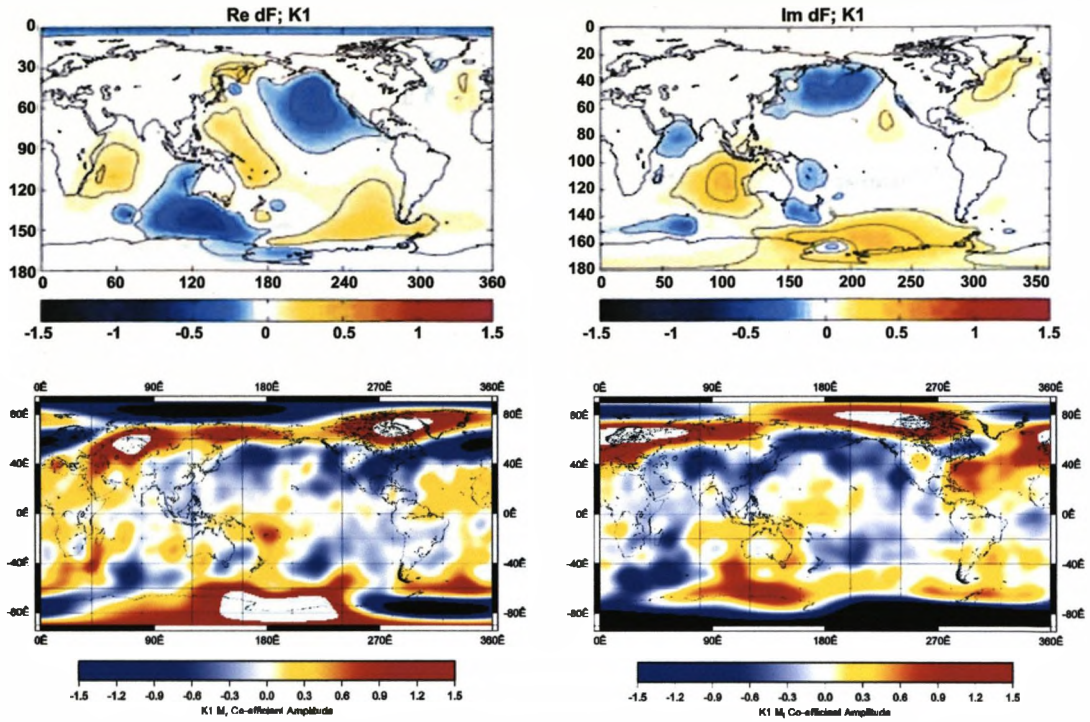

Figure 4.18: A comparison between numerical tidal predictions of the K1 tidal constituent from Kuvshinov and Olsen [2005] (upper row) and an equivalent from the model derived as part of this investigation (bottom row). M_r and M_i (or equivalent) parameters are shown in the left and right columns respectively. Note that all predictions are made at an altitude of 430 km.

data must be included in future volumes of model data to improve radial model stability and prediction accuracy.

4.5 Discussion

The various analyses presented in this chapter have attempted to extend the previous work of others (Tyler et al. [2003], Maus and Kuvshinov [2004]) in an effort to expand the understanding of tidal magnetic fields around the globe. However, while comparison with the work of Tyler et al. [2003] suggested that harmonic modelling was an adequate way of studying tidal fields, at high latitudes the influence of external tidal fields on oceanic tidal field isolation was clear (figure 4.10). Also, the methodology did not appear to have sufficient resolution to resolve tidal signals at the poles in a satisfactory manner. Therefore, an improved modelling method has been employed, that removes the restriction of resolution entirely, whilst also accounting for data uncertainties, both technical and physical (i.e., external tidal field) in a more sophisticated manner. However, while the resulting model has succeeded in producing tidal magnetic fields that agree more closely with Tyler et al. [2003] and appears to have made a significant step forward in terms of tidal modelling, when compared with numerical equivalents very little coherence is seen, with high volumes of small scale variability (when

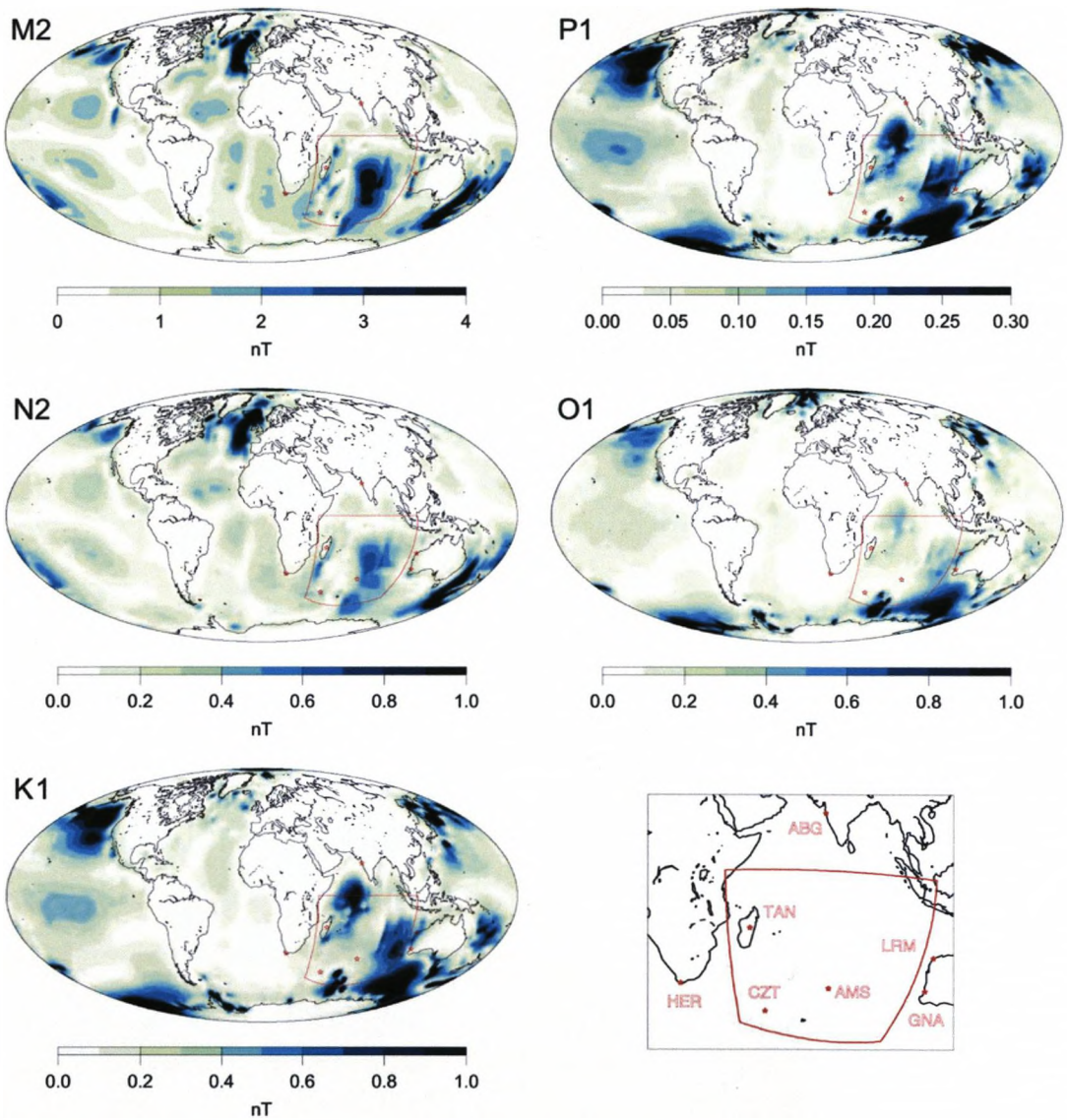

Figure 4.19: Numerical predictions of the radial tidal field magnitude (at ground level) of M2, P1, N2, O1 and K1 tidal constituents made by Maus and Kuvshinov [2004].

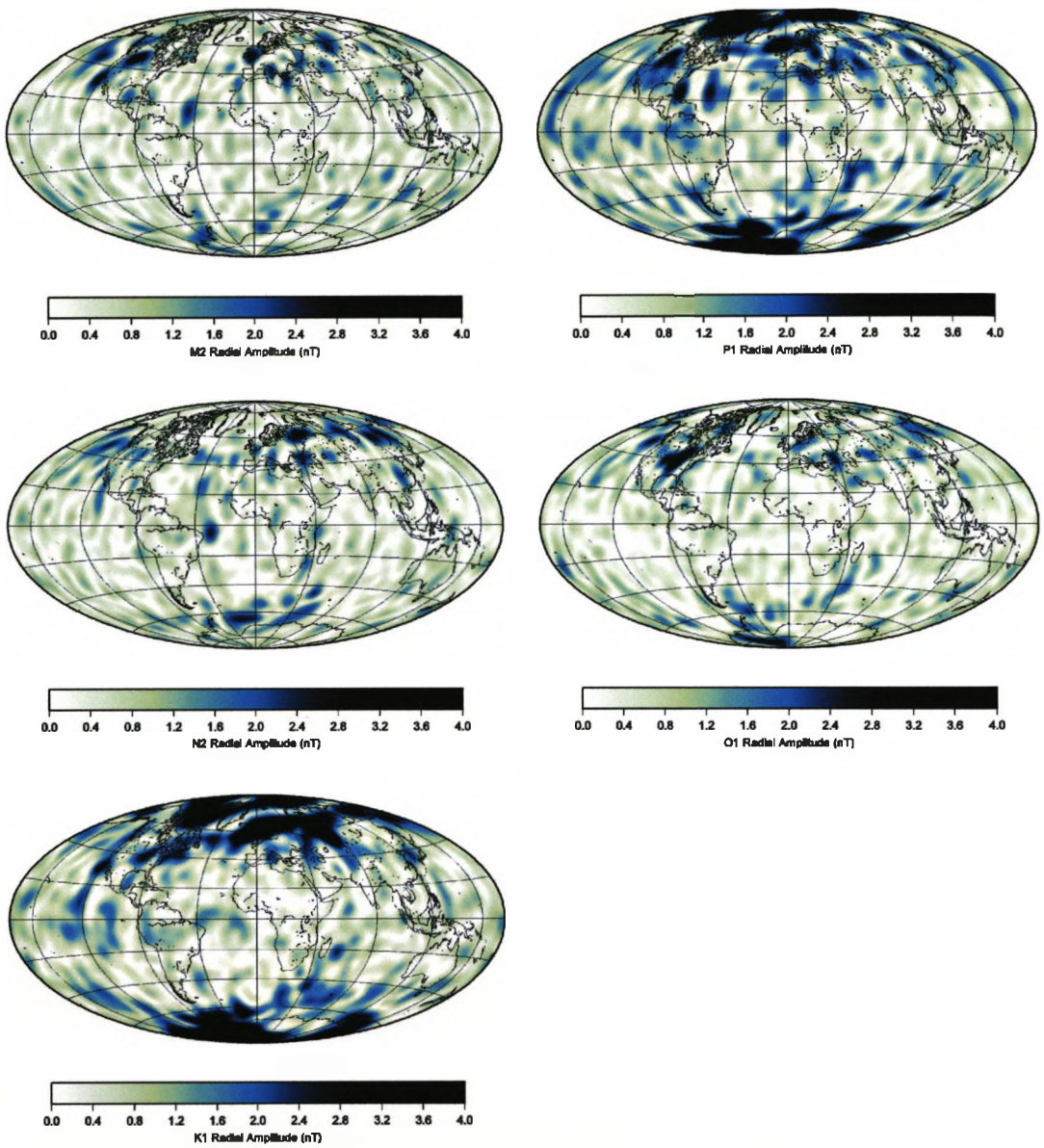

Figure 4.20: Numerical predictions of radial tidal field magnitude (at ground level) made using the tidal field model presented throughout this section. Predictions of M2, P1, N2, O1 and K1 constituents have been made to compare the accuracy of this model against the numerical predictions of Maus and Kuvshinov [2004] shown in figure 4.19.

compared to numerical solutions), suggesting that issues regarding external fields were not dealt with as thought. A lack of comparability (high magnitudes and excessive noise/ringing) with numerical solutions at ground level also suggests the model is not radially constrained, although the lack of low altitude observations in model data means this limitation is of little surprise. However, the stability of the modelling methodology used here suggests that if additional low altitude/observatory data are included, along with more comprehensive data selection and error estimates, future versions should see a vast improvement in model quality.

4.6 Summary

In this chapter, details of a new tidal field modelling methodology have been presented, along with preliminary feasibility analyses and a first edition of the resulting tidal field model. Using data from three satellite magnetic observation platforms (CHAMP, Ørsted and SAC-C), along with strict data selection criteria, over 1 million data points have been used in its derivation. The modelling framework presented is the first of its kind to estimate explicitly the full tidal vector field generated by 16 major tidal constituents, achieved by integrating along track filtering (usually used to remove external field effects from analysis data) into the error estimates of the model (which also include comprehensive attitude error estimations). The resulting model has been shown to be consistent with previous studies of this type (when considered in a filtered form) and to a lesser extent with numerical M2, O1 and K1 magnetic fields (at satellite altitude) and numerous fields at ground level. Therefore, it is thought future iterations of the model may benefit from more stringent data selection criteria, along with more comprehensive error estimates, while increased input data (particularly when attempting to model longer period tides, for example monthly, semi-annual and annual), both satellite and ground based, should improve the quality of future models of this type a great deal.

Chapter 5

Large Scale Wave Motion in the Global Oceans: Rossby/planetary waves

5.1 Introduction

Previously, this thesis has focussed on the study of periodic ocean flow processes, both globally (chapter 4) and on a localised (chapter 3) basis, with varying degrees of success in each case. In contrast, the work within this chapter aims to identify the magnetic signature of large scale wave motion in the global oceans, with the earlier work of Tyler et al. [1999] suggesting that the flow of Rossby/planetary waves across the global oceans would be an ideal low-frequency wave mechanism to target. Therefore, this study seeks to identify the motionally induced magnetic signal associated with oceanic Rossby waves within the geomagnetic record.

The chapter begins with an introduction to Rossby/planetary waves (what they are, how they are generated, prediction of their existence from wave theory and evidence of that existence from oceanography), followed by a discussion of the analysis methods applied, the results of the analysis and their implications for future magnetic investigation of this type of flow process.

5.2 Oceanographic Background

5.2.1 What are Rossby/planetary Waves?

Rossby waves, often referred to as planetary waves (due to their planetary scale and origin being heavily linked to Earth rotation), are large scale waveforms that play a vital role in many oceanic and atmospheric processes. In the oceans, Rossby waves are one of a hand full of processes capable of transmitting information from eastern to western basin

boundaries (Gill [1982]) and are also vital in the western intensification of circulation gyres (Gill [1982]), western boundary current replenishment (e.g., the Gulf stream), general ocean circulation (Jacobs et al. [1994]) and global climate (McPhaden [1994]). However, while early observation of atmospheric Rossby waves supported the physical existence theory developed by Carl-Gustav Rossby in the 1930s, oceanic Rossby waves are more elusive, primarily due to the dimensions of a typical wave. With small surface amplitudes (several cms) and large wavelengths (100s of kms), the ratio of the two scales means that oceanic Rossby waves are almost invisible to in-situ observation methods. Therefore, oceanic evidence to support Rossby's theory was only found with the advent of remote satellite ocean observation (sea surface height/temperature, etc).

5.2.2 Rossby Wave Generation Mechanism

Like all other oceanic waves, Rossby waves are generated when the ocean is locally perturbed. In the case of Rossby waves, these perturbations can take the form of local wind forcing, buoyancy effects (as a result of heating and cooling) in the ocean interior or at the basin's eastern edge, or as an emission product of coastally trapped Kelvin waves [McWilliams, 2006] (propagating polewards along the eastern boundary of a basin). Work by Chelton and Schlax [1996] has also suggested that bathymetry plays a role, with theoretical mechanisms suggested by Rhines [1969], Barnier [1988] & Gerdes and Wübber [1991]. However, Kelvin wave emission aside, it is the manner in which Rossby wave generation and propagation is facilitated that sets them apart from other wave types, processes controlled by potential vorticity conservation and latitude dependent coriolis forces.

On a rotating body such as the Earth, all fluids acquire a quantity known as potential vorticity (PV), consisting of a combination of both planetary (f, also known as the coriolis parameter) and relative (ζ) vorticities. While f is a measure of the spin imparted on a fluid due to Earth rotation and can be written as;

$$f = 2\Omega \sin\theta \tag{5.1}$$

(where Ω is the rotation rate of the Earth and θ is latitude), ζ quantifies the spin placed upon a fluid by effects other than Earth rotation (mean ocean flow, wind stress, etc).

Now, consider a single fluid parcel existing in equilibrium at a latitude θ_0. Whilst the parcel remains at latitude θ_0, the fluid will remain in this state (allowing zonal, E-W movement), as f is stable and PV conserved. However, if the parcel is perturbed in a N-S, meridional direction to a new latitude $\pm\theta_1$, the fluid is no longer in equilibrium due to a change in f, initiated by the change in its latitude (equation 5.1); therefore, to conserve PV the fluid adjusts ζ to compensate. As planetary vorticity varies from $+f$ at the North pole, to 0 at the equator and $-f$ at the South pole, any northward perturbations will result in a negative ζ adjustment, while southerly perturbations will result in an increase in ζ, which due to its rotational properties will result in a rotation of the fluid (positive = anti-clockwise, negative

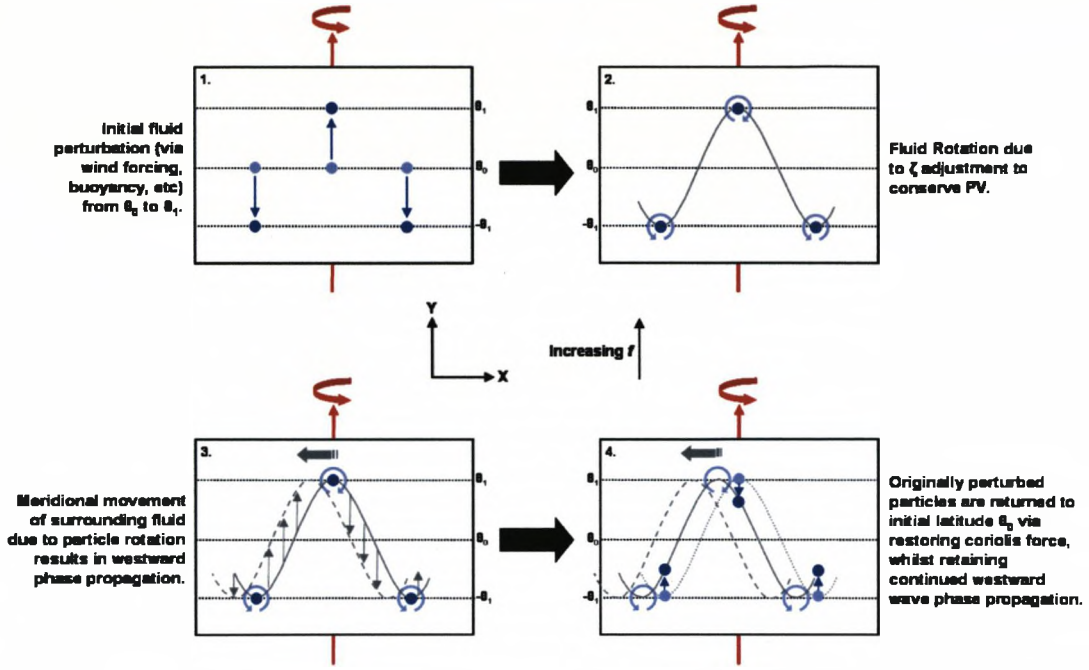

Figure 5.1: A Schematic diagram describing the generation and propagation of an oceanic Rossby wave, from system perturbation to continued westward wave propagation.

= clockwise), with the sense of these rotations being controlled by the rotational sense of the Earth.

Once this series of rotating perturbed particles is established, wave propagation is initiated (a process shown graphically in figure 5.1). Considering the ζ induced rotations depicted in this figure and their influence on the surrounding fluid, wave propagation can be understood. Focussing on a fluid particle perturbed to the North, due to its rotation fluid to the East of the particle will be entrained to the South, while fluid to the West will move to the North. In contrast, for a particle perturbed to the South, fluid to the East is entrained to the North while fluid to the West moves to the South (alternate entrainment directions are caused by opposing rotational senses of the two perturbed fluid particles). Therefore, while fluid motion is locally restricted to the N-S direction, the wavefront migrates to the West (a key feature of Rossby waves).

While PV conservation is a key factor in the initiation and westward propagation of Rossby waves, the mechanism by which fluid particles are returned to their equilibrium position relies on the coriolis effect. Where moving particles, fluid of other wise, are considered in a rotating frame (as when standing on the Earth), as they attempt to move along a linear path they are deflected, to the right in the northern hemisphere and to the left in the southern hemisphere (the amount of deflection is latitude dependent). The effects of this deflection can be seen schematically in figure 5.2, with the source of these deflections (coriolis force) providing the Rossby wave restoring force (see figure 5.3). Therefore, as a perturbed fluid particle (now rotating due to ζ compensation) moves around its rotational path, a coriolis

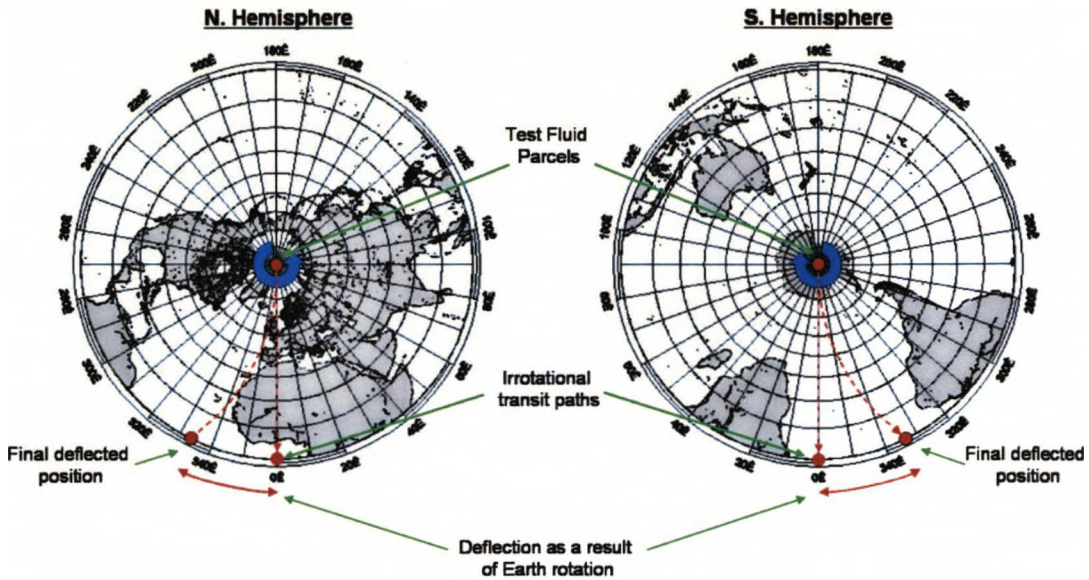

Figure 5.2: A schematic diagram illustrating the deflection of linearly moving objects, when considered in a rotating reference frame.

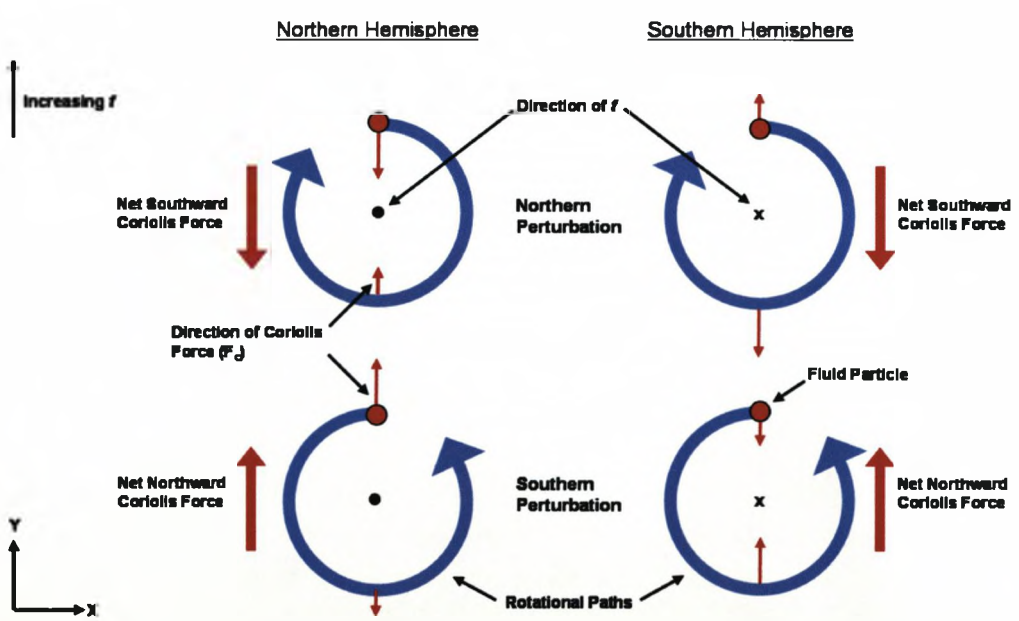

Figure 5.3: A schematic illustration of the Rossby wave restoring force, applied to both northern (left) and southern hemisphere (right) initial fluid perturbations.

force ($\mathbf{F_c}$) defined as;

$$\mathbf{F_c} = -f \times \mathbf{u} \tag{5.2}$$

(where f is the coriolis parameter (planetary vorticity) and $\mathbf{u}$ is fluid velocity) will act upon it due to its movement. However, due to the latitude dependence of $\mathbf{F_c}$ (through the inclusion of f), while the forces exerted at eastward and westward orbital extremes cancel, the force exerted on the fluid at the poleward extreme of its rotational path is always greater than that exerted at the equatorward extreme, producing a net meridional force that acts on the fluid (southward net force for northward perturbations and northward net force for southward perturbations), returning it back to its unperturbed initial latitude and equilibrium position (with no additional ζ induced rotation, removing coriolis force action). Note that all three wave generation, propagation and restoring mechanisms function fully using both complete wavetrains and single wave pulses, a dynamical property of Rossby waves that will require additional consideration further into this investigation.

The final unique feature of Rossby waves is their latitude dependent phase velocities (with higher velocities occurring towards the equator), that like many things in this system arise due to the inclusion of the coriolis parameter in their calculation;

$$c = u - \beta\lambda^2 \tag{5.3}$$

where $\mathbf{c}$ is the calculated phase speed of the wave, $\mathbf{u}$ is the mean East-West background flow speed, λ is the specific wavelength of the wave and $\beta = \frac{df}{d\theta}$ (the meridional gradient of f). In this equation, positive is taken as eastward, therefore the minus sign here again indicates that phase speed is always westward.

5.2.3 Prediction of Rossby Waves from Wave Theory

Hough [1897] first derived the mathematical existence of Rossby waves using a set of linearised equations, describing large scale, unforced, low-frequency motion in a spherical system about a state of rest. Rossby et al. [1939] & Rossby [1940] subsequently expressed these solutions in a cartesian system, approximating equation 5.1 as a linear relationship, $f = f_0 + \beta y$, where y is the meridional displacement from a reference latitude, f_0 is the coriolis parameter at the reference latitude and β is as in equation 5.3. The solution of these equations takes the form of an infinite series of vertically structured wave modes (LeBlond and Mysak [1978], Gill [1982]), with vertical complexity increasing and phase speed decreasing as a function of mode number n. The lowest order mode ($n = 0$), known as the barotropic mode due to its depth invariance, is the fastest propagating wave, typically crossing an ocean basin in ~ 1 week. Its depth invariance also suggests larger mass transports, making it an attractive study target. Unfortunately, due to its high phase speed, this mode cannot be monitored with sufficient resolution by modern magnetic satellites (CHAMP, Ørsted & SAC-C) and so this investigation instead focuses on the weaker, slower moving (1-20 cms^{-1}, see figure 5.4), surface intensified, first baroclinic mode ($n = 1$).

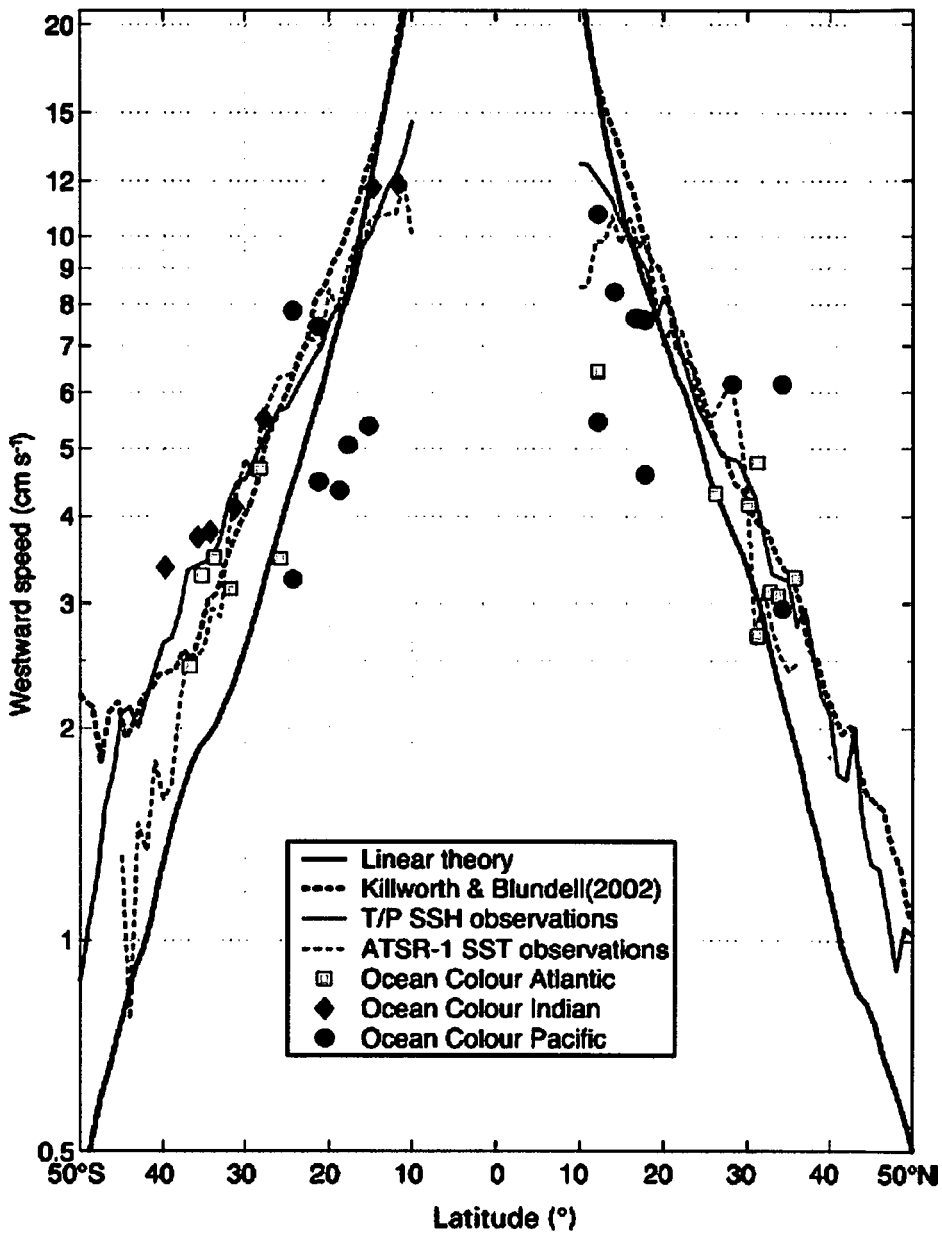

Figure 5.4: Theoretical and observed Rossby wave phase speeds (*from Challenor et al. [2004]*).

However, in recent years these theoretical solutions have been shown to be far from complete (see Chelton and Schlax [1996] among others), with linear wave theory consistently underestimating (often 1-2 times) phase speeds at many latitudes (particularly in the tropics) when considered against the analysis of satellite-based oceanographic data. As a result, standard linear theory has been re-evaluated in recent years to account for more complex aspects of ocean dynamics, with one of the most significant leaps forward being made by Killworth et al. [1997]. Here, standard theory was adapted to account for mean East-West ocean flows, rather than the rest state hypothesed in earlier work. Figure 5.4 shows that the inclusion of this additional complexity has greatly reduced the disparity seen between theoretical and observationally derived phase velocities, although differences do still exist, with more recent contributions (see Chelton et al. [1998], Killworth and Blundell [1999, 2003a,b]) attempting to reduce this gap further.

5.2.4 Satellite Oceanographic Evidence of Rossby Wave Activity in the Global Oceans

Since the introduction of satellite oceanographic observation spacecraft, there has been an explosion of evidence to support the existence of oceanic Rossby waves, from all manner of data sources. While most evidence is from conventional altimeter data (TOPEX/POSEIDON in particular, see Chelton and Schlax [1996], Cipollini et al. [1997] & Angell et al. [1998]), datasets of other observable sea surface variables have also been used extensively in the search for these waves, notably ocean colour and temperature data (e.g., see Cipollini et al. [2000b,a], Hill et al. [2000]). Figure 5.5 illustrates how numerous oceanic datasets can all identify similar wave signatures, on this occasion in the Indian ocean. It is due to the high density of oceanic investigations in this region (Cipollini et al. [2000b,a], Hill et al. [2000], Challenor et al. [2004]) compared to other ocean basins, that this magnetic study focuses on the Indian ocean, specifically the 25°S meridian (to allow direct comparison with the work of Cipollini et al. [2000b,a]).

5.3 Analysis Methods 'Borrowed' from Oceanography

5.3.1 Hovmöller/Longitude - Time (LT) Plots

The most widely used analysis technique to be included in this analysis is the Hovmöller (LT) plot (a technique also used recently in the study of Earth's core dynamics [Finlay, 2005]). Popular because of its simplicity, the LT plot uses the strict westward phase propagation of Rossby waves to its advantage, eliminating latitudinal data variability by reducing 3D data into a simple longitude (x-axis), time (y-axis) format, centred about a chosen meridian. Any signals due to Rossby waves are presented as persistent SE-NW trending lineations of positive (crests) or negative (troughs) amplitude (see figure 5.6). Latitude dependent wave velocities are accommodated, with the angle between lineations and the horizontal giving a measure of

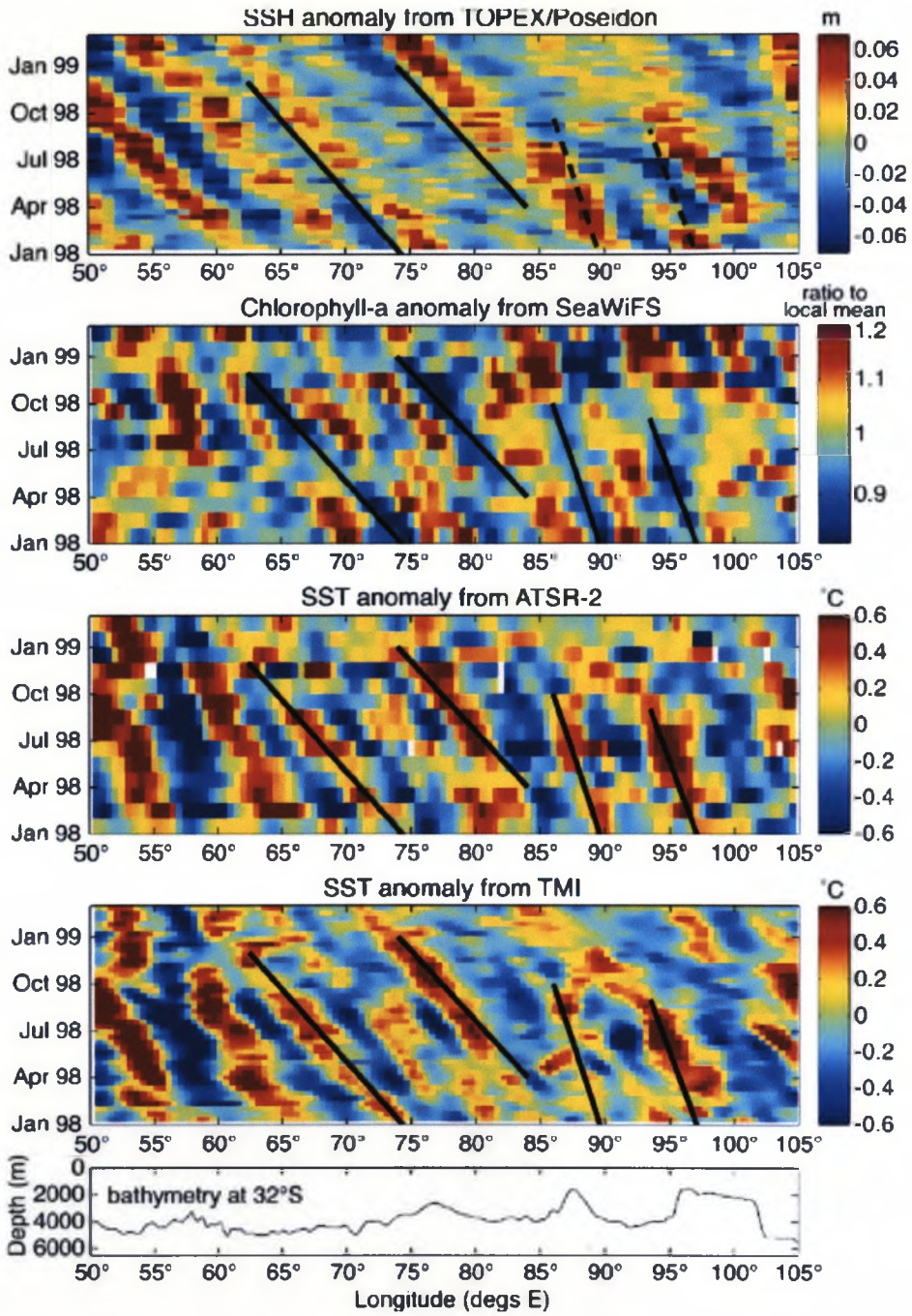

Figure 5.5: Evidence of Rossby wave activity within the Indian ocean at 32°S, captured in 4 different oceanographic datasets. Upper panel: altimetry, second panel: ocean colour and panels 3 and 4 display 2 forms of surface temperature data. The lower panel displays basin bathymetry, as this may play a role in modifications of wave phase speed across the basin. *Taken from Challenor et al. [2004]*

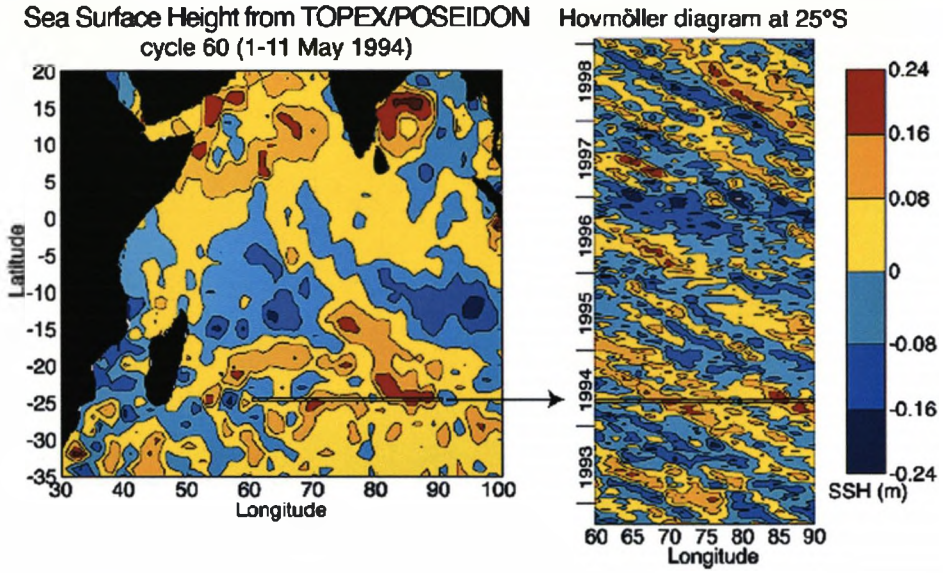

Figure 5.6: An example Hovmöller (LT) plot (*from Cipollini et al. [2006]*), derived using TOPEX/POSEIDON altimeter data, centred on 25°S.

phase speed. Repeating this procedure at multiple meridians, a latitude dependent velocity profile that can be compared with theoretical velocities can be determined.

5.3.2 Radon Transform

While the LT plot is crucial in the study of oceanic Rossby waves, the method of calculating wave speeds is considered highly inaccurate, often being calculated manually using a pencil and ruler, resulting in a rather subjective analysis, prone to human error.

One method that accurately calculates the angle of any lineations found is the Radon transform, which takes a typical LT plot (or any other image) and identifies consistent straight lines within it. The transform is achieved by calculating the integral of the image along a series of parallel lines lying orthogonal to a baseline, at an angle θ to the horizontal axis of the image (the distance of each integral line along the baseline is given by x', the origin of which is the centre of the image). Therefore, if an integral line (x', θ) lies parallel to an image lineation, its integral value will be large and a high value plotted in the corresponding pixel of the transform. Conversely, if the integral line lies perpendicular to the image lineation, a lower integral value will be placed in the transform. Therefore, a continuous Rossby wavetrain will appear as a vertical stripe (at a single value of θ) of alternating high and low amplitude peaks, with each peak (positive or negative) corresponding to a single wave crest or trough, while single wave pulses appear as solitary peaks. The mathematical representation of a Radon transform is given by;

$$H\left(x',\theta\right) = \int_{t'} h\left(x,t\right)\Big|_{\substack{x = x'\cos\theta - t'\sin\theta \\ t = x'\sin\theta + t'\cos\theta}} dt' \tag{5.4}$$

where $H\left(x^{'},\theta\right)$ is the radon transform (at a baseline distance of $x^{'}$ and angle θ) of a longitude (x), time (t) image $h\left(x,t\right)$, based around a $\left(x^{'},t^{'}\right)$ co-ordinate system (a representation of x,t co-ordinates, rotated by θ). The process is also shown schematically in figure 5.7, with synthetic tests shown in figure 5.8. The total variance of the transform for each value of θ can also be calculated, identifying any preferred angles from within the original LT plot, with corresponding wave speeds being calculated by applying trigonometric relationships to the angle of peak variance.

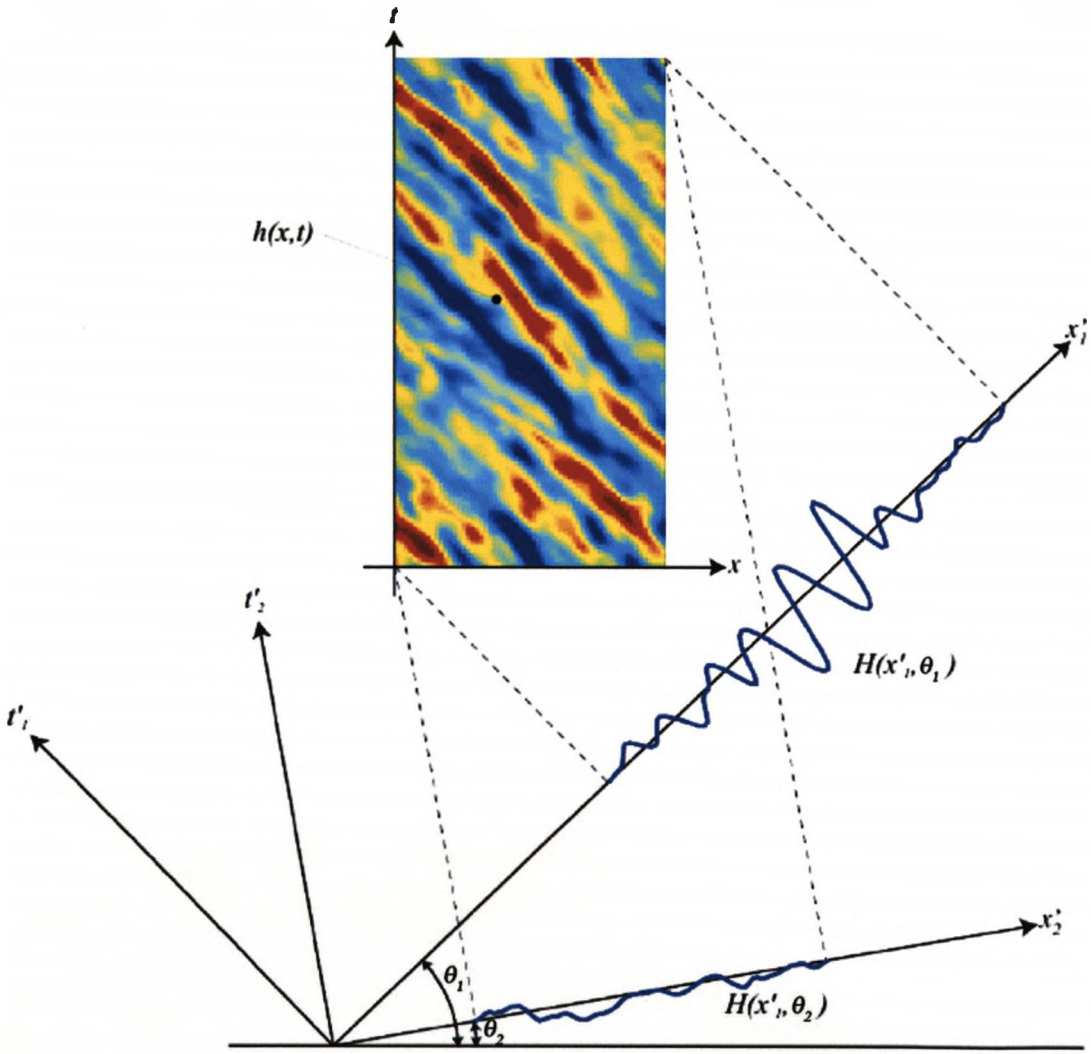

Figure 5.7: A schematic diagram outlining the application of the Radon transform to an oceanic Hovmöller plot (*adapted from Cipollini et al. [2006].*)

5.3.3 2-Dimensional Fourier Transform

An alternative to the Radon transform is the 2-Dimensional Fourier transform (2D-FT), a process that transforms an image into frequency(f)-wavenumber(k) space to determine its

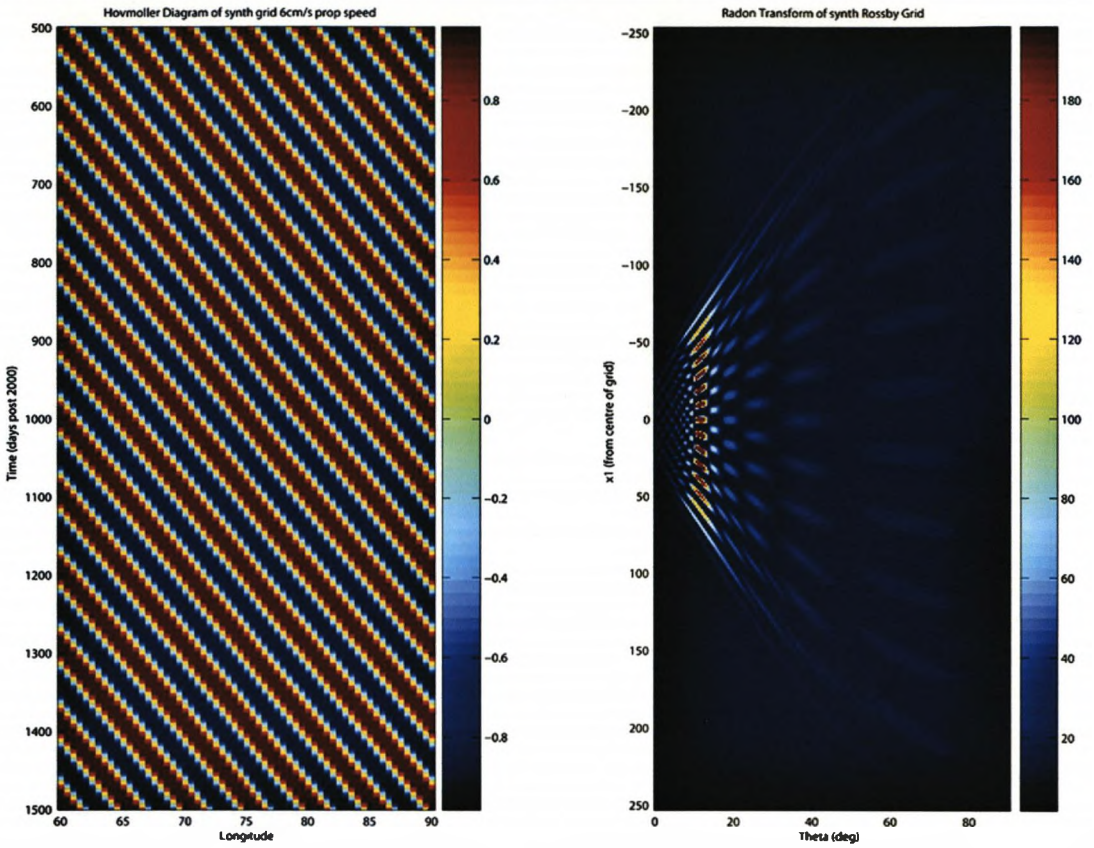

Figure 5.8: Results of a synthetic test of the Radon transform method. The left hand panel shows a synthetic LT plot with a 6cms^{-1} westward wave speed, while the right hand panel displays its Radon transform.

spectral characteristics, from which wave speeds can be determined. This involves extending a standard 1D Fourier transform into the second dimension, via two sequential 1D transforms, the first applied vertically through the image, before the resulting spectrum is transformed again in the horizontal direction (see Gubbins [2004] for more detailed information on the 2D-FT). A typical spectrum is shown in figure 5.9, although other examples can be found throughout the natural sciences (see Tokmakian and Challenor [1993], Traon and Minster [1993] & Cipollini et al. [2006]). In the case of figure 5.9, the author has applied a 2D-FT to LT plots of both satellite altimeter and temperature records, resulting in highly comparable spectra. However, while these spectra display both positive (eastward propagation) and negative (westward propagation) wavenumbers, only positive frequencies are shown as the periodicity of the transform introduces a reflection of positive frequencies into negative values, making them unphysical and of little use. Figure 5.9 also reveals consistent pixelation of the transform spectra. This occurs because the images being transformed, like all real data (including this study), are not infinitely long, continuous functions, but instead consist of discrete grids, $M \times N$ pixels in size (where m and n are the corresponding pixel indices), with axis resolutions (pixel dimensions) of Δx, Δt (where again, x is longitude and t is time),

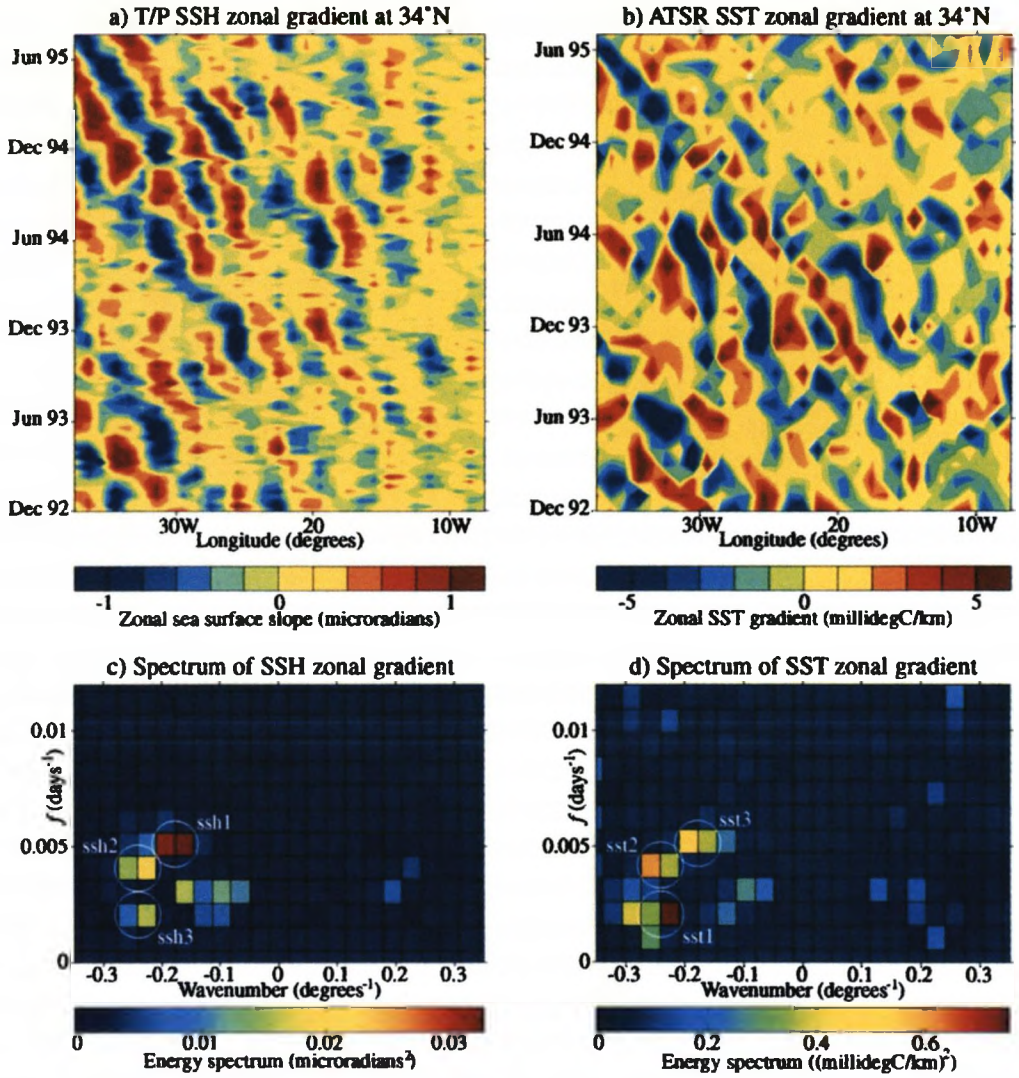

Figure 5.9: An example of the 2D-FT method, applied to both satellite altimeter (left) and surface temperature (right) data (*taken from Cipollini et al. [1997]*).

resulting in an image $h(m\Delta x, n\Delta t)$. Therefore, its 2D-FT must also take the discrete form;

$$H(k,f) = \Delta x \Delta t \sum_{m=1}^{M} \sum_{n=1}^{N} h(m\Delta x, n\Delta t)\, e^{-j2\pi(k\Delta x + f\Delta t)} \tag{5.5}$$

with the transform $H(k,f)$ being computed on a discrete grid $H(p\Delta k, q\Delta f)$, where $p = 1 \ldots M$, $q = 1 \ldots N$. The lower limits of the k (wavenumber), f (frequency) axes (also axis resolution) are given by $\Delta k = 1/(M\Delta x)$, $\Delta f = 1/(N\Delta t)$ while their upper limits are determined by $1/\Delta x$ and $1/\Delta t$ respectively.

As with all analytical methods, the 2D-FT approach has both advantages and drawbacks. Positively, the method separates numerous spectral components from within a complex image (see Cipollini et al. [2006] for a particularly relevant example), particularly useful as Rossby waves have been shown to alter their characteristics during transit across a basin, both in

terms of wave speed, amplitude and initiation/termination positions (possibly caused by bottom topography, Chelton and Schlax [1996], Killworth and Blundell [1999, 2003a,b]). However, the approach struggles to analyse very noisy data (similar to that used in this study) and inconsistent wave signatures (as signals must be strictly periodic to obtain an accurate spectrum.) Therefore, many recent studies have opted to abandon the 2D-FT in favour of the Radon transform, particularly when analysing very noisy data. However, to give the best chance of identifying Rossby wave signatures in satellite magnetic records, both methods are used during this investigation.

5.4 Analysis Results

5.4.1 Analysis Data

In a similar manner to the oceanographic study of Rossby waves, in-situ magnetic measurements are also disregarded, the reason being that the small magnetic contributions these waves are thought to produce will be difficult to distinguish from random noise when their unique spatial characteristics (for example, westward phase propagation) cannot be considered. However, while observatory records have been eliminated from this analysis, numerous satellite data sources are available for use (see §2.1.2 for detailed information on each satellite). Unfortunately, while they all provide the resolution and precision required, their orbital configurations drastically affect their viability for use. To determine the most suitable observations to use in this investigation, all the data from each spacecraft (processed in accordance with §2.2) have been used to generate LT plots at a series of latitudes (see figures 5.10, 5.11 & 5.12), so their zonal and meridional data coverage through time can be examined. Note that as this investigation requires large volumes of data (to produce consistent LT plots), only non repeat orbit, scalar observations are considered.

Immediately, the spatial patterns shown in figures 5.10 & 5.11 rule out the use of CHAMP and Ørsted data in this investigation, due to incompatible orbital configurations, resulting in prolonged periods of unacceptably sparse longitudinal data coverage (e.g., $\sim$ MJD 1300 in figure 5.10) that persist into analysis grids (see figure 5.13). However, while CHAMP and Ørsted data have been disregarded, figure 5.12 suggests that the SAC-C satellite possesses adequate data coverage to be used in this investigation (as the lack of high latitude observations is not an issue here). Unfortunately, while the longitudinal coverage of the SAC-C spacecraft is generally very even, the presence of several temporal gaps in coverage (MJD 1050 $\rightarrow$ 1300 in particular) means that only 1 section of this data can be utilised. (MJD 400 $\rightarrow$ 1050). This data is further reduced by disregarding any observations made outside of the study area (latitude: $-5^{\circ} \rightarrow -45^{\circ}$, longitude: 30°E $\rightarrow$ 130°E), before being selected using identical criteria to those outlined in §3.7.

Post selection, unselected and selected datasets are reduced into 2D LT plots in accordance with §3.5.3, with axes limits of longitude: 50°E $\rightarrow$ 110°E & time: MJD 400 $\rightarrow$ 1050. However,

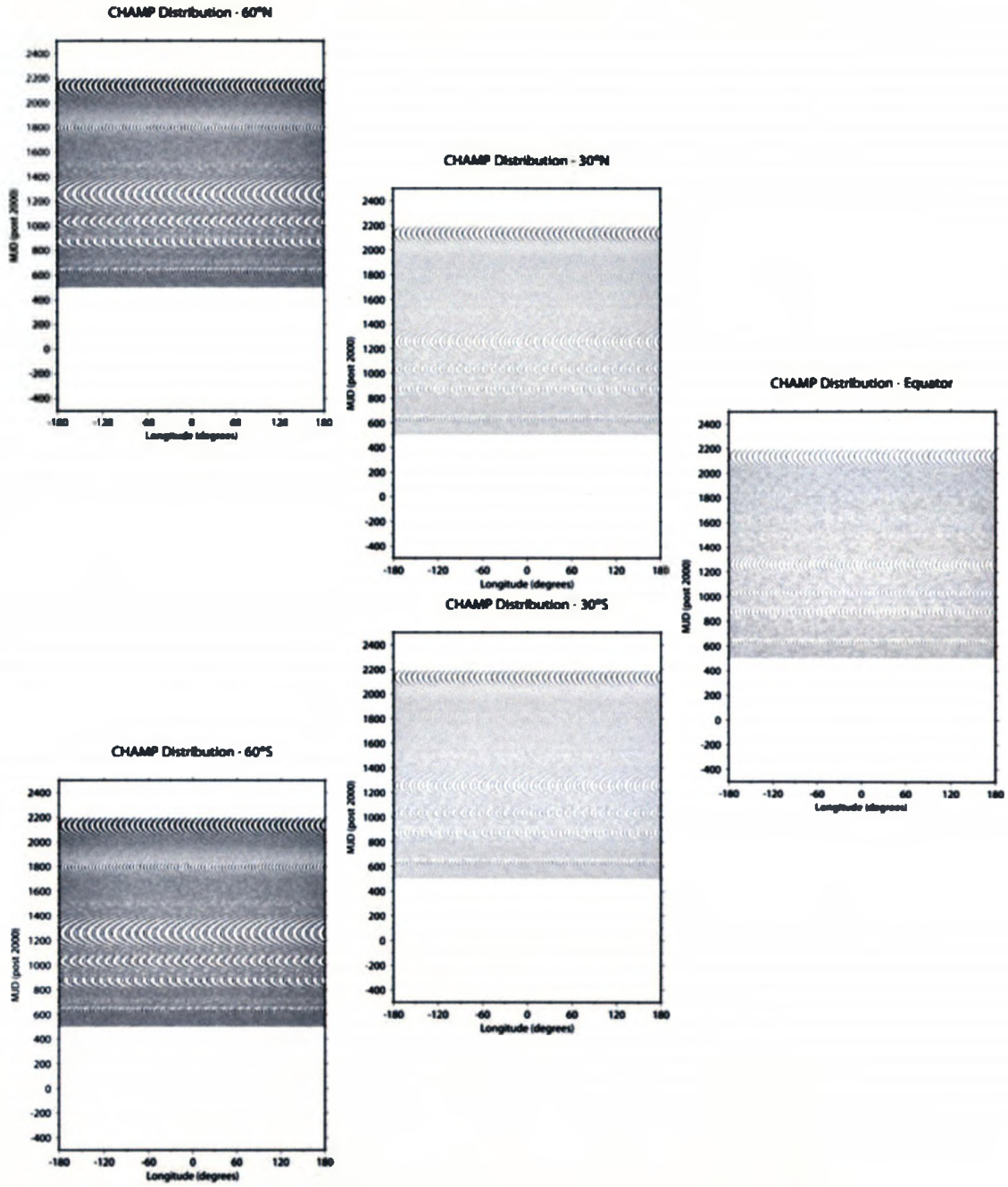

Figure 5.10: Data distribution plots constructed using CHAMP observations. All data points recorded within $\pm 2.5^{\circ}$ of the latitude indicated within each image are plotted. Images at $\pm 87.5^{\circ}$ are omitted, as the large data volumes present in these regions are too dense to allow the visual identification of repeat orbit signatures.

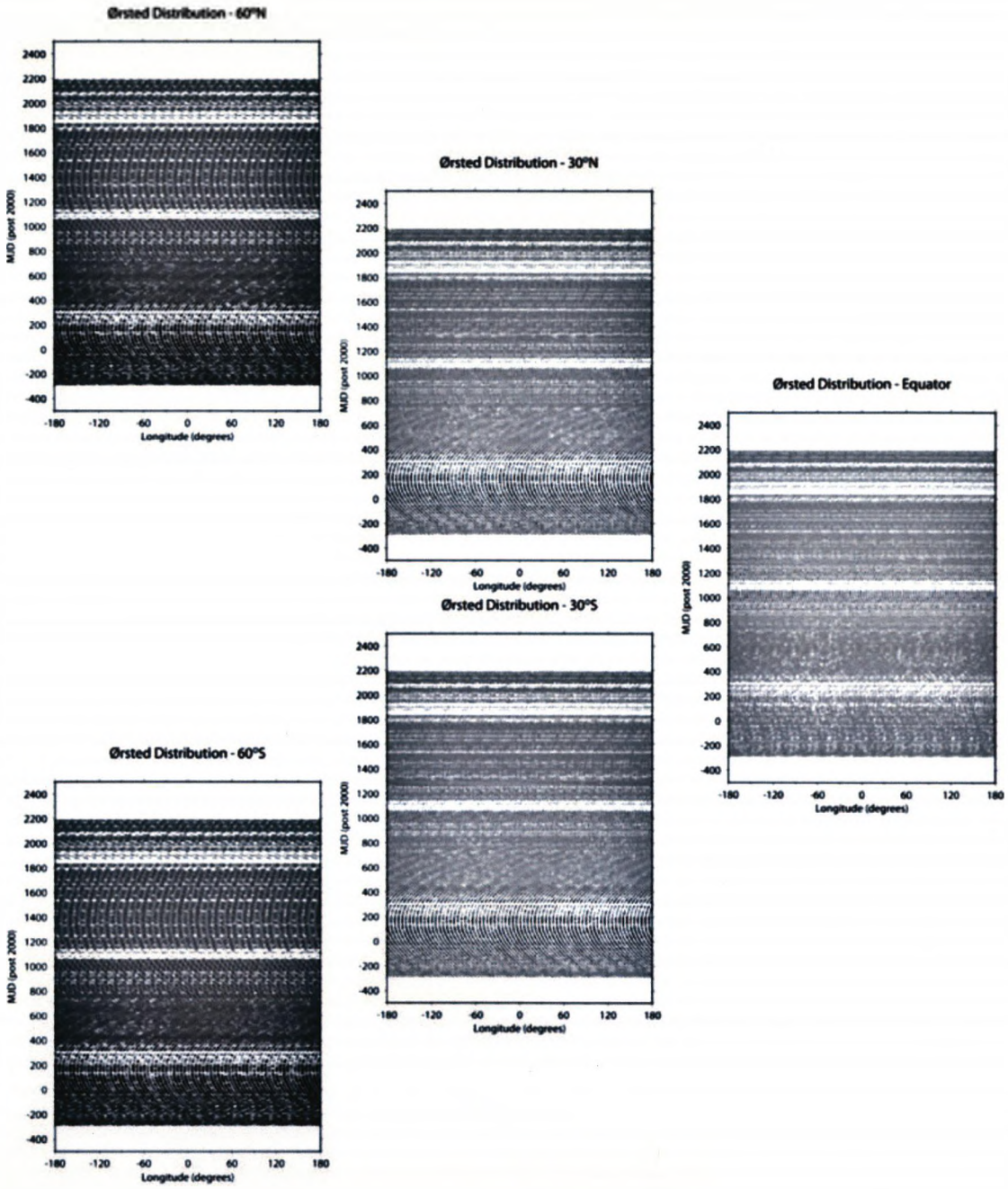

Figure 5.11: Data distribution plots constructed using Ørsted observations. All data points recorded within $\pm 2.5^{o}$ of the latitude indicated in each image are plotted. Images at $\pm 87.5^{o}$ are omitted, as no data are recorded at these high latitudes due to restrictions in the satellite's orbital configuration.

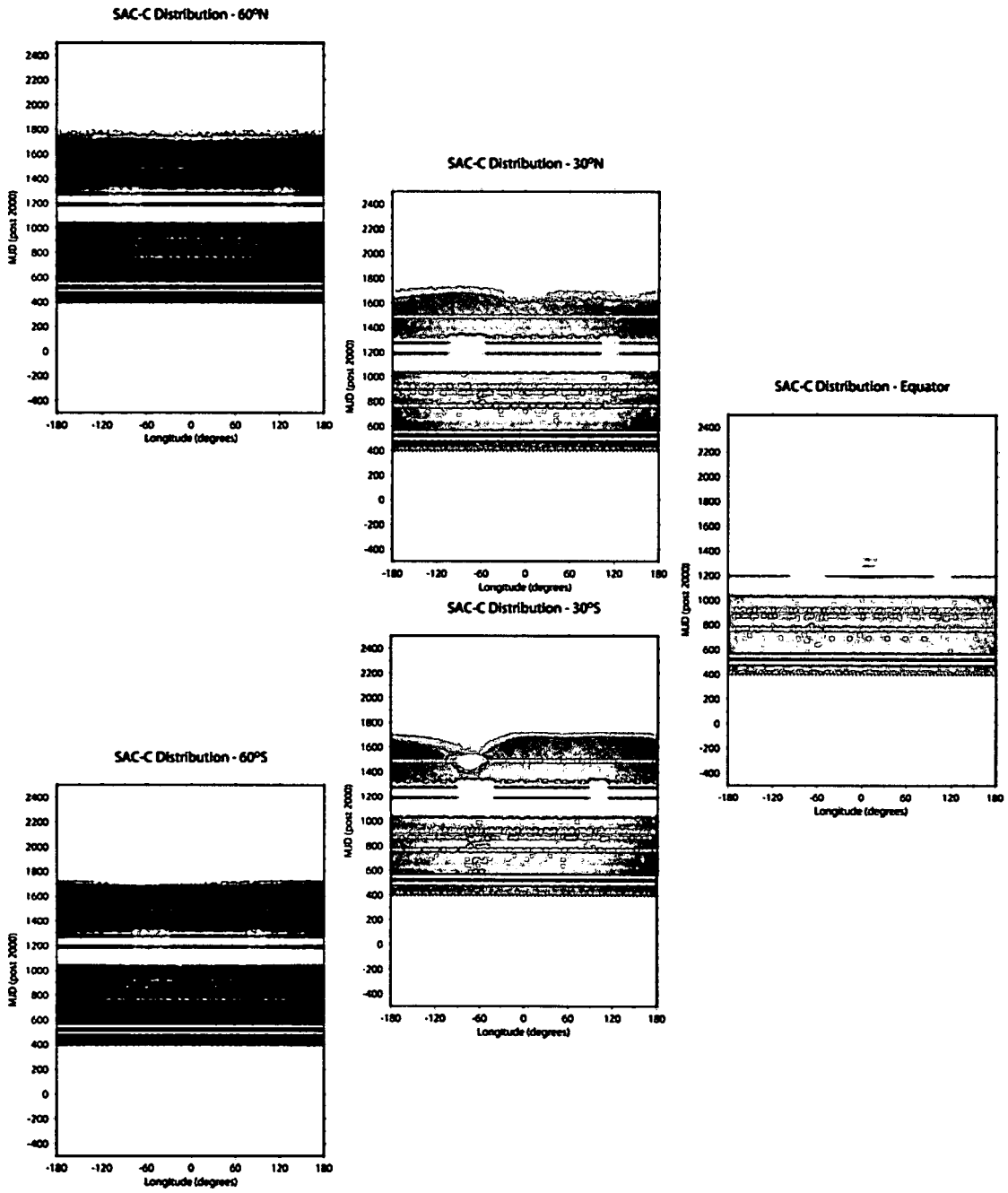

Figure 5.12: Data distribution plots constructed using SAC-C observations. All data points recorded within $\pm 2.5^{\circ}$ of the latitude indicated within each image are plotted. Images at $\pm 87.5^{\circ}$ are omitted, as due to orbital restrictions, no data are recorded at these high latitudes.

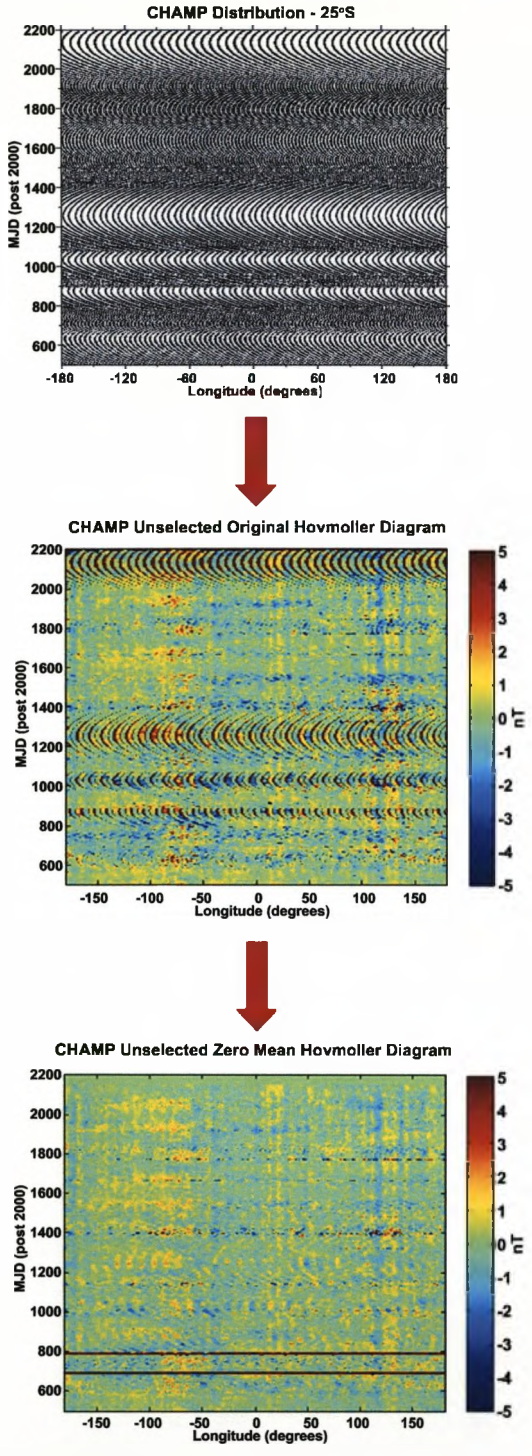

Figure 5.13: An example of the disruptive effects of uneven data distribution on Hovmöller plots. Coherent spatial patterns, seen in distributions of CHAMP scalar observations, are clearly transferred to the LT plots shown in the centre and right hand panels (generated using a 5° latitude × 5° longitude ×10 day search window). Importantly, any one of these signals could corrupt the results of an analysis conducted using this data.

to ensure that the search window dimensions used during this process do not affect the resulting analysis, numerous data grids are constructed (all with a fixed resolution of 2.5 days × 0.25° longitude), each utilising a different combination of temporal (10 days, 20 days & 30 days) and spatial (3° latitude × 4° longitude, 5° latitude × 5° longitude, 7° latitude × 7° longitude & 10° latitude × 10° longitude) search window dimensions.

Subsequently, several pre-analysis processing measures are also applied to each LT plot, to both enhance and remove particular data characteristics (a similar process is described by Hill et al. [2000]). The details of this processing are shown in a flow diagram in figure 5.14, with their graphical details shown in figures 5.15 & 5.16.

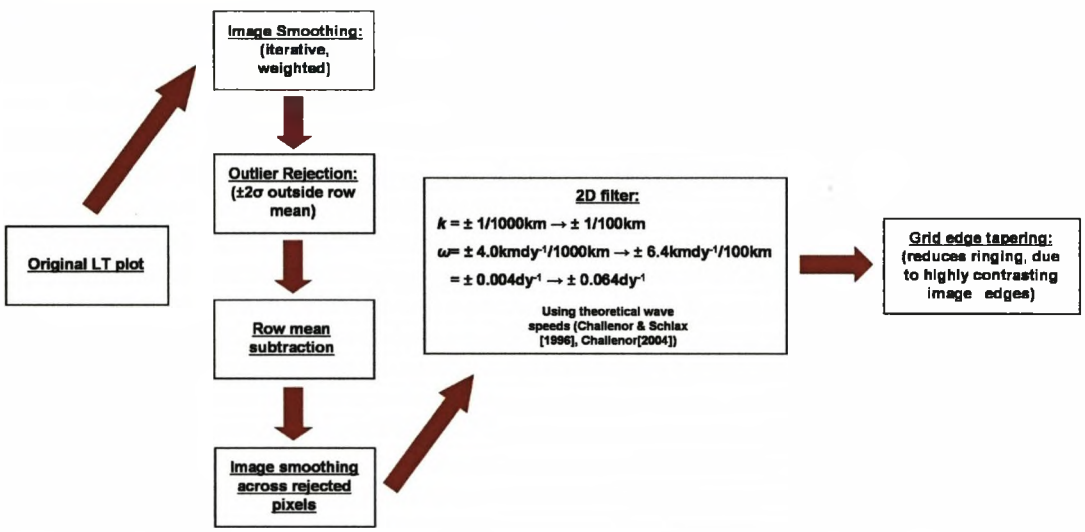

Figure 5.14: A flow diagram, illustrating the sequence of pre-analysis processing steps employed during this investigation.

5.4.2 Theoretically Derived Analysis Results

To identify the presence of Rossby waves in the results that follow, a range of theoretical transform angles to which the waves should adhere, have been calculated. Using theoretical wave speeds from Challenor et al. [2004], velocities ranging from 3.25 cms^{-1} (ocean colour data) to 6.5 cms^{-1} (surface temperature) have been determined. Using these velocities, a range of transit times for a single wave crossing the study area can be calculated (Note that longitudinal distance is converted to km and wave speed to km/day.):

$$\begin{aligned}\text{Longitude conversion: } 60^{o} \text{ at } 25^{o}\text{S} &= 60 \times (\cos(25) \times 111.19 \text{ km}) \\ &= 6046.34 \text{ km}\end{aligned}$$

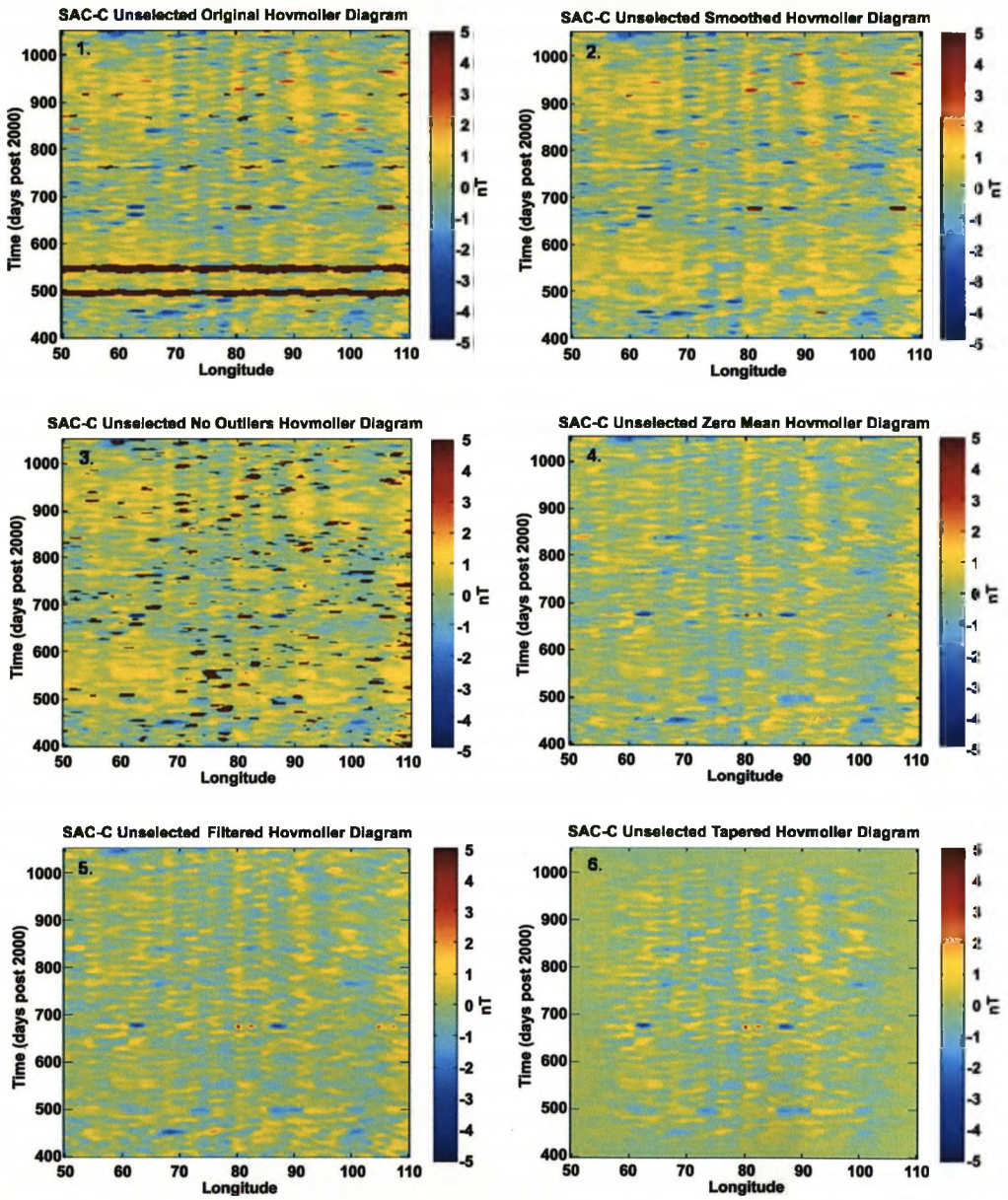

Figure 5.15: A series of plots, illustrating the effect of the processing stages identified in figure 5.14 on a sample LT grid. The grid in this example was generated using a data reduction search window with dimensions of 3° latitude × 4° longitude × 10 days.

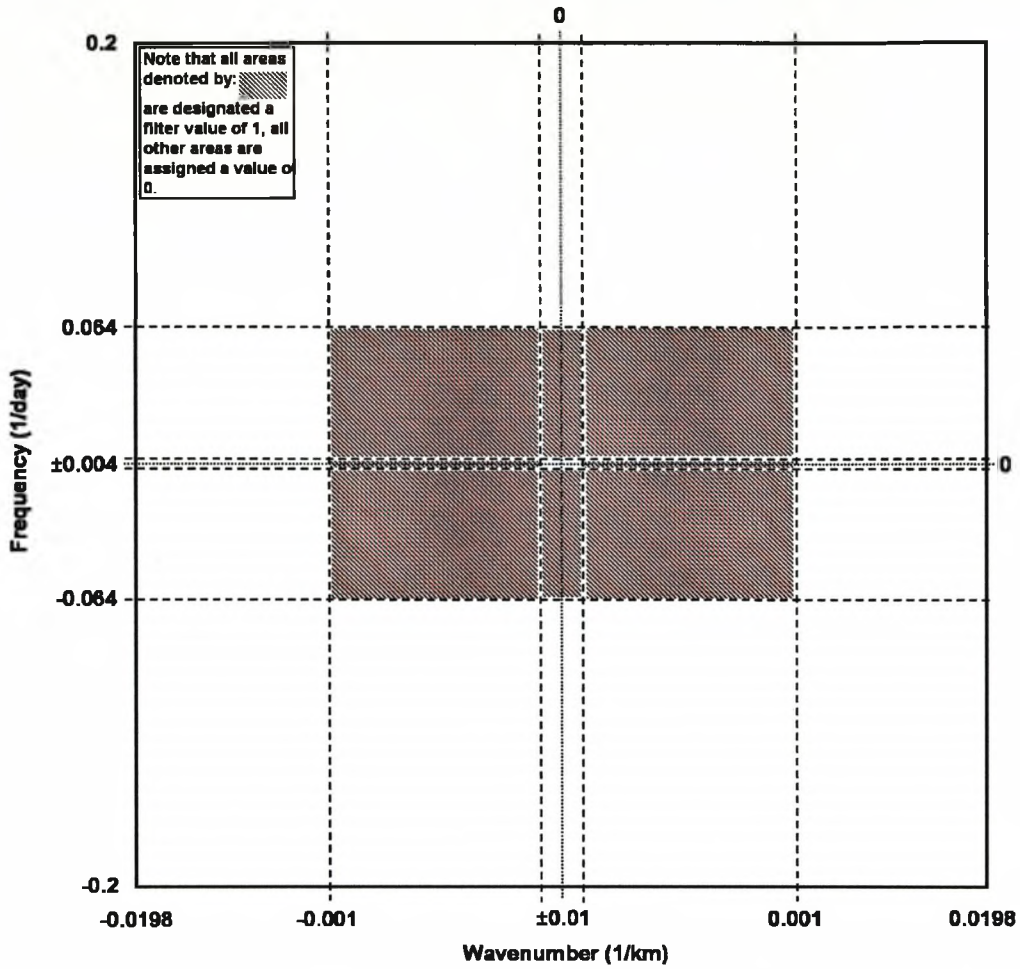

Figure 5.16: A schematic illustration showing the 2D filter configuration used during this investigation. Note that the minimum axes values (determined by the time span and longitudinal width of each data grid) of $\frac{1}{650}\text{days}^{-1}$ (frequency) and $\frac{1}{6046.34}\text{km}^{-1}$ or $\frac{1}{60}\text{degrees}^{-1}$ (wavenumber), have not been plotted to preserve image clarity.

$$\text{Velocity conversion: } \frac{\left(3.25\ \text{cms}^{-1}\right) \times 86400\ \text{secs}}{(1000 \times 100)\,\text{cm}} = 2.808\ \text{km/day}$$

$$\frac{\left(6.5\ \text{cms}^{-1}\right) \times 86400\ \text{secs}}{(1000 \times 100)\,\text{cm}} = 5.616\ \text{km/day}$$

$$\text{Transit times: } \frac{6046.34\ \text{km}}{5.616\ \text{km/day}} = 1077\ \text{days (4 s.f)}$$

$$\frac{6046.34\ \text{km}}{2.808\ \text{km/day}} = 2153\ \text{days (4 s.f.)}$$

These transit times must then be expressed, along with the longitudinal width of the study area, as the number of image pixels they encompass (governed by image resolution);

$$\text{Longitudinal width: } \left(\frac{60^o}{0.25^o}\right) = 240 \text{ pixels}$$

$$\text{Transit times: } \left(\frac{1077 \text{ days}}{2.5 \text{ days}}\right) = 430.8 \text{ pixels}$$

$$\left(\frac{2153 \text{ days}}{2.5 \text{ days}}\right) = 861.2 \text{ pixels}$$

as the Radon transform algorithm treats any plot as a M×N pixel image. From here, the range of lineation angles created by these waves (with respect to the horizontal) can be calculated:

$$\phi_1 = \tan^{-1}\left(\frac{430.8}{240}\right) \text{ pixels} \rightarrow \phi_2 = \tan^{-1}\left(\frac{861.2}{240}\right) \text{ pixels}$$

$$\phi_1 = 60.88^o \rightarrow \phi_2 = 74.4^o$$

However, due to the trigonometric configuration of the Radon transform (figure 5.7), the lineation angles ϕ_1 & ϕ_2 calculated above, will be shown in corresponding Radon transforms at angles θ_1 & θ_2, calculated by $90^o - \phi_2$ and $90^o - \phi_1$ respectively. Therefore, for this investigation, all first mode baroclinic Rossby wave signals should according to theory, have transform angles between 15.6^o and 29.12^o.

5.4.3 LT plots

In this sub-section, LT plots are presented (see figures 5.17, 5.18, 5.19 & 5.20) and a visual analysis of their content given. (Note that for this visual inspection, edge tapering is omitted, although in subsequent sections the process has been applied.)

None of these images display the clear, inclined lineations sought. Instead, the only distinct feature is a series of sub-vertical stripes of alternating polarity, only present in plots generated using the more restrictive 3^o latitude × 4^o longitude and 5^o latitude × 5^o longitude search windows. This restriction would suggest that this feature is likely to be a processing artifact, a suggestion supported by their prominent periodicity and lack of any magnitude reduction when considering images derived using selected data (figures 5.19 & 5.20).

5.4.4 Radon Transform Results

To investigate the remaining variability within these LT images, this sub-section presents Radon transforms of LT plots shown in §5.4.3. Note that the transforms, shown in figures

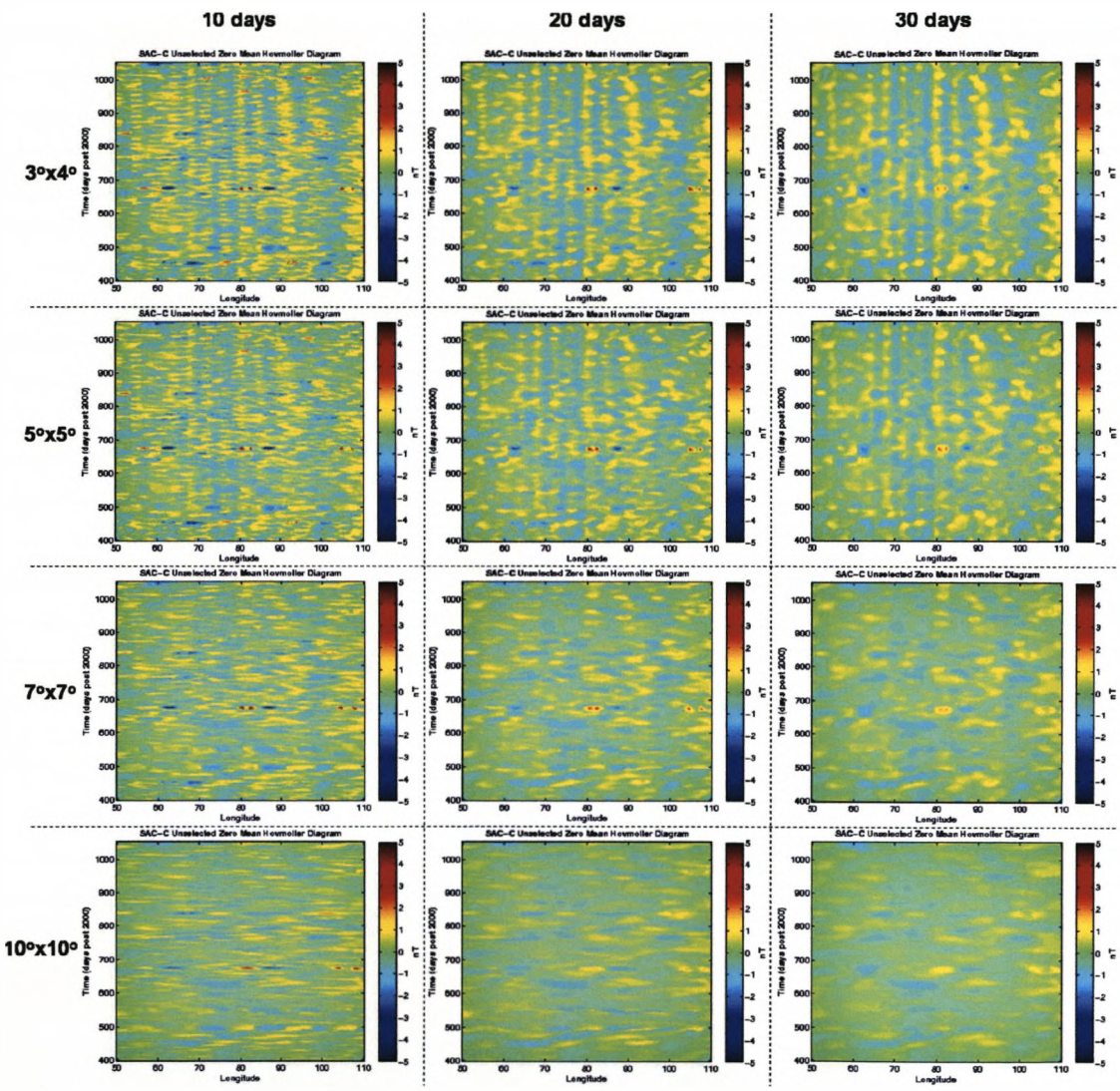

Figure 5.17: Hovmöller plots, generated using unselected SAC-C scalar observations. Each LT plot is constructed using a unique configuration of search window dimensions in the data reduction process (§3.5.3). The combination of these parameters is given by the label on each row (spatial) and column (temporal).

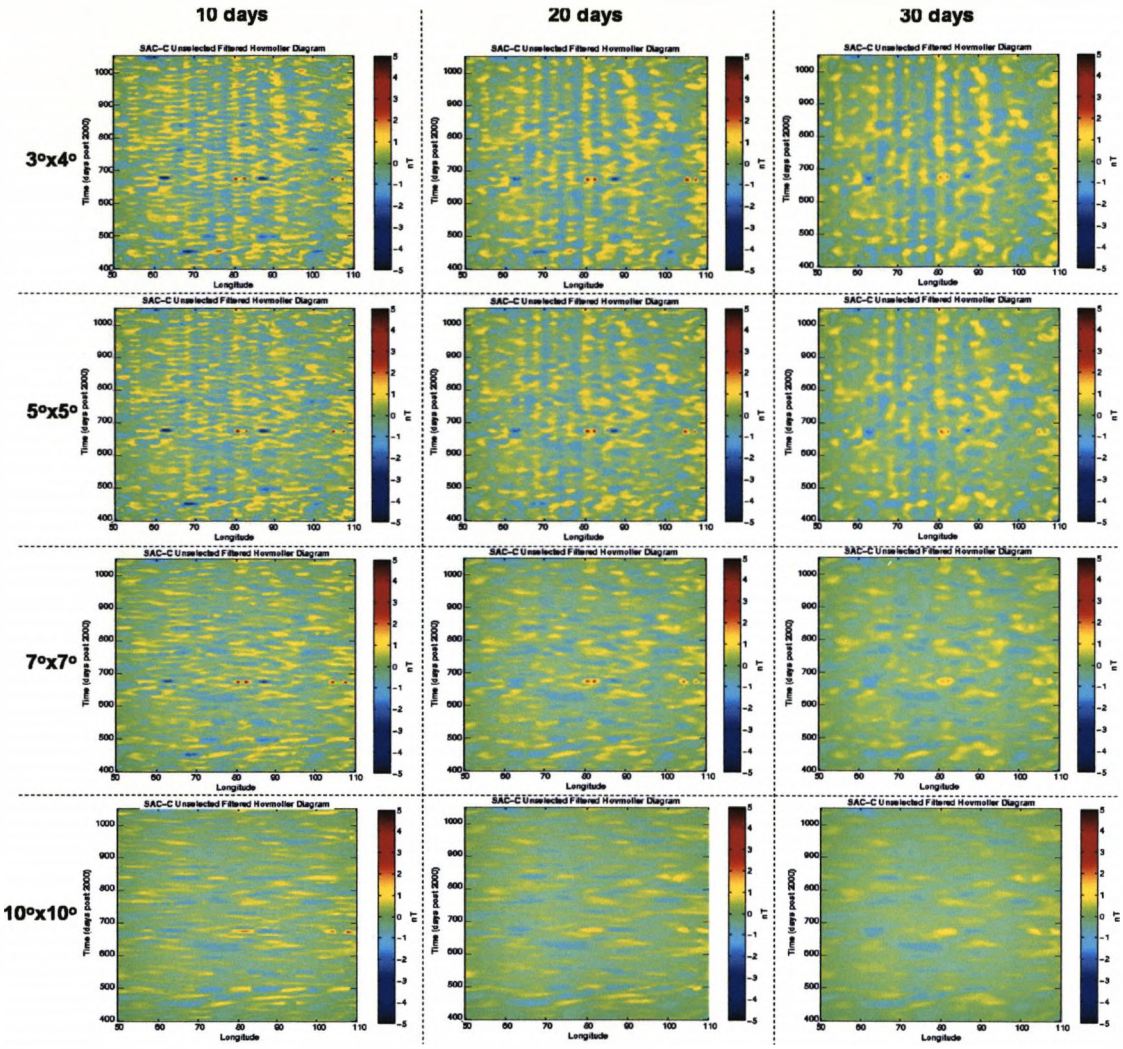

Figure 5.18: Hovmöller plots generated from unselected SAC-C scalar observations. Each image represents a filtered version of the equivalent image from figure 5.17. As before, the search window dimensions used to construct these grids are indicated by row and column labels.

5.21, 5.22, 5.23 & 5.24, only display angles corresponding to westward signal propagation ($0^o \rightarrow 90^o$).

These images are far more complex than the idealised synthetic transform shown in figure 5.8. However, while both selected and unselected transforms display similar small-scale variability at high angles, their low angle characteristics vary greatly. While selected transforms display mainly large-scale single-polarity variability, across both sub-vertical and low angles (likely a result of extensive smoothing of sparse grids, resulting from limited data volumes [see figure 5.25]) and provide rather inconclusive results, their unselected counterparts show variability on a much smaller scale. However, none of these images display any high amplitude signals within the range of target angles identified in §5.4.2, with the only persistent feature taking the form of two low amplitude peaks, located at an angle of $\sim 27^o$ and $x' \sim \pm 37.5$. Given

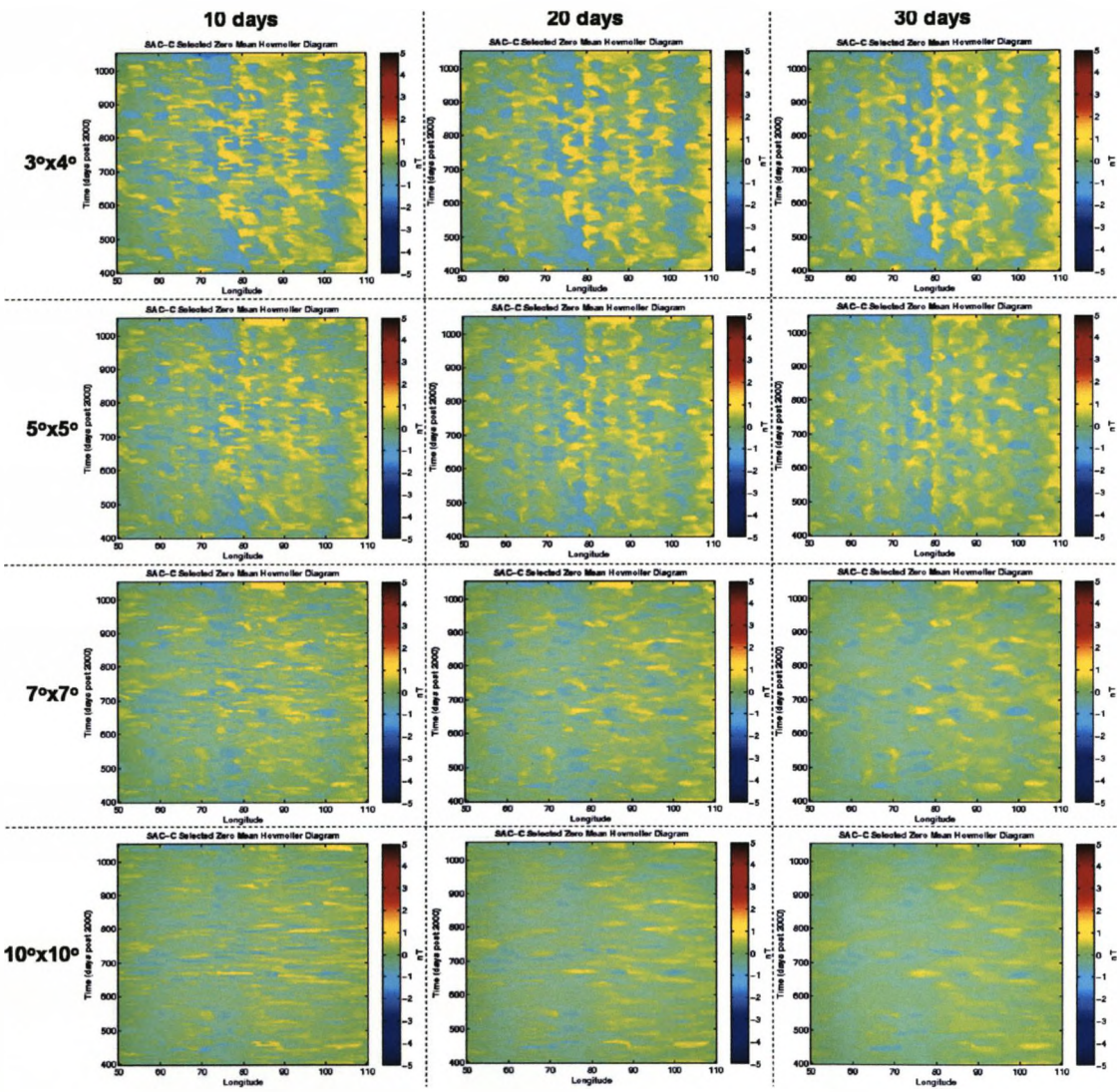

Figure 5.19: Hovmöller plots, generated using selected SAC-C scalar observations. Each LT plot is constructed using a unique configuration of search window dimensions in the data reduction process (§3.5.3). The combination of these parameters is given by the label on each row (spatial) and column (temporal).

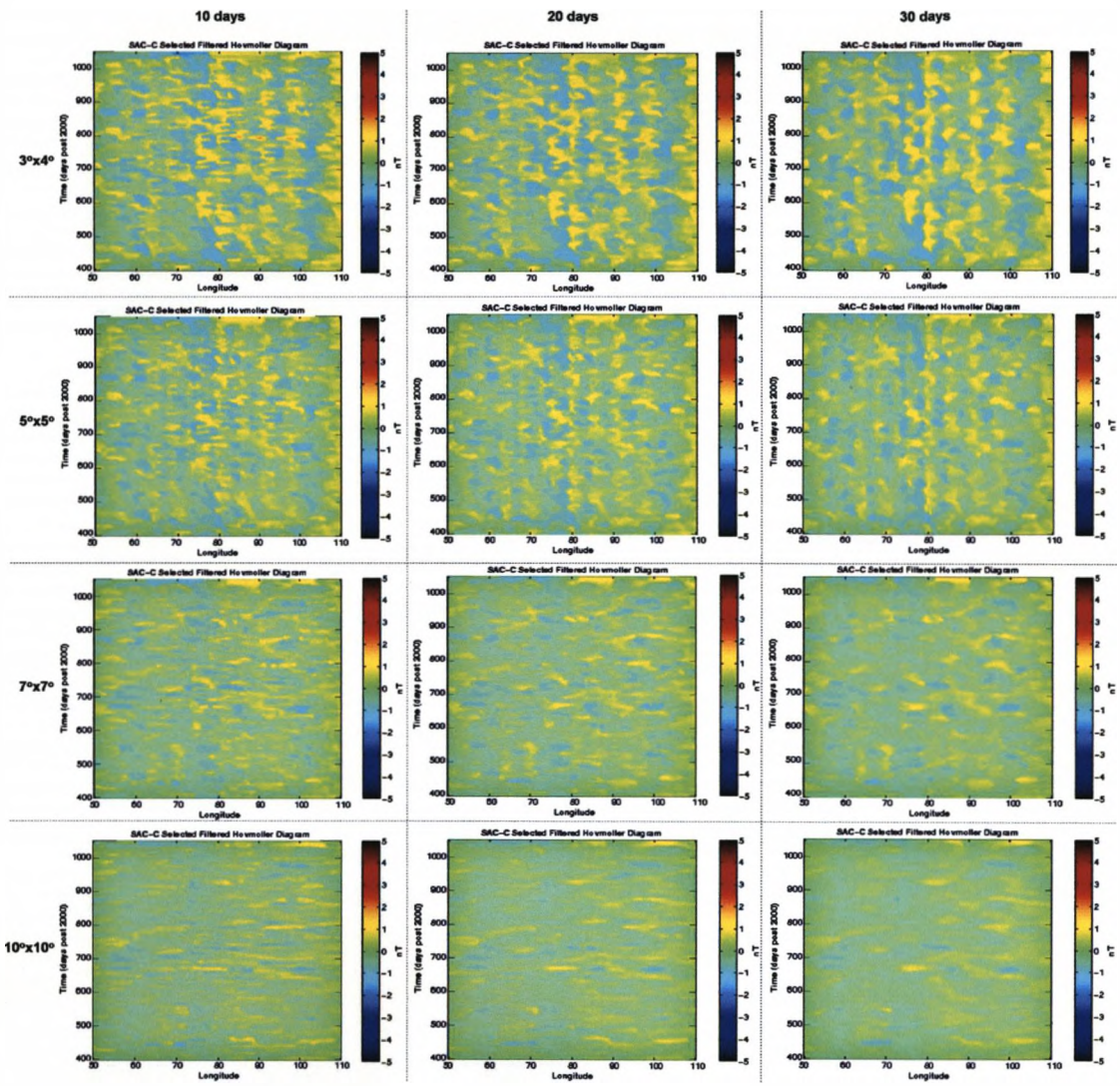

Figure 5.20: Hovmöller plots generated from selected SAC-C scalar observations. Each image represents a filtered version of the equivalent image from figure 5.19. As before, the search window dimensions used to construct these grids are indicated by row and column labels.

the low magnitude of these signals (relative to the remaining variability in each image), their validity could be questionable, particularly when their limited abundance within each image is considered.

In order to simplify the complex variability these transforms present, variance plots (calculated as a function of transform angle) of the transforms shown in figures 5.21, 5.22, 5.23 & 5.24 have been derived (figures 5.26, 5.27, 5.28 & 5.29). The advantage of these plots over a standard transform map is the ability to separate true signal from random noise more cleanly - while random noise tends to cancel when stacked, consistent signal will persist and become more prominent. Inspecting these plots it is clear that many are indeed far simpler than the transforms from which they were derived. Immediately, the high angle variability seen in most selected transforms has gone (suggesting this region of variability was a product of noise) and similarly, when considering plots derived from unselected transforms, very little variability seems to have transferred from map to graph form. However, unlike in the selected case, where no distinctive variability is seen within the range of target angles, when considering unselected plots, two small peaks in variance can be identified (peaks in plots from more restrictive transforms appear with higher prominence), both within the target range ($\sim 17^{o} \rightarrow 18^{o}$ & $\sim 27^{o}$) identified previously, although the lower angle peak is of lower magnitude and is less distinct. However, whether these peaks are robust features, attributable to real signal is unclear and they certainly are not definitive evidence of Rossby wave activity. Indeed, if the target angles are adjusted, removing velocities provided by superceded linear theory and all non-Indian ocean derived ocean colour data, the lower limit of the target range increases to 26.24^{o} (5.75 cms^{-1}), eliminating the lower angle peak from consideration entirely. Therefore, the Radon transforms and variance plots presented in this sub-section suggest the presence of a magnetic signal with the correct angular characteristics ($\sim 27^{o}$) within SAC-C data. However, its prominence and magnitude vary with changing processing restrictions, casting doubt over its validity, although the limited abundance of appropriate peaks in the corresponding Radon transforms (figures 5.21 & 5.23) may account for the reduced variance magnitudes of the peak.

5.4.5 2-Dimensional Fourier Transform Results

One of the major advantages of the 2D-FT approach is the treatment of noise vs. coherent signal. While the spectral characteristics of noise will tend to be distributed randomly throughout a spectrum, a coherent signal will tend to be organised along a single linear path, known as the dispersion relation (see figure 5.30). The dispersion relation;

$$c = \frac{f}{k} \tag{5.6}$$

links the phase speed of a waveform (c), to its frequency (f) and wavenumber (k). Therefore, any Rossby wave induced signals resulting from this analysis should follow a linear trend, determined by the phase speed of the wave. In this case, the theoretical phase speed for this

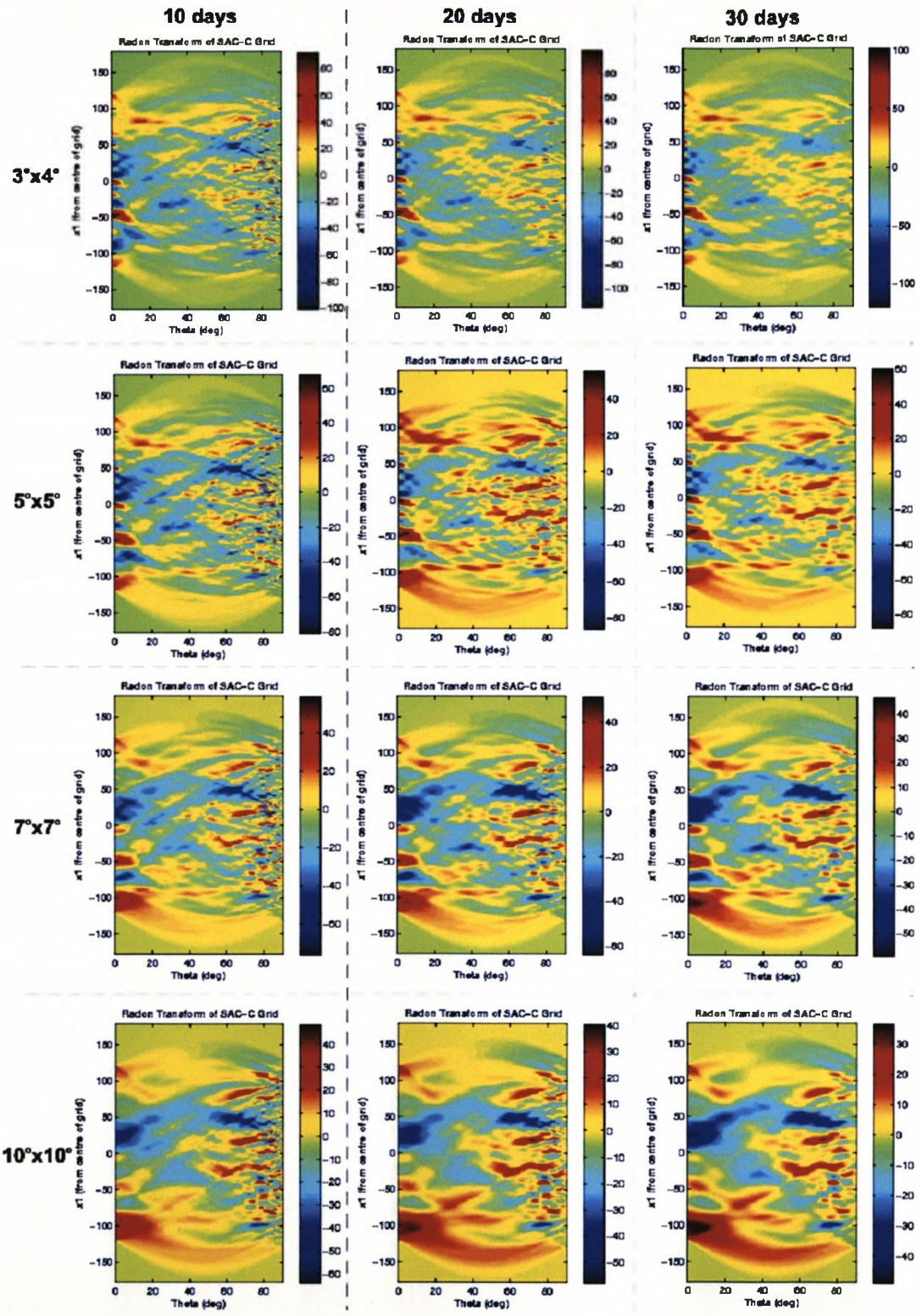

Figure 5.21: Radon transforms of the LT plots shown in figure 5.17. Each of the transforms in this figure, corresponds to the LT plot in the same location in figure 5.17.

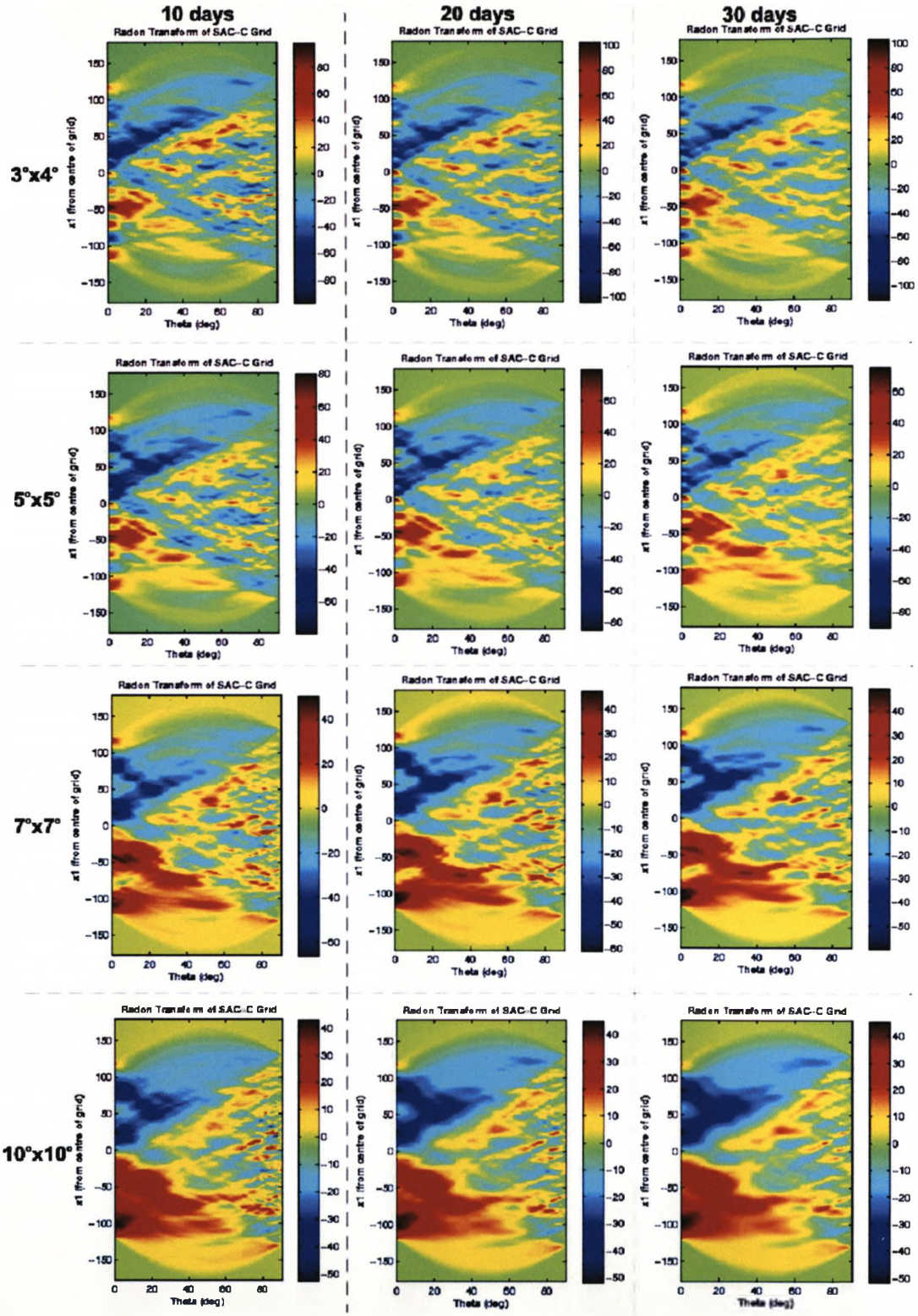

Figure 5.22: Radon transforms of the LT plots shown in figure 5.19. Each of the transforms in this figure, corresponds to the LT plot in the same position in figure 5.19.

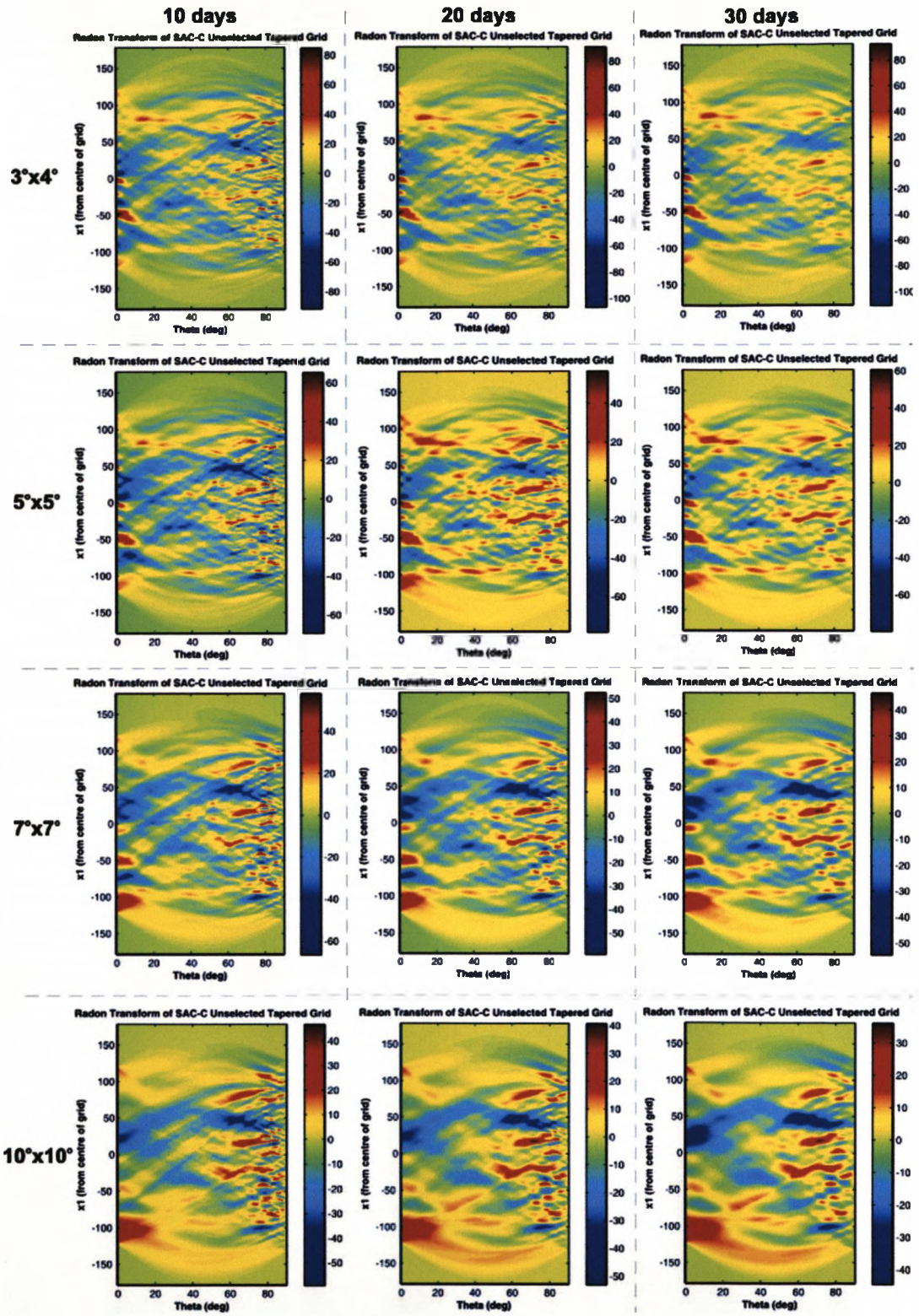

Figure 5.23: Radon transforms of the LT plots displayed in figure 5.18. Each of the transforms in this figure, corresponds to the LT plot in figure 5.18 with the same position.

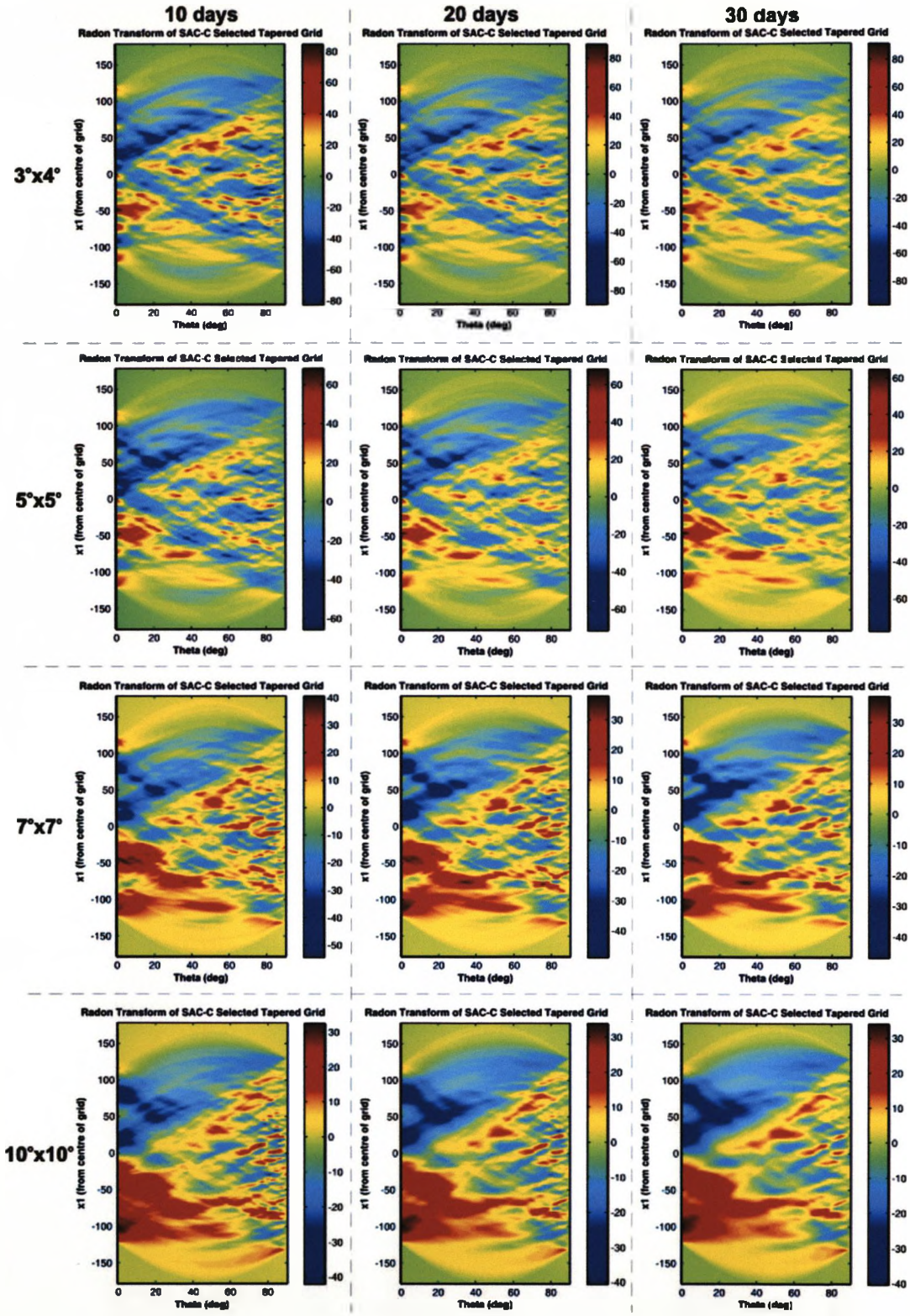

Figure 5.24: Radon transforms of the LT plots displayed in figure 5.20. Each of the transforms in this figure, corresponds to the LT plot with the same position in figure 5.20.

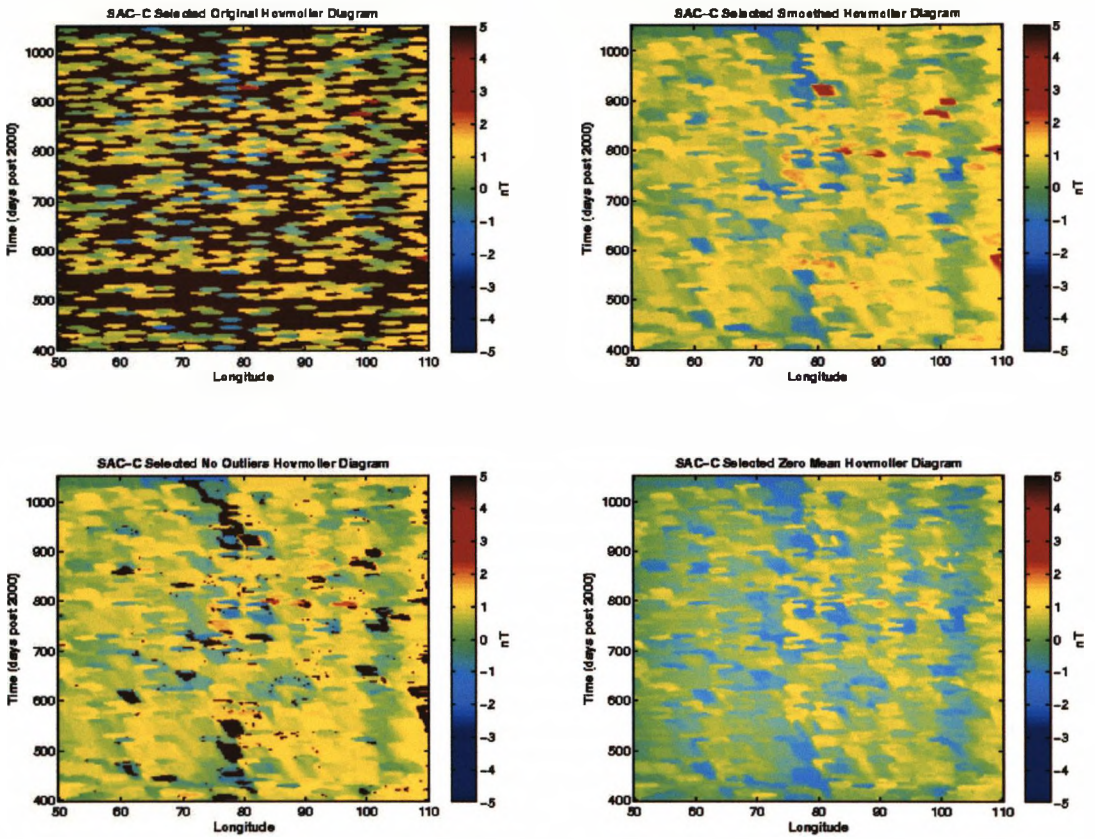

Figure 5.25: A series of plots, illustrating both the sparsity in data coverage when using selected data (upper left panel) and the effect of several processing steps (upper right: gap smoothing, lower left: outlier rejection & lower right: row mean subtraction) applied to these grids in an effort to rectify this limitation. Note that the LT grid in the upper left panel is derived using a 3° latitude × 4° longitude × 10 day data reduction search window.

latitude (6 cms^{-1}), as predicted by Killworth and Blundell [2003a,b], has been used. The resulting dispersion line is marked on the results of this analysis (shown in figures 5.31, 5.32, 5.33 & 5.34 and derived using LT plots displayed in §5.4.3) as a red dashed line.

Unfortunately, inspection of these figures reveals no distinct linear trends along the marked dispersion line, although could a Rossby wave signal nevertheless be present? Plots displayed in figure 5.35 suggest that while the distance between generation points of individual magnetic fields (generated by a wave crest or trough) is fixed (by the wave), changing the wavelength of those fields (governed by ambient field strength & direction, flow strength, etc) can result in an observed magnetic field (sum of individual fields) with a wavelength equal to either that of the wave, or infinity (individual fields cancel). Therefore, while in most cases Rossby wave signals should adhere to the dispersion line plotted and their absence suggests a lack of any signal, there is a small possibility that magnetic conditions have caused the removal of any signals through cancellation or that Rossby wave signals conform to a single spectral configuration, resulting in a single peak in the corresponding spectra (although no such peaks have been noted).

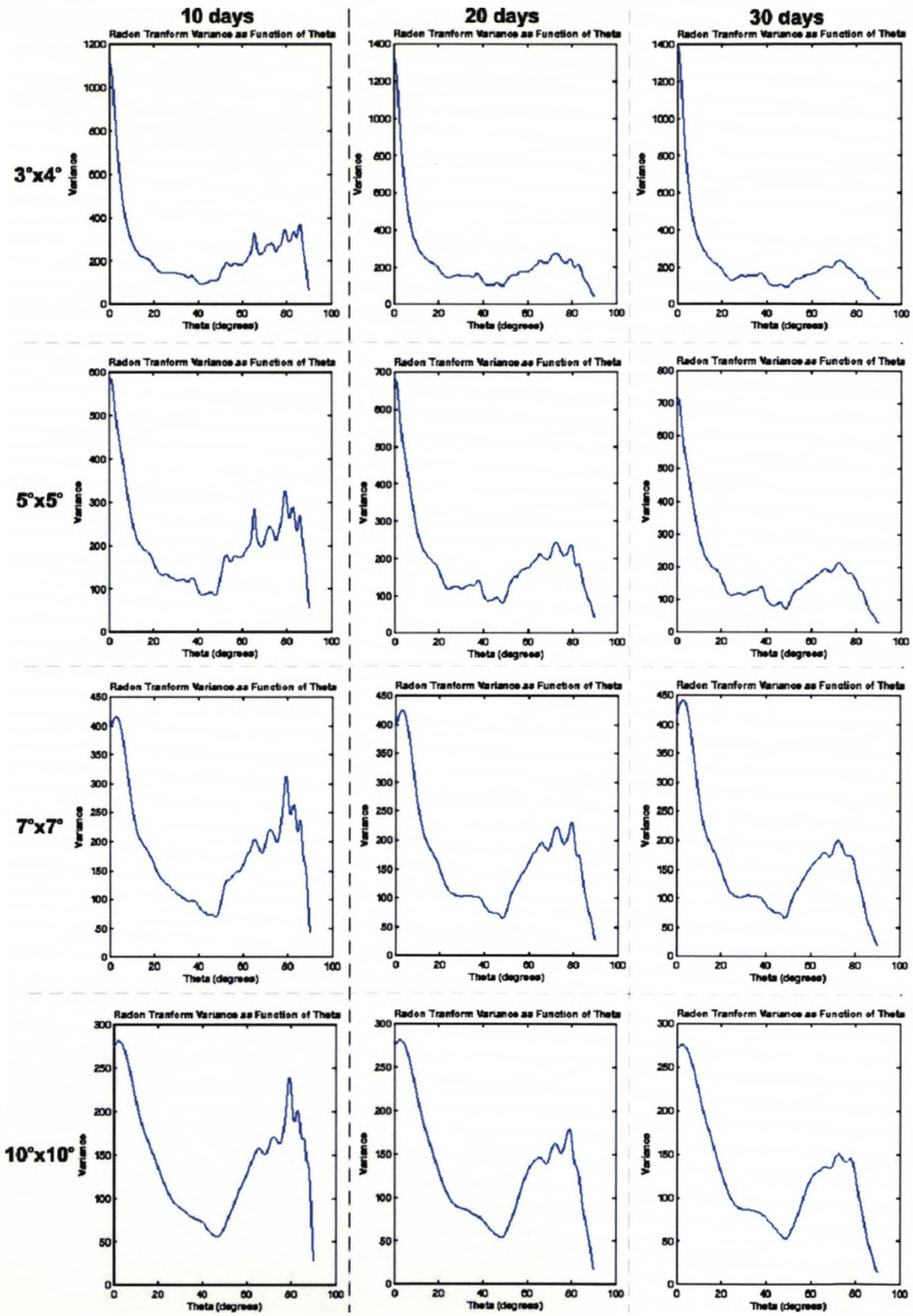

Figure 5.26: Plots of data variance (calculated as a function of transform angle), generated from the Radon transforms displayed in figure 5.21. These images aim to indicate angles (showing as peaks in data variance) within each image, that exhibit coherent linear signals (indicative of Rossby wave activity).

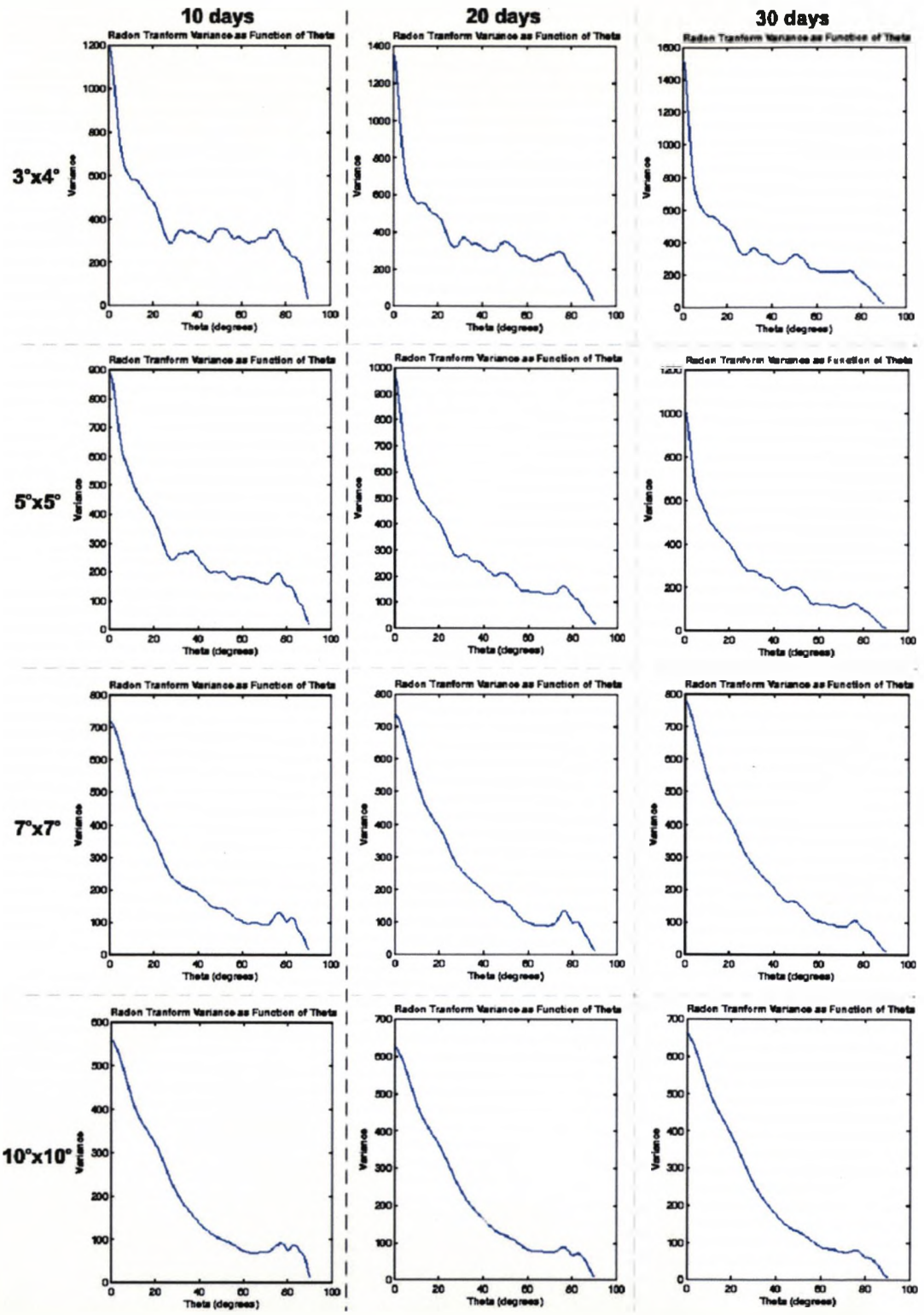

Figure 5.27: Plots of data variance (calculated as a function of transform angle), generated from the Radon transforms shown in figure 5.22. These images aim to indicate angles (showing as peaks in data variance) within each image, that exhibit coherent linear signals (indicative of Rossby wave activity).

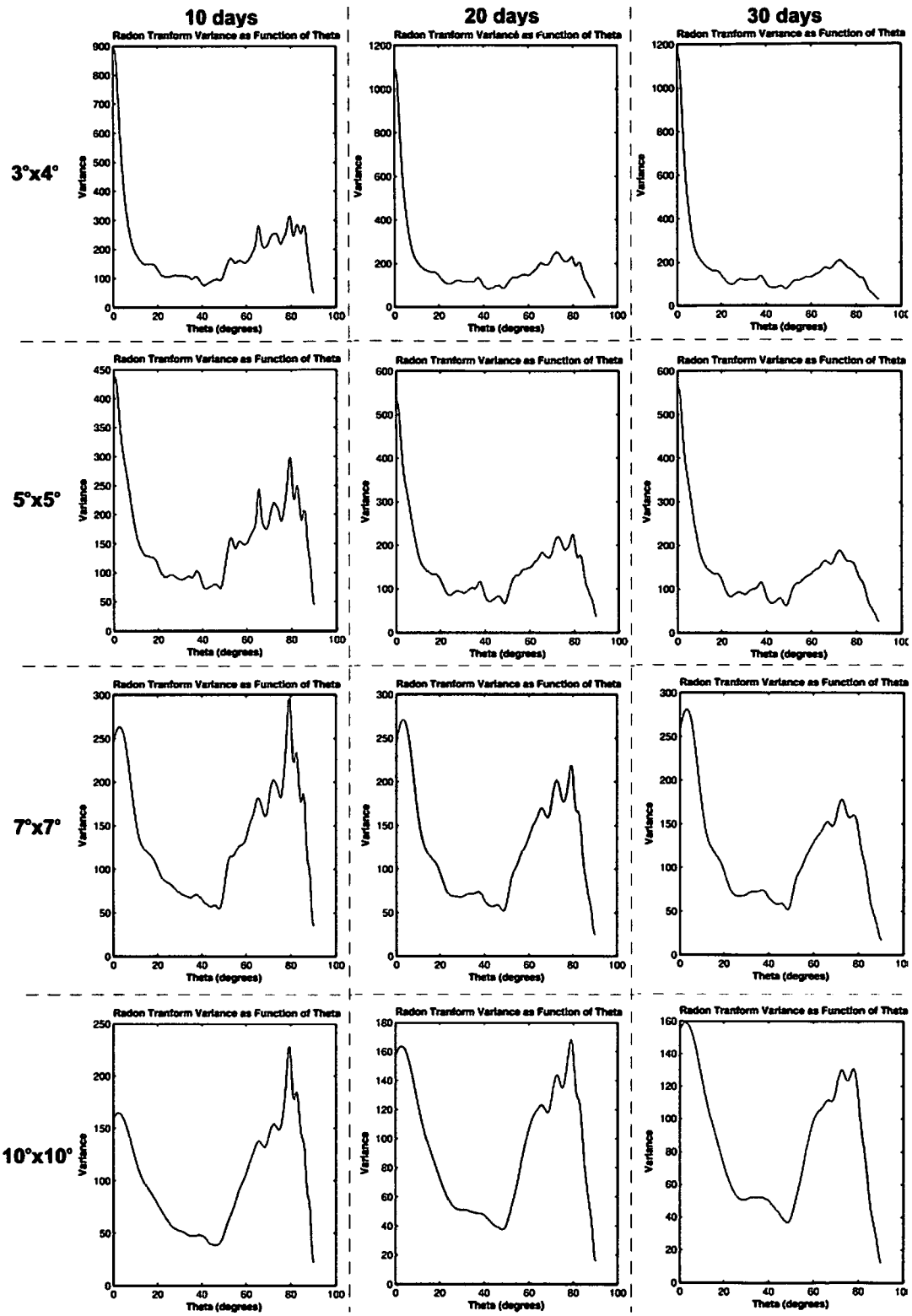

Figure 5.28: Plots of data variance (calculated as a function of transform angle), generated from the Radon transforms displayed in figure 5.23. These images aim to indicate angles (showing as peaks in data variance) within each image that exhibit coherent linear signals (indicative of Rossby wave activity).

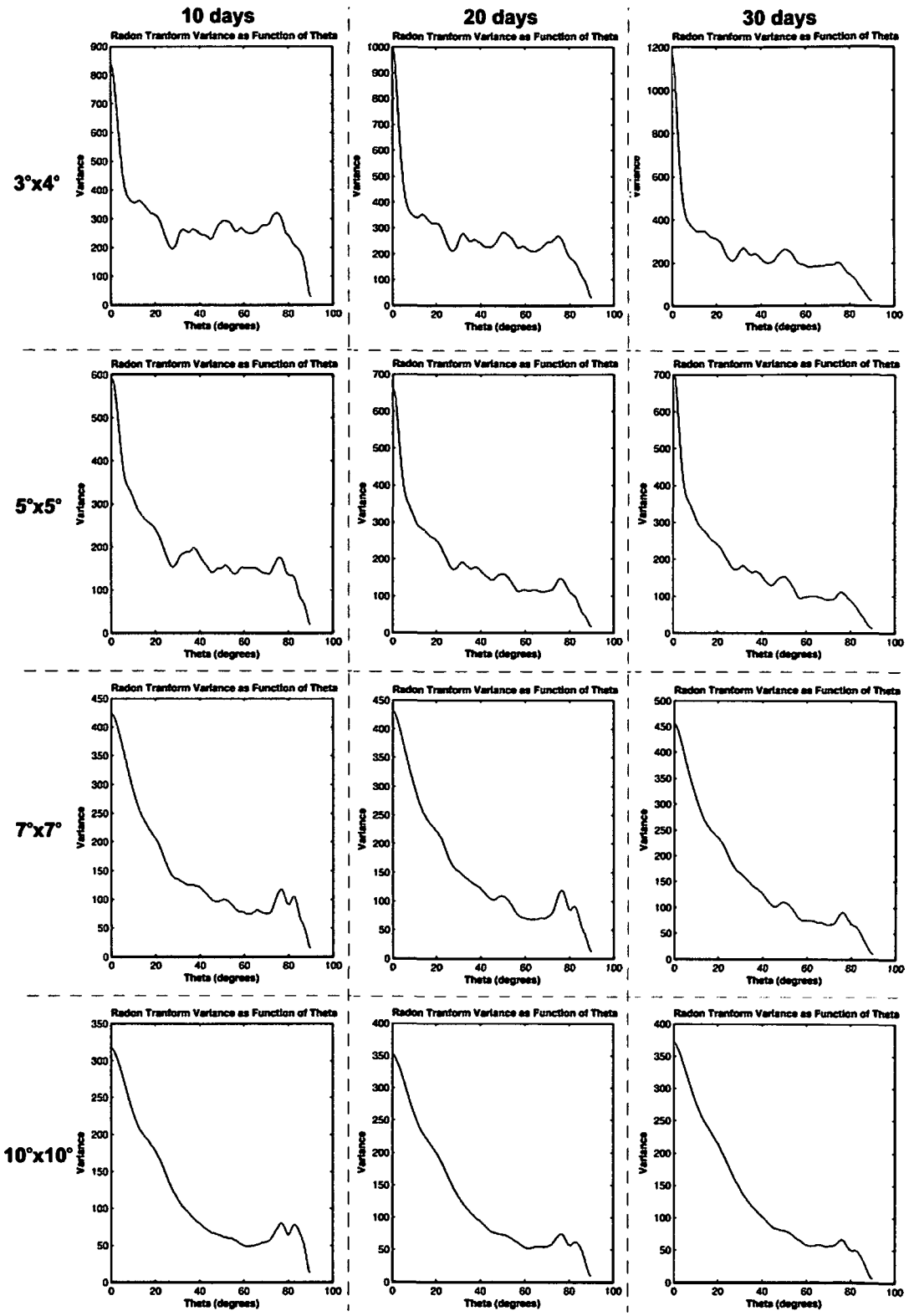

Figure 5.29: Plots of data variance (calculated as a function of transform angle), derived from the Radon transforms shown in figure 5.24. These images aim to indicate angles (showing as peaks in data variance) within each image, that exhibit coherent linear signals (indicative of Rossby wave activity).

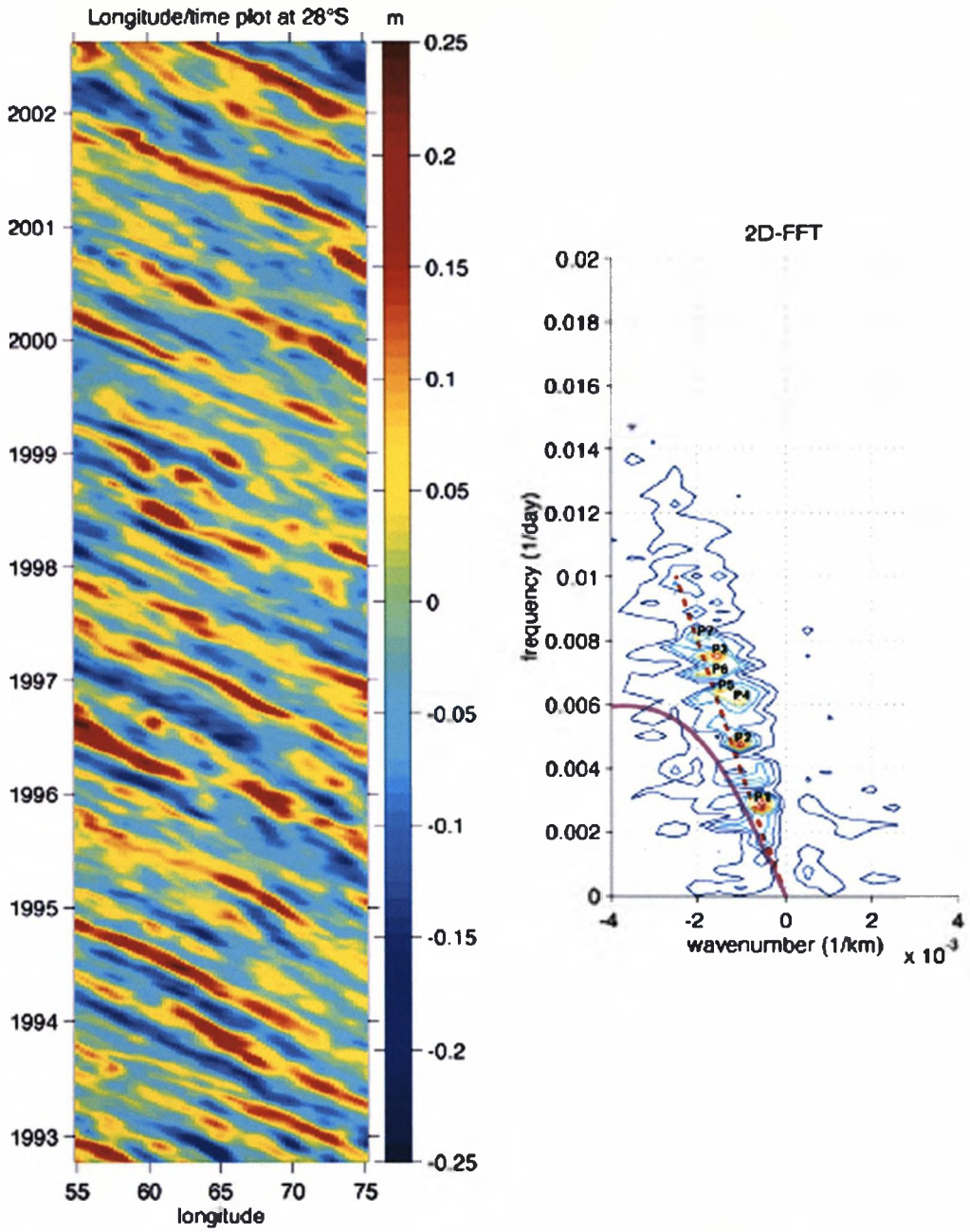

Figure 5.30: An example of a 2D-FT analysis conducted on satellite altimeter data (*from Cipollini et al. [2006]*). The left panel presents a standard LT plot of the observations, while the panel on the right displays its 2D-FT. The magenta line shown in the transform represents a dispersion relation with Rossby radius of 42.9km. The red dashed line in this image represents a wave speed of 4.7cms^{-1} (predicted by Killworth et al. [1997] as the theoretical wave speed for this latitude). Note that all spectral peaks associated with this wave system are aligned to the dashed line (P^1, P^2, etc), suggesting that linear series of peaks in a transform, such as the one shown here, could be linked to the same wave system.

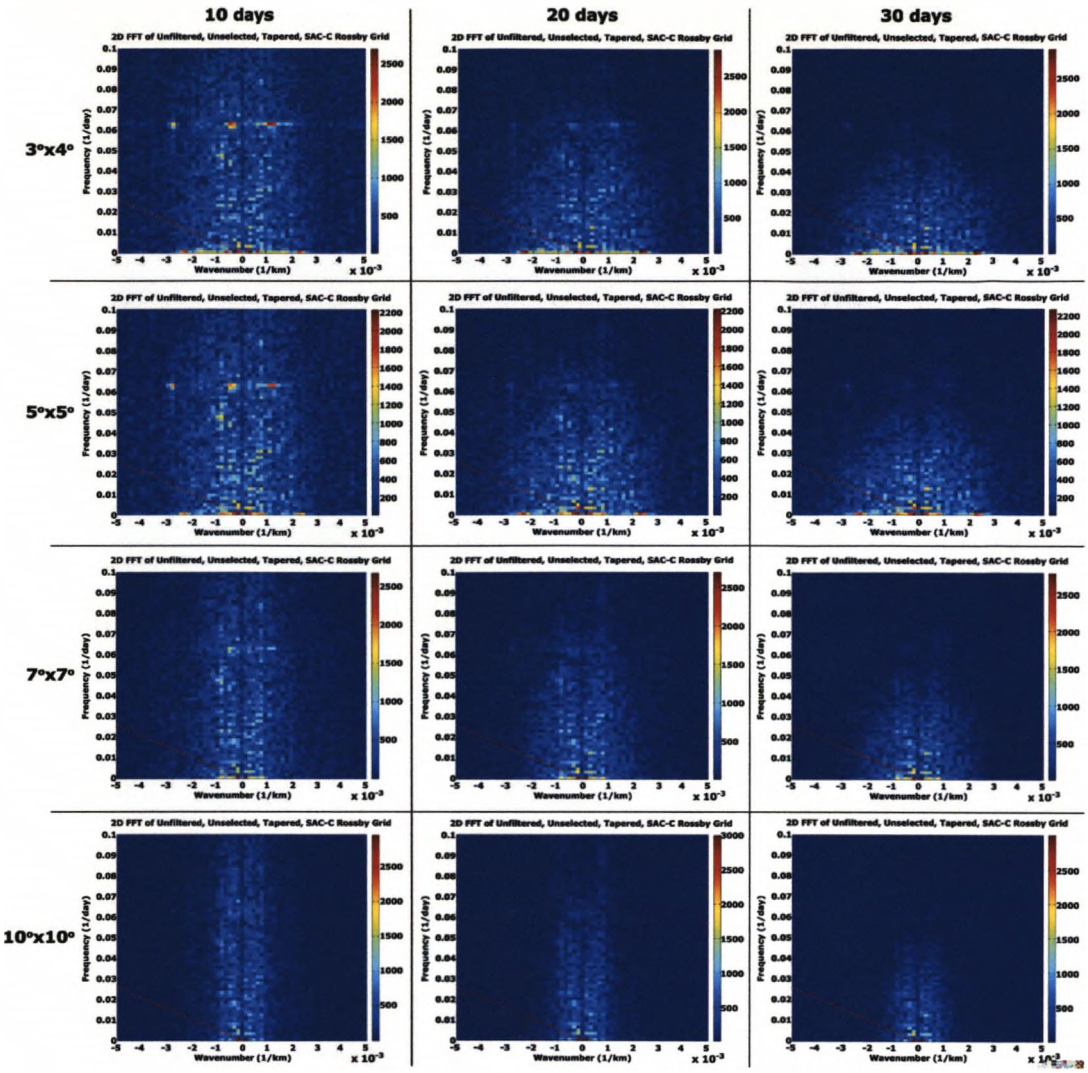

Figure 5.31: 2D Fourier transforms of unselected, unfiltered SAC-C based LT plots shown in figure 5.17. The red dashed line in these images represents the 6cms^{-1} Rossby wave dispersion relation.

5.5 Discussion

At the beginning of this investigation, it was stated that the focus would be the first baroclinic Rossby mode, due to the stronger barotropic mode being too fast to monitor using current satellite data sources. This unfortunate restriction immediately posed the question as to whether the first baroclinic mode would generate a magnetic field of sufficient magnitude to be identified above background noise. Unfortunately, as yet the answer to this question is 'no', as many of the results presented as part of this investigation have failed to provide any hint of Rossby wave activity. The only positive evidence is provided by small amplitude peaks in plots of Radon transform variance (see figures 5.26 & 5.28), where the transform angle of the signals corresponds well with angles predicted using theoretical wave speeds (§5.4.2). Unfortunately, similar signals are not found in corresponding 2D-FT spectra (figures 5.31,

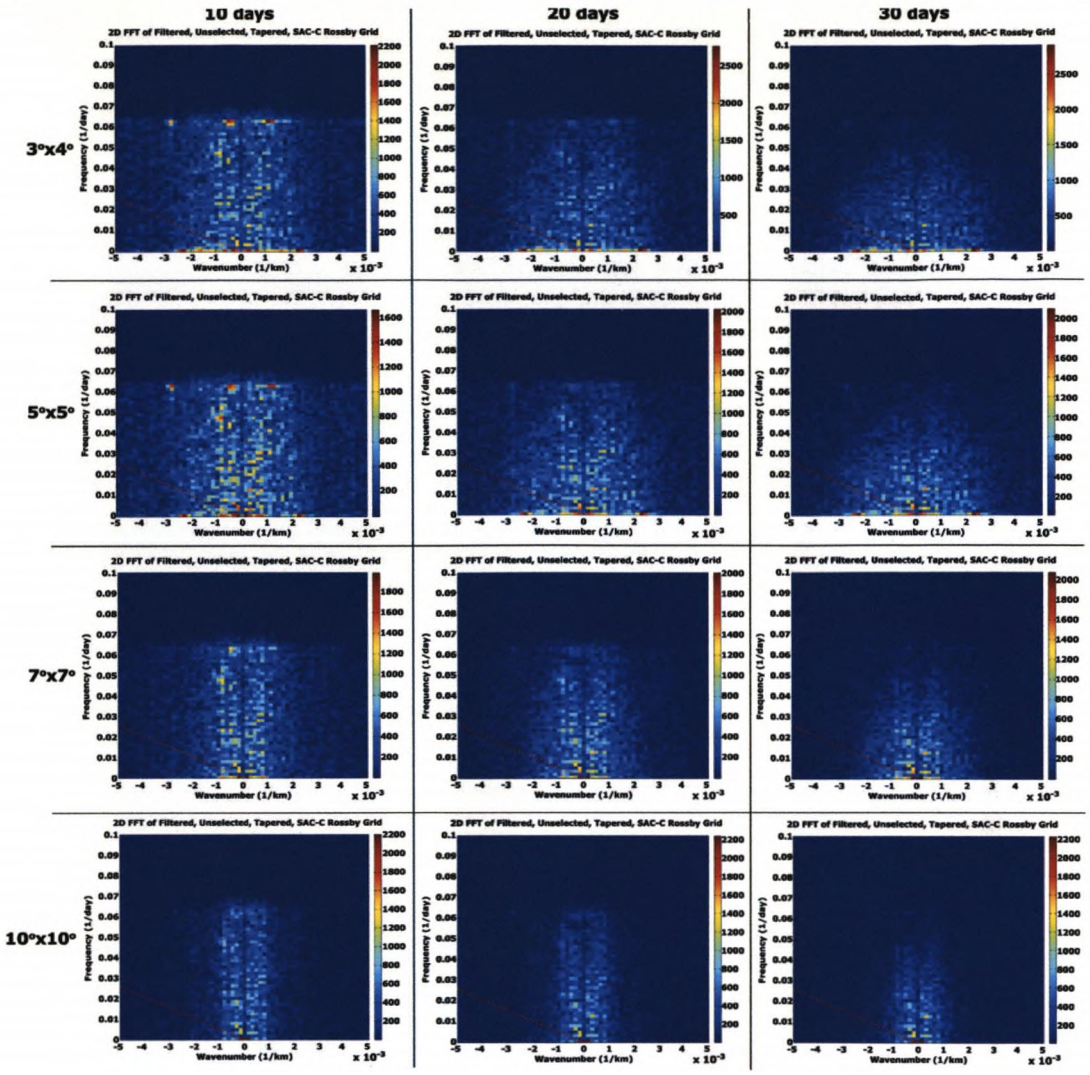

Figure 5.32: 2D Fourier transforms of unselected, filtered SAC-C LT plots displayed in figure 5.18. The red dashed line in these images represents the 6cms^{-1} Rossby wave dispersion relation.

5.32, 5.33 & 5.34), suggesting this feature may be a consequence of data noise (even though this process is compromised slightly, by uncertainties in the behaviour of signal spectral characteristics [§5.4.5]). Therefore, assuming that the study of barotropic Rossby waves remains beyond the limits of satellite technology for the foreseeable future, the only way a definitive identification of Rossby wave generated magnetic fields can be achieved is through comparison of these observational results with numerical calculations, at which point any similarities may act to validate the results presented in this chapter.

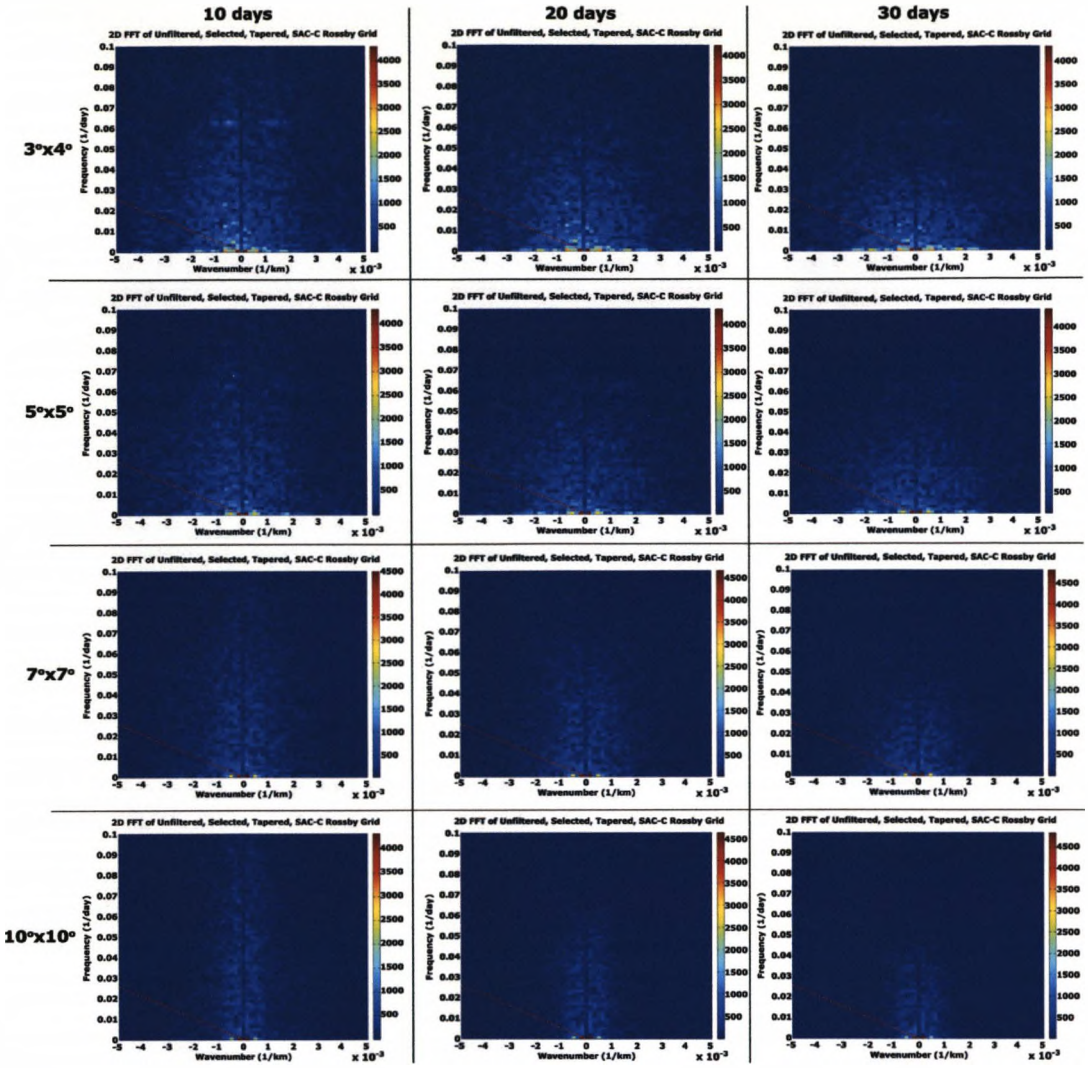

Figure 5.33: 2D Fourier transforms of selected, unfiltered SAC-C based LT plots shown previously in figure 5.19. The red dashed line displayed in these images represents the 6cms^{-1} Rossby wave dispersion relation.

5.6 Summary

In this chapter, the details of an in-depth feasibility study of oceanic first mode, baroclinic Rossby wave generated, magnetic fields have been given. Satellite magnetic observations from the SAC-C spacecraft have been analysed using numerous signal processing techniques, in an effort to identify the magnetic response to these large-scale wave motions in the magnetic record. Unfortunately, the results of the investigation have been inconclusive, often showing weak signals that may not even be oceanically driven. However, it is unknown whether the limited results found throughout this investigation are the result of unfavourable geomagnetic conditions preventing a substantial magnetic field from being generated, or whether this investigation focuses on a baroclinic Rossby mode that will quite likely produce a much smaller magnetic field than its faster moving barotropic relative (on account of its surface

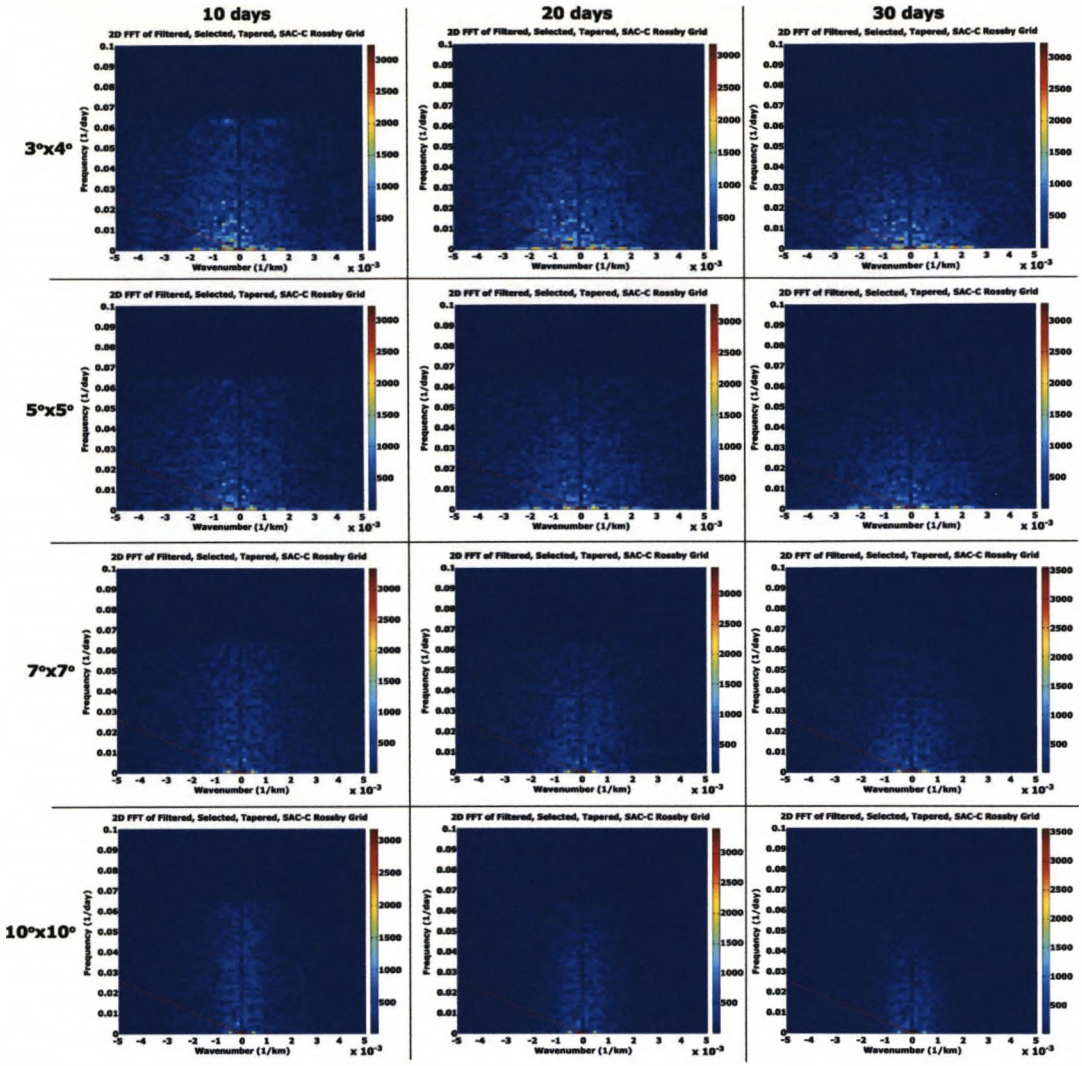

Figure 5.34: 2D Fourier transforms of selected, filtered SAC-C derived LT plots shown in figure 5.20. The red dashed line show in these images represents the 6cms^{-1} Rossby wave dispersion relation.

intensification and lower mass transport). In summary, taking into consideration the findings presented here, and the theoretical and oceanographic arguments made at the start of the investigation, the future identification of magnetic fields generated as a consequence of oceanic Rossby waves is unlikely to prove successful, until either more sophisticated analysis methods are developed to identify weak signals in noisy data, or improved data coverage allows the study of the faster, stronger-flowing first barotropic mode. Until that time comes, the introduction of numerical models (and the associated magnetic field predictions) that can be validated against physical observations, may provide additional evidence to suggest the presence of Rossby wave generated signals in geomagnetic records.

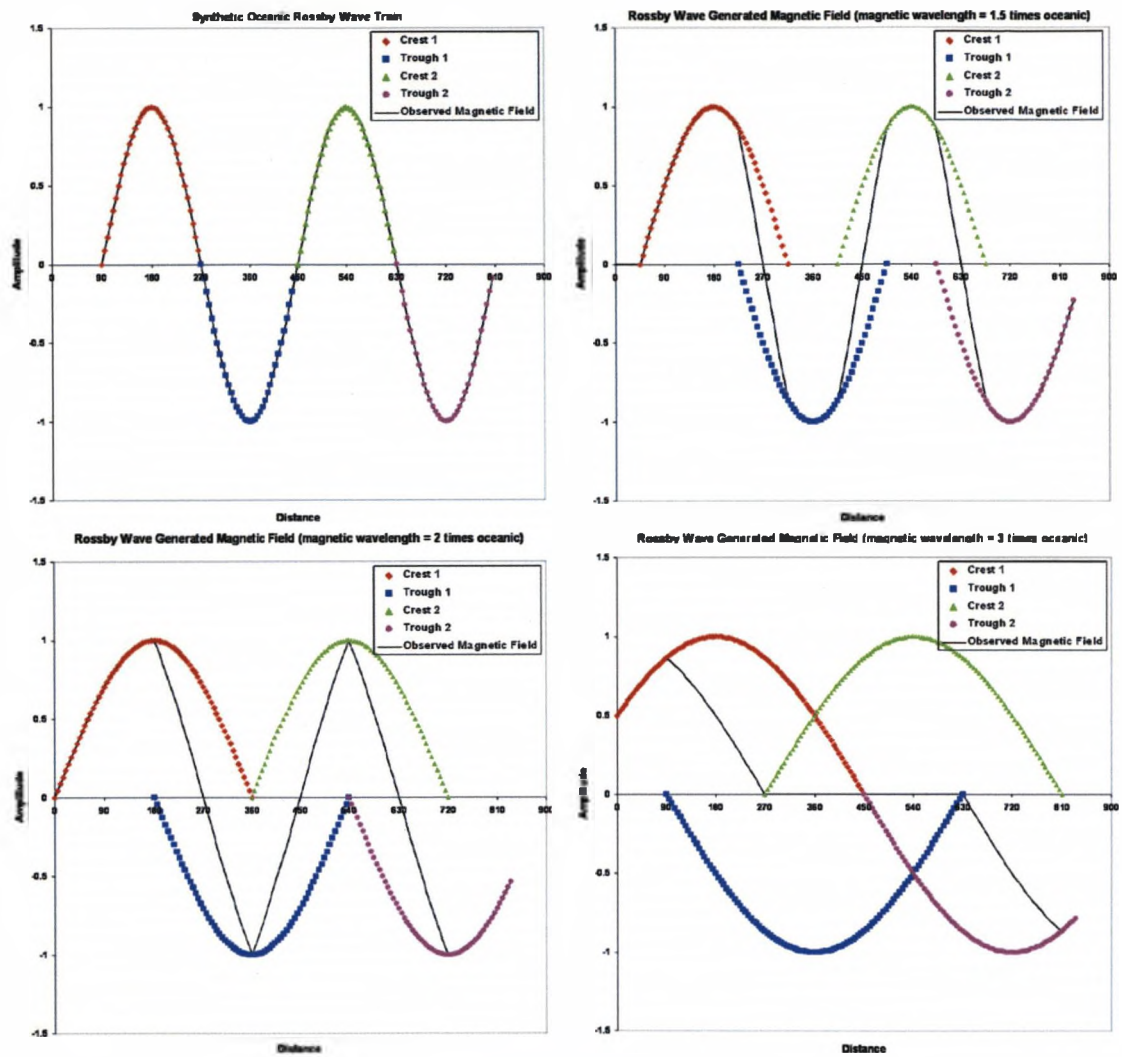

Figure 5.35: A series of plots illustrating the effect of variable single field wavelength on observed magnetic field wavelength (when single field separation is fixed). The upper left plot shows the profile of a typical Rossby wave, with a wavelength and period prescribed by its wave speed. The other 3 plots in the figure display examples of magnetic fields this wave may generate. While the wavelength of these magnetic fields may vary individually (upper right: 1.5 × oceanic, lower left: 2 × oceanic & lower right: 3 × oceanic), because the separation of their generation points is fixed, in most cases the wavelength and frequency of the observed magnetic field remains constant with the oceanic wave.

Chapter 6

Research Conclusions and Future Possibilities

In this final chapter, the findings of this thesis will be summarised and their place within oceanography and geomagnetism discussed. This chapter will also attempt to address each of the scientific aims established at the beginning of this thesis, before a model for future work on this topic is suggested and the impact of forthcoming advances in geomagnetic field observation discussed.

6.1 Work Summary & Main Scientific Findings

1. **Development of automated data preparation suites (chapter 2):**

   Semi-automated data preparation routines have been developed to generate analysis datasets configured specifically to study oceanically generated magnetic fields. These routines also allow regular updating of data volumes as observations are released from their respective sources, requiring minimum input from the data user.

2. **Development of harmonic modelling code & testing (chapter 3):**

   When investigating periodic phenomena it is clear that, given the non-continuous nature of magnetic observations, traditional Fourier methods are difficult to implement. Therefore an approach has been used whereby a 3 parameter harmonic function (equation 3.1) is fitted to observations to estimate their frequency content. To ensure the method's stability extensive synthetic testing has been conducted, which attempts to replicate numerous aspects of observations in a controlled environment.

3. **Identification of localised periodic flow in multiple magnetic datasets (chapter 3):**

   Analyses of satellite and ground based magnetic data within and around the Argentine basin (S. Atlantic) have identified a localised magnetic signature, consistent with generation by a circulation with $\sim$ 25 day rotational period, previously identified in

oceanographic studies of the region (Fu et al. [2001], Tai and Fu [2005], Hughes et al. [2007]). While statistical analysis of magnetic observations revealed the possible presence of a global scale overprinting field with a similar frequency (figures 3.20 & 3.21), harmonic modelling has shown strong indications that magnetic fields matching anticipated characteristics have been found, particularly in Port Stanley observatory data (figure 3.22), with maximum field magnitudes up to 1.5 nT (1 -1.5 nT at ground level (PST: figure 3.22) and 0.1 - 0.5 nT at satellite altitude (CHAMP & SAC-C: figure 3.44)).

4. **Identification/verification of tidally generated magnetic fields using 3 parameter harmonic modelling (chapter 4):**

   A preliminary investigation of tidally generated magnetic fields has been conducted, using a combination of CHAMP satellite observations and the harmonic modelling technique used and tested extensively in chapter 3. Low latitude estimates of numerous tidal constituents have be made, with estimates of the M2 tidal field being verified through comparison with the previously published work of Tyler et al. [2003] (figure 4.7). Estimates of tidal fields in the polar regions are also presented (figure 4.10), their identification facilitated by extensive data selection prior to analysis. Unfortunately, no previously published estimates of polar tidal fields exist to allow comparison, while field magnitudes are consistently higher than equivalents at lower latitudes, suggesting an influence from ionospheric tidal fields or other noise sources (e.g. other external fields).

5. **Development of a multi-constituent tidal field modelling methodology (chapter 4):**

   To facilitate the observational modelling of complete tidal fields, a new modelling approach has been designed. The method integrates harmonic modelling and spherical harmonic expansions, producing a model that represents tidal fields as series of spherical harmonic expansions, each modulated by a tidal frequency (equation 4.2). As a result, the need for data binning is removed, while incomplete tidal estimates [Tyler et al., 2003, Maus and Kuvshinov, 2004] are avoided with the inclusion of along track filtering (previously applied as a pre-analysis processing stage) and satellite attitude estimates in the model formulation as an error covariance matrix $\mathbf{C_e^{-1}}$ (equation 4.4). The modelling framework is also designed in a modular fashion, allowing the investigation of an infinite number of tidal constituents with a single inversion (computing power permitting).

6. **Production of a multi-constituent tidal magnetic field model (chapter 4):**

   Using the newly established modelling methodology, a magnetic field model of 16 major tidal constituents has been presented. This data driven approach is favoured, as when working with satellite data, ionospheric and oceanic tides (which share operational

frequencies and are driven by the same underlying astronomical effects) are both considered internal field sources, making separation by direct source modelling difficult. When the resulting model is compared (in filtered form) with previously published estimates (Tyler et al. [2003]) the two are comparable (figures 4.7 & 4.14), suggesting the method being used is robust. However, comparisons with unfiltered numerical field estimates (Maus and Kuvshinov [2004], Kuvshinov and Olsen [2005]) yield poorer results (figures 4.16, 4.17 & 4.18), with the introduction of high amplitude short wavelength variability, particularly when evaluated at ground level (figure 4.20). Importantly, the absence of similar features in oceanically driven numerical estimates suggests these highly variable model estimates are influenced by ionospheric tidal fields, included in the model as a consequence of both oceanic and ionospheric tidal field sources being considered as internal field sources by the satellite data being modelled (the modelling methodology used cannot distinguish between contributions from numerous internal field sources using a single dataset). This hypothesis is supported by the presence of similar variability in earlier estimates of polar tidal fields, also thought to be heavily influenced by external tidal fields (figure 4.10). Fortunately, given the apparent success when considering filtered tidal estimates, it is suggested that more stringent pre-modelling data processing and increased volumes of model data (including previously absent low altitude/ground observations) may substantially improve the quality of future models.

7. **Production of Rossby wave isolation scripts & testing (chapter 5):**

   Scripts have been developed and tested (using physically relevant synthetic data) to identify magnetic fields generated by large-scale wave motion in the form of oceanic Rossby waves. The scripts include the generation of Hovmöller plots (using any satellite data source), along with the 2D Fourier and Radon transforms responsible for Rossby wave identification within those plots.

8. **Isolation of Rossby wave motion in the Indian ocean (chapter 5):**

   Detailed analysis of SAC-C satellite data (used for the consistency of its spatial distribution) using a variety of analytical methods has revealed few positive signs of Rossby wave generated fields. The only positive signs are presented as small secondary peaks in plots of Radon transform variance (figures 5.26 & 5.28), results not supported in 2D Fourier transforms of the same data. The lack of prominent signals may be heavily linked to the restriction of this investigation to first baroclinic Rossby waves, rather than stronger barotropic waves which propagate too quickly to be adequately resolved by current magnetic observations. While baroclinic waves can be resolved, their variability with depth means that mass transports comparable with barotropic waves are thought to be a rare occurrence. As a result, baroclinic waves are unlikely to produce magnetic fields as strong as those generated by barotropic waves, reducing the chances of observing these fields during analysis.

6.2 Proposed Solutions to the Major Scientific Aims of the Project

At the beginning of this thesis, key scientific aims were identified. This section addresses those aims, drawing on the findings presented throughout the thesis to form a synthesised understanding of where research on this topic stands.

1. **Generation of automated data preparation routines:**

   Before any of the scientific research attached to this thesis could be conducted, this aim had to be addressed. Due to the variety of flows investigated in this thesis, numerous magnetic datasets were involved. Therefore, scripts developed to remove any unwanted field contributions before analysis began were a priority. These processing routines are described in chapter 2, removing contributions from a chosen main field model, along with the additional data processing required for the removal of along track filters (e.g., individual satellite track isolation) and data selection (if required). Unfortunately, data must be downloaded manually from the relevant data source and the most appropriate main field model (CO2003, CHAOS or CM4) specified, making the scripts only semi-automated. However, their use throughout the investigations presented in this thesis has proved invaluable, as the availability of datasets that do not require additional processing has proved both highly convenient and efficient. Importantly, these routines are not limited to the study of ocean effects and are suitable for any application where field sources not currently parameterised in main field models are the target.

2. **Extending work on global tides, using more sophisticated analysis techniques:**

   While tidal magnetic fields have been identified previously in both satellite (Tyler et al. [2003]) and observatory (Maus and Kuvshinov [2004]) data, the use of along track filtering limited these studies to signal identification alone. Therefore, no estimates of the full tidal field have ever been provided when analysing magnetic observations. Chapter 4 presented an extensive tidal investigation that attempted to advance on previous studies, beginning with the identification of filtered tidal estimates using harmonic modelling (§4.3.2), which corresponded well with the previous work of Tyler et al. [2003] (the successes of Tyler et al. [2003] & Maus and Kuvshinov [2004] when using this method would lead to its use throughout chapters 3 & 4 of this thesis). This preliminary investigation was advanced with the introduction of the modelling methodology introduced in §4.4, with the aim of replacing filtered estimates with a model of the full tidal field generated by numerous tidal constituents. Unfortunately, severe deficiencies in the model (possibly due to ionospheric tidal fields) were found when compared against numerically produced estimates (from an oceanographic base). However, comparison of a filtered version of the model with Tyler et al. [2003] gave confidence in the approach being used, suggesting that modifications to input data

and their treatment before modelling would result in model improvements, although separation of oceanic and ionospheric tidal fields will always be difficult when using this approach. This work implies that, for the first time, it is possible to produce estimates of tidal magnetic contributions which can be used by the geomagnetic community. Importantly, this model does not rely on numerical calculations, a preference when applying it to magnetic data prior to further analysis. However, the lack of a reliable model from this study has knock-on effects, as tide-free datasets have not been available for the analysis of smaller flows.

3. **Investigation of smaller scale/amplitude flows using tide-free magnetic datasets:**

   While tides produce the most dominant global scale, periodic oceanic magnetic fields and have already been addressed, magnetic fields associated with other corner-stone flow types are also investigated throughout this thesis (chapters 3 & 5). Note that while spatially complex, non-periodic flows have been studied previously (e.g., Lilley et al. [2004], Tyler [2005], Manoj et al. [2006]), these processes are clearly very difficult to understand and so preference has been given to the study of localised periodic flow (in the form of a small circulation in the Argentine basin) and large scale, well structured wave motion (Rossby waves). However, the limited results from these studies (chapters 3 & 5 respectively) highlight that as attention moves away from the dominance of global tides, successful field isolation becomes more difficult. These studies also illustrate that periodic flows are easier to identify, while spatial scale is only a secondary factor in field isolation. However, it should be noted that while localised Argentine flow is largely barotropic (which should produce larger magnitude fields due to larger mass transports), analysis of Rossby waves focused on the first baroclinic mode (as barotropic waves move too quickly to be sampled by current magnetic satellites) and so magnetic fields of comparable magnitude are unlikely, although the unique spatial/propagational characteristics of Rossby waves should be identifiable using the methods implemented. When geostrophic/ageostrophic flow regimes and ambient magnetic field configurations are considered, it is clear that oceanically generated magnetic fields will always struggle to match the magnitudes their mass transports promise, possibly explaining the small field magnitudes identified throughout this thesis.

6.3 A Model for Future Work

This thesis has shown that investigation of oceanically generated magnetic fields is far from simple and so to maximise future successes, using the results of this thesis, I suggest the following plan for future study.

An obvious first target is global tides. While this topic has been visited several times before (including chapter 4 of this thesis), no comprehensive model of its contributions to the geomagnetic field has been provided. Given the magnitude of these fields (3-4 nT at satel-

lite altitude) compared to other flow types studied here (1-2 nT), it is clear that until an accurate representation of tidal fields is provided (using magnetic observations), successful investigation of other flows will be difficult.

From this point, it is suggested that study focuses on other periodic targets, ordering them in terms of their estimated field magnitude and spatial scale (specific field conditions may reduce or enhance fields, although mass transport represents a good estimate of induced field magnitude), while targets should ideally be highly geostrophic and barotropic. Once periodic flow is exhaustively investigated, attention should turn to non-periodic flows, again prioritising by estimated field magnitude and spatial scale. Note that due to difficulties seen in this thesis (when investigating Rossby waves), the probability of success in each case must be established (due to data restrictions, etc) and unsuitable targets temporarily passed over.

The final analysis target is general ocean circulation. While this is possibly the most exciting proposition and of most use outside geomagnetism within the realm of oceanography, its non-periodic nature and highly complex spatial characteristics mean that identifying a suitable analysis technique may be difficult. It must also be noted that in a similar manner to the connection between oceanic and ionospheric tides experienced in chapter 4, the effects of steady ocean circulation may be extremely difficult to separate from lithospheric contributions. Therefore, it is advised that analysis of general circulation is avoided until other, simpler flows are comprehensively understood.

How, may technical advances affect the working plan outlined above? Simply put, any data or field model based advances can only improve estimates of ocean generated effects. While the improvement of field models is inevitable, the introduction of newer, more sophisticated magnetic satellites is also a given. Indeed, the launch of the SWARM satellite constellation in 2010 should prove revolutionary for geomagnetism, not only in terms of data accuracy and volume, but also in terms of the sophisticated ways its dual altitude, single plus a pair configuration can be utilised, with mission simulations using synthetic SWARM data having already promised improvements in ocean generated field estimation (Olsen et al. [2006a]).

In summary, this thesis has attempted to improve the existing understanding of oceanically generated magnetic fields through the detailed study of global and local scale, periodic and non-periodic flow. These studies have illustrated the difficulties associated with identifying magnetic fields of this type, while also establishing a suggested plan for optimal future investigation. Ultimately this thesis has shown that, at present, the level of understanding of these fields is not sufficient to be of great use to oceanographers, although their potential for use within other aspects of geomagnetism in the near future (with the addition of further research) is undeniable.

Appendix A

Supplementary Results from Argentine Basin Analysis

In this appendix, additional findings relating to chapter 3 (using full length, interpolated observatory time series) are presented, generated using selected methods from the study. Therefore, differences between results are due solely to the additional data used here.

A.1 Statistical Analysis

In this section, several full length observatory series (shown in figure A.1) are statistically investigated. As in chapter 3, analysis begins with the plotting of the filtered PST field vector (selected and unselected) through time within a 3D space. As before, these vector wander plots (shown in figure A.2) show hints of 25 day period circulatory behaviour, embedded within a complicated background structure, which is investigated using frequency spectra of PST vector time series (shown in figure A.3). Unlike previously, in some cases the spectra display considerable 25 day ($\sim$ 0.04 cpd) variability, particularly in selected Y component data. However, the absence of a similar feature in figure 3.18 suggests this signal has arisen due to the additional data involved.

To investigate these results further, PST and NGK filtered time series are compared with the CEOF mode of Hughes et al. [2007] (that describes the target circulation from an oceanic viewpoint). This stage of the analysis begins with the calculation of frequency dependent coherence between the CEOF mode (at 40°S, 43°W) and magnetic time series (figure A.4). Note that as before (chapter 3), all magnetic series are decimated to match the CEOF mode's three day sampling. As in chapter 3, coherence plots are complex and exhibit no clear peaks anywhere in the region of 25 days (coherences are also consistently below the 95% significance levels displayed in each panel of the image), although series from both observatories appear simpler after data selection, indicating this processing is having a positive effect.

The second stage of this comparison takes the form of spatial correlations between the pre-

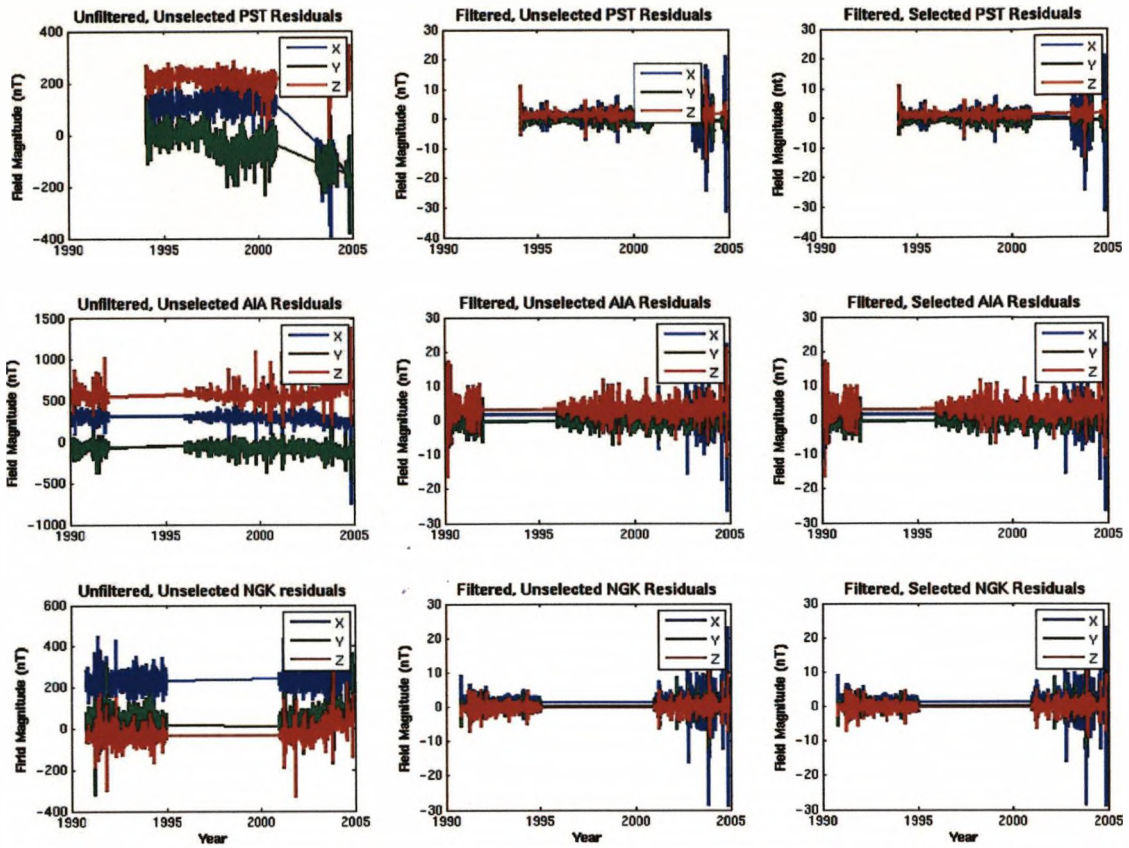

Figure A.1: Plots of unselected, unfiltered residuals (left) and both unselected (centre) and selected (right) filtered residuals used in this analysis. Data from PST occupy the top row, AIA the central row and NGK the bottom row.

viously introduced CEOF mode and NGK & PST selected and unselected, filtered magnetic series, generating the maps shown in figures A.5 & A.6. These images clearly indicate that additional series length has had a minimal effect on correlations (although long series correlations are generally statistically significant over a wider region of the basin). While small differences can be seen between short (figures 3.20 & 3.21) and long series versions of the maps, correlation magnitudes are still marginal, while their spatial behaviour remains largely consistent, resembling the circulation phase distribution identified by Fu et al. [2001] & Hughes et al. [2007]. However, similar distributions in NGK correlations suggest this feature is not oceanic and due to either a global scale field source or the projection of the CEOF structure onto correlations, facilitated by their low magnitudes.

These statistical tests have shown that extensive gap interpolation has not resulted in a dramatic deterioration of analysis results presented in chapter 3. Instead, in one case (figure A.3) results appear to have improved, with the addition of $\sim$ 25 day signals in the Y component of selected PST data, the same series that showed strong 25 day variability figure 3.22. However, the lack of improvement in other results casts doubt over whether this improvement is due to increased series length or happenstance.

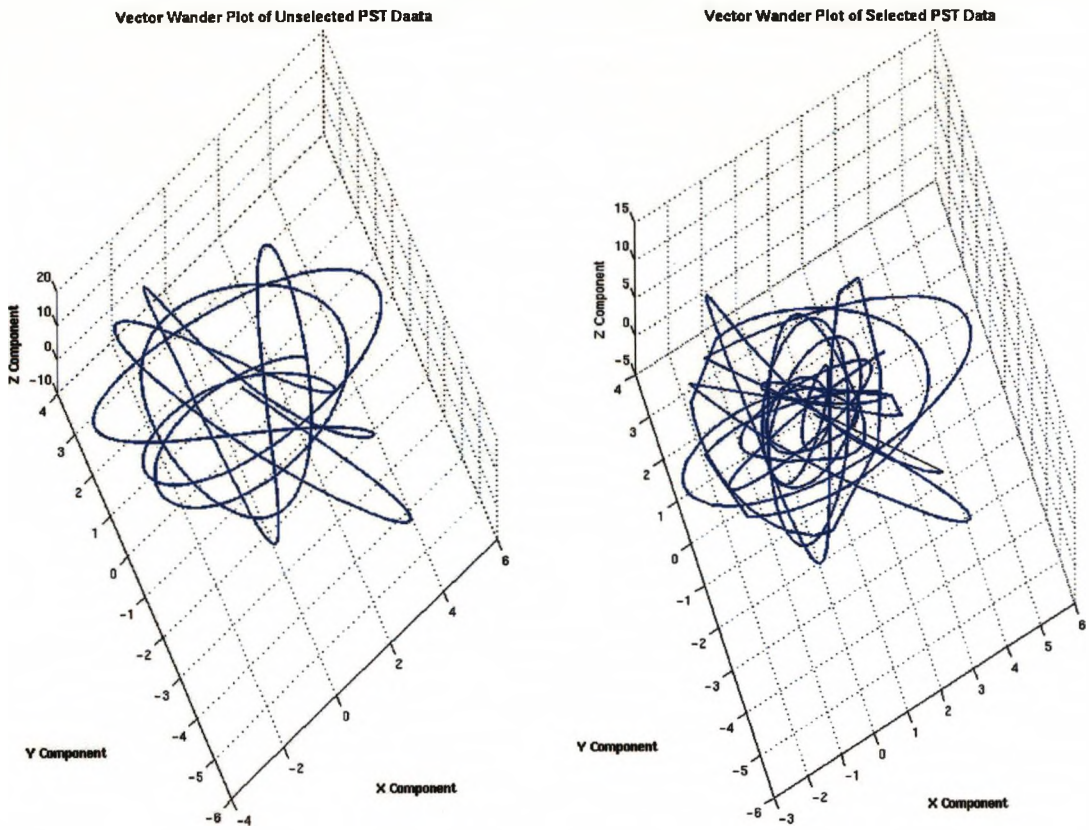

Figure A.2: Vector wander plots of 100 days of filtered PST residuals, both in unselected (left) and selected (right) forms.

A.2 Full Series EOF Analyses

In this section single and dual station EOF analyses, conducted using full length NGK, PST & AIA observatory series are presented. Once again, this section aims to determine whether full length interpolated series positively or adversely affect analysis results.

A.2.1 Single Observatory EOF Analyses

This subsection presents single station EOF analyses of PST & NGK data. Figures A.7 & A.8 graphically display the directional details of the resulting EOF modes, with further details shown in table A.1 and frequency spectra of each mode's expansion series shown in figure A.9. These results indicate that while mode details differ from those shown in chapter 3 (unsurprising when substantial additional data are analysed), these EOF modes are still difficult to understand, although interestingly the 3rd PST mode has a dominant Z component (in both selected and unselected forms), a desirable characteristic identified in chapter 3. Unfortunately, due to the limited number of modes in these analyses it is difficult to confidently state that this mode is an indicator of oceanic circulation and so dual station EOF analyses of PST and AIA series are conducted.

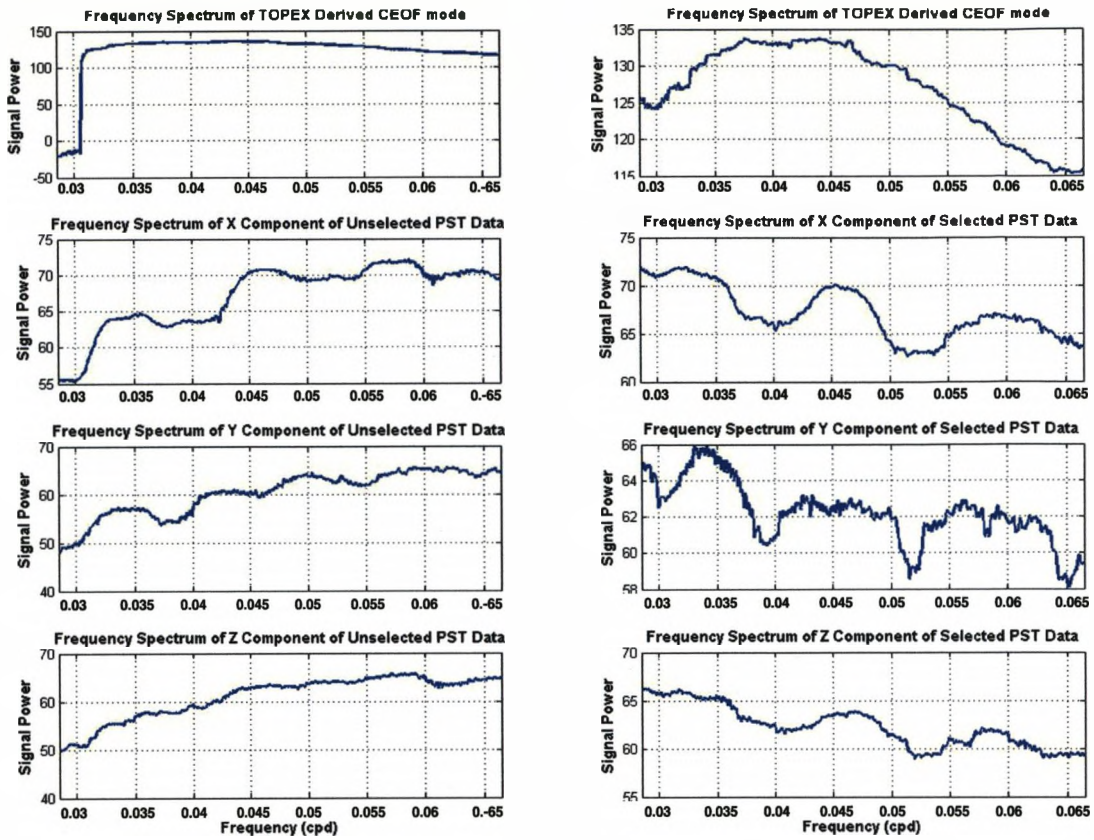

Figure A.3: Frequency spectra of unselected (left) and selected (right) PST data. Note that observatory time series have been decimated to 3 day sampling to match the reference Hughes et al. [2007] CEOF time series (shown in the top row).

	PST filtered EOFs			NGK filtered EOFs		
	1st	**2nd**	**3rd**	**1st**	**2nd**	**3rd**
X	-0.9428 (-0.9428)	0.1290 (0.1281)	-0.3074 (-0.3076)	-0.8888 (-0.8879)	-0.1066 (-0.1088)	0.4457 (0.4470)
Y	0.0559 (0.0556)	0.9702 (0.9707)	0.2356 (0.2339)	0.3705 (0.3731)	0.4051 (0.3981)	0.8358 (0.8380)
Z	-0.3287 (-0.3286)	-0.2050 (-0.2035)	0.9219 (0.9223)	0.2697 (0.2691)	-0.9080 (-0.9109)	0.3205 (0.3129)
% var	79.54 (79.55)	14.59 (14.59)	5.87 (5.86)	81.38 (81.28)	12.69 (12.83)	5.93 (5.89)

Table A.1: Mode statistics for single station EOF analyses shown in figures A.7 & A.8. Statistics of modes calculated using selected data are in brackets.

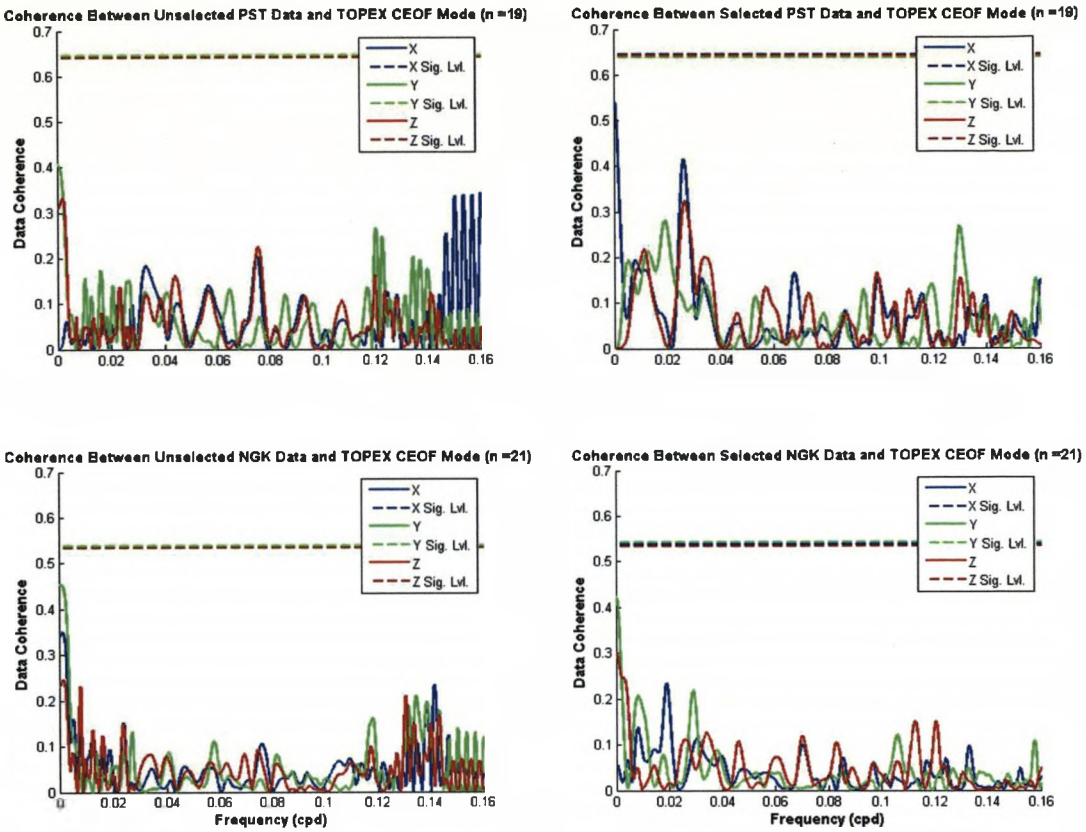

Figure A.4: Plots of coherence between PST (top) & NGK (bottom) time series and the CEOF mode derived by Hughes et al. [2007]. Coherences of unselected magnetic data feature on the left, while those using selected data are placed on the right. 95% significance levels for each magnetic component are marked in panels as dashed lines of appropriate colour, while degrees of freedom (n) used to calculate these levels are shown in the title of each panel.

A.2.2 Dual Observatory EOF Analyses:

Graphical results of PST/AIA dual station EOF analyses are shown in figures A.10 & A.11, with technical details and frequency spectra of mode expansion series shown in table A.2 & figure A.12 respectively. Similarly to single station analyses, the directional details of dual station modes vary significantly from equivalents in chapter 3. However, the direction of the 6th mode is consistent with the chapter 3 equivalent, once again showing strong PST Z and weak AIA Z components (although showing a larger disparity than before), while the percentage variance each mode accounts for is also consistent with short series analyses. Importantly, the 6th mode must again be questioned, as its forced direction (discussed in chapter 3) must be considered. Also, frequency spectra shown in figures A.9 & A.12 do not display prominent signals around the target frequency of 0.04 cpd, casting further doubt over the source of highlighted EOF modes.

These statistical and EOF analyses have illustrated that in most circumstances, longer time series do not result in drastic modifications to analysis results, the only major difference

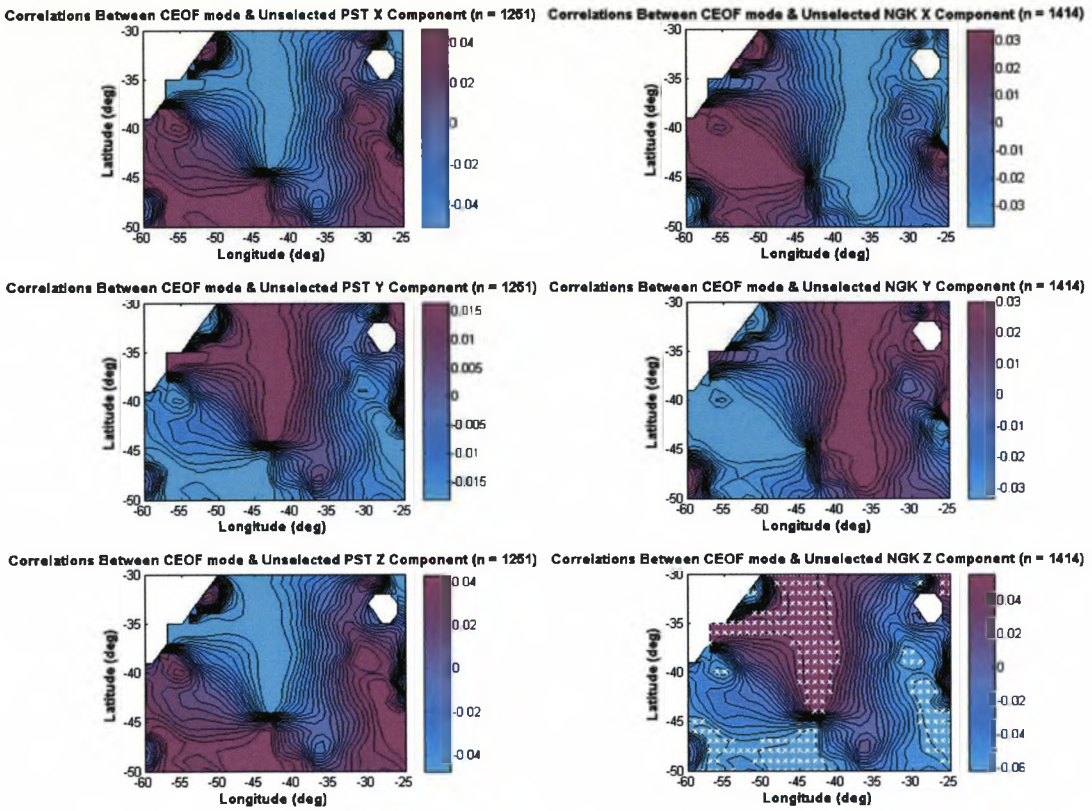

Figure A.5: Correlations between PST (left) & NGK (right) observatory series and the CEOF mode of Hughes et al. [2007]. In this case all observatory series are filtered and unselected. Locations of statistically significant correlations (at the 95% level) are shown as white crosses, with the degrees of freedom available to determine significances (n) shown in the title of each panel.

	1st	2nd	3rd	4th	5th	6th
PST X	0.7634 (0.7724)	0.0922 (0.0240)	0.5079 (0.4891)	0.0385 (0.0025)	-0.0979 (0.0982)	0.3737 (0.3923)
PST Y	-0.0345 (-0.0359)	-0.2448 (-0.2390)	0.0523 (0.0775)	0.6856 (0.7087)	-0.6578 (0.6347)	-0.1830 (-0.1746)
PST Z	0.2333 (0.2510)	0.1967 (0.1790)	0.3004 (0.3312)	-0.0059 (-0.0229)	0.1787 (-0.1738)	-0.8858 (-0.8744)
AIA X	0.5868 (0.5531)	-0.3855 (-0.3957)	-0.6847 (-0.7041)	-0.1068 (-0.0800)	-0.0074 (0.0060)	-0.1640 (-0.1880)
AIA Y	0.0061 (-0.0091	-0.3490 (-0.3615)	0.0803 (0.1019)	0.5860 (0.5514)	0.7209 (-0.7388)	0.0929 (0.0944)
AIA Z	0.1313 (0.1818)	0.7890 (0.7893)	-0.4169 (-0.3727)	0.4167 (0.4321)	0.0780 (-0.1068)	0.0813 (0.0825)
% var	50.94 (49.29)	23.92 (24.35)	11.88 (11.81)	7.72 (8.46)	3.33 (3.55)	2.21 (2.53)

Table A.2: Mode statistics of PST/AIA dual station EOF analyses. Statistics of modes derived using selected data are shown in brackets.

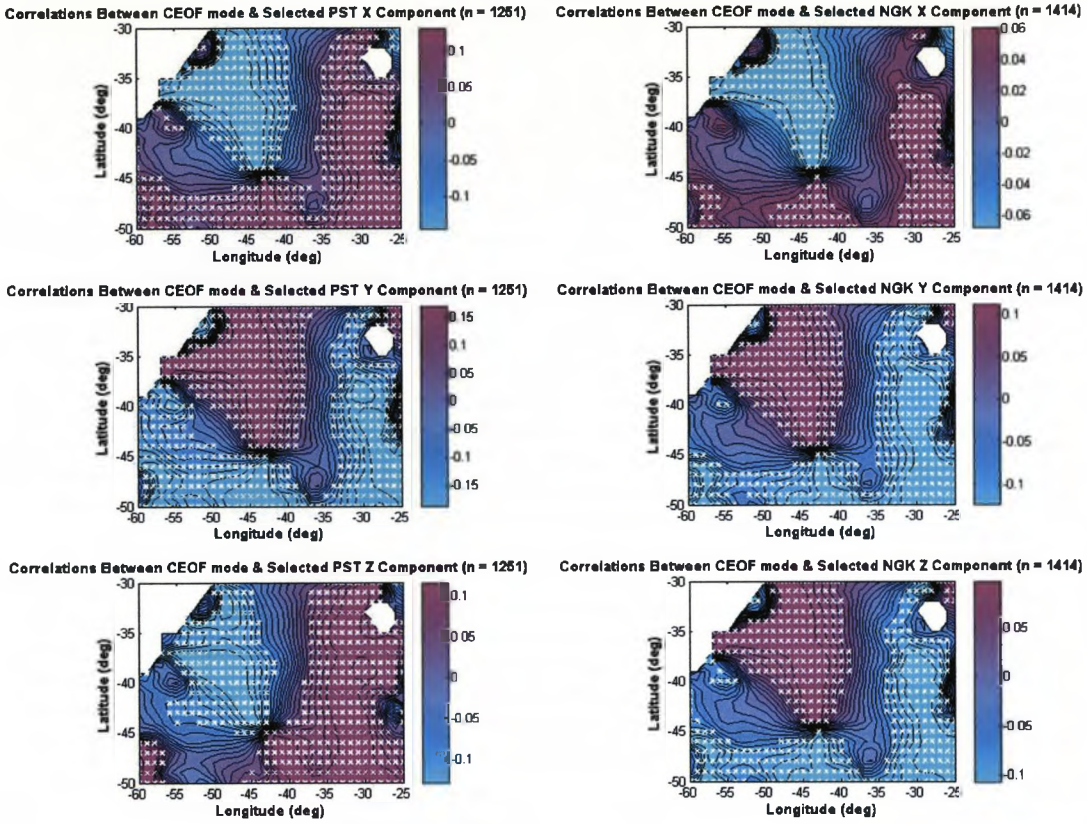

Figure A.6: Correlations between PST (left) & NGK (right) observatory series and the CEOF mode of Hughes et al. [2007]. In these plots all correlations are calculated using filtered, selected observatory series. Locations of statistically significant correlations (at the 95% level) are shown as white crosses, with the degrees of freedom available to determine significances (n) shown in the title of each panel.

being the presence of a $\sim$ 25 day signal in figure A.3. Importantly, regardless of whether EOF analyses use long or short time series, the overall conclusions are the same. While single station EOFs remain too simplistic to form solid hypotheses, dual station EOF modes show possible oceanic content in the final (6th) mode, although the technical limitations of EOF methods and the lack of 25 day signals in associated expansion series (figure A.12) may reduce the robustness of these findings.

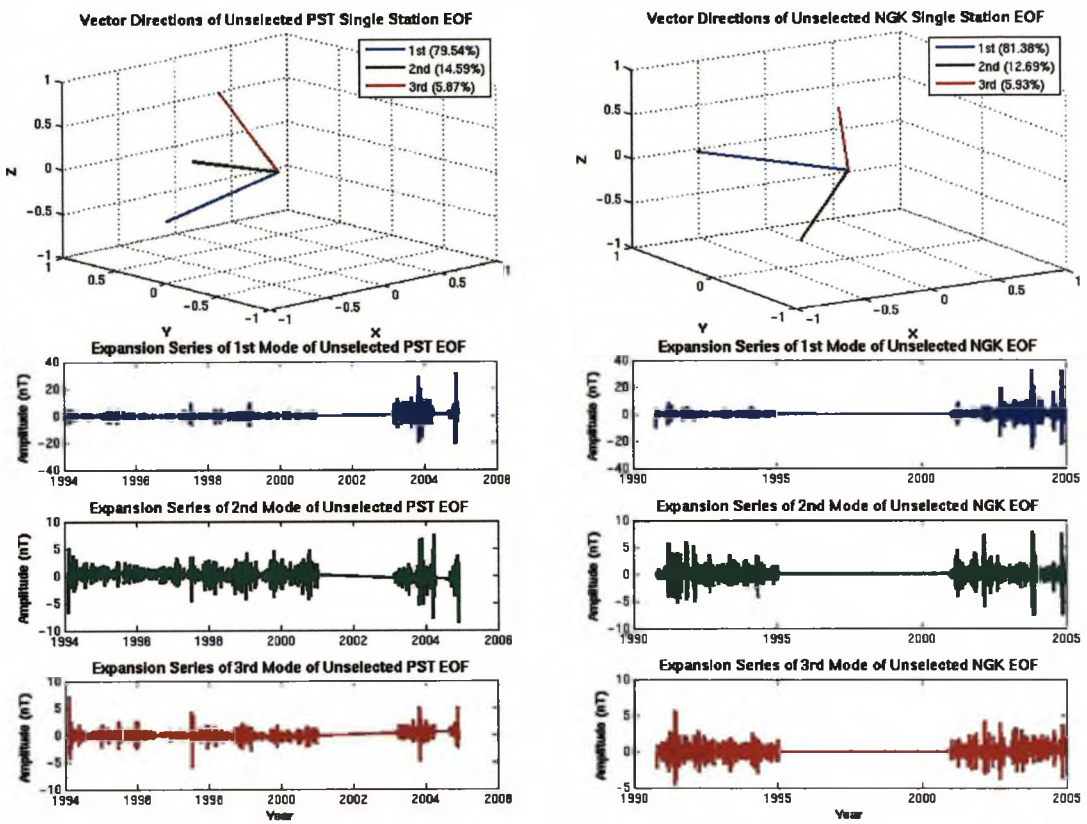

Figure A.7: Graphical results of single station EOF analyses conducted using full length, unselected PST (left) and NGK (right) time series. The upper half of the figure displays the vector directions of each EOF mode, while the lower half displays their expansion series.

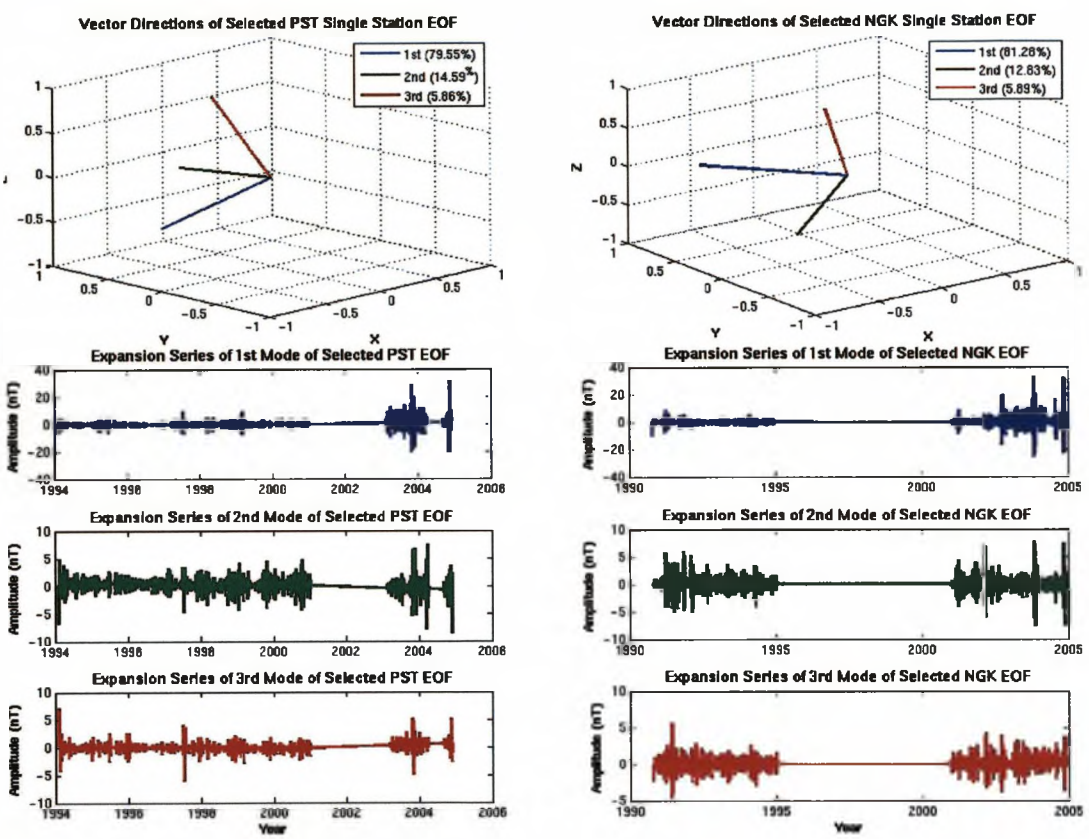

Figure A.8: Graphical results of single station EOF analyses conducted using full length, selected PST (left) and NGK (right) time series. The upper half of the figure shows the directional information of each EOF mode, while the lower half displays their counterpart expansion time series.

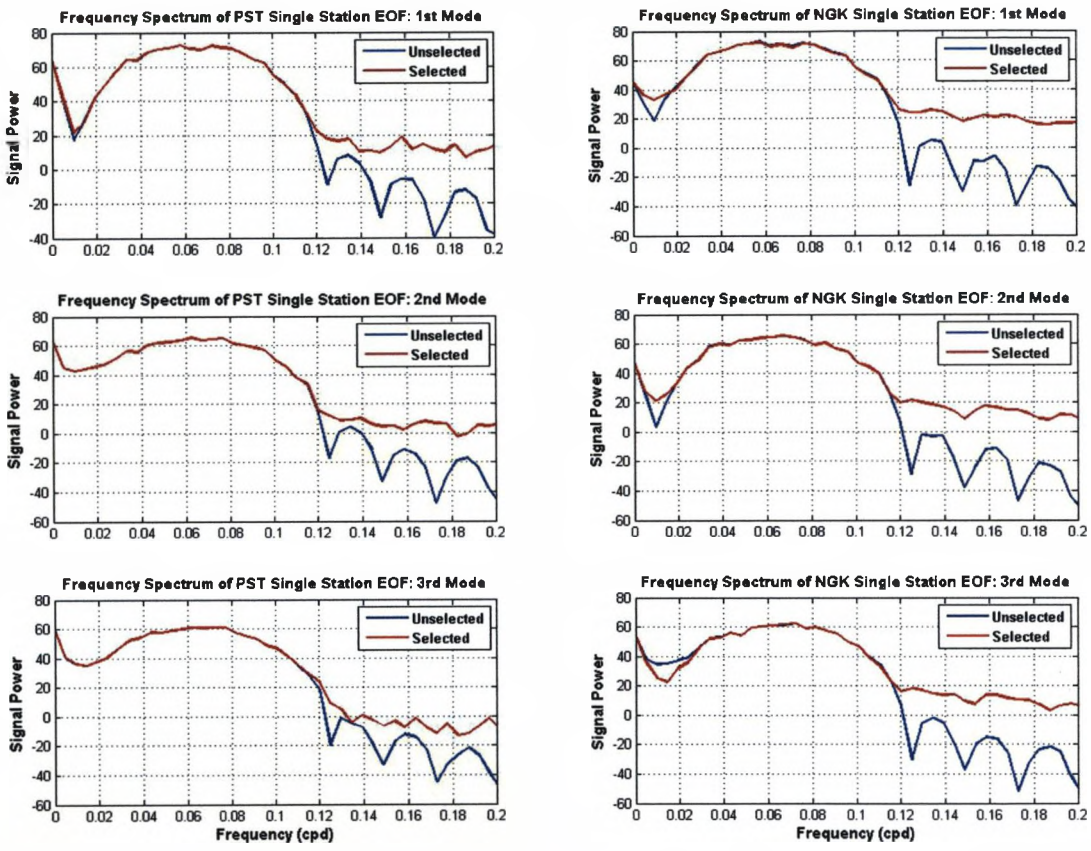

Figure A.9: Frequency spectra of expansion series presented in figures A.7 & A.8 (PST on the left, NGK on the right). Spectra calculated using unselected data are displayed in blue and those using selected data in red.

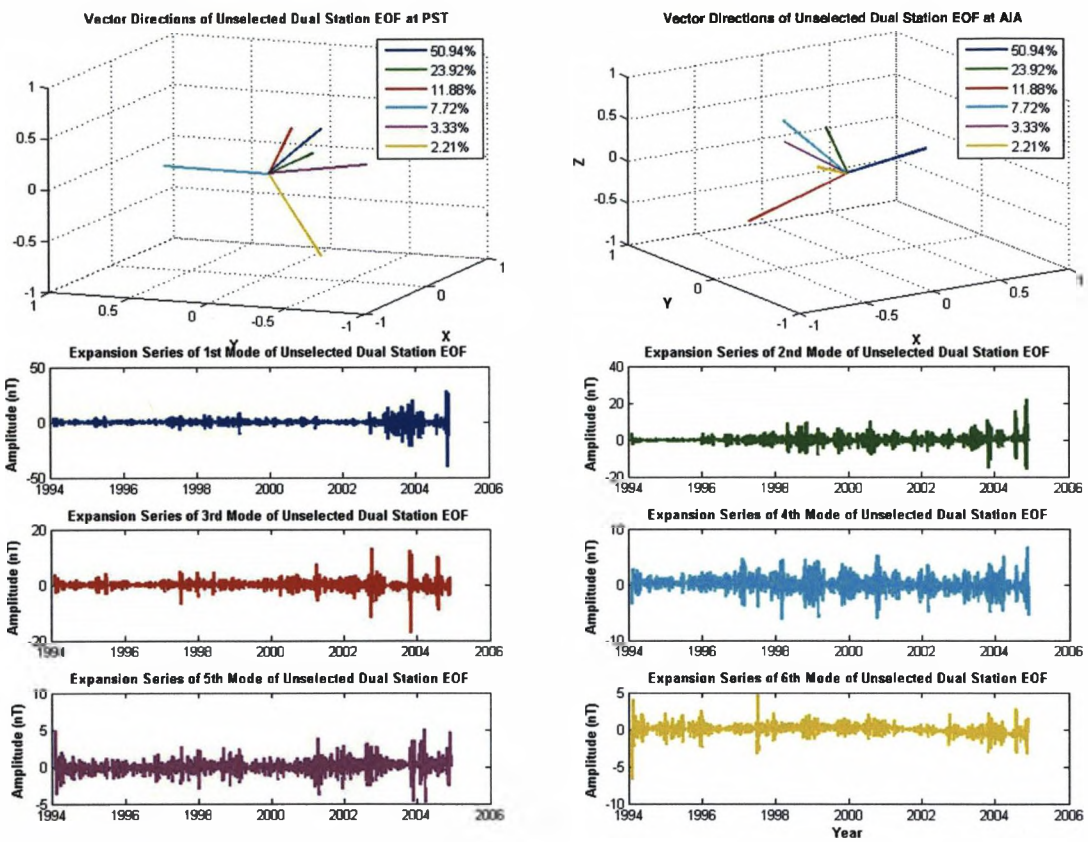

Figure A.10: Graphical results of a dual station EOF analysis of filtered, unselected PST/AIA series. Directions for all 6 modes are shown in the upper half of the figure (PST on the left, AIA on the right),while the lower half displays the expansion time series of the 6 modes.

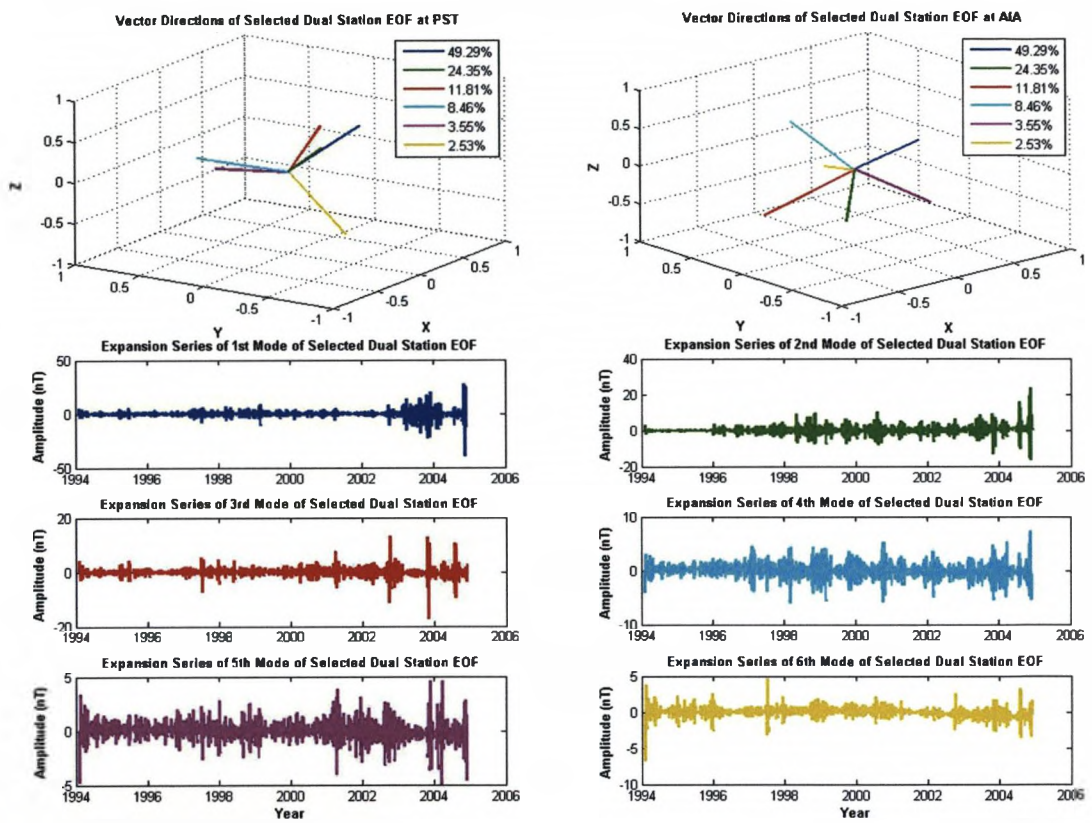

Figure A.11: Graphical details of filtered, selected PST/AIA dual station EOF modes. Directions of all 6 modes are shown in the upper half of the figure (PST on the left, AIA on the right), while the lower half displays their expansion time series.

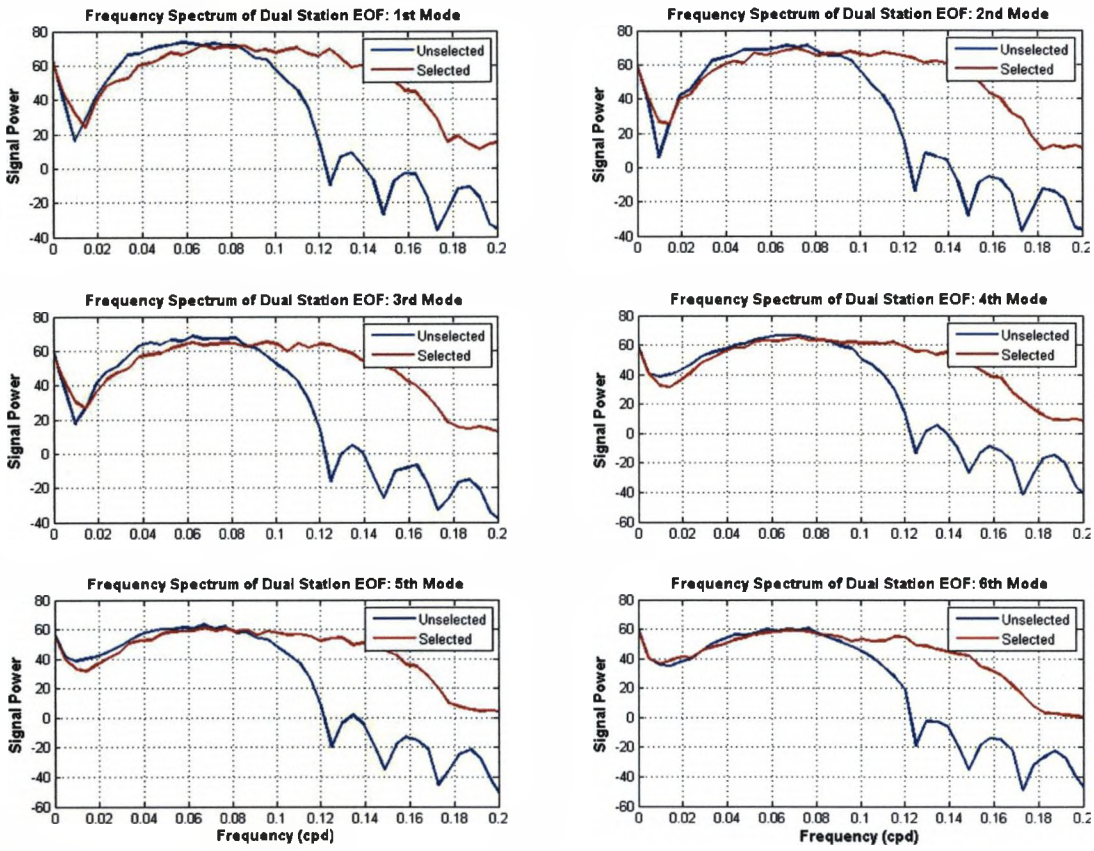

Figure A.12: Frequency spectra of dual station EOF expansion time series presented in figures A.10 & A.11. Spectra calculated using unselected data are displayed in blue and those from selected data in red.

Bibliography

J. P. Angell, T. R. Robinson, and S. P. Lawrence. TOPEX observations of Kelvin, Rossby and tropical instability waves in the pacific ocean. *Advance in Space Research*, 22:1561–1565, 1998.

B. Barnier. A numerical study on the influence of the mid-atlantic ridge on nonlinear first-mode baroclinic Rossby waves generated by seasonal winds. *Journal of Physical Oceanography*, 18:417–433, 1988.

J. Behrens, N. Rakowsky, W. Hiller, D. Handorf, M. Läuter, J. Päpke, and K. Dethloff. amatos: Parallel adaptive mesh generator for atmospheric and oceanic simulation. *Ocean Modelling*, 10:171–183, 2005.

M. Berhanu, R. Monchaux, S. Fauve, N. Mordant, F. Pétrélis, A. Chiffaudel, F. Daviaud, B. Dubrulle, L. Marié, F. Ravelet, Ph. Odier, J. F. Pinton, and R. Volk. Magnetic field reversals in an experimental turbulent dynamo. *Europhysics Letters*, 77, 2007.

H. Björnsson and S. A. Venegas. *A manual for EOF and SVD analyses of climatic data.* Department of Atmospheric and Oceanic Sciences & Centre for Climate and Global Change Research, McGill University, Montréal, Québec, 1997.

J. Bloxham and D. Gubbins. The secular variation of Earth's magnetic field. *Nature*, 317: 777–781, 1985.

J. Bloxham, D. Gubbins, and A. Jackson. Geomagnetic secular variation. *Phil. Trans. R. Soc. Lond. A*, 329:415–502, 1989.

J. Bloxham and A. Jackson. Time-dependent mapping of the magnetic field at the core-mantle boundary. *Journal of Geophysical Research-Solid Earth*, 97:19537–19563, 1992.

B. A. Buffet. Earth's core and the geodynamo. *Science*, 288:2007–2012, 2000.

B. A. Buffet, H. E. Huppert, J. R. Lister, and A. W. Woods. Analytical model for solidification of the Earth's core. *Nature*, 356:329–331, 1992.

E. C. Bullard, C. Freedman, H. Gellman, and J. Nixon. The westward drift of the Earth's magnetic field. *Phil. Trans. R. Soc. Lond. A*, 243:67–92, 1950.

P. G. Challenor, P. Cipollini, D. Cromwell, K. L. Hill, G. D. Quartly, and I. S. Robinson. Global characteristics of Rossby wave propagation from multiple satellite datasets. *International Journal of Remote Sensing*, 25:1297–1302, 2004.

D. B. Chelton, R. A. de Szoeke, M. G. Schlax, K. E. Naggar, and N. Siwertz. Geographical variability of the first baroclinic Rossby radius of deformation. *Journal of Physical Oceanography*, 28:433–460, 1998.

D. B. Chelton and M. G. Schlax. Global observations of oceanic Rossby waves. *Science*, 272: 234–238, 1996.

A. Chulliat. Geomagnetic secular variation generated by a tangentially geostrophic flow under frozen-flux assumption - II. Sufficient conditions. *Geophys. J. Int*, 157:537–552, 2004.

A. Chulliat and G. Hulot. Geomagnetic secular variation generated by a tangentially geostrophic flow under the frozen-flux approximation - I. Necessary conditions. *Geophys. J. Int*, 147:237–246, 2001.

P. Cipollini, P. G. Challenor, D. Cromwell, K. L. Hill, G. D. Quartly, and I. S. Robinson. Remote sensing of oceanic Rossby waves: new techniques and results. In *Geoscience and Remote Sensing Symposium, 2000. Proceedings, IGARSS 2000. IEEE 2000 International*, volume 5, pages 1824–1826, 2000a.

P. Cipollini, P. G. Challenor, D. Cromwell, G. D. Quartly, and S. Raffaglio. Detection of Rossby waves in ocean colour data. In *Geoscience and Remote Sensing Symposium, 2000. Proceedings, IGARSS 2000. IEEE 2000 International*, volume 5, pages 1821–1823, 2000b.

P. Cipollini, D. Cromwell, M. S. Jones, G. D. Quartly, and P. G. Challenor. Concurrent altimeter and infrared observations of Rossby wave propagation near 34°N in the northeast Atlantic. *Geophysical Research Letters*, 24:889–892, 1997.

P. Cipollini, G. D. Quartly, P. G. Challenor, D. Cromwell, and I. S. Robinson. *Manual of remote sensing vol.6 - Remote sensing of the marine environment.* ASPRS Publications, 2006.

A. C. Coward, B. A. de Cuevas, and D. J. Webb. Early results from a $1/12^{o} \times 1/12^{o}$ global ocean model. Poster presentation at WOCE conference, 2002.

N. Ducet, P. Y. Le Traon, and G. Reverdin. Global high-resolution mapping of ocean circulation from TOPEX/POSEIDON and ERS-1 and -2. *Journal of Geophysical Research*, 105:19477–19498, 2000.

G. D. Egbert, A. F. Bennett, and M. G. G. Foreman. TOPEX/POSEIDON tides estimated using a global inverse model. *Journal of Geophysical Research*, 99:24821–24852, 1994.

C. C. Finlay. *Hydromagnetic waves in Earth's core and their influence on geomagnetic secular variation.* PhD thesis, The University of Leeds, School of Earth and Environment, 2005.

R. Ford, C. C. Pain, M. D. Piggott, A. J. H Goddard, C. R. E. Oliveira, and A. P. Umpleby. A non-hydrostatic finite-element for three-dimensional stratified ocean flows. Part I: model formulation. *Monthly Weather Review*, 132:2816–2831, 2004a.

R. Ford, C. C. Pain, M. D. Piggott, A. J. H Goddard, C. R. E. Oliveira, and A. P. Umpleby. A non-hydrostatic finite-element for three-dimensional stratified ocean flows. Part II: model validation, 2004b.

C. M. R. Fowler. *The solid Earth.* Cambridge University Press, 1990.

Lee Lueng Fu, Benny Cheng, and Bo Qiu. 25-day period large-scale oscillations in the Argentine basin revealed by the TOPEX/POSEIDON altimeter. *Journal of Physical Oceanography*, 31:506–517, 2001.

R. Gerdes and C. Wübber. Seasonal variability of the north Atlantic ocean - a model intercomparison. *Journal of Physical Oceanography*, 21:1300–1322, 1991.

A. E. Gill. *Atmosphere-ocean dynamics.* Academic Press, 1982.

N. Gillet, D. Brito, D. Jault, and H. C. Hataf. Experimental and numerical studies of magnetoconvection in a rapidly rotating spherical shell. *J. Fluid Mech.*, 580:123–143, 2007.

David Gubbins. *Time series analysis and inverse theory for geophysicists.* Cambridge, 2004.

R. Harkema and G. L. Weatherly. A compilation of moored current meter data in the Argentine basin: April 25, 1987 - March 14, 1988. Technical report cmf-89-01, Dept. of Oceanography, Florida State University, 1989.

K. Hemant and S. Maus. Geological modelling of the new CHAMP magnetic anomaly maps using a geographical information system technique. *Journal of Geophysical Research*, 110: B12103, 2005.

K. L. Hill, I. S. Robinson, and P. Cipollini. Propagation characteristics of extratropical planetary waves observed in the ASTR global sea surface temperature record. *Journal of Geophysical Research C (Oceans)*, 105:21927–21945, 2000.

R. Holme. Modelling of attitude error in vector magnetic data: application to Ørsted data. *Earth Planets Space*, 52:1187–1197, 2000.

R. Holme and O. de Viron. Geomagnetic jerks and a high-resolution length-of-day profile for core studies. *Geophys. J. Int*, 160:435–439, 2005.

R. Holme, N. Olsen, M. Rother, and H. Lühr. CO2 - a CHAMP magnetic field model. In C. Reigber, H. Lühr, and P. Schwintzer, editors, *First CHAMP Mission Results for Gravity, Magnetic and Atmospheric Studies*, pages 220–225. Springer Verlag, Berlin, 2003.

Richard Holme and Jeremy Bloxham. The treatment of attitude errors in satellite geomagnetic data. *Physics of the Earth and Planetary Interiors*, 98:221–233, 1996.

S. S. Hough. On the application of harmonic analysis to the dynamical theory of the tides, Part I, On Laplace's "oscillations of the first species", and on the dynamics of the ocean currents. *Philos. Trans. Roy. Soc. A*, 189:201–257, 1897.

C. W. Hughes, V. N. Stepanov, L. L. Fu, B. Barnier, and G. W. Hargreaves. Three forms of variability in Argentine basin ocean bottom pressure. *Journal of Geophysical Research*, 112:C01011, 2007.

A. Jackson, A. R. T. Jonkers, and M. R. Walker. Four centuries of geomagnetic secular variation from historical records. *Phil. Trans. R. Soc. Lond. A*, 358:957–990, 2000.

G. A. Jacobs, H. E. Hulbert, J. C. Kindle, E. J. Metzger, J. L. Mitchell, W. J. Teague, and A. J. Wallcraft. Decade-scale trans-Pacific propagation and warming effects of an El Nino anomaly. *Nature*, 370:360–363, 1994.

P. D. Killworth and J. R. Blundell. The effect of bottom topography on the speed of long extratropical planetary waves. *Journal of Physical Oceanography*, 29:2689–2710, 1999.

P. D. Killworth and J. R. Blundell. Long extratropical planetary wave propagation in the presence of slowly varying mean flow and bottom topography. Part I: The local problem. *Journal of Physical Oceanography*, 33:784–801, 2003a.

P. D. Killworth and J. R. Blundell. Long extratropical planetary wave propagation in the presence of slowly varying mean flow and bottom topography. Part II: Ray propagation and comparison with observations. *Journal of Physical Oceanography*, 33:802–821, 2003b.

P. D. Killworth, D. B. Chelton, and R. A. de Szoeke. The speed of observed and theoretical long extratropical planetary waves. *Journal of Physical Oceanography*, 27:1946–1966, 1997.

M. G. Kivelson and C. T. Russell. *Introduction to space physics.* Cambridge University Press, 1995.

M. Korte and C. G. Constable. Continuous geomagnetic field models for the past 7 millenia: 2. CALS7K. *Geochem. Geophys. Geosys*, 6, 2005.

M. Korte, A. Genevey, C. G. Constable, U. Frank, and E. Schnepp. Continuous geomagnetic field models for the past 7 millenia: 1. A new global data compilation. *Geochem. Geophys. Geosys*, 6, 2005.

A. Kuvshinov and N. Olsen. 3-D modelling of the magnetic fields due to ocean tidal flow. In C. Reigber, H. Lühr, P. Schwintzer, and J. Wickert, editors, *Earth Observation with CHAMP: Results from Three Years in Orbit*, pages 359–365. Springer Berlin Heidelberg, 2005.

R. A. Langel. The main field. In J. A. Jacobs, editor, *Geomagnetism*, volume 1, chapter 4. Academic, San Diego, Calif, 1987.

P. H. LeBlond and L. A. Mysak. *Waves in the ocean.* Elsevier, 1978.

Vincent Lesur, Susan Macmillan, and Alan Thomson. A magnetic field model with daily variations of the magnetospheric field and its induced counterpart in 2001. *Geophys. J. Int*, 160:79–88, 2005.

F. E. M. Lilley, A. White, G. S. Heinson, and K. Procko. Seeking a seafloor magnetic signal from the Antarctic Circumpolar Current. *Geophys. J. Int*, 157:175–186, 2004.

S. R. C. Malin. Worldwide distribution of geomagnetic tides. *Phil. Trans. R. Soc. Lond. A*, 274:551–594, 1973.

M. Mandea and J-L. Le Mouël. A geomagnetic jerk for the end of the 20th century? *Earth and Planetary Science Letters*, 183:369–373, 2000.

C. Manoj, A. Kuvshinov, S. Maus, and H. Lühr. Ocean circulation generated magnetic signals. *Earth Planets Space*, 58:429–437, 2006.

S. Maus and A. Kuvshinov. Ocean tidal signals in observatory and satellite magnetic measurements. *Geophysical Research Letters*, 31:L15313, 2004.

S. Maus, H. Lühr, M. Rother, K. Hemant, G. Balasis, P. Ritter, and C. Stolle. Fifth-generation lithospheric magnetic field model from CHAMP satellite measurements. *Geochem. Geophys. Geosys*, 8, 2007a.

S. Maus, M. Rother, K. Hemant, C. Stolle, H. Lühr, A. Kuvshinov, and N. Olsen. Earth's lithospheric magnetic field determined to spherical harmonic degree 90 from CHAMP satellite measurements. *Geophys. J. Int*, 164:319–330, 2006.

S. Maus, T. Sazonova, K. Hemant, J. D. Fairhead, and D. Ravat. National Geophysical Data Center candidate for the World Digital Magnetic Anomaly Map. *Geochem. Geophys. Geosys*, 8, 2007b.

J. D. McKnight. Lunar daily geomagnetic variations in New Zealand. *Geophys. J. Int*, 122: 889–898, 1995.

M. J. McPhaden. The eleven-year El Nino. *Nature*, pages 326–327, 1994.

James C. McWilliams. *Fundamentals of geophysical fluid dynamics.* Cambridge University Press, 2006.

J. L. Le Mouël, T. Madden, J. Ducruix, and V. Courtillot. Decade fluctuations in geomagnetic westward drift and earth rotation. *Nature*, 290:763–765, 1981.

N. Olsen, R. Haagmans, T. J. Sabaka, A. Kuvshinov, S. Maus, M. E. Purucker, M. Rother, V. Lesur, and M. Mandea. The *Swarm* End-to-End mission simulator study: A demonstration of separating the various contributions of Earth's magnetic field using synthetic data. *Earth Planets Space*, 58:359–370, 2006a.

N. Olsen, R. Holme, G. Hulot, T. Sabaka, T. Neubert, L. Tøffner-Clausen, F. Primdahl, J. Cain, C. Constable, V. Golovkov, A. Jackson, P. Kotzé, B. Langlais, S. Macmillan, M. Mandea, J. Merayo, L. Newitt, M. Purucker, T. Risbo, M. Stampe, A. Thomson, and C. Voorhies. Ørsted initial field model. *Geophysical Research Letters*, 27, No.22:3607–3610, 2000.

N. Olsen, H. Lühr, T. J. Sabaka, M. Mandea, M. Rother, L. Tøffner-Clausen, and S. Choi. CHAOS - A model of the Earth's magnetic field derived from CHAMP, Ørsted and SAC-C magnetic satellite data. *Geophys. J. Int*, 166:67–75, 2006b.

N. Olsen and M. Mandea. Investigation of a secular variation impulse using satellite data: The 2003 geomagnetic jerk. *Earth and Planetary Science Letters*, 255:94–105, 2007.

C. C. Pain, M. D. Piggott, A. J. H. Goddard, F. Fang, G. J. Gorman, D. P. Marshall, M. D. Eaton, P. W. Power, and C. R. E. de Oliveira. Three-dimensional unstructured mesh ocean modelling. *Ocean Modelling*, 10:5–33, 2005.

F. Ponchaut, F. Lyard, and C. Le Provost. An analysis of the tidal signal in the WOCE sea level dataset. *Journal of Atmospheric and Oceanic Technology*, 18:77–91, 2001.

R. W. Preisendorfer. *Principal component analysis in meteorology and oceanography.* Elsevier, 1988.

M. E. Purucker and J. Dyment. Satellite magnetic anomalies related to seafloor spreading in the South Atlantic ocean. *Geophysical Research Letters*, 27:2765–2768, 2000.

P. B. Rhines. Slow oscillations in an ocean of varying depth: Part 1. Abrupt topography. *J. Fluid Mech.*, 37:161–189, 1969.

P. Ritter and H. Lühr. Search for magnetically quiet CHAMP polar passes and the characteristics of ionospheric currents during the dark season. *Annales Geophysicae*, 24:2997–3009, 2004.

P. H. Roberts and G. A. Glatzmaier. Geodynamo theory and simulations. *Reviews of Modern Physics*, 72:1081–1123, 2000.

C. G. Rossby. Planetary flow patterns in the atmosphere. *Q. J. Metero. Soc.*, 66:68–87, 1940.

C. G. Rossby, J. Smith, and J. Bloggs. Relations between variations in the intensity of the zonal circulation of the atmosphere and the displacements of the semi-permanent centers of action. *J. Mar. Res.*, 2:38–55, 1939.

Terence J. Sabaka, Nils Olsen, and Robert A. Langel. A comprehensive model of the quiet-time, near Earth magnetic field: phase 3. *Geophys. J. Int*, 151:32–68, 2002.

Terence J. Sabaka, Nils Olsen, and Michael E. Purucker. Extending comprehensive models of the Earth's magnetic field with Ørsted and CHAMP data. *Geophys. J. Int*, 159:521–547, 2004.

T. B. Sanford. Motionally induced electric and magnetic fields in the sea. *Journal of Geophysical Research*, 76:3476–3492, 1971.

P. M. Saunders, A. C. Coward, and B. A. de Cuevas. Circulation of the Pacific ocean seen in a global ocean model (OCCAM). *J. Geophys. Res.*, 104:18281–18299, 1999.

D. J. Stevenson. Models of the Earth's core. *Science*, 214:611–619, 1981.

C. K. Tai and L. L. Fu. The 25-day-period large-scale oscillations in the Argentine basin revisited. *Journal of Physical Oceanography*, 35:1473–1479, 2005.

R. T. Tokmakian and P. G. Challenor. Observations in the Canary basin and the Azores frontal region using Geosat data. *Journal of Geophysical Research*, 98:4761–4773, 1993.

P. Y. Le Traon and J. F. Minster. Sea level variability and semiannual Rossby waves in the south Atlantic subtropical gyre. *Journal of Geophysical Research*, 98:12315,12326, 1993.

N. A. Tsyganenko. A model of the near magnetosphere with a dawn-dusk asymmetry. 1. Mathematical structure. *Journal of Geophysical Research*, 107, 2002a.

N. A. Tsyganenko. A model of the near magnetosphere with a dawn-dusk asymmetry. 2. Parameterisation and fitting to observations. *Journal of Geophysical Research*, 107, 2002b.

R. Tyler, S. Maus, and H. Lühr. Satellite observations of magnetic fields due to ocean tidal flow. *Science*, 299:239–241, 2003.

R. H. Tyler. A simple formula for estimating the magnetic fields generated by tsunami flow. *Geophysical Research Letters*, 32:L09608, 2005.

R. H. Tyler, J. M. Oberhuber, and T. B. Sanford. The potential for using ocean generated electromagnetic fields to remotely sense ocean variability. *Phys. Chem. Earth (A)*, 24, No.4:429–432, 1999.

Robert H. Tyler and Lawrence A. Mysak. Electromagnetic fields generated by a three dimensional global ocean circulation. *Journal of Geophysical Research*, 102, No.C3:5531–5551, 1997.

Frédéric Vivier, Ernst Maier-Riemer, and Robert H. Tyler. simulations of magnetic fields generated by the Antarctic Circumpolar Current at satellite altitude: can geomagnetic measurements be used to monitor the flow? *Geophysical Research Letters*, 31:L10306, 2004.

W. Weijer, F. Vivier, and H. A. Dijkstra. Multiple oscillatory modes of the Argentine basin. Part I: statistical analysis. *Journal of Physical Oceanography*, 37:2855–2868, 2007a.

W. Weijer, F. Vivier, and H. A. Dijkstra. Multiple oscillatory modes of the Argentine basin. Part II: the spectral origin of basin modes. *Journal of Physical Oceanography*, 37:2869–2881, 2007b.